UNIVERSITY OF CALGARY

High-Resolution Infrared Spectroscopy of van der Waals Clusters of Nitrous Oxide, Carbon Dioxide and OCS-R Complexes

by

Jalal Norooz Oliaee

A THESIS

SUBMITTED TO THE FACULTY OF GRADUATE STUDIES

IN PARTIAL FULFILLMENT OF THE REQUIREMENTS FOR THE

DEGREE OF DOCTOR OF PHILOSOPHY

DEPARTMENT OF PHYSICS AND ASTRONOMY

CALGARY, ALBERTA

May, 2013

Abstract

Weakly-bound van der Waals complexes containing OCS and various hydrocarbons, and clusters of N_2O, and CO_2 are studied by means of their rotationally-resolved infrared spectra. Clusters are generated in a pulsed supersonic jet expansion with two slit-shaped nozzles and probed with a tuneable diode laser.

Study of OCS-R complexes (R indicates certain hydrocarbons with chain or ring structures) commenced with the study of OCS-acetylene complex in the region of ν_1 stretching fundamental of OCS ($\sim$ 2060 cm^{-1}). Two bands are observed and assigned to near-parallel and T-shaped isomers of OCS-acetylene. In addition to the normal species, the deuterated isotopic form is also studied.

Simple looking bands characteristic of a T-shaped structure are observed for complexes formed between OCS and ethylene, allene, propyne, dimethylacetylene, benzene, and cyclooctatetraene. All the bands are observed to be red-shifted from the OCS monomer ν_1 frequency.

Infrared bands in the CO_2 ν_3 region ($\sim$ 2350 cm^{-1}) are assigned to carbon dioxide clusters, $(CO_2)_N$, with N = 6, 7, 9, 10, 11, 12, and 13. Assignments are aided by cluster calculations using two reliable CO_2 intermolecular potential functions. These are the largest molecular clusters studied by infrared spectroscopy with rotational resolution. Two highly symmetric isomers with S_6 and S_4 symmetries are observed for $(CO_2)_6$. $(CO_2)_{13}$ is also symmetric with S_6 symmetry, but all the remaining clusters are asymmetric tops. The bands have increasing blue-shifts with increasing cluster size, similar to predictions of resonant dipole-dipole model but considerably larger in magnitude.

N_2O tetramer is studied in the region of N_2O ν_1 fundamental ($\sim$ 2220 cm^{-1}). The previously observed oblate isomer of $(N_2O)_4$ is studied with considerably higher resolution. Isotopic substitution has confirmed a structure with D_{2d} symmetry for this isomer. In addi-

tion to the oblate isomer, a new prolate isomer of $(N_2O)_4$ with S_4 symmetry is observed.

Acknowledgements

First and foremost, I would like to express my sincerest gratitude to my supervisor Dr. Nasser Moazzen-Ahmadi for all his support, patience, and scientific guidance throughout my Ph.D. studies. My special thanks also goes to Dr. A.R.W. McKellar for his helps and fruitful discussions. I also would like to thank Dr. Christoph Simon and Dr. Jörn Davidsen for accepting to be members of my supervisory committee and their inspiring questions during our committee meetings. Thanks to Dr. Pierre-Nicholas Roy (from University of Waterloo) and Dr. Simon Trudel who generously accepted to serve as examiners.

I would like to mention our former group members in the laser spectroscopy lab, Mahin and Nader, whom I learnt from and enjoyed working with. Also, technical assistance of Lanny Murdock is greatly appreciated.

I would like to acknowledge my friends Khabat, Sadegh and many others for providing moral support. I greatly acknowledge the helps of Mehdi and my long-life family friends, Majid and Saeid who helped me to settle down in Calgary.

My very special and heartfelt thanks is dedicated to my parents, Razieh and Hassan, for their encouragement and unconditional support. My warm gratitude goes to my sisters and brother, Shirin, Farzane, and MohammadJavad for their kindness and good wishes. Presence of Farzane here in Calgary in 2010 brought me joy and delight. At last but not least, I would like to thank my very kind wife, Marjan, for her loving care in the past couple of years. Words are not enough to say how she gives me hope and endless love in my life.

Table of Contents

List of Tables

List of Figures and Illustrations

Chapter 1

Introduction

1.1 Weak intermolecular interactions

Weak intermolecular forces are responsible for various phenomena in nature, ranging from physics and chemistry to biology. Examples include condensation, solvation, aerosol formation [3], protein conformation [4], and adsorption of atoms and molecules on surfaces [5]. Physical properties of matter such as melting point and boiling point, viscosity, surface tension, molar density, specific heat capacity, etc. depend on intermolecular forces. A simple example showing the significant role of intermolecular interaction, is in water which has a lower density than in the solid phase. This is the reason for ice to float on water which is vital to marine life.

Weak van der Waals forces were first recognized as attractive forces between neutral particles of dense gases, representing themselves as deviations from the ideal gas law. Particles attraction is mainly due to interaction between dipole moments. The dipole moment of a molecule may be a permanent dipole moment possessed by a polar molecule, or an induced dipole moment within a non-polar molecule caused by a polar molecule, or a transient dipole. In any case, the potential for the interaction of dipoles, when their angular distribution is taken into account, is inversely proportional to the sixth power of distance (i.e. $\propto 1/r^6$). The dipole-dipole interaction is the dominant term in the interactions between neutral molecules but there are higher order terms which include dipole-multipole and multipole-multipole interactions. The potential energy for these interactions drop much faster than the dipole-dipole interaction.

van der Waals forces are in fact the sum of attractive multipole-multipole forces which are dominant in the long range and electrostatic repulsive forces that dominate in the short

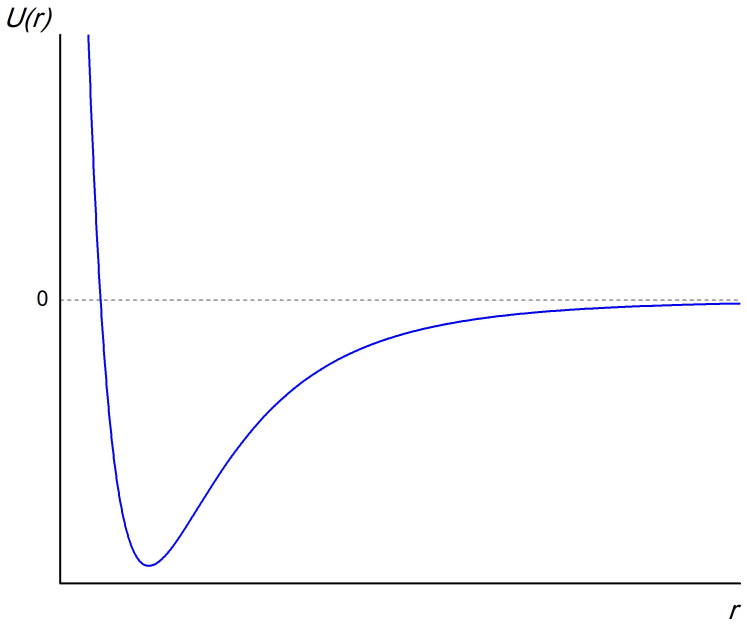

Figure 1.1: The potential energy curve due to the sum of repulsive and attractive contributions to the van der Waals intermolecular force.

range. Repulsive forces are due to the electrostatic repulsion between positively-charged nuclei and repulsion between negatively-charged electron clouds of different molecules. The competition of repulsive and attractive forces results in a potential with a shallow minimum as depicted in Figure 1.1. This potential can be modeled using various model potentials such as Lennard-Jones potential or Morse potential.

A combination of molecules held together in the potential minimum by intermolecular forces is referred to as a complex. The term "cluster" is customarily used when the molecules within a complex are of the same type. Weak intermolecular interactions such as van der Waals forces or Hydrogen bonds are responsible for the formation of molecular clusters. Molecular clusters represent intermediate states between gas and condensed phases of matter. Individual molecules in the gas phase coalesce to form binary (dimer), ternary (trimer), quaternary (tetramer) and larger size clusters which eventually lead to the liquid and solid phases. Because of the drastic increase in the number of possible geometries with the cluster

size, many condensation pathways can be taken in forming a given cluster. However, the contribution of each of the elements of the intermolecular interaction in condensation dynamics is not well understood in chemistry and physics. Theoretical and *ab initio* studies employ principles of quantum mechanics to describe contributions of each element in condensation pathways by calculating possible structures for molecular clusters and their relative binding energies. Although technological advances has enabled the use of computers and supercomputers in performing high-level *ab initio* calculation, experimental spectroscopic studies provide indisputable accurate results for direct measurement of intermolecular forces against which the theory can be benchmarked. The motivation behind studying weakly-bound clusters is therefore to find out which pathways are preferentially followed and to understand the factors determining these pathways.

At room temperature, kT is greater than the binding energies of van der Waals clusters. Therefore van der Waals clusters can not stabilize because of thermal agitations. An effective cooling technique to generate weakly-bound clusters is supersonic jet expansion where high pressure gas of desired molecules seeded in a buffer gas (usually a rare gas) expands adiabatically into a high vacuum chamber through an orifice. The speed of the flow may exceed the local speed of sound that is why the term "supersonic" is used. This results in a great reduction of internal energy of molecules and translational, rotational, and vibrational degrees of freedom of molecules cool down such that van der Waals forces find an opportunity to take over and form complexes. As a consequence of cooling of rotational and vibrational degrees of freedom, only the lowest rotational and vibrational energy levels are populated which results in a drastic simplification of ro-vibrational spectra and its analysis. Structural studies of molecular complexes and clusters formed in the supersonic jet can be carried out by means of high-resolution microwave or infrared spectroscopy. Infrared spectroscopy has the additional advantage of revealing information about vibrational dynamics and provides a handle on both polar and non-polar molecules.

The laser spectroscopy lab at the University of Calgary uses a pulsed jet apparatus with slit-shaped nozzles along with a tuneable diode laser probe in the infrared region. This supersonic jet system has two prominent features. First, the laser is operated in rapid-scan mode with continuous background subtraction that reduces the noise level in the recorded spectra. Second, an astigmatic multi-pass cell is incorporated in the vacuum chamber which allows for nearly 180 laser passes through the molecular beam in order to increase the absorption path-length.

1.2 Present thesis

The present thesis is mainly concerned with spectroscopic identification and structure determination of molecular clusters. Particularly, a number of T-shaped OCS-hydrocarbon complexes, large clusters of CO_2 having between 6 to 13 carbon dioxide molecules, and $(N_2O)_4$. In the following sections the motivation behind each study together with an overview of previous works and the present work is presented.

1.2.1 OCS-R complexes

Carbonyl sulfide is the most abundant sulfur gas in the atmosphere and on the other hand, hydrocarbons (indicated by R) play an essential role in atmospheric chemistry. Therefore, study of intermolecular interactions between carbonyl sulfide and hydrocarbons sheds light on their role in atmospheric chemistry.

In 1999, the first spectrum of OCS$-C_2H_2$ was observed in the microwave region by Peebles and Kuczkowski in which the two monomers where in a planar nearly-parallel arrangement [6]. After the assignment of the parallel isomer, there were still unassigned lines in their spectra, subsequent analysis of which led to the discovery of another planar isomer but with a T-shaped configuration (with HCCH as the top of the T, OCS as the stem, and the S atom adjacent to the C≡C bond) [7]. Chapter 4 presents the results of studies on

the same parallel and T-shaped isomers of OCS$-C_2H_2$ in the infrared region by exciting the OCS ν_1 fundamental vibration. Study of OCS$-C_2H_2$ triggered the study of interaction of OCS with other small hydrocarbons. Infrared spectra of seven chain and ring hydrocarbons are described in Chapter 5, many of which exhibit a relatively simple rotation-vibration band structure characteristic of a T-shaped configuration. When the hydrocarbon is a ring species, "wheel and axle" or "daisy shaped" may better explain the structure. In this study, the OCS molecule serves as a probe which interacts with the charge distribution of the hydrocarbon molecule.

Although in the case of OCS$-C_2H_2$ it is indicated, both theoretically and experimentally, that the T-shaped isomer is a higher energy isomer, but for the rest of OCS$-$R complexes, the exact energy ordering of the T-shaped structure needs to be settled by detailed experimental and theoretical studies.

1.2.2 CO_2 clusters

Binary and ternary clusters provide a convenient starting point for the study of intermolecular potential energy surface and have been the subject of study in many instances. However, study of larger molecular clusters becomes a more difficult task due to the drastic increase in the number of parameters involved and also the high resolution required to study their structures. Only a few detailed experimental studies on clusters with 4 or more molecular units are reported in the literature [8–12].

In spite of importance of atmospheric CO_2 for the earth and other planets, only dimers and trimers have previously been studied. The dimer has a planar slipped parallel structure with centrosymmetric C_{2h} symmetry [13]. The structure of the CO_2 dimer and two isomers of CO_2 trimer are illustrated in Figure 1.2. A planar isomer for CO_2 trimer was first observed in 1987 [14]. This isomer was found to be a symmetric top with a planar cyclic structure having C_{3h} symmetry. There were spectral evidence and theoretical predictions for an energetically comparable trimer isomer with C_2 symmetry that was later confirmed by experiment [15].

Recent work on CO_2 dimer and trimers has focused on the study of various Isotopologues [16, 17], and the detection of intermolecular combination bands [2, 17] which provide important information on the intermolecular vibrational modes. Although larger clusters of CO_2 have been probed using a number of techniques [18–27], but $(CO_2)_3$ remained the largest cluster for which explicit infrared bands provided rotationally-resolved structure.

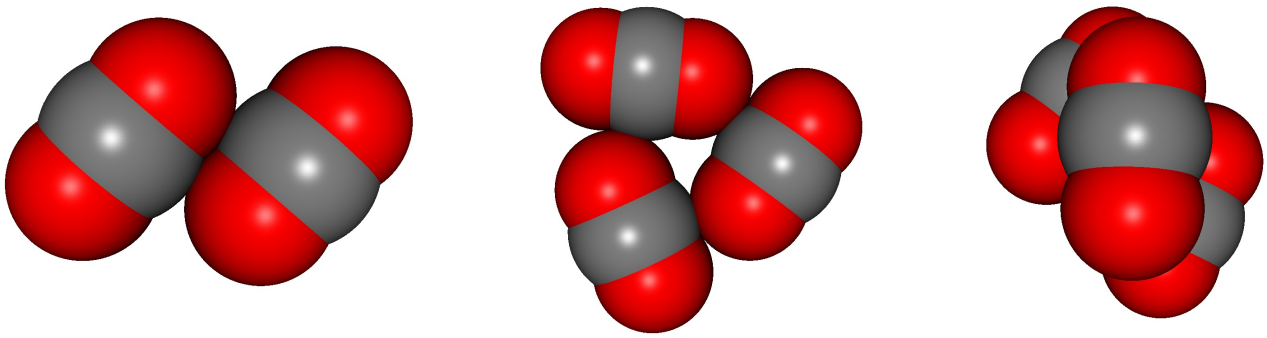

Figure 1.2: Experimentally derived structures for dimer and trimers of CO_2. CO_2 dimer with C_{2h} symmetry (left); planar cyclic isomer of CO_2 trimer with C_{3h} symmetry (middle); and barrel-shaped isomer of the CO_2 trimer with C_2 symmetry (right).

Recently, in a communication article, explicit identification of infrared transitions for clusters of CO_2 with $6 - 13$ molecules in the ν_3 region (~ 2350 cm^{-1}) was reported by the Laser Spectroscopy group at the University of Calgary [28]. These are the largest molecular clusters to be characterized by their rotationally-resolved spectra. The results presented in that communication article are supplemented and extended in another paper which is presented in Chapter 6. Assignments of rotation-vibrational bands are aided by cluster structure calculations of Takeuchi [1], which uses a widely-tested empirical potential function of Murthy et al. [29] This function is fitted to solid CO_2 lattice frequencies and it also works well for the dimer and trimer [15]. $(CO_2)_N$ with $N = 6 - 13$ are all asymmetric rotors except $(CO_2)_6$ and $(CO_2)_{13}$ which are symmetric tops. Proceeding in cluster size, two isomers are observed for CO_2 hexamer, one with S_6 symmetry and another one with S_4 symmetry. The structure of the hexamer with S_6 symmetry is formed by stacking two

cyclic CO_2 trimers with coincident symmetry axes but with the "top" and "bottom" trimers rotated by 60° with respect to one another. The structure of the other hexamer with S_4 symmetry can be explained as consisting of a ring of four equivalent monomers capped at the "top" and "bottom" by a pair of equivalent monomers. $(CO_2)_7$ is unsymmetrical and consists of five monomers in an approximately planar pentagonal ring with the remaining monomers above and below the ring. Proceeding in cluster size from $(CO_2)_7$ up to $(CO_2)_{11}$, additional monomers start to form a stack of two staggered pentagonal rings. $(CO_2)_{12}$ can be thought of as a "cup" of 11 monomers with one monomer inside the cup. $(CO_2)_{13}$ has a highly symmetric structure where a central CO_2 monomer is surrounded by an icosahedral cage. $(CO_2)_8$ is not experimentally observed due to a gap in laser coverage around 2357.5 cm^{-1}. These results provide critical tests for theoretical cluster models and open up new possibilities for experiments. These results will be presented in more detail in Chapter 6.

1.2.3 N_2O clusters

Nitrous oxide is a highly influential greenhouse gas with long-term environmental impacts. Thus, clusters of nitrous oxide have been the subject of extensive theoretical and experimental studies for a long time.

Miller et al. have systematically studied N_2O systems in a progressive manner [12,30,31]. These cluster systems are depicted in Figure 1.3(b)-(d). The first high resolution spectrum of N_2O dimer was recorded in the region of $\nu_1 + \nu_3$ vibrational combination of the monomer. From this spectrum, the first reliable structure for a non-polar isomer of $(N_2O)_2$ was found to be planar with slipped-antiparallel monomer units with the oxygen atoms in the interior position (C_{2h} symmetry). The trimer structure was found to be essentially that of a slightly distorted nonpolar dimer with an additional N_2O monomer lying above it with no specific symmetry (C_1 symmetry). During their search for the trimer in the $\nu_1 + \nu_3$ region of N_2O, Miller et al. identified a spectrum corresponding to an oblate top ($I_a = I_b$) which was assigned to the nitrous oxide tetramer. The combination of the experimental and *ab inito*

results provided a highly symmetric structure for the tetramer where the four monomer units were approximately parallel with alternating orientations but the exact tilt angle could not be determined.

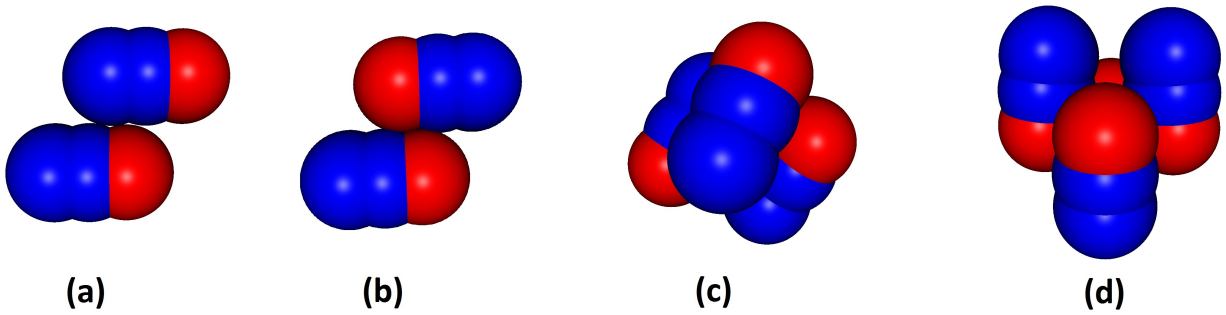

Figure 1.3: Structures for N_2O clusters; (a) polar isomer of N_2O dimer; (b) the non-polar N_2O dimer with C_{2h} symmetry; (c) N_2O trimer with no symmetry element; (d) oblate N_2O tetramer with D_{2d} symmetry.

In the past few years, significant progress on complexation of nitrous oxide has been made by the Laser Spectroscopy group at the University of Calgary [32–41]. This includes: observation of a polar isomer for $(N_2O)_2$ in the ν_1 fundamental region of N_2O where the two monomers are aligned almost parallel to each other (Figure 1.3 (a)) [32]; isotopic effects in the infrared spectra of the polar and non-polar $(N_2O)_2$ to refine the structural parameters [33]; measurement of infrared spectra of the polar and non-polar $(N_2O)_2$ in the 1280 cm^{-1} region of the ν_3 fundamental [34]; measurement and revised analysis of the torsional combination band of the non-polar $(N_2O)_2$ [35]; fundamental bands of the mixed $^{14}N_2O$–$^{15}N_2O$ and new combination bands of $(^{14}N_2O)_2$ and $(^{15}N_2O)_2$ involving the intermolecular geared bending mode [36]; observation and analyses of five new fundamental bands of the nitrous oxide trimer [37]; intermolecular combination bands of the $(N_2O)_3$ [38]; observation of two highly symmetric isomers for N_2O tetramer (Chapter 7) [39]; observation of nitrous oxide pentamers [40]; and observation of the anti-geared bending mode combination band of the non-polar $(N_2O)_2$ using a quantum cascade laser (QCL) [41].

Chapter 7 represents the observation of the same N_2O tetramer as that observed by Miller et al. [12] but in the ν_1 fundamental band region ($\sim$ 2200 cm^{-1}). The observations include the normal $(^{14}N_2^{16}O)_4$ species, as well as three isotopically substituted forms, $(^{15}N_2^{16}O_2)_4$, $^{14}N_2^{16}O$–$(^{15}N_2^{16}O)_3$, and $(^{14}N_2^{16}O)_3$–$^{15}N_2^{16}O$ whose observations helped in determining the structure that has D_{2d} symmetry. Since the present observed linewidth (<0.002 cm^{-1}) is considerably smaller than those of Miller et al.($\approx$ 0.010 cm^{-1}) [12], the structural parameters are likely to be more accurate. In addition, a new distinct isomer of $(N_2O)_4$ which turned out to be a prolate ($I_b = I_c$) symmetric rotor with S_4 symmetry is observed. The structure of the prolate $(N_2O)_4$ can be thought of as a "sandwich" composed of two non-polar N_2O dimers with one stacked on top of the other and rotated by 90°. The geometry of N_2O tetramers provides one more step on the bridge to the condensed phase.

Organization of the thesis is as follows. A brief overview of theoretical background necessary for analyzing rotation-vibrational spectra is given in Chapter 2. Chapter 3 describes in some detail the experimental apparatus. Chapters 4 and 5 are devoted to investigation of complexation of OCS molecule with various hydrocarbons (the hydrocarbons being acetylene, ethylene, ethane, allene, propyne, diacetylene, dimethylacetylene, benzene, cyclohexane, and cyclo-octatetraene). Chapter 6 represents the results of the experiments on CO_2 clusters which significantly extends the spectroscopic studies of CO_2 clusters to larger clusters containing up to 13 CO_2 monomers and Chapter 7 reports the observation of two distinct highly symmetric isomers for $(N_2O)_4$.

Chapter 2

Theoretical Background

In this chapter the underlying theory for understanding of molecular rotation-vibration spectra is presented. The basic models, rigid rotor and harmonic oscillator, give the lowest order approximation of the rotational and vibrational energy levels, respectively. Non-rigidity and anharmonicity effects result in higher order terms in the molecular Hamiltonian. Also, application of group theory in symmetry labeling of molecular energy levels, determining selection rules, and statistical weights is demonstrated.

2.1 Molecular Hamiltonian

Molecular clusters and complexes are made up of two or more molecular units and each molecule, in turn, is a collection of nuclei and electrons that are held together by certain forces. Thus, the general molecular Hamiltonian $\hat{H}$ will contain terms describing each of the nuclei and electrons as well as terms pertaining to interactions between nuclei and electrons.

$$\hat{H} = \hat{T} + V + \hat{H}_{es} + \hat{H}_{hfs} \tag{2.1}$$

where $\hat{T}$ is the non-relativistic kinetic energy operator, V is the electrostatic energy, $\hat{H}_{es}$ is related to electron's spin magnetic moment and includes the spin-orbit and spin-spin interaction terms. $\hat{H}_{hfs}$ is due to the nuclear hyper-fine structure that originates from the interaction of the magnetic and electric moments of the nuclei with the other electric and magnetic moments existing in the molecule.

The total kinetic energy, $\hat{T}$, can be written as [42, Section 7.1],

$$\hat{T} = \hat{T}_{CM} + \hat{T}^0 + \hat{T}' \tag{2.2}$$

where $\hat{T}_{CM}$ is the kinetic energy of the center of mass, $\hat{T}^0$ is the intramolecular kinetic energy and $\hat{T}'$ includes cross terms in intramolecular kinetic energy. So, Equation (2.1) can be written as,

$$\hat{H} = \hat{T}_{CM} + \underbrace{\hat{T}^0 + \hat{T}' + V + \hat{H}_{es} + \hat{H}_{hfs}}_{\hat{H}_{int}} \tag{2.3}$$

$$\hat{H} = \hat{T}_{CM} + \hat{H}_{int} \tag{2.4}$$

This way, the Hamiltonian is decomposed into two parts. One part that describes the internal motions in the molecule, i.e. $\hat{H}_{int}$, and one part that only shows the translational motion of the center of mass, i.e. $\hat{T}_{CM}$.

$\hat{H}_{int}$ can be written as,

$$\hat{H}_{int} = \hat{H}_{rve} + \hat{H}_{es} + \hat{H}_{hfs} \tag{2.5}$$

where $\hat{H}_{rve}$ is the spin-free ro-vibronic Hamiltonian,

$$\hat{H}_{rve} = \hat{T}^0 + \hat{T}' + V. \tag{2.6}$$

$\hat{H}_{int}$ does not involve the coordinates of the center of mass of the molecule. Because of this separation of coordinates, wavefunctions can be written as,

$$\Phi = \Phi_{CM}\Phi_{int} \tag{2.7}$$

where

$$\hat{T}_{CM}\Phi_{CM} = E_{CM}\Phi_{CM} \tag{2.8}$$

$$\hat{H}_{int}\Phi_{int} = E_{int}\Phi_{CM} \tag{2.9}$$

The translational wavefunction, Φ_{CM}, can be obtained from Equation (2.8) as,

$$\Phi_{CM} = e^{i\boldsymbol{k}\cdot\boldsymbol{R}_{CM}} \tag{2.10}$$

in which $\boldsymbol{R}_{CM}$ is the position vector of the center of mass, $\boldsymbol{k}\hbar = \boldsymbol{P}_{CM}$ is the classical translational momentum, and

$$k = \frac{\sqrt{2ME_{CM}}}{\hbar} \tag{2.11}$$

with M and E_{CM} being the total mass of the molecule and translational energy of the center of mass, respectively. As Equation (2.10) suggests, the translational motion of the molecule is solely described by the $\boldsymbol{k}$ vector. Since high-resolution infrared spectroscopy only deals with rotational and vibrational states of molecules, therefore from this point, this thesis is not concerned about the translational momentum of molecular states and concentrates on the complete internal dynamics Hamiltonian, $\hat{H}_{int}$, and its eigenstates, Φ_{int}.

In practice, for molecules in singlet electronic ground state with unresolved hyper-fine structure, $\hat{H}_{int}$ can safely be approximated with $\hat{H}_{rve}$. Although for the general case this approximation is not valid, rovibronic energy levels are a good approximation to molecular energy levels. The neglected terms ($\hat{H}_{es}$ and $\hat{H}_{hfs}$) result in shifts and splittings of these energy levels. Thus, energy levels are given by the rovibronic Schrödinger equation,

$$\hat{H}_{rve}\Phi_{rve} = E_{rve}\Phi_{rve}. \tag{2.12}$$

In general, it is very difficult to solve the rovibronic Schrödinger equation (Equation (2.12)) without first making simplifying approximations. The main approximation is the Born-Oppenheimer approximation. As a result of this approximation, the rovibronic Schrödinger equation is solved by first solving the electronic Schrödinger equation at fixed nuclear co-ordinates, and then solving the rotation-vibration Schrödinger equation. In making this approximation it is assumed that the motions of the electrons are unaffected by the motions of the nuclei and, on the time scale of their motion, only depend on nuclear positions. This thesis will only focus on rovibrational energy levels as infrared light is not energetic enough for excitation of electronic states which happen in the UV or visible region of electromagnetic spectrum. Hence, as far as infrared spectroscopy is concerned, for a molecular system in ground electronic state, the zero of energy can be taken to be the electronic energy.

In solving the rotation-vibration Schrödinger equation, in the lowest order of approximation, molecular system is treated as a rigid rotor and vibrational motions are modeled as a system of harmonic oscillators. The rotation-vibration Schrödinger equation obtained

after this approximation is separable and the eigenfunctions are the product of a rotational wavefunction in three variables (Euler angles) and a vibrational wavefunction which is the product of $(3N-6)$ harmonic oscillator wavefunctions, where N is the number of atoms in a molecule with a non-linear structure.

In order to achieve more precise rotation-vibration energy levels, additional terms for non-rigidity of molecular structure and anharmonicity of potential functions have to be included in the molecular Hamiltonian.

2.2 Euler Angles

The general molecular Hamiltonian (Equation (2.1)) is constructed based on a coordinate system for which both the origin and orientation of axes are fixed in the space. This coordinate system is called the space-fixed system. Another coordinate system parallel to the space-fixed system with its origin at molecule's center of mass is chosen to isolate the translational motion (Equation (2.4)). A third coordinate system parallel to the space-fixed system but with its origin at the nuclear centre of mass facilitates the separation of the electronic and nuclear coordinates in the rovibronic Hamiltonian of Equation (2.12).

Now, in order to facilitate the separation of the rotation-vibration Schrödinger equation into rotational and vibrational parts, a molecule-fixed axis system, (x, y, z), is introduced. This right-handed axis system has its origin at the nuclear center of mass of the molecule and its orientation is defined by the nuclear coordinates, and specified by Euler angles (θ, ϕ, χ). The rotational wavefunctions will be functions of these Euler angles.

Euler angles accomplish a transformation from the space-fixed coordinate system to the molecule-fixed coordinate system. Figure 2.1 illustrates the situation. Three successive rotations are required to perform this transformation:

- First, rotate (X, Y, Z) by ϕ about the Z axis to obtain $X'NZ$.

- Then rotate $X'Nz$ about N by θ to obtain $X''NZ$.

- Finally, rotation of $X''Nz$ about z by χ yields the (x, y, z) system.

The Euler angles are restricted to the ranges $0 \leq \theta \leq \pi$, $0 \leq \phi \leq 2\pi$, $0 \leq \chi \leq 2\pi$.

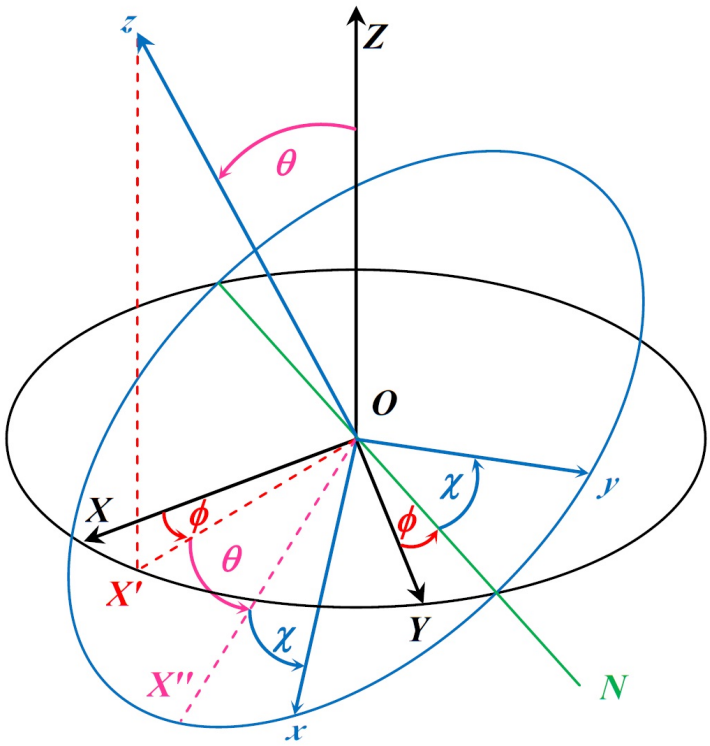

Figure 2.1: Euler angles relating the space-fixed axes (X, Y, Z) and molecule-fixed axes (x, y, z). Line of nodes, labeled N, is the intersection of XY and xy planes

For any nucleus in the molecule, we can relate its coordinates in the (X, Y, Z) and (x, y, z) systems by writing

$$\begin{bmatrix} x \\ y \\ z \end{bmatrix} = \begin{bmatrix} \lambda_{xX} & \lambda_{xY} & \lambda_{xZ} \\ \lambda_{yX} & \lambda_{yY} & \lambda_{yZ} \\ \lambda_{zX} & \lambda_{zY} & \lambda_{zZ} \end{bmatrix} \begin{bmatrix} X \\ Y \\ Z \end{bmatrix}, \tag{2.13}$$

where

$$\lambda_{xX} = \cos(\angle xOX), \quad \ldots \tag{2.14}$$

are the elements of the direction cosine matrix. The direction cosines can be expressed in terms of the Euler angles as the following

$$\lambda_{xX} = \cos\theta \cos\phi \cos\chi - \sin\phi \sin\chi,$$

$$\lambda_{yX} = -\cos\theta\cos\phi\sin\chi - \sin\phi\cos\chi, \tag{2.15}$$
$$\lambda_{zX} = \sin\theta\cos\phi,$$

$$\lambda_{xY} = \cos\theta\sin\phi\cos\chi + \cos\phi\sin\chi,$$
$$\lambda_{yY} = -\cos\theta\sin\phi\sin\chi + \cos\phi\cos\chi, \tag{2.16}$$
$$\lambda_{zY} = \sin\theta\sin\phi,$$

$$\lambda_{xZ} = -\sin\theta\cos\chi,$$
$$\lambda_{yZ} = \sin\theta\sin\chi, \tag{2.17}$$
$$\lambda_{zZ} = \cos\theta,$$

2.3 Angular Momentum

In the molecular Hamiltonian, expressions for the components of the angular momentum operator relative to the molecule-fixed x, y and z axes are needed. In order to obtain these expressions, one must first calculate them in the space-fixed reference frame and then project them onto the molecule-fixed axes. This can be done using the direction cosine matrix elements (Equations (2.15) - (2.17)).

$$\begin{bmatrix} \hat{J}_x \\ \hat{J}_y \\ \hat{J}_z \end{bmatrix} = \begin{bmatrix} \cos\theta\cos\phi\cos\chi & \cos\theta\sin\phi\cos\chi & -\sin\theta\cos\chi \\ -\sin\phi\sin\chi & +\cos\phi\sin\chi & \\ -\cos\theta\cos\phi\sin\chi & -\cos\theta\sin\phi\sin\chi & \sin\theta\sin\chi \\ -\sin\phi\cos\chi & +\cos\phi\cos\chi & \\ \sin\theta\cos\phi & \sin\theta\sin\phi & \cos\theta \end{bmatrix} \begin{bmatrix} \hat{J}_X \\ \hat{J}_Y \\ \hat{J}_Z \end{bmatrix}, \tag{2.18}$$

Using equations in (2.18) for the components of angular momentum, and defining the three momentum operators $\hat{P}_\theta = -i\dfrac{\partial}{\partial\theta}$, $\hat{P}_\phi = -i\dfrac{\partial}{\partial\phi}$ and $\hat{P}_\chi = -i\dfrac{\partial}{\partial\chi}$ the required relations can be

obtained as follows [43]:

$$\hat{J}_x = \sin\chi\hat{P}_\theta - \csc\theta\cos\chi\hat{P}_\phi + \cot\theta\cos\chi\hat{P}_\chi, \tag{2.19}$$

$$\hat{J}_y = \cos\chi\hat{P}_\theta + \csc\theta\sin\chi\hat{P}_\phi - \cot\theta\sin\chi\hat{P}_\chi, \tag{2.20}$$

$$\hat{J}_z = \hat{P}_\chi. \tag{2.21}$$

Operators in Equations (2.19) - (2.21) can now be squared to form the rotational Hamiltonian

$$\hat{H}_{rot} = \frac{\hat{J}_x^2}{2I_x} + \frac{\hat{J}_y^2}{2I_y} + \frac{\hat{J}_z^2}{2I_z}. \tag{2.22}$$

where I_x, I_y, and I_z are the principal moments of inertia. Instead of solving the Schrödinger equation directly, rotational energy levels can be found by using commutation properties of various operators. For this purpose, expressions for components of angular momentum along the space-fixed axes are needed. These expressions can be derived in the same way as the components for molecule-fixed axes.

$$\hat{J}_X = -\sin\phi\hat{P}_\theta + \csc\theta\cos\phi\hat{P}_\chi - \cot\theta\cos\phi\hat{P}_\phi, \tag{2.23}$$

$$\hat{J}_Y = \cos\phi\hat{P}_\theta + \csc\theta\sin\phi\hat{P}_\chi - \cot\theta\sin\phi\hat{P}_\phi, \tag{2.24}$$

$$\hat{J}_Z = \hat{P}_\phi. \tag{2.25}$$

The operator for the total angular momentum of the rigid rotor is

$$\hat{J}^2 = \hat{J}_x^2 + \hat{J}_y^2 + \hat{J}_z^2 = \hat{J}_X^2 + \hat{J}_Y^2 + \hat{J}_Z^2. \tag{2.26}$$

Having explicit expressions for components of angular momentum in both space-fixed frame and molecule-fixed frame, it is straightforward algebra to obtain the commutation relations

$$[\hat{J}_i, \hat{J}_j] = +i\sum_k \epsilon_{ijk}\hat{J}_k \qquad \text{for} \quad i,j,k = X, Y, \textit{ or } Z, \tag{2.27}$$

and

$$[\hat{J}_\alpha, \hat{J}_\beta] = -i\sum_\gamma \epsilon_{\alpha\beta\gamma}\hat{J}_\gamma \qquad \text{for} \quad \alpha,\beta,\gamma = x, y, \textit{ or } z. \tag{2.28}$$

where ϵ_{ijk} is the well-known Levi-Civita symbol that takes a value of +1 if ijk is a cyclic permutation, -1 if ijk is non-cyclic permutation, and 0 in case of repeated indices [42, Section 10.3]. It is worth noting that the commutation relations of the components of the angular momentum in the space-fixed frame is different from those of molecule-fixed frame.

Any component of angular momentum in the space-fixed frame commutes with any component in the moclecule-fixed system, that is

$$[\hat{J}_i, \hat{J}_\alpha] = 0, \quad \text{For } i = X, Y, Z, \quad \text{and} \quad \alpha = x, y, \textit{ or } z. \tag{2.29}$$

Also,

$$[\hat{J}^2, \hat{J}_x] = [\hat{J}^2, \hat{J}_X] = 0, \tag{2.30}$$

$$[\hat{J}^2, \hat{J}_y] = [\hat{J}^2, \hat{J}_Y] = 0, \tag{2.31}$$

$$[\hat{J}^2, \hat{J}_z] = [\hat{J}^2, \hat{J}_Z] = 0, \tag{2.32}$$

Using the above equations it can be shown that

$$[\hat{H}_{rot}, \hat{J}^2] = 0, \tag{2.33}$$

$$[\hat{H}_{rot}, \hat{J}_Z] = 0, \tag{2.34}$$

and

$$[\hat{H}_{rot}, \hat{J}_z] = +i \left(\frac{1}{2I_x} - \frac{1}{2I_y} \right) (\hat{J}_x \hat{J}_y + \hat{J}_y \hat{J}_x) \tag{2.35}$$

Therefore, the set of commuting operators that share a common set of eigenfunctions are

$$[\hat{H}_{rot}, \hat{J}^2] = 0, \quad [\hat{H}_{rot}, \hat{J}_Z] = 0, \quad \text{and} \quad [\hat{J}^2, \hat{J}_Z] = 0. \tag{2.36}$$

So, two quantum numbers are needed to label the rotational wavefunctions. These are J, the quantum number for the magnitude of the total angular momentum, and m, the quantum number for the component of angular momentum along the space-fixed axes. The quantum numbers J and m can take the following values

$$J = 0, 1, 2, \ldots \tag{2.37}$$

and

$$m = -J, -J+1, \ldots, J-1, J \tag{2.38}$$

2.4 Rigid rotor energy levels

For any rigid three-dimensional body, there exists a 3×3 moment of inertia tensor $\mathbf{I}$. In an arbitrary (x, y, z) system, the moment of inertia tensor can be written as

$$\mathbf{I} = \begin{pmatrix} I_{xx} & I_{xy} & I_{xz} \\ I_{yx} & I_{yy} & I_{yz} \\ I_{zx} & I_{zy} & I_{zz} \end{pmatrix} \tag{2.39}$$

where the diagonal elements are

$$I_{xx} = \sum_n m_n (y_n^2 + z_n^2) \tag{2.40}$$

$$I_{yy} = \sum_n m_n (x_n^2 + z_n^2) \tag{2.41}$$

$$I_{zz} = \sum_n m_n (x_n^2 + y_n^2) \tag{2.42}$$

and off-diagonal elements are

$$I_{xy} = I_{yx} = -\sum_n m_n x_n y_n \tag{2.43}$$

$$I_{xz} = I_{xz} = -\sum_n m_n x_n z_n \tag{2.44}$$

$$I_{yz} = I_{zy} = -\sum_n m_n y_n z_n \tag{2.45}$$

and index n runs over all the particles in the system of masses.

The moment of inertia tensor can be diagonalized to yield three eigenvalues that can, in principle, have distinct values. These eigenvalues are called the *principal moment of inertia*, and the corresponding eigenvectors are referred to as the *principal moment of inertia axes*. These axes are labeled a, b and c and the moment of inertia tensor will take a diagonal form

if written with respect to the (a, b, c) axes. This labelling scheme is such that the c-axis is the axis about which the moment of inertia has its maximum value and the moment of inertia about the a-axis has its minimum value. Which means

$$I_c \geq I_b \geq I_a \tag{2.46}$$

With these conventions, the rotational Hamiltonian, in the lowest order, can be written as

$$\hat{H}_{rot} = A\hat{J}_a^2 + B\hat{J}_b^2 + C\hat{J}_c^2 \tag{2.47}$$

where A, B and C are inversely proportional to I_a, I_b and I_c and are called rotational constants. In units of Hz, they are

$$A = \frac{\hbar}{4\pi I_a}, \qquad B = \frac{\hbar}{4\pi I_b}, \qquad C = \frac{\hbar}{4\pi I_c} \tag{2.48}$$

There are six possible ways to map the unordered set of axes, (x, y, z), onto the ordered set, (a, b, c), depending on the values of moment of inertia of the particular molecular system under study. These possibilities are tabulated in Table 2.1.

Table 2.1: Six ways of mapping (x, y, z) onto (a, b, c). Superscripts r and l refer to right-handed or left-handed coordinate systems, respectively.

	I^r	I^l	II^r	II^l	III^r	III^l
x	b	c	c	a	a	b
y	c	b	a	c	b	a
z	a	a	b	b	c	c

Depending on the values of the three principal moment of inertia, molecules can be classified into five categories. These are:

- Linear molecules, $I_b = I_c$, $I_a = 0$; for example, CO_2.

- Prolate symmetric tops, $I_a < I_b = I_c$; for example, CH_3Cl.

- Oblate symmetric tops, $I_a = I_b < I_c$; for example, BF_3.

- Spherical top molecules, $I_a = I_b = I_c$; for example, SF_6 and CH_4.

- Asymmetric Molecules, $I_a < I_b < I_c$; for example, H_2O.

2.4.1 Linear Molecules

For a linear molecule $I_b = I_c$ and $I_a = 0$. a-axis is along the molecule's axis while b- and c-axes can be any direction perpendicular to the inter-nuclear a-axis. A linear molecule does not rotate about its a-axis. Therefore the rotational Hamiltonian for rigid linear molecule, in the absence of any external fields, can be expressed as:

$$\hat{H}_{rot} = B\hat{J}_b^2 + C\hat{J}_c^2 \tag{2.49}$$

But, $B = C$,

$$\hat{H}_{rot} = B\hat{J}_b^2 + B\hat{J}_c^2 = B\hat{J}^2 \tag{2.50}$$

The Schrödinger equation can be solved for this case.

$$E_{rot}(J) = BJ(J+1) \quad \text{and} \quad \Phi_{J,m} = Y_{J,m}(\theta, \phi) \tag{2.51}$$

where $Y_{J,m}(\theta, \phi)$'s are the spherical harmonics. A noteworthy remark is that energy levels do not depend on m and levels with a certain J and $m = -J, -J+1, \ldots, +J-1, +J$ have the same energy. So, each level is $(2J+1)$-fold degenerate.

2.4.2 Symmetric Top Molecules

Symmetric tops are defined as having two of the principal moment of inertia equal and different from the third one, which has a non-zero value. For symmetric top molecules, the z-axis is taken to be along the symmetry axis of the molecule. In the case of prolate tops, the symmetry axis is the a-axis and for oblate top molecules the symmetry axis is the c-axis. In another words, the I^r representation is adopted for prolate tops and III^r representation for oblate tops. Therefore Equation (2.35) will be transformed to

$$[\hat{H}_{rot}, \hat{J}_a] = +i\left(\frac{1}{2I_b} - \frac{1}{2I_c}\right)(\hat{J}_b\hat{J}_c + \hat{J}_c\hat{J}_b) = 0 \quad \text{for prolate} \quad (I_b = I_c), \tag{2.52}$$

and

$$[\hat{H}_{rot}, \hat{J}_c] = +i\left(\frac{1}{2I_a} - \frac{1}{2I_b}\right)(\hat{J}_a\hat{J}_b + \hat{J}_b\hat{J}_a) = 0 \quad \text{for oblate} \quad (I_a = I_b). \tag{2.53}$$

The rest of the equations will be derived for prolate tops but similar equations hold for oblate tops with k_a, $|J, k_a, m\rangle$, and $\hat{J}_a$ replaced by k_c, $|J, k_c, m\rangle$, and $\hat{J}_c$, respectively.

Equation (2.52) together with Equations (2.36) imply that now $\hat{H}_{rot}$, $\hat{J}^2$, $\hat{J}_Z$, and $\hat{J}_a$ share a common set of eigenfunctions, $|J, k_a, m\rangle$, with the following eigenvalues

$$\hat{H}_{rot}|J, k_a, m\rangle = E_{rot}|J, k_a, m\rangle \tag{2.54}$$

$$\hat{J}^2|J, k_a, m\rangle = J(J+1)|J, k_a, m\rangle \tag{2.55}$$

$$\hat{J}_Z|J, k_a, m\rangle = m|J, k_a, m\rangle \tag{2.56}$$

$$\hat{J}_a|J, k_a, m\rangle = k_a|J, k_a, m\rangle \tag{2.57}$$

where k_a is the quantum number associated with the projection of the total angular momentum onto the symmetry axis of the molecule in molecule-fixed frame and can take the following values,

$$k_a = -J, -J+1, \ldots, J-1, J \tag{2.58}$$

Using Equations (2.47) and (2.54) - (2.57), rotational energy levels can be obtained for a prolate top.

$$\hat{H}_{rot}|J, k_a, m\rangle = \left(A\hat{J}_a^2 + B\hat{J}_b^2 + C\hat{J}_c^2\right)|J, k_a, m\rangle \tag{2.59}$$

$$= \left(A\hat{J}_a^2 - B\hat{J}_a^2 + B\hat{J}_a^2 + B\hat{J}_b^2 + C\hat{J}_c^2\right)|J, k_a, m\rangle \tag{2.60}$$

$$= \left[B\hat{J}^2 + (A-B)\hat{J}_a^2\right]|J, k_a, m\rangle \tag{2.61}$$

Therefore,

$$E_{rot}(J, k_a) = BJ(J+1) + (A-B)k_a^2. \tag{2.62}$$

Each J level has $(2J+1)$ different k_a states corresponding to the different possible projections of J on the molecular symmetry axis. Each (J, k_a) level then has $(2J+1)$ different m levels corresponding to the different possible projections of J on the Z-axis. In free space, for $k \neq 0$, each (J, k_a) level is $2(2J+1)$-fold degenerate because states with $\pm k_a$ have the same energy, and for $k = 0$ the degeneracy is reduced to $(2J+1)$-fold.

In a similar fashion, energy levels for oblate tops are

$$E_{rot}(J, k_c) = BJ(J+1) + (C-B)k_c^2. \tag{2.63}$$

It should be noted that the coefficient of k_c is negative for oblate tops and rotational energy decreases with increasing k_c.

It can be shown that symmetric top wavefunctions, apart from a normalization constant, are the same as the elements of Wigner's rotation matrix, $\mathcal{D}^J_{m,k_a}(\phi, \theta, \chi)$ [43]. That is

$$|J, k_a, m\rangle = \sqrt{\frac{2J+1}{8\pi^2}} \mathcal{D}^J_{m,k_a}(\phi, \theta, \chi)^* \tag{2.64}$$

where

$$\mathcal{D}^J_{m,k_a}(\phi, \theta, \chi) = \langle J, m | \mathcal{R}(\phi, \theta, \chi) | J, k_a \rangle, \tag{2.65}$$

and $\mathcal{R}(\phi, \theta, \chi)$ is the rotation operator given by

$$\mathcal{R}(\phi, \theta, \chi) = e^{-i\phi \hat{J}_Z} e^{-i\theta \hat{J}_Y} e^{-i\chi \hat{J}_z}. \tag{2.66}$$

but

$$\mathcal{D}^J_{m,k_a}(\phi, \theta, \chi)^* = (-1)^{m-k_a} \mathcal{D}^J_{-m,-k_a}(\phi, \theta, \chi) \tag{2.67}$$

So, Equation (2.64) reads,

$$|J, k_a, m\rangle = (-1)^{m-k_a} \sqrt{\frac{2J+1}{8\pi^2}} \mathcal{D}^J_{-m,-k_a}(\phi, \theta, \chi). \tag{2.68}$$

These wavefunctions serve as a basis set for the wavefunctions of asymmetric top molecules.

2.4.3 Spherical Top Molecules

For a spherical top, all the rotational constants are identical, i.e. $A = B = C$, and there is no preferred axis in the molecule-fixed frame. C_{60} is an example of such a molecule. The rotational Hamiltonian of Equation (2.47) takes the following form

$$\hat{H}_{rot} = B\hat{J}_a^2 + B\hat{J}_b^2 + B\hat{J}_c^2 = B\hat{J}^2. \tag{2.69}$$

and rotational energy levels are

$$E_{rot}(J) = BJ(J+1). \tag{2.70}$$

In the absence of external fields and higher order terms, all energy levels are $(2J+1)^2$-fold degenerate

2.4.4 Asymmetric Molecules

For an asymmetric top, rotational constants have distinct values and thus the rotational Hamiltonian cannot be simplified as it would for symmetric molecules. This means that it is not possible to decompose the Hamiltonian so that one component is solely dependent on $\hat{J}^2$ and one component on $\hat{J}_z$, since there is no preferred axis in the molecule-fixed frame. Also, $\hat{H}_{rot}$ and $\hat{J}_z$ do not commute, as Equation (2.35) suggests, thus $\hat{H}_{rot}$ is not diagonal in k_a (or k_c) and k_a (or k_c) is no longer a good quantum number. This essentially means that the rotational motion cannot be described in terms of a conserved motion about a particular axis of the molecule. Therefore, no explicit expression for energy levels can be obtained except for the low-lying rotational energy levels.

The way to solve the rotational Schrödinger equation is to set up the Hamiltonian matrix in the basis of symmetric top wavefunctions and diagonalize it to obtain the energies and wavefunctions. The wavefunctions are obtained as a linear combination of symmetric top wavefunctions with coefficients that are functions of A, B, and C. The expression for asymmetric top rotational Hamiltonian can be written in any of the representations in Table 2.1. Apparently I^r and III^r representations are appropriate for the limiting cases of a prolate top and an oblate top, respectively. So, it is wise to know whether the molecule is near-oblate, near-prolate or very asymmetric. The degree of asymmetry can be quantified by κ, Ray's asymmetry parameter,

$$\kappa = \frac{2B - A - C}{A - C}. \tag{2.71}$$

$\kappa = -1$ and $\kappa = +1$ correspond to the prolate and oblate limit, respectively. Any value

between -1 and $+1$ represents an asymmetric top molecule, and $\kappa = 0$ represents the most asymmetric case.

Thus, for a particular molecule, one will map the unordered set (x, y, z) onto the ordered set (a, b, c) such that the terms which tend to spoil the symmetric top form of the Hamiltonian are as small as possible.

Here, the I^r representation and prolate top wave functions, $|J, k_a, m\rangle$, will be used to obtain asymmetric top wavefunctions and energy levels. Instead, III^r representation and oblate top wavefunctions, $|J, k_c, m\rangle$, could be used which will yield the same energy levels as the I^r representation, but wavefunctions will look different since the Euler angles are defined differently.

With this convention, the rotational Hamiltonian is

$$\hat{H}_{rot} = A\hat{J}_z^2 + B\hat{J}_x^2 + C\hat{J}_y^2, \tag{2.72}$$

which can be rewritten in a more useful form, as

$$\hat{H}_{rot} = \frac{B+C}{2}\hat{J}^2 + \left(A - \frac{B+C}{2}\right)\hat{J}_z^2 + \frac{B-C}{4}\left[(\hat{J}_m^+)^2 + (\hat{J}_m^-)^2\right] \tag{2.73}$$

where $\hat{J}_m^+$ and $\hat{J}_m^-$ are the angular momentum ladder operators in the molecule-fixed frame defined in the same way as the corresponding operators in the space-fixed frame

$$\hat{J}_m^\pm = \hat{J}_x \pm i\hat{J}_y, \qquad \text{(molecule-fixed frame)} \tag{2.74}$$

$$\hat{J}_s^\pm = \hat{J}_X \pm i\hat{J}_Y, \qquad \text{(space-fixed frame)} \tag{2.75}$$

with the following commutation relations

$$[\hat{J}_z, \hat{J}_m^\pm] = \mp\hat{J}_m^\pm, \tag{2.76}$$

$$[\hat{J}_Z, \hat{J}_s^\pm] = \pm\hat{J}_s^\pm. \tag{2.77}$$

There is a change in the sign for the commutators in the molecule-fixed frame so that $\hat{J}_m^+$ ladders down and $\hat{J}_m^-$ ladders up [43],

$$\hat{J}_m^\pm|J, k_a, m\rangle = \sqrt{J(J+1) - k_a(k_a \mp 1)}|J, k_a \mp 1, m\rangle, \tag{2.78}$$

while

$$\hat{J}_s^{\pm}|J,k_a,m\rangle = \sqrt{J(J+1)-m(m\pm 1)}|J,k,m\pm 1\rangle. \tag{2.79}$$

In order to determine matrix elements of the Hamiltonian, the matrix elements of $(\hat{J}_m^+)^2$ and $(\hat{J}_m^-)^2$ have to be determined first. So,

$$\begin{aligned}(\hat{J}_m^{\pm})^2|J,k_a,m\rangle &= \sqrt{J(J+1)-k_a(k_a\mp 1)}\hat{J}_m^{\pm}|J,k_a\mp 1,m\rangle \\ &= \sqrt{J(J+1)-k_a(k_a\mp 1)}\sqrt{J(J+1)-(k_a\mp 1)(k_a\mp 2)}|J,k_a\mp 2,m\rangle\end{aligned} \tag{2.80}$$

So, in summary, the only non-vanishing matrix elements needed to set up the Hamiltonian matrix are

$$\langle J,k_a,m|\hat{J}^2|J,k_a,m\rangle = J(J+1), \tag{2.81}$$

$$\langle J,k_a,m|\hat{J}_z^2|J,k_a,m\rangle = k_a^2, \tag{2.82}$$

$$\langle J,k_a\mp 2,m|(\hat{J}_m^{\pm})^2|J,k_a,m\rangle = \sqrt{[J(J+1)-k_a(k_a\mp 1)]\,[J(J+1)-(k_a\mp 1)(k_a\mp 2)]}. \tag{2.83}$$

It can be seen that $\hat{H}_{rot}$ for an asymmetric top has non-vanishing matrix elements only between states of the same J and m, and between states which have the same k_a value or which have k_a values differing by two. This results in factorization of the Hamiltonian matrix into blocks, one block for each J value. Due to the $(2J+1)$-fold degeneracy in m, each block will be consisting of $(2J+1)$ identical blocks, one for each m value. However, in the absence of external fields, the m degeneracy will only represent itself in the intensity. So, only $m=0$ states can be considered. Each J block ($m=0$) can be block diagonalized to four blocks by constructing sum $(+)$ and difference $(-)$ combinations of $|J,K,0\rangle$ and $|J,-K,0\rangle$ wavefunctions, where $K=|k_a|$. The four blocks are called, E^+, E^-, O^+, and O^- depending on whether they are $+$ or $-$ combinations of symmetric top functions and whether K is even or odd. The dimensions of each of these blocks, for a given J, are

$$J \text{ even } \begin{cases} \dim(E^+) & = (J+2)/2 \\ \dim(E^-,O^+,O^-) & = J/2 \end{cases} \tag{2.84}$$

and

$$J \text{ odd} \begin{cases} \dim(E^-) & = (J-1)/2 \\ \dim(E^+, O^+, O^-) & = (J+1)/2 \end{cases} \tag{2.85}$$

Below, the energies and wavefunctions for the states with $J = 0, 1$, and 2 will be discussed. As mentioned before, the m label can be suppressed so that the basis functions are labeled as $|J, k_a\rangle$.

The $J = 0$ block of the Hamiltonian matrix is a 1×1 block involving the $J = k_a = 0$ basis set wavefunction. This matrix element is equal to zero. So,

$$E_{rot}(J = 0) = 0 \tag{2.86}$$

and

$$\Phi_{rot}(J = 0) = \sqrt{\frac{1}{8\pi^2}} \tag{2.87}$$

The $J = 1$ block is a 3×3 matrix involving $|1, -1\rangle$, $|1, 0\rangle$, and $|1, +1\rangle$ basis functions. In this basis set, using Equations (2.81) - (2.83), it can be shown that the $J = 1$ block looks like

$$\begin{array}{c} \\ \langle 1,-1| \\ \langle 1,0| \\ \langle 1,+1| \end{array} \begin{array}{c} \begin{array}{ccc} |1,-1\rangle & |1,0\rangle & |1,+1\rangle \end{array} \\ \begin{bmatrix} A + \frac{B+C}{2} & 0 & \frac{B-C}{2} \\ 0 & B + C & 0 \\ \frac{B-C}{2} & 0 & A + \frac{B+C}{2} \end{bmatrix} \end{array} \tag{2.88}$$

This matrix can be re-arranged according to even and odd values of K. This gives

$$\begin{array}{c} \\ \langle 1,-1| \\ \langle 1,+1| \\ \langle 1,0| \end{array} \begin{array}{c} \begin{array}{ccc} |1,-1\rangle & |1,+1\rangle & |1,0\rangle \end{array} \\ \left[\begin{array}{cc|c} A + \frac{B+C}{2} & \frac{B-C}{2} & 0 \\ \frac{B-C}{2} & A + \frac{B+C}{2} & 0 \\ \hline 0 & 0 & B + C \end{array}\right] \end{array} \tag{2.89}$$

Hence, the matrix is block diagonalized into a 2×2 block and a 1×1 block. This matrix can be further simplified if combinations of symmetric top wavefunctions are considered.

The sum and difference combinations are labeled $|J, K, E^{\pm}\rangle$ and $|J, K, O^{\pm}\rangle$. i.e.

$$|1, 1, O^{+}\rangle = \frac{1}{\sqrt{2}}[|1, +1\rangle + |1, -1\rangle], \tag{2.90}$$

$$|1, 1, O^{-}\rangle = \frac{1}{\sqrt{2}}[|1, +1\rangle - |1, -1\rangle], \tag{2.91}$$

and

$$|1, 0, E^{+}\rangle = |1, 0\rangle, \tag{2.92}$$

and there is no E^{-} according to Equation (2.85). These functions are eigenfunctions of $\hat{H}_{rot}$ and thus the eigenvalues are given by the diagonal matrix elements of $\hat{H}_{rot}$ in these superposition states. Using Equations (2.81) - (2.83) together with Equation (2.73) it is straightforward to show that

$$E_{rot}(1, 1, O^{+}) = \frac{1}{2}\left[\langle 1, +1| + \langle 1, -1|\right] \hat{H}_{rot} \left[|1, +1\rangle + |1, -1\rangle\right] = A + B, \tag{2.93}$$

$$E_{rot}(1, 1, O^{-}) = \frac{1}{2}\left[\langle 1, +1| - \langle 1, -1|\right] \hat{H}_{rot} \left[|1, +1\rangle - |1, -1\rangle\right] = A + C, \tag{2.94}$$

$$E_{rot}(1, 0, E^{+}) = \langle 1, 0|\hat{H}_{rot}|1, 0\rangle = B + C. \tag{2.95}$$

In this basis, the $J = 1$ block takes the form,

$$\begin{array}{c} \\ \langle 1,1,O^{+}| \\ \langle 1,1,O^{-}| \\ \langle 1,0,E^{+}| \end{array} \begin{array}{c} \begin{array}{ccc} |1,1,O^{+}\rangle & |1,1,O^{-}\rangle & |1,0,E^{+}\rangle \end{array} \\ \begin{bmatrix} A+B & 0 & 0 \\ 0 & A+C & 0 \\ 0 & 0 & B+C \end{bmatrix} \end{array}, \tag{2.96}$$

where the $J = 1$ block is diagonalized into three 1×1 blocks, in agreement with Equation (2.85).

The $J = 2$ block is a 5×5 matrix that diagonalizes into one 2×2 block and three 1×1 blocks. The appropriate basis functions are

$$|2, 2, E^{+}\rangle = \frac{1}{\sqrt{2}}\left[|2, +2\rangle + |2, -2\rangle\right], \tag{2.97}$$

$$|2, 2, E^{-}\rangle = \frac{1}{\sqrt{2}}\left[|2, +2\rangle - |2, -2\rangle\right], \tag{2.98}$$

$$|2,1,O^+\rangle = \frac{1}{\sqrt{2}}\left[|2,+1\rangle + |2,-1\rangle\right], \tag{2.99}$$

$$|2,1,O^-\rangle = \frac{1}{\sqrt{2}}\left[|2,+1\rangle - |2,-1\rangle\right], \tag{2.100}$$

and

$$|2,0,E^+\rangle = |2,0\rangle. \tag{2.101}$$

The $J = 2$ block in this basis is

$$\begin{array}{c} \\ \langle 2,0,E^+| \\ \langle 2,2,E^+| \\ \langle 2,2,E^-| \\ \langle 2,1,O^+| \\ \langle 2,1,O^-| \end{array} \begin{array}{c} \begin{array}{ccccc} |2,0,E^+\rangle & |2,2,E^+\rangle & |2,2,E^-\rangle & |2,1,O^+\rangle & |2,1,O^-\rangle \end{array} \\ \left[\begin{array}{ccccc} 3(B+C) & \sqrt{3}(B-C) & 0 & 0 & 0 \\ \sqrt{3}(B-C) & 4A+B+C & 0 & 0 & 0 \\ \hline 0 & 0 & 4A+B+C & 0 & 0 \\ 0 & 0 & 0 & A+4B+C & 0 \\ 0 & 0 & 0 & 0 & A+B+4C \end{array}\right] \end{array}.$$

From the three 1×1 blocks, the following energies are obtained

$$E_{rot}(2,2,E^-) = 4A + B + C, \tag{2.102}$$

$$E_{rot}(2,1,O^+) = A + 4B + C, \tag{2.103}$$

and

$$E_{rot}(2,1,O^-) = A + B + 4C \tag{2.104}$$

The eigenvalues of the top-left 2×2 block matrix are labeled as $E^{\pm}_{rot}(2,E^+)$, and they are

$$E^{\pm}_{rot}(2,E^+) = 2A + 2B + 2C \pm 2\sqrt{(B-C)^2 + (A-C)(A-B)}, \tag{2.105}$$

and the eigenfunctions $\Phi^{\pm}_{rot}(J,E^+)$ are

$$\Phi^{+}_{rot}(2,E^+) = \frac{1}{\sqrt{2}}\left[c^-|2,0,E^+\rangle + c^+|2,2,E^+\rangle\right], \tag{2.106}$$

and

$$\Phi^{-}_{rot}(2,E^+) = \frac{1}{\sqrt{2}}\left[c^+|2,0,E^+\rangle - c^-|2,2,E^+\rangle\right], \tag{2.107}$$

where

$$c^{\pm} = \left\{ 1 \pm \frac{2A - B - C}{\left[3(B-C)^2 + (2A-B-C)^2\right]^{1/2}} \right\}^{1/2} . \tag{2.108}$$

The two functions, $\Phi^{\pm}_{rot}(2, E^+)$, are a mixture of $k_a = 0$ and $k_a = \pm 2$ wavefunctions with coefficients that depend on the rotational constants. So, $\Phi^{\pm}_{rot}(2, E^+)$, are not eigenfunctions of $\hat{J}_z$ and this is the reason that k_a is said not to be a *good* quantum number. There are two ways of labeling the energy levels of asymmetric tops. The energy levels can be designated by $J_{K_a K_c}$ where $K_a = |k_a|$ and $K_c = |k_c|$ refer to the prolate top and oblate top levels with which that particular asymmetric top level correlates. The correlation diagram is shown in Figure 2.2. Using this designation, asymmetric top levels can also be referred to as being ee, eo, oe, or oo depending on whether K_a and K_c are even (e) or odd (o), respectively. A second useful way of labeling the states is using the J_τ designation, where $\tau = K_a - K_c$. This designation has the useful property that if states of a given J are labeled in decreasing τ value (τ runs from J to $-J$) then this is also the order of decreasing energy. Asymmetric rotor energy levels with $J = 0, 1, 2, 3$ are shown in Table 2.2 using both designations.

Table 2.2: Algebraic relations for the asymmetric rotor energy levels with $J = 0, 1, 2$ and 3.

J_τ	$J_{K_a K_c}$	E_{rot}
0_0	0_{00}	0
1_1	1_{10}	$A + B$
1_0	1_{11}	$A + C$
1_{-1}	1_{01}	$B + C$
2_2	2_{20}	$2A + 2B + 2C + 2\sqrt{(B-C)^2 + (A-C)(A-B)}$
2_1	2_{21}	$4A + B + C$
2_0	2_{11}	$A + 4B + C$
2_{-1}	2_{12}	$A + B + 4C$
2_{-2}	2_{02}	$2A + 2B + 2C - 2\sqrt{(B-C)^2 + (A-C)(A-B)}$

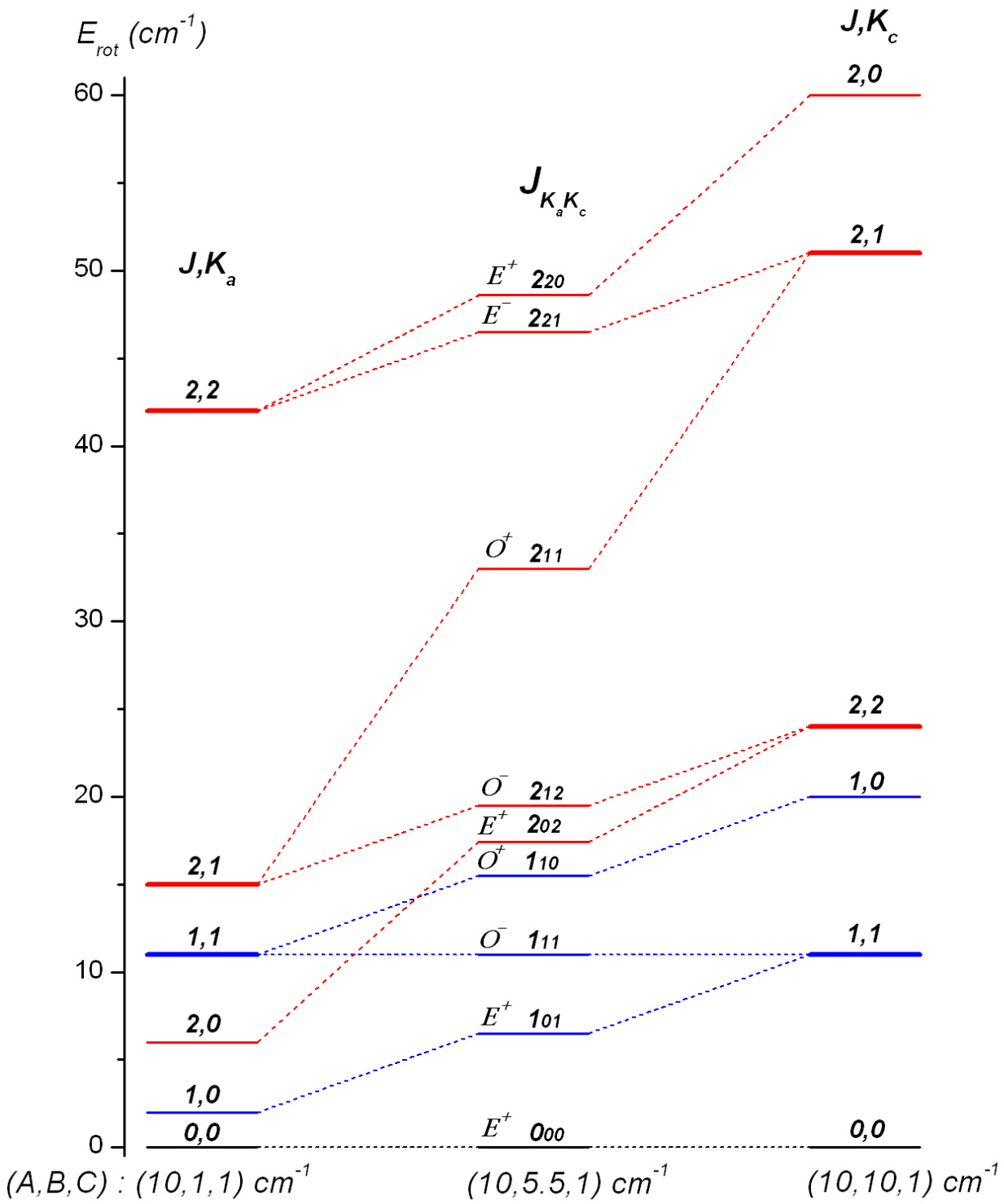

Figure 2.2: The correlation diagram of the $J = 0$ (black), $J = 1$ (blue), and $J = 2$ (red) energy levels of a rigid "very asymmetric" molecule (i.e. $\kappa = 0$) with those of the prolate and oblate top, on the left and right, respectively. Note that the levels of a given J do not cross.

2.5 Semi-rigid rotor and centrifugal distortion constants

The previous section dealt with rotation of rigid molecules, but in reality, molecules and especially weakly-bound molecular complexes are far from being rigid. As the molecule rotates, atoms experience a centrifugal force that distorts the inter-nuclear positions. Figure 2.3 illustrates a simple mass-spring model for a diatomic molecule. For this situation an expression can be obtained for the stretching of the internuclear separation, r, by allowing the bond length to stretch from its equilibrium, r_e, to r_c under the action of the centrifugal force.

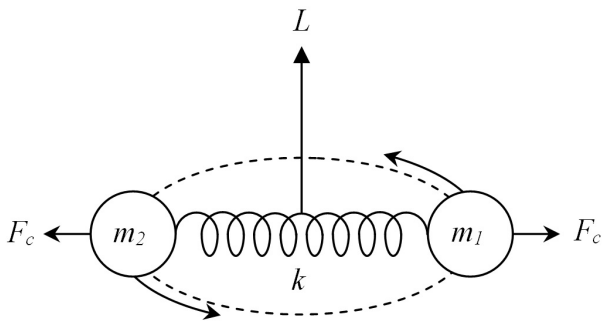

Figure 2.3: Simple mass-spring model for a non-rigid diatomic molecule.

$$F_c = \mu r_c \omega^2 = \frac{\hat{J}^2}{\mu r_c^3} \tag{2.109}$$

where μ is the reduced mass. The centrifugal force is balanced by the Hooke's law restoring force

$$F_r = k(r_e - r_c). \tag{2.110}$$

Also, $k = \mu\omega_e^2$, where ω_e is the equilibrium vibration frequency, and $B \propto 1/2\mu r_e^2$. After some algebra (Appendix A), it can be shown that

$$\hat{H}_{rot} = B\hat{J}^2 - D\hat{J}^4. \tag{2.111}$$

where

$$D = \frac{4B_e^3}{\omega_e^2}. \tag{2.112}$$

The rotational energy for a non-rigid diatomic molecule as modified by centrifugal distortion is

$$E_{rot} = BJ(J+1) - D\left[J(J+1)\right]^2 = \left[B - DJ(J+1)\right] J(J+1) \tag{2.113}$$

The negative sign in front of D is introduced in order to make D a positive number. The constant D is called the *centrifugal distortion constant*. The centrifugal distortion increases the internuclear separation r, which decreases the effective B-value of a pure rotational transition, $B_{eff.} = B - DJ(J+1)$. The transition frequency can be written as

$$\nu_{J\to J+1} = E_{rot}(J+1) - E_{rot}(J) = 2\left[B - 2D(J+1)^2\right](J+1). \tag{2.114}$$

It should be noted that the rotational constants also depend on the vibrational states. For instance, a diatomic molecule at an excited vibrational state spends more of its time at a larger r than in the ground vibrational state which means a decrease in the rotational constant B.

In fact, there are additional higher order distortion corrections that lead to the following rotational energy expression

$$E_{rot} = BJ(J+1) - D[J(J+1)]^2 + H[J(J+1)]^3 + L[J(J+1)]^4 + M[J(J+1)]^5 + \cdots, \tag{2.115}$$

where D, H, L, and M are the quartic (4^{th} power of J), sextic (6^{th} power of J), octic (8^{th} power of J), and dectic (10^{th} power of J) centrifugal distortion constants. In order to observe the contribution of each of the centrifugal distortion terms in the rotational energy, the values of the first few distortion constants for carbon monoxide in the ground vibrational state are given as an example, $B(\nu = 0) = 57.6359683$ GHz, $D(\nu = 0) = 0.1835055$ MHz, $H(\nu = 0) = 0.1725$ Hz, and $L(\nu = 0) = 3.1 \times 10^{-7}$ Hz [44].
Although the treatment here is rough, it applies to both diatomic and linear polyatomic molecules.

In the same way, the effect of centrifugal forces on symmetric top molecules adds correction terms to the energy expression. For the case of a prolate top the energy expression in

Equation (2.62), up to quartic distortion terms, becomes

$$E_{rot}(J,k_a) = BJ(J+1) - D_J[J(J+1)]^2 + (A-B)k_a^2 - D_K k_a^4 - D_{JK}J(J+1)k_a^2, \quad (2.116)$$

There are now three diagonal centrifugal distortion constants D_J, D_K, and D_{JK} and the transition frequencies are given by

$$\nu_{J\to J+1} = E_{rot}(J+1,K) - E_{rot}(J,K) \quad (2.117)$$

$$= 2B(J+1) - 4D_J(J+1)^3 - 2D_{JK}(J+1)k_a^2. \quad (2.118)$$

For a given $J \to J+1$ transition, the constant D_{JK} splits transitions with different k_a. Also, off-diagonal distortion terms may be added to the energy expression of a symmetric top depending on its symmetry. Higher order corrections to energy levels of a symmetric top are given by sextic and octic centrifugal distortion constants as

$$E_{dist.}^{Sextic} = H_J[J(J+1)]^3 + H_{JK}[J(J+1)]^2k_a^2 + H_{KJ}[J(J+1)]k_a^4 + H_K k_a^6,$$

$$E_{dist.}^{Octic} = L_J[J(J+1)]^4 + L_{JJK}[J(J+1)]^3k_a^2 + L_{JK}[J(J+1)]^2k_a^4 + L_{KKJ}[J(J+1)]k_a^6 + L_K k_a^8.$$

There are similar expressions for an oblate top where k_a is replaced by k_c.

Depending on the symmetry of an asymmetric top molecule, in addition to diagonal centrifugal distortion parameters stated above with capital letters, there are off-diagonal centrifugal distortion parameters that are represented by lowercase letters. They are

$$\begin{aligned} \text{Off-diagonal quartic constants}: &\quad d_J \text{ and } d_K, \\ \text{Off-diagonal sextic constants}: &\quad h_J, h_{JK}, \text{ and } h_K, \\ \text{Off-diagonal octic constants}: &\quad l_J, l_{JK}, l_{KJ}, \text{ and } l_K. \end{aligned}$$

The exact expression for rotational energy levels of an asymmetric top containing off-diagonal distortion terms depend on the reduced form of Hamiltonian being used [45].

2.6 Harmonic Oscillator

For the vibrational motions of a molecule, a harmonic oscillator model can be used as the base model. In general, for a molecule with N atoms, there exists $3N-6$ ($3N-5$ for linear molecules) vibrational modes and each of the modes can be considered as a harmonic oscillator. Although, in reality, the potential function for molecular vibrations is anharmonic, the simple harmonic oscillator model provides a reasonable approximation of vibrational energy levels for small values of vibrational quantum number, v, but will be insufficient as v grows or if the anharmonicity effects are non-negligible.

The one-dimensional harmonic oscillator Schrödinger equation is

$$\hat{H}_{ho}\Phi_v = \frac{1}{2}(\hat{P}^2 + \omega^2 Q^2) = E_v \Phi_v, \tag{2.119}$$

where Q is the mass-weighted normal coordinate and $\hat{P} = -i\hbar\partial/\partial Q$ is its conjugate momentum. Eigenvalues obtained from this equation are

$$E_v = \left(v + \frac{1}{2}\right)\hbar\omega, \tag{2.120}$$

and the eigenfunctions are

$$\Phi_v = N_v H_v(\sqrt{\frac{\omega}{\hbar}}Q)e^{-\omega Q^2/2\hbar}, \tag{2.121}$$

where $H_v(\sqrt{\frac{\omega}{\hbar}}Q)$ is the Hermite polynomial of degree v and N_v is the normalization constant given by

$$N_v = \left(\frac{\sqrt{\omega}}{\sqrt{\hbar\pi}2^v v!}\right)^{\frac{1}{2}}. \tag{2.122}$$

The harmonic oscillator Hamiltonian for a molecule is

$$\hat{H}_{vib} = \frac{1}{2}\sum_{r=1}^{3N-6}(\hat{P}_r^2 + \omega_r^2 Q_r^2) \tag{2.123}$$

The vibrational eigenfunction for the molecule can be written as the product of the eigenfunctions for each of the normal coordinates,

$$\Phi_{vib} = \Phi_{v_1}(Q_1)\Phi_{v_2}(Q_2)\cdots\Phi_{v_{3N-6}}(Q_{3N-6})$$

$$= \exp\left[-\frac{1}{2}\sum_{r=1}^{3N-6}\frac{\omega_r}{\hbar}Q_r^2\right]\prod_{r}^{3N-6}N_{v_r}H_{v_r}(\sqrt{\frac{\omega_r}{\hbar}}Q_r), \tag{2.124}$$

and the eigenvalues are

$$E_{vib} = \sum_{r=1}^{3N-6}\left(v_r + \frac{1}{2}\right)\hbar\omega_r. \tag{2.125}$$

2.6.1 Anharmonicity

A more realistic model for the vibration of molecules is an anharmonic oscillator where higher order terms in the vibrational potential function are taken into account. Morse potential function is a practical one-dimensional potential for diatomic molecules and it could, in principle, be applied to any two nuclei in the molecule to simulate the vibrations between those nuclei. Morse potential, unlike the harmonic oscillator, allows for anharmonicity and also asymptotically approaches a dissociation limit at large internuclear separation rather than having unlimited bound states in the harmonic oscillator model. The Morse potential function is

$$V_{vib}(r) = D\left(1 - e^{-\beta(r-r_e)}\right)^2. \tag{2.126}$$

Here, D is the dissociation energy and r_e is the distance between the nuclei at equilibrium. The vibrational energy levels for Morse potential can analytically be obtained,

$$E_{vib}(v) = \omega_e(v + \frac{1}{2}) - \omega_e\chi_e(v + \frac{1}{2})^2. \tag{2.127}$$

where ω_e and $\omega_e\chi_e$, in units of cm^{-1}, are

$$\omega_e = \beta\left(\frac{D\hbar \times 10^2}{\pi c\mu}\right),$$
$$\omega_e\chi_e = \frac{\hbar\beta^2 \times 10^2}{4\pi\mu c}.$$

Figure 2.4 shows the first few vibrational energy levels for the Morse potential and the corresponding harmonic oscillator potential. There are other model potentials which take higher order terms into account but they will not be discussed in this thesis.

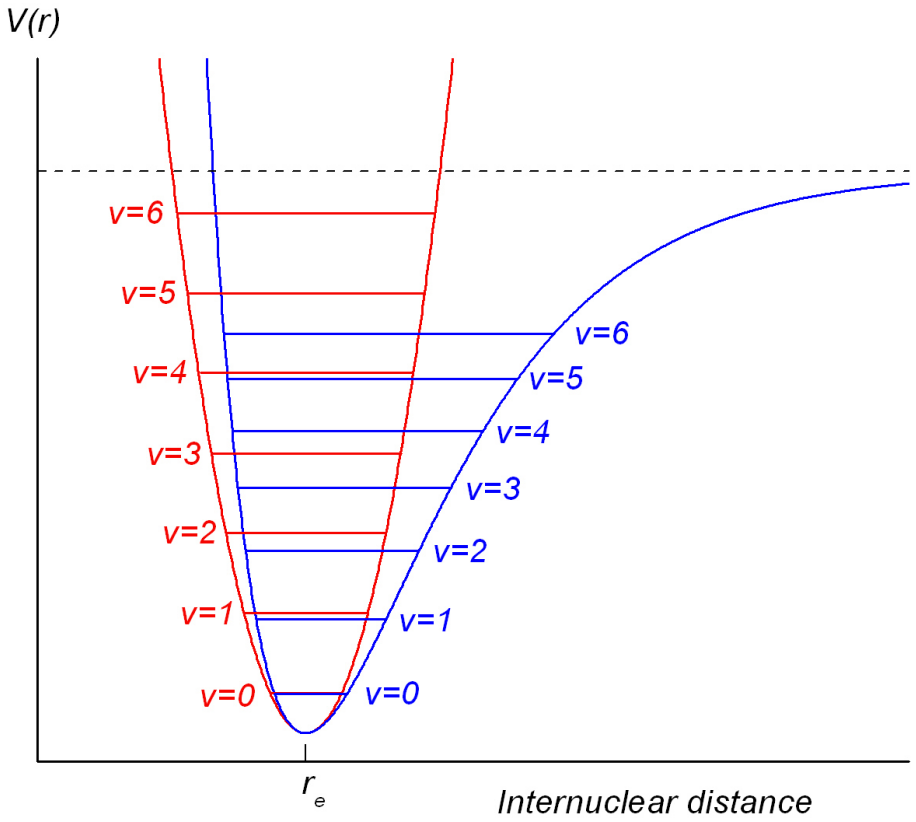

Figure 2.4: Morse (blue) and harmonic (red) potentials. The first few vibrational energy levels are shown for both potentials to illustrate how harmonic oscillator approximation fails as v increases. Arbitrary units are used

2.7 Notes on Symmetry

2.7.1 Molecular symmetry (MS) group

In order to classify the energy levels of a molecule according to their symmetries, it is essential to recognize its symmetry group. The symmetry group of a molecule is a group whose elements do not alter the energy of the molecule; or in more mathematical terms, the elements of the symmetry group commute with the Hamiltonian of the molecule. Different molecules have different symmetry groups and different symmetry groups have different irreducible representations which are readily tabulated in character tables. The irreducible representation labels, also called symmetry labels, are straightforward to determine and are

very helpful in understanding spectra of a given molecule. The symmetry labels are used to efficiently determine nuclear spin statistical weights, identify the states that can be connected by a transition in the presence of electromagnetic radiation, and to determine the states that can or cannot interact as a result of adding a perturbation term to the Hamiltonian.

The CNPI (Complete Nuclear Permutation Inversion) group contains all possible permutations of identical nuclei in the molecule and their combination with the inversion operator. The elements of the CNPI group all commute with the Hamiltonian of the isolated molecule in free space, and therefore the CNPI group is a symmetry group of that molecule. The irreducible representations of the CNPI group of a molecule can be used to label its energy levels. However, this is not always a wise task to do because the symmetry labels are used to label energy levels that can be distinguished in the experimental results. For instance, for a molecule in an electronic state in which there are two or more versions of the equilibrium structure, between which tunneling does not occur or the resolution of the experimental spectrum is not high enough to detect the tunneling splittings, use of CNPI group is more detailed than necessary. To sufficiently symmetry label the energy levels a subgroup of the CNPI group, called the molecular symmetry (MS) group, is used. The MS group is obtained from the CNPI group by removing all unfeasible elements. The MS group is the symmetry group whose elements commute with the complete internal Hamiltonian $\hat{H}_{int}$ (or $\hat{H}_{rve}$). Therefore, elements of the MS group is used to label the rovibronic energy levels of the molecule. Also, there are two "near symmetry groups" whose elements do not commute with the $\hat{H}_{int}$ (or $\hat{H}_{rve}$). They are molecular rotation groups and the molecular point groups. However, all elements of the molecular rotation group commute with rigid rotator Hamiltonian and all elements of the molecular point group commute with the vibronic Hamiltonian. Therefore, the rotation group is used to only symmetry label the rotational levels and the point group is used to label the vibronic levels. These concepts are applied to the energy levels of the T-shaped isomer of OCS$-C_2H_2$ in the next subsections.

2.7.2 Symmetry classification of rotational wavefunctions

The T-shaped isomer of OCS−C_2H_2 is an asymmetric top with an equilibrium structure that belongs to the C_{2v}(M) MS group. The character table of C_{2v}(M) group is shown in Table 2.3 and structure of the T-shaped isomer of OCS−C_2H_2 complex is illustrated in Figure 2.5.

Table 2.3: Character table of the C_{2v}(M) molecular symmetry group.

$C_{2v}(M)$:	E	$(12)(34)$	E^*	$(12)(34)^*$		
C_{2v}:	E	C_{2a}	σ_{ab}	σ_{ac}		
Equiv. rot. :	R^0	R_a^π	R_c^π	R_b^π		
A_1 :	1	1	1	1	:	$T_a, \alpha_{aa}, \alpha_{bb}, \alpha_{cc}$
A_2 :	1	1	-1	-1	:	$\hat{J}_a, \alpha_{bc}, \Gamma^*$
B_1 :	1	-1	-1	1	:	$T_c, \hat{J}_b, \alpha_{ab}$
B_2 :	1	-1	1	-1	:	$T_b, \hat{J}_c, \alpha_{ac}$

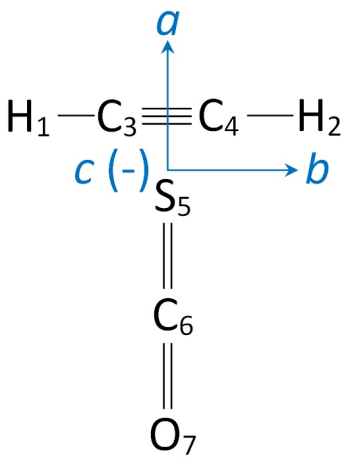

Figure 2.5: Structure of the T-shaped isomer of OCS−C_2H_2 showing the principal axes.

The elements of the C_{2v}(M) molecular symmetry group are the ones in the top row of Table 2.3. E is the identity operator and leaves the molecule unchanged. $(12)(34)$ is the permutation operator which replaces atom 1 with 2 and atom 3 with 4. E^* is the inversion operator and inverts the spatial coordinates of all the nuclei and electrons with respect to the origin (molecule's center of mass). $(12)(34)^*$ is the combination of E^* and $(12)(34)$ operators. Each element of the MS group of a molecule causes a certain change in the Euler angles of the molecule. The change in the Euler angles can be represented as an equivalent rotation.

These equivalent rotations are identified in the third row of Table 2.3. For symmetric top molecules the notation R_α^π and R_z^β is used for equivalent rotations. Where the rotation R_α^π, represents a rotation of the (x, y, z) axes through π radians about an axis in the xy plane making an angle α with the x axis, and R_z^β is a rotation by β radians about the z axis (α, and β are measured in a right handed sense about the z axis). But, for asymmetric top molecules, the notation R_a^π, R_b^π, and R_c^π is used.

In order to determine the transformation properties of any symmetric top or asymmetric top wavefunction in an MS group, it is needed to determine the general effect of the rotation operations R_α^π and R_z^β on any symmetric top function by determining their effects on the ladder operators and on the function $|J, 0, 0\rangle$ [42]. This is done using,

$$R_z^\beta|J, k, m\rangle = e^{ik\beta}|J, k, m\rangle, \tag{2.128}$$

and

$$R_\alpha^\pi|J, k, m\rangle = (-1)^J e^{-2ik\alpha}|J, -k, m\rangle. \tag{2.129}$$

where J is an integer. In the absence of external fields, the m-degeneracy can be neglected.

The rotational wavefunctions of the T-shaped isomer of OCS$-C_2H_2$ in I^r representation are linear combinations of symmetric top rotational wavefunctions $|J, k_a, m\rangle$, and in III^r representation, they are linear combinations of $|J, k_c, m\rangle$ wavefunctions. By classifying both the $|J, k_a, m\rangle$ basis wavefunctions and the $|J, k_c, m\rangle$ basis wavefunctions in the C_{2v}(M) MS group and considering the correlation of their symmetry labels, the symmetry labels for asymmetric top wavefunctions can be determined.

In the I^r representation, $R_a^\pi = R_z^\pi$, $R_c^\pi = R_{\pi/2}^\pi$, $R_b^\pi = R_0^\pi$, and one can take $R^0 = R_z^0$. Hence, the effect of rotation operations on the $|J, k_a = 0, m\rangle$ functions can be obtained using Equations (2.128) and (2.129), as

$$R_z^0|J, k_a = 0, m\rangle = |J, k_a = 0, m\rangle, \tag{2.130}$$

$$R_z^\pi|J, k_a = 0, m\rangle = |J, k_a = 0, m\rangle, \tag{2.131}$$

$$R^{\pi}_{\pi/2}|J,k_a=0,m\rangle = (-1)^J|J,k_a=0,m\rangle, \tag{2.132}$$

$$R^{\pi}_{0}|J,k_a=0,m\rangle = (-1)^J|J,k_a=0,m\rangle. \tag{2.133}$$

For the pair of functions $|J,k_a,m\rangle$ and $|J,-k_a,m\rangle$, one can similarly obtain

$$R^{0}_{z}|J,\pm k_a,m\rangle = |J,\pm k_a,m\rangle, \tag{2.134}$$

$$R^{\pi}_{z}|J,\pm k_a,m\rangle = (-1)^{k_a}|J,\pm k_a,m\rangle, \tag{2.135}$$

$$R^{\pi}_{\pi/2}|J,\pm k_a,m\rangle = (-1)^{J+k_a}|J,\mp k_a,m\rangle, \tag{2.136}$$

$$R^{\pi}_{0}|J,\pm k_a,m\rangle = (-1)^{J}|J,\mp k_a,m\rangle. \tag{2.137}$$

The characters produced by symmetric top wavefunctions are obtained from the trace of the rotation operators in matrix form in the basis of symmetric top wavefunctions. The characters for $|J,k_a=0,m\rangle$ functions are straightforward to calculate. The rotation operators in matrix form in the basis of $|J,\pm k_a,m\rangle$ wavefunctions are:

$$\chi(R^0_z) = trace\begin{bmatrix}1 & 0\\ 0 & 1\end{bmatrix} = 2, \qquad \chi(R^\pi_z) = trace\begin{bmatrix}(-1)^{k_a} & 0\\ 0 & (-1)^{k_a}\end{bmatrix} = 2(-1)^{k_a},$$

$$\chi(R^\pi_{\pi/2}) = trace\begin{bmatrix}0 & (-1)^{J+k_a}\\ (-1)^{J+k_a} & 0\end{bmatrix} = 0, \qquad \chi(R^\pi_0) = trace\begin{bmatrix}0 & (-1)^{J}\\ (-1)^{J} & 0\end{bmatrix} = 0.$$

So, the representations generated by prolate symmetric top wavefunctions, $|J,k_a,m\rangle$, are

	E	$(12)(34)$	E^*	$(12)(34)^*$
Equiv. rot. :	R^0_z	R^π_z	$R^\pi_{\pi/2}$	R^π_0
$\Gamma_{\|J,k_a=0,m\rangle}$	1	1	$(-1)^J$	$(-1)^J$
$\Gamma_{\|J,\pm k_a,m\rangle}$	2	$2(-1)^{k_a}$	0	0

Similar to the treatment above for I^r convention, the representations generated by the functions $|J,k_c=0,m\rangle$, and $|J,\pm k_c,m\rangle$ can be obtained. In the III^r representation, $R^\pi_a = R^\pi_0$, $R^\pi_c = R^\pi_z$, $R^\pi_b = R^\pi_{\pi/2}$, and one can take $R^0 = R^0_z$. This results in

	E	$(12)(34)$	E^*	$(12)(34)^*$
Equiv. rot. :	R_z^0	R_0^π	R_z^π	$R_{\pi/2}^\pi$
$\Gamma_{\|J,k_c=0,m\rangle}$	1	$(-1)^J$	1	$(-1)^J$
$\Gamma_{\|J,\pm k_c,m\rangle}$	2	0	$2(-1)^{k_c}$	0

These representations can be written in terms of the irreducible representation of the C_{2v}(M) group as the following,

$$\Gamma_{rot} = a_1\Gamma_{A_1} \oplus a_2\Gamma_{A_2} \oplus a_3\Gamma_{B_1} \oplus a_4\Gamma_{B_2}, \tag{2.138}$$

where the coefficients are calculated using

$$a_i = \frac{1}{h}\sum_R \chi^{\Gamma_{rot}}[R]\,\chi^{\Gamma_i}[R]^*, \tag{2.139}$$

where h is the order of the group and R runs over all the elements of the group. The result of reduction of the above representations as a function of J, and $K_a = |k_a|$, and $K_c = |k_c|$ is collected in Table 2.4.

Table 2.4: Representation of the C_{2v}(M) group for the T-shaped isomer of OCS−C_2H_2 generated by basis functions $|J, k_a, m\rangle$ and $|J, k_c, m\rangle$.[a]

K_a		Γ_{rot}	K_c		Γ_{rot}
0	J even	A_1	0	J even	A_1
	J odd	A_2		J odd	B_2
even		$A_1 \oplus A_2$	even		$A_1 \oplus B_2$
odd		$B_1 \oplus B_2$	odd		$A_2 \oplus B_1$

[a] $K_a = |k_a|$, $K_c = |k_c|$

The symmetry species of the asymmetric rotor wavefunctions can be determined by correlating between the K_a and K_c labels given in Table 2.4. Figure 2.6 shows this correlation. Alternatively, one could set up + and - combinations of $|J, K_a, m\rangle$ and $|J, -K_a, m\rangle$ functions and determine their transformation properties. In any case, it turn out that the symmetry species for a rigid rotor state $J_{K_aK_c}$ depends only on the evenness and oddness of K_a and K_c, and the result is summarized in Table 2.5 where "ee" is any state $J_{K_aK_c}$ for which K_a and K_c are even, and "eo" is any state for which K_a is even and K_c odd, etc.

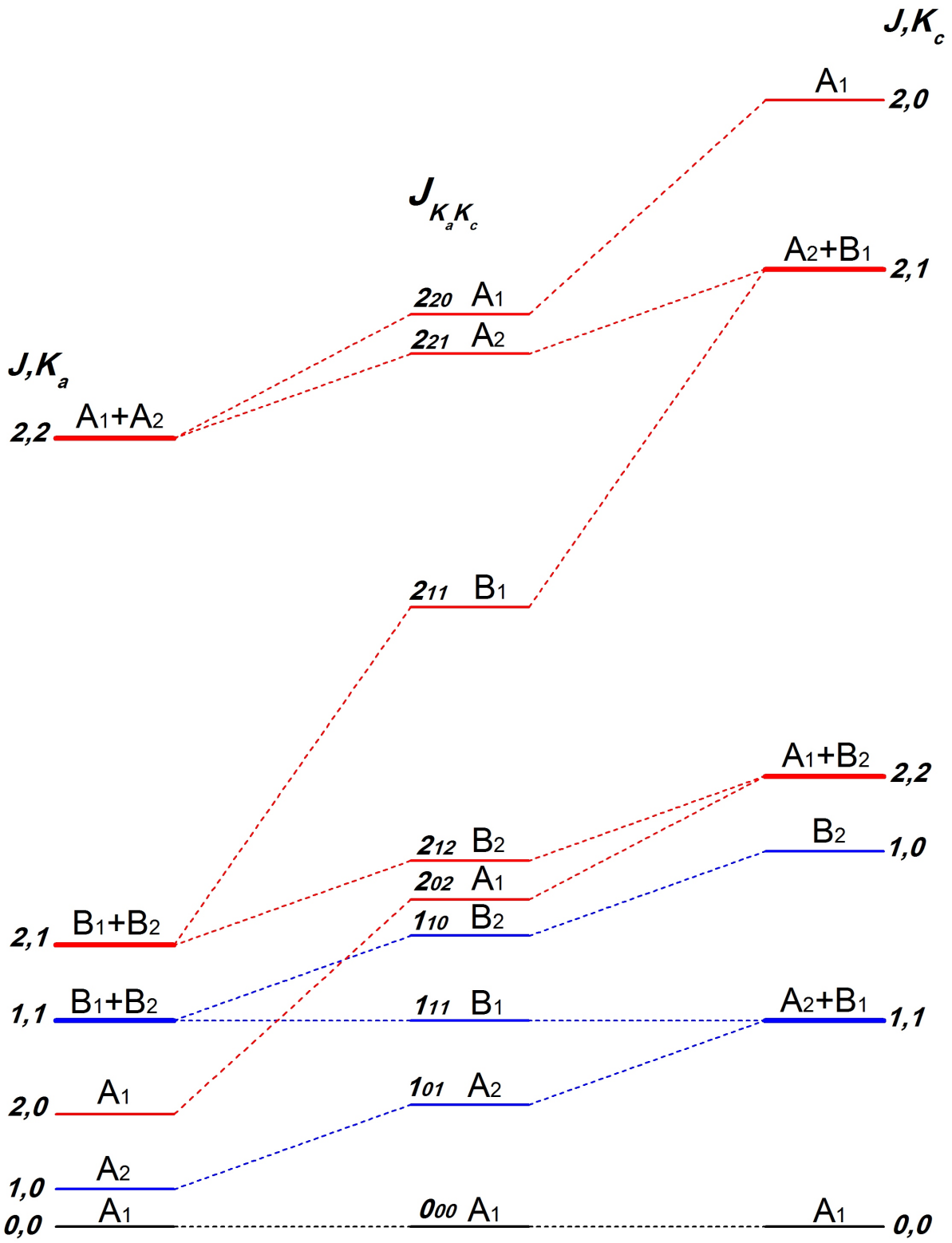

Figure 2.6: The C_{2v}(M) symmetry labels for the asymmetric rotor energy levels of T-shaped OCS−C_2H_2 (center) and their correlation with the prolate rotor (left) and oblate rotor (right) levels.

Table 2.5: Symmetry species of $J_{K_aK_c}$ levels of T-shaped OCS$-C_2H_2$ in the C_{2v}(M) group.

K_aK_c	Γ_{rot}	K_aK_c	Γ_{rot}
ee	A_1	oe	B_2
eo	A_2	oo	B_1

A concise way of determining the symmetry species of asymmetric tops, once the equivalent rotations of each MS group element is determined, follows from the "asymmetric top symmetry rule", which states that:

The ee functions will transform as the totally symmetric representation, the eo functions as the representation having +1 for R_a^π (and -1 for R_b^π and R_c^π), the oe functions as the representation having +1 for R_c^π (and -1 for R_a^π and R_b^π), and the oo functions as the representation having +1 under R_b^π (and -1 for R_a^π and R_c^π).

This rule is based on the fact that the asymmetric rotor Hamiltonian is invariant to the Euler angle transformations caused by a two-fold rotation about the a, b, or c axis. The molecular rotation group is hence the group $\boldsymbol{D}_2 = \{E, R_a^\pi, R_b^\pi, R_c^\pi\}$, for which the character table is given in Table 2.6 . The results obtained in Table 2.5 are also included.

Table 2.6: The character table of the group $\boldsymbol{D}_2$ and the species of the asymmetric top functions $|J_{K_aK_c}\rangle$ in the group.

		E	R_a^π	R_b^π	R_c^π	K_aK_c	Symmetry of J_α
A	:	1	1	1	1	ee	
B_a	:	1	1	-1	-1	eo	J_a
B_b	:	1	-1	1	-1	oo	J_b
B_c	:	1	-1	-1	1	oe	J_c

2.7.3 Molecular point group

Molecular point groups consist of a certain definite set of symmetry operations (rotations, reflections, and rotation-reflections). They are called "point groups" because the center of mass of the molecule remains unchanged under all symmetry operations and all of the symmetry elements meet at this point. Any three-dimensional object can be classified as

"belonging" to one point group. The point group symmetry of an object is determined from the following:

$\boldsymbol{C}_n$	one n-fold rotation axis,
$\boldsymbol{C}_{nv}$	one n-fold rotation axis and n reflection planes containing this axis,
$\boldsymbol{C}_{nh}$	one n-fold rotation axis and one reflection plane perpendicular to this this axis,
$\boldsymbol{D}_n$	one n-fold rotation axis and n two-fold rotation axes perpendicular to it,
$\boldsymbol{D}_{nd}$	those of $\boldsymbol{D}_n$ plus n reflection planes containing the n-fold rotation axis and bisecting the angles between the n two-fold rotation axes,
$\boldsymbol{D}_{nh}$	those of $\boldsymbol{D}_n$ plus one reflection plane perpendicular to the n-fold rotation axis,
$\boldsymbol{S}_n$	one alternating axis of symmetry (about which rotation by $2\pi/n$ radians followed by reflection in a plane perpendicular to the axis is a symmetry operation).

In naming the point groups the *Schönflies notation* has been used, and other possible point groups are: $\boldsymbol{T}$, $\boldsymbol{T}_d$, $\boldsymbol{O}$, $\boldsymbol{O}_h$, $\boldsymbol{I}$, $\boldsymbol{I}_h$, and $\boldsymbol{K}_h$. The point groups $\boldsymbol{T}_d$, $\boldsymbol{O}_h$, and $\boldsymbol{I}_h$ consists of all rotation, reflection, and rotation-reflection symetry operations of a regular tetrahedron, cube, and icosahedron, respectively. $\boldsymbol{T}$, $\boldsymbol{O}$, and $\boldsymbol{I}$ are the rotational subgroups of these point groups, respectively. The point group, $\boldsymbol{K}_h$ consists of all the rotation, reflection, and rotation-reflection symmetry operations of a sphere. The point group for the T-shaped isomer of OCS$-$C$_2$H$_2$ is C_{2v} for which the elements are shown in the second row of Table 2.3.

As mentioned before, the elements of the molecular point group do not commute with the full Hamiltonian but they do commute with the vibrational Hamiltonian and electronic Hamiltonian. Therefore, the molecular point group is not used for labeling rovibronic states (rotational levels), but rather for labeling vibrational and electronic states and for studying vibronic interactions. For a rigid non-linear molecule, the molecular point group is isomorphic to the molecular symmetry group, and the effect of each element in the molecular point group on vibronic variables is the same as its partner in the molecular symmetry group. Therefore,

the same character table and irreducible representation labels are used for both groups, and classification of vibronic states is the same using either group. In the next subsection, a simple example of determining the symmetry species for a few of the vibrational modes of the T-shape isomer of OCS$-C_2H_2$ is presented.

2.7.4 Symmetry classification of vibrational wavefunctions

Symmetry species of the vibrational wavefunctions of the T-shaped isomer of OCS$-C_2H_2$ can be determined by finding the transformation properties of the Cartesian displacements associated with each of the atoms under the effect of symmetry operations of the C_{2v} point group. Hence, the representation generated by the Cartesian coordinates, Γ_{Car}, can be obtained which in turn reduces to the irreducible representation of the C_{2v} group. The OCS$-C_2H_2$ complex has six atoms ($N = 6$) and therefore, has twelve ($3N-6$) modes. Here, the attention will be given to the OCS ν_1 (C=O bond stretch), C_2H_2 ν_1 (C$-$H symmetric stretch), and C_2H_2 ν_3 (C$-$H asymmetric stretch) modes within the T-shaped isomer of OCS$-C_2H_2$. Figure 2.7 shows arbitrary x-axis displacements for the hydrogen atoms (atoms 1 and 2), and z-axis displacements for the carbon and oxygen atoms (atom 6 and 7).

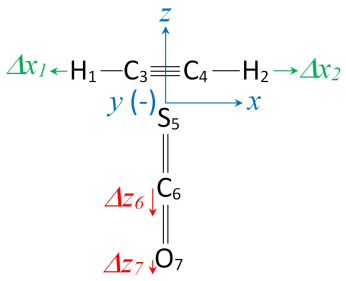

Figure 2.7: Arbitrary displacement vectors pertaining to the OCS ν_1, C_2H_2 ν_1, and C_2H_2 ν_3 vibrations within the T-shaped isomer of OCS$-C_2H_2$ (in I^r basis).

The effect of each of the elements of the C_{2v} group on the displacements Δx_1, Δx_2, Δz_6, and Δz_7, and the representations generated by these Cartesian displacements are as the following

C_{2v}	E	C_{2a}	σ_{ab}	σ_{ac}
Δx_1	Δx_1	Δx_2	Δx_1	Δx_2
Δx_2	Δx_2	Δx_1	Δx_2	Δx_1
${\Gamma_{vib}}^{\text{C-H}}$:	2	0	2	0
Δz_6	Δz_6	Δz_6	Δz_6	Δz_6
Δz_7	Δz_7	Δz_7	Δz_7	Δz_7
${\Gamma_{vib}}^{\text{O=C}}$:	2	2	2	2

The representations ${\Gamma_{vib}}^{\text{C-H}}$, and ${\Gamma_{vib}}^{\text{O=C}}$ can be written in terms of the irreducible representation of the C_{2v} point group. For the O=C bond stretch within the OCS monomer,

$$\Gamma_{vib}^{\text{O=C}} = 2A_1, \tag{2.140}$$

From the character table of C_{2v} group (Table 2.3), it can be seen that one of the zero-frequency normal coordinates, T_a, also transforms as A_1. This normal coordinate is related to the translational motion of the center of mass of the complex along the a axis. Subtracting this from ${\Gamma_{vib}}^{\text{O=C}}$, the symmetry species of the O=C vibrational mode is found to be A_1.

For the C−H bond stretches, the representation ${\Gamma_{vib}}^{\text{C-H}}$ is reduced as,

$$\Gamma_{vib}^{\text{C-H}} = A_1 \oplus B_2. \tag{2.141}$$

The A_1 and B_2 symmetry species are respectively attributed to the symmetric and anti-symmetric stretches of the two C−H bonds. These results are collected below

Vibrational Mode	Symmetry
O=C bond stretch	A_1
C-H symmetric stretch	A_1
C-H anti-symmetric stretch	B_2

The same procedure can be taken for all twelve vibrational modes of the complex, including intramolecular and intermolecular vibrations, to obtain their symmetry species.

2.7.5 Selection rules

As mentioned before, symmetry labels are used to identify the states that can be connected by a transition in the presence of electromagnetic radiation. A "vibrationally allowed" transition must satisfy the following symmetry condition [42]

$$\Gamma''_{vib} \otimes \Gamma'_{vib} \supset \Gamma(\mu_\alpha) = \Gamma(T_\alpha), \qquad \alpha = x, y, \text{or } z \; (a, b, \text{or } c) \tag{2.142}$$

where Γ''_{vib} and Γ'_{vib} are the symmetry species for the ground and excited vibrational states respectively, μ_α is the component of the electric dipole moment along inertial axis α, and T_α is the corresponding translational coordinate. The symmetry species of the translational coordinates, $\Gamma(T_\alpha)$, can be found in the right-most column of character tables.

The rovibronic transitions selection rules are obtained from

$$\Gamma''_{rve} \otimes \Gamma'_{rve} \supset \Gamma^*, \tag{2.143}$$

where $\Gamma_{rve} = \Gamma_{elec} \otimes \Gamma_{vib} \otimes \Gamma_{rot}$, and Γ^* is called the electric dipole representation. Γ^* is the representation of the MS group that has character $+1$ under all permutations and character -1 under all permutation inversions. For transitions occurring between the same electronic state, Equation (2.143) can be written as,

$$\Gamma''_{rv} \otimes \Gamma'_{rv} \supset \Gamma^*, \tag{2.144}$$

where $\Gamma_{rv} = \Gamma_{vib} \otimes \Gamma_{rot}$.

As an example, Equation (2.142) will be applied to the vibrational modes of the T-shaped OCS$-C_2H_2$ discussed in subsection 2.7.4 to determine the infrared active vibrations. The ground vibrational state always transforms as the totally symmetric representation of the MS group (i.e. A_1 in the case of C_{2v}(M)).

For the OCS O=C bond stretch, and C_2H_2 symmetric C-H stretch,

$$\Gamma''_{vib} \otimes \Gamma'_{vib} = A_1 \otimes A_1 = A_1 \supset \Gamma(T_a)$$

$$\text{but } \not\supset \Gamma(T_b)$$

$$\text{and } \not\supset \Gamma(T_c)$$

Therefore, OCS ν_1, and C_2H_2 ν_1 are allowed by symmetry and their dipole moment lies along the a axis. For the anti-symmetric C-H stretch of the C_2H_2,

$$\Gamma''_{vib} \otimes \Gamma'_{vib} = A_1 \otimes B_2 = B_2 \supset \Gamma(T_b)$$

$$\text{but } \not\supset \Gamma(T_a)$$

$$\text{and } \not\supset \Gamma(T_c)$$

So, the anti-symmetric C-H stretching mode of the C_2H_2 unit contains only b-type transition.

Now that the symmetry species of the vibrational levels are known and the rotational wavefunction are also symmetry-labeled (subsection 2.7.2), one can determine the symmetry species and obtain the selection rules for rovibrational states. Symmetry labels for ground and excited rovibrational states of the OCS ν_1 excitation ($A_1 \rightarrow A_1$) are:

Γ_{rot}	Γ''_{vib}	Γ'_{vib}	$\Gamma''_{rv} = \Gamma''_{vib} \otimes \Gamma_{rot}$	$\Gamma'_{rv} = \Gamma'_{vib} \otimes \Gamma_{rot}$
A_1 (ee)	A_1	A_1	A_1 (ee)	A_1 (ee)
A_2 (eo)	A_1	A_1	A_2 (eo)	A_2 (eo)
B_2 (oe)	A_1	A_1	B_2 (oe)	B_2 (oe)
B_1 (oo)	A_1	A_1	B_1 (oo)	B_1 (oo)

Using Equation (2.144), the allowed rovibrational transitions are summarized in Table 2.7.

Table 2.7: Selection rules and transition types for the allowed rovibrational transitions of the OCS ν_1 excitation ($A_1 \rightarrow A_1$)

$\Gamma''_{rv} \rightarrow \Gamma'_{rv}$	$\Gamma''_{rv} \otimes \Gamma'_{rv} \supset \Gamma^* = A_2$	$\Delta K_a, \Delta K_c$	transition type
A_1 (ee) $\rightarrow$ A_2 (eo)	$A_1 \otimes A_2 = A_2$	$\Delta K_a = 0, \Delta K_c = \pm 1$	a-type
A_2 (eo) $\rightarrow$ A_1 (ee)	$A_2 \otimes A_1 = A_2$		
B_2 (oe) $\rightarrow$ B_1 (oo)	$B_2 \otimes B_1 = A_2$		
B_1 (oo) $\rightarrow$ B_2 (oe)	$B_1 \otimes B_2 = A_2$		

2.8 Statistical weights

Appearance of some features in molecular spectra such as intensity alternation, specific intensity patterns, and missing specific levels can be explained by different statistical weights of rovibronic states due to nuclear spin. These features are often useful in assigning and confirmation of assignment of molecular spectra.

The complete internal dynamics wavefunction, Φ_{int}, is the product of the rovibronic wavefunction, Φ_{rve}, and the nuclear spin wavefunction, Φ_{ns}. That is,

$$\Phi_{int} = \Phi_{rve}\Phi_{ns}. \tag{2.145}$$

As a result of the Pauli exclusion principle, the complete internal wavefunctions Φ_{ns} must be invariant under (even/odd) permutations of identical bosons in the molecule and under any even permutation of identical fermions. But, Φ_{int} will change sign under an odd permutation of identical fermions. These can be written as,

$$P_{(odd)}\Phi_{int} = \Phi_{int} \qquad \text{for bosons,} \qquad P_{(odd)}\Phi_{int} = -\Phi_{int} \qquad \text{for fermions,} \tag{2.146}$$

$$P_{(even)}\Phi_{int} = \Phi_{int} \qquad \text{for bosons and fermions.} \tag{2.147}$$

In addition, the complete internal wavefunction Φ_{int} can have + or - parity under the effect of the inversion operator (E^* in MS group). That is,

$$E^*\Phi_{int} = \pm\Phi_{int}. \tag{2.148}$$

Using Equations (2.146) through (2.148), the symmetry species of the complete internal wavefunction can be determined. To set up a valid basis wavefunction for Φ_{int}, a rovibronic state having symmetry Γ_{rve} (in the MS group) can only be combined with a nuclear spin state having symmetry Γ_{ns} (in the MS group) if the product of these symmetries contains Γ_{int}.

A rovibronic state (with symmetry Γ_{rve}) can only be combined with a nuclear spin state (with symmetry Γ_{ns}), to form a basis function for Φ_{int}, if the product of these symmetries

contains Γ_{int}. That is to have

$$\Gamma_{rve} \otimes \Gamma_{ns} \supset \Gamma_{int}. \tag{2.149}$$

It is possible that no nuclear spin state exists that has the right symmetry for combination with a particular rovibronic state and this rovibronic state will be "missing" although such a rovibronic state is perfectly acceptable eigenstate of the rovibrational Hamiltonian. Missing of some levels and different statistical weights for different rovibronic states, results in patterns that are found in the relative intensities of spectral lines. These intensity patterns are referred to as "intensity alternations".

In order to find the representation Γ^{sw}_{rve} of the MS group that gives the allowed rovibronic states and their nuclear spin statistical weights, one needs to find the characters $\chi^{sw}_{rve}[P]$ under the operations of the MS group (nuclear permutation operation P, or permutation-inversion P^*). The following formulae provide a simple way of obtaining characters $\chi^{sw}_{rve}[P]$, [42]

$$\chi^{sw}_{rve}[P] = 2\prod(2I_a+1)(-1)^{(2I_a)(n_a-1)}, \tag{2.150}$$

and

$$\chi^{sw}_{rve}[P^*] = 0. \tag{2.151}$$

The product contains one factor for each set of n_a nuclei having I_a permuted by P (including sets of one nucleus for which $n_a = 1$). The characters in Γ^{sw}_{rve} are zero for all permutation-inversion operations in the MS group. Spin statistical weights for the T-shaped OCS$-C_2H_2$ will be worked out below.

Each nucleus is left alone under the effect of operation E, therefore the nuclei of OCS$-C_2H_2$ are divided into 7 sets,

$a = 1$, E leaves the hydrogen atom numbered 1 unchanged, so $n_1 = 1$ and $I_1 = 1/2$.

$a = 2$, E leaves the hydrogen atom numbered 2 unchanged, so $n_2 = 1$ and $I_2 = 1/2$.

$a = 3$, E leaves the carbon atom numbered 3 unchanged, so $n_3 = 1$ and $I_3 = 0$.

$a = 4$, E leaves the carbon atom numbered 4 unchanged, so $n_4 = 1$ and $I_4 = 0$.

$a = 5$, E leaves the sulfur atom numbered 5 unchanged, so $n_5 = 1$ and $I_5 = 0$.

$a = 6$, E leaves the carbon atom numbered 6 unchanged, so $n_6 = 1$ and $I_6 = 0$.

$a = 7$, E leaves the oxygen atom numbered 7 unchanged, so $n_7 = 1$ and $I_7 = 0$.

Therefore using Equation (2.150), the character can be found

$$\begin{aligned}\chi^{sw}_{rve}[E] = 2 \times \{&[2 \times \frac{1}{2} + 1](-1)^{2\frac{1}{2}(1-1)} \\ &[2 \times \frac{1}{2} + 1](-1)^{2\frac{1}{2}(1-1)} \\ &[2 \times 0 + 1](-1)^{2\times 0(1-1)} \\ &[2 \times 0 + 1](-1)^{2\times 0(1-1)} \\ &[2 \times 0 + 1](-1)^{2\times 0(1-1)} \\ &[2 \times 0 + 1](-1)^{2\times 0(1-1)} \\ &[2 \times 0 + 1](-1)^{2\times 0(1-1)} \\ &[2 \times 0 + 1](-1)^{2\times 0(1-1)}\}\end{aligned}$$

$$\chi^{sw}_{rve}[E] = 8$$

The operation (12)(34), performs a permutation on the two hydrogen atoms (numbered 1, 2) as well as a permutation of the carbon atoms (numbers 3, 4) within the C_2H_2 monomer. Thus,

$a = 1$, (12)(34) permutes the hydrogen atoms numbered 1 and 2, so $n_1 = 2$ and $I_1 = 1/2$.

$a = 2$, (12)(34) permutes the carbon atoms numbered 3 and 4, so $n_2 = 2$ and $I_2 = 0$.

$a = 3$, (12)(34) leaves the sulfur atom numbered 5 unchanged, so $n_3 = 1$ and $I_3 = 0$.

$a = 4$, (12)(34) leaves the carbon atom numbered 6 unchanged, so $n_4 = 1$ and $I_4 = 0$.

$a = 5$, (12)(34) leaves the oxygen atom numbered 7 unchanged, so $n_5 = 1$ and $I_5 = 0$.

So, the character for (12)(34)

$$\begin{aligned}\chi^{sw}_{rve}[(12)(34)] = 2 \times \{&[2 \times \frac{1}{2} + 1](-1)^{2\frac{1}{2}(2-1)} \\ &[2 \times 0 + 1](-1)^{2\times 0(2-1)}\end{aligned}$$

$$[2 \times 0 + 1](-1)^{2\times 0(1-1)}$$

$$[2 \times 0 + 1](-1)^{2\times 0(1-1)}$$

$$[2 \times 0 + 1](-1)^{2\times 0(1-1)}$$

$$\chi^{sw}_{rve}[(12)(34)] = -4$$

For the two permutation-inversion operators, E^* and $(12)(34)^*$, using Equation (2.151)

$$\chi^{sw}_{rve}[E^*] = 0 \qquad \text{and} \qquad \chi^{sw}_{rve}[(12)(34)^*] = 0.$$

Therefore, the representation Γ^{sw}_{rve} is

	E	$(12)(34)$	E^*	$(12)(34)^*$
Γ^{sw}_{rve} :	8	-4	0	0

This representation is reduced to the following

$$\Gamma^{sw}_{rve} = A_1 \oplus A_2 \oplus 3B_1 \oplus 3B_2. \tag{2.152}$$

The statistical weights of rovibronic states of the T-shaped OCS$-C_2H_2$ are given in Table 2.8.

Table 2.8: Symmetry species of $J_{K_aK_c}$ levels of T-shaped OCS$-C_2H_2$ in the C_{2v}(M) group.

Γ^{sw}_{rve}	Statistical Weight	Γ^{sw}_{rve}	Statistical Weight
A_1 (ee)	1	B_2 (oe)	3
A_2 (eo)	1	B_1 (oo)	3

This results in an intensity alternation of 1:3 for K_a = even:odd in the spectrum of OCS$-C_2H_2$ (Figure 4.3) in agreement with a C_{2v} symmetry.

Chapter 3

Experimental Apparatus

3.1 Supersonic Jet Expansion

The supersonic jet expansion technique provides a source of weakly-bound van der Waals complexes and clusters in the laboratory. A supersonic jet is formed by allowing a high pressure gas of desired molecules to expand into a low pressure region through an orifice. During the very first moment of the expansion, molecules collide with each other very frequently and due to these collisions the velocity distribution profile narrows down as Figure 3.1 shows.

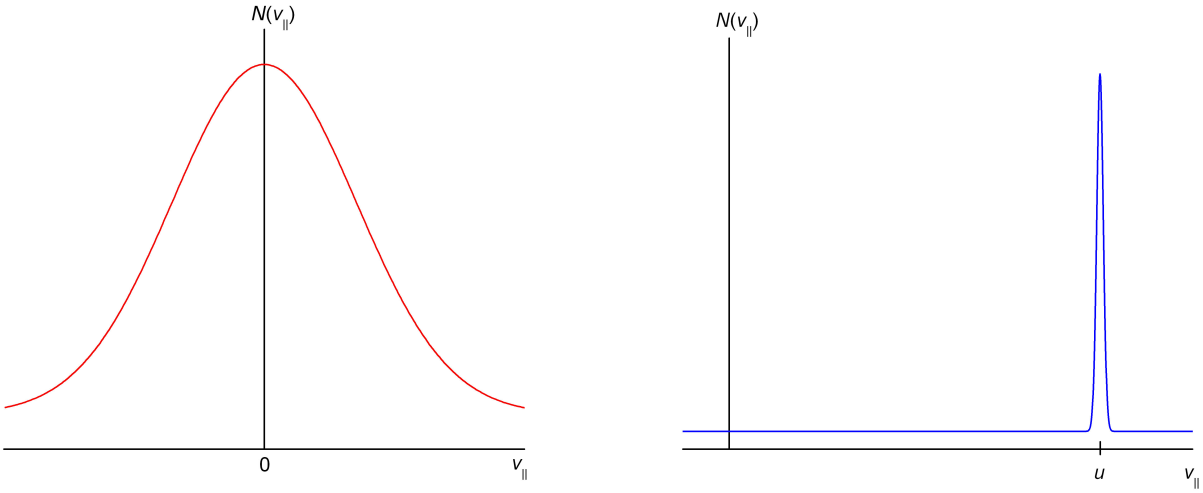

Figure 3.1: Change in the distribution profile of the parallel component of velocity before a jet expansion with a Maxwellian distribution (left) into a cold directional molecular flow with mean flow velocity of u (right).

This expansion can be well approximated by an adiabatic process because the expansion happens so fast that virtually no heat exchange with the surrounding can occur. This results in cooling of internal degrees of freedom of the molecules involved in the expansion. Considering a mole of the gas being expanded with mass m, one can write an expression for

the total energy before and after the expansion. That is

$$U_0 + P_0V_0 + \frac{1}{2}mu_0^2 = U + PV + \frac{1}{2}mu^2 \tag{3.1}$$

where $U = U_{tr} + U_{rot} + U_{vib}$ is the sum of internal energies, PV is the potential energy of volume V of gas at pressure P, and $\frac{1}{2}mu^2$ is the kinetic flow energy of the gas expanding with the mean velocity u. Subscripts zero refer to the state of the gas before the expansion.

Before the expansion, if the mass flow through the orifice is small compared to the total mass of the gas, thermal equilibrium implies $u_0 = 0$. Since the expansion occurs in the vacuum chamber, the pressure after the expansion is very small. Therefore equation 3.1 can be approximated as

$$U_0 + P_0V_0 = U + \frac{1}{2}mu^2, \tag{3.2}$$

or

$$U - U_0 = \frac{f}{2}k_B(T - T_0) = P_0V_0 - \frac{1}{2}mu^2, \tag{3.3}$$

where f is the number of degrees of freedom. This equation demonstrates that a molecular beam can be obtained with small internal energy, if most of the initial energy is converted into kinetic flow energy. The flow velocity u may exceed the local velocity of sound, hence the word "supersonic" is used. This condition is usually described in terms of the Mach number, M, being greater than unity. The Mach number is defined as the ratio of the bulk flow velocity to the local speed of sound.

The flow velocity of the expansion gas approaches the terminal value w [46]

$$w = \sqrt{\frac{5k_BT_0}{m}}. \tag{3.4}$$

In this equation, k_B is the Boltzmann constant, m is the mass of expansion gas particles, and the expansion gas is assumed to be monoatomic. For $T_0 = 300\,K$ the terminal velocities for He and Ar are $1770\,m/s$ and $560\,m/s$, respectively. The local speed of sound, v_s, is proportional to the square root of the translational temperature and therefore decreases as

the expansion proceeds

$$v_s = \sqrt{\frac{\gamma k_B T}{m}}. \tag{3.5}$$

$\gamma = 5/3$ is the adiabatic index for a monoatomic gas. So, Mach number can be obtained from equations (3.4) and (3.5) as

$$M = \frac{w}{v_s} = \sqrt{\frac{3T_0}{T}} \tag{3.6}$$

The flow becomes supersonic because of a sudden decrease in the temperature of the jet. A schematic diagram of a supersonic expansion beam is depicted in Figure 3.2. When the high pressure gas enters the high vacuum region, gas molecules collide with the background gas (with typical pressure of 10^{-7} Torr) and produce a shockwave boundary where the flow becomes subsonic. The shaded area in Figure 3.2 shows the supersonic region with Mach number equal to or much greater than one. Shading from dark to light represents a decrease in the density, temperature, and number of collisions along the expansion axis. The region where number of collisions drops and molecules experience no or very few collisions is referred to as the "zone of silence". In this collision-less environment weak van der Waals forces dominate over the thermal motions and can form complexes. This region starts somewhere from 1 cm to 3 cm downstream the nozzle and may extend for about 2 cm and longer, depending on the carrier gas and orifice size [47]. The zone of silence is the most appropriate region for spectroscopy experiments. The supersonic flow terminates in the axial direction at the Mach disk.

Before the expansion, all degrees of freedom of gas molecules are in equilibrium and temperatures attributed to each degree is equal to the gas temperature. That is $T_0 = T_{tr} = T_{rot} = T_{vib}$. But during the expansion there exists no equilibrium between the different degrees of freedom. This is because collision cross-section for rotation-translation energy transfer is smaller than the elastic collision cross-section which cools down the translational degree of freedom and the collision cross-section for vibration-translation energy transfer is even smaller than that of rotation-translation [47]. The jet is therefore described by a

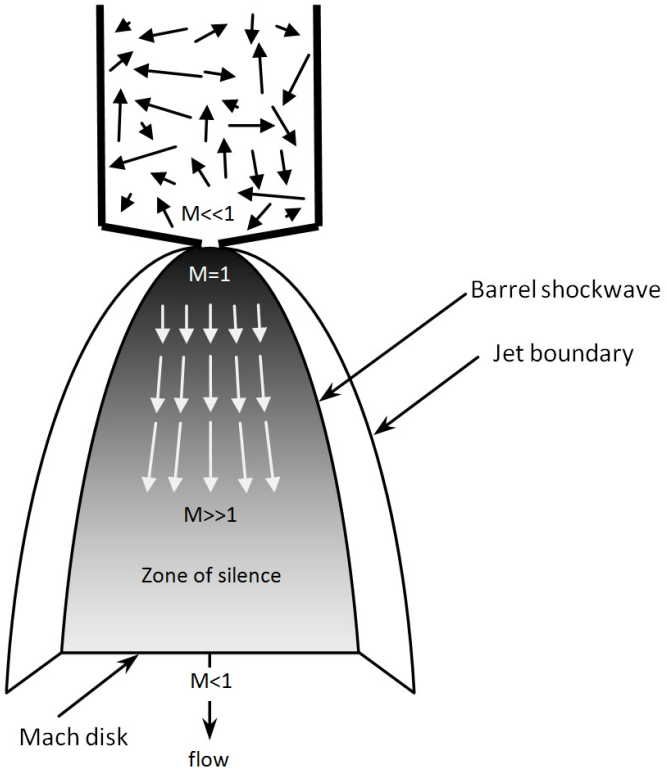

Figure 3.2: A schematic diagram of supersonic jet cross section.

set of temperatures $T_{tr} < T_{rot} < T_{vib}$. This temperature ordering can be understood by looking at the energy spacing of translational, rotational, and vibrational levels. For many molecules, energy spacing of vibrational levels varies from a couple of hundred to several thousand wavenumbers (say 100 - 4000 cm^{-1}). Rotational energy levels are separated by a few hundredths of a wavenumber to a couple of ten wavenumbers (say 0.05 - 20 cm^{-1}) and translational energy levels practically from a continuum.

The significance of cooling in spectroscopy lies in the fact that in a cold molecular beam the population of molecular levels are concentrated in the lowest vibration-rotation levels and thus the spectrum greatly simplifies and the number of absorption lines is reduced. Also, when the molecular beam is probed perpendicular to the jet flow, reduction of Doppler broadening in observed transitions makes it possible to resolve the rotational structure. This is due to the small transverse velocity component of jet molecules. The resolution of the

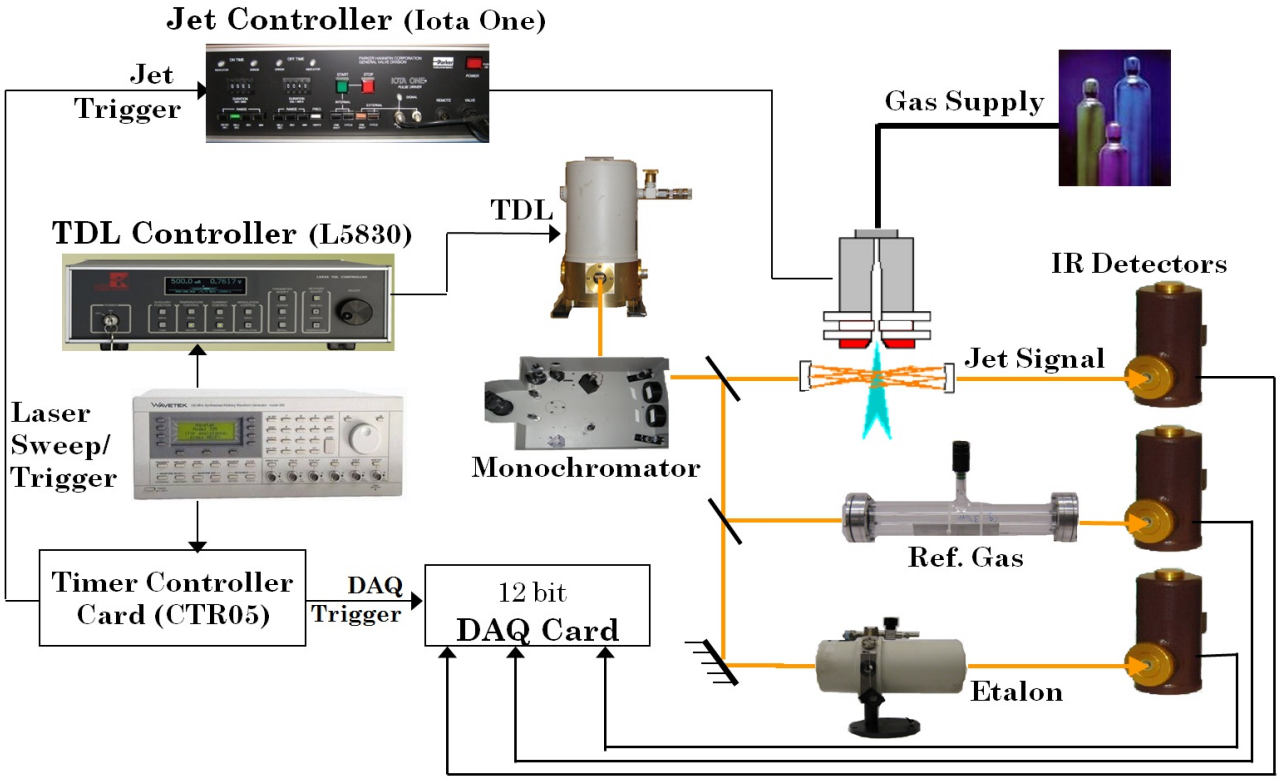

Figure 3.3: Schematic diagram of the experimental setup showing different parts and the links between them.

observed spectra which is limited by the residual Doppler broadening, is typically around 0.0017 cm^{-1} (or 50 MHz).

A number of experimental design have been proposed that use the supersonic jet expansion technique [48–52]. The experimental setup that is used to obtain the results presented in this thesis is based on a more recent design [53] that utilizes a tuneable diode laser in rapid scan mode. This setup will be described in the following sections. A schematic diagram of the experimental setup is shown in Figure 3.3.

3.2 Dual nozzle supersonic jet system at the University of Calgary

3.2.1 Supersonic jet chamber and Vacuum pumps

A NW250 six-way vacuum cross is used for the jet chamber. The vacuum chamber is mounted on a Varian VHS-10 diffusion pump. A pneumatic gate valve separates the vacuum chamber from the diffusion pump. The diffusion pump is backed by an Edwards E2M275 mechanical pump that is located in a separate room at a distance of about 3 meters in order to minimize the noise and vibrations caused by the mechanical pump. A schematic diagram of the vacuum system including the jet chamber, diffusion pump, mechanical pumps, valves, and vacuum gauges is shown in Figure 3.4, and Figure 3.5 is a photograph showing the actual vacuum chamber, diffusion pump and the pneumatic gate valve separating them during the construction of the apparatus in 2003.

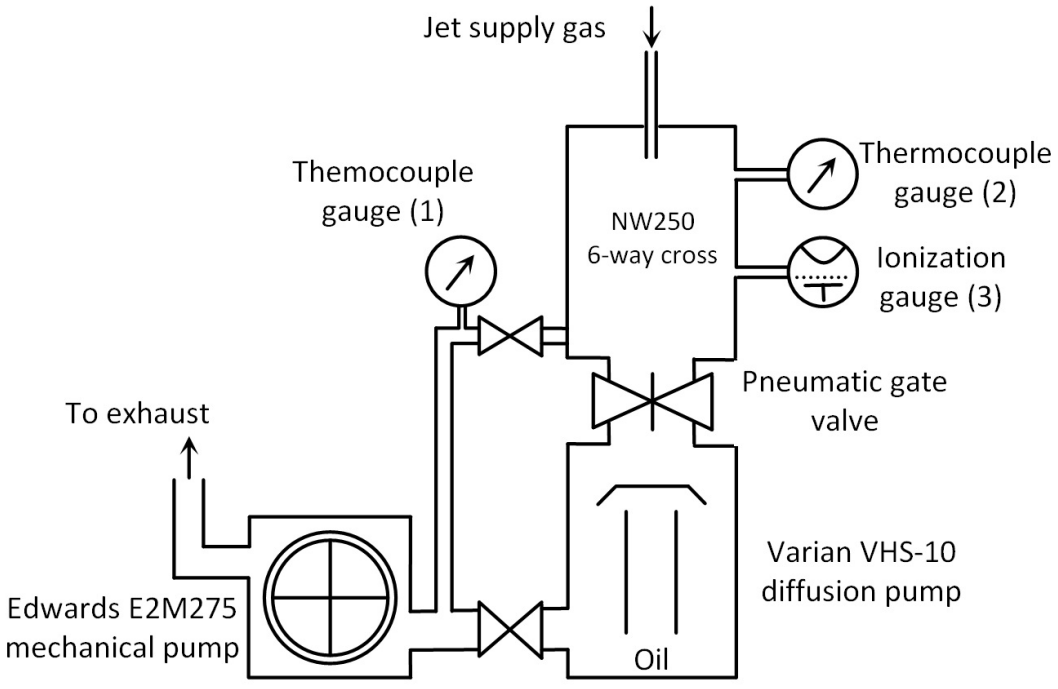

Figure 3.4: Vacuum system including the vacuum chamber, diffusion pump, mechanical pump, valves, and vacuum gauges.

During operation of the jet, the average gas flow can be monitored using a thermocouple

Figure 3.5: Photograph of the vacuum system showing the six-way vacuum chamber, diffusion pump, and the pneumatic gate valve in the middle.

vacuum gauge in the backing line (gauge 1 in Figure 3.4). The vacuum chamber background pressure generally measures 10^{-7} Torr using an Edward Active Inverted Magnetron ionization gauge (gauge 3 in Figure 3.4) mounted on the six-way vacuum cross. However during the jet operation the pressure inside the vacuum chamber reaches as high as 10^{-4} Torr.

3.2.2 Pulsed Valves and Nozzles

The supersonic jet is generated using two identical side-by-side pulsed valves (General Valve Series 9) manufactured by Parker Hannifin Corporation. The valves are located entirely inside the vacuum chamber and are connected to a manifold which is connected to a quarter-inch gas supply tube. Gas tube can be easily lowered or raised to adjust the distance from the nozzles to the probing laser beam. The valves are made of corrosion-resistant materials and can operate in a pressure range of up to 85 atmospheres. The repetition rate can be as high as 125 Hz. Figure 3.6 shows the cross section of the pulsed valve with its interior compartments.

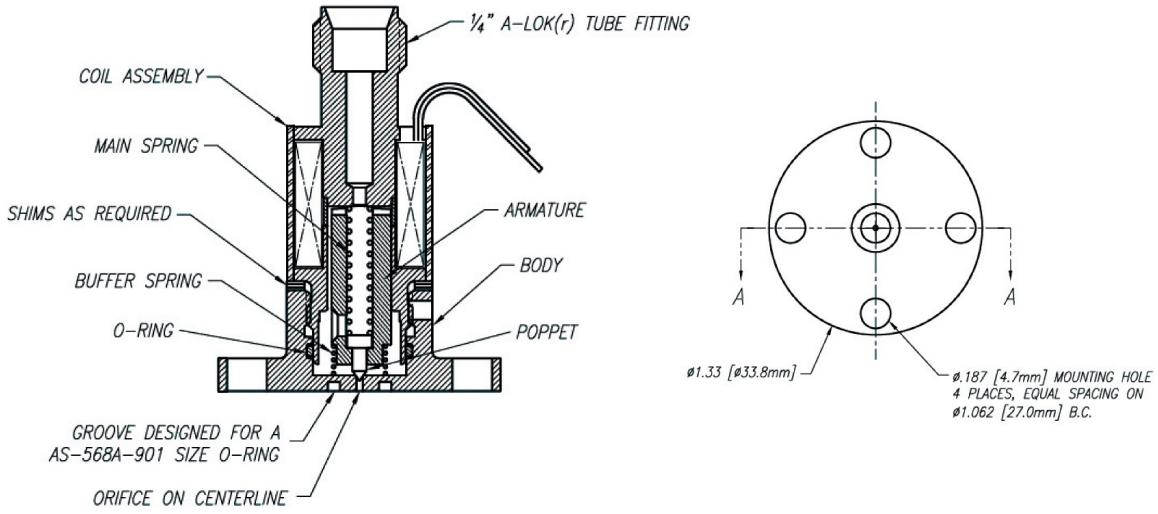

Figure 3.6: Cross section of General Valve Series 9 showing interior compartments (left), and the bottom view of the flange (right). Figure courtesy of Parker Hannifin.

In order to increase the laser interaction pathlength with jet molecules, slit-shaped noz-

zles are used which distribute the expansion gas along the laser beam. In addition to an increase in the signal to noise ratio, slit nozzles also enhance the formation of weakly bound complexes [54]. For this setup, a multi-channel block is attached to the bottom face of the pulsed valve flange. The multi-channel block has six holes with different diameters that establish a uniform distribution of the expansion gas along the nozzle. The slit through which the gas expands is formed by a pair of adjustable jaws that mount on the block. In all of the experiments for which the results are presented in this thesis, the jaws separation was 25 μm. The effective length of each slit nozzle is approximately 30 mm which results in an increase of a factor of 2 in absorption path length compared to a slit nozzle without a multi-channel block. [33]. Figure 3.7 illustrates the design of multi-channel block and the jaws.

Works presented in Chapters 4 and 5 have utilized the supersonic jet apparatus in 2009 with only one pulsed valve, before the addition of the second pulsed valve. The rest of the results are obtained with two pulsed valves. Figure 3.8 shows a photograph of the single nozzle and dual nozzle configurations inside the vacuum chamber.

3.3 Light source and optics

3.3.1 Laser

The coherent infrared light for spectroscopy of molecular clusters in the jet is provided by means of a tuneable diode laser (TDL). The laser is mounted in a liquid nitrogen (LN_2) Dewar (L5736 manufactured by Laser Photonics). Therefore, the laser can be cooled down to the boiling point of liquid nitrogen, i.e. 77 K. However, for temperatures down to about 60 K, evaporative cooling of LN_2 is required. Higher laser temperatures, up to about 150 K, can be accessed by the L5736 built-in heater. The wavelength of the laser can be tuned by changing the current and temperature of the laser.

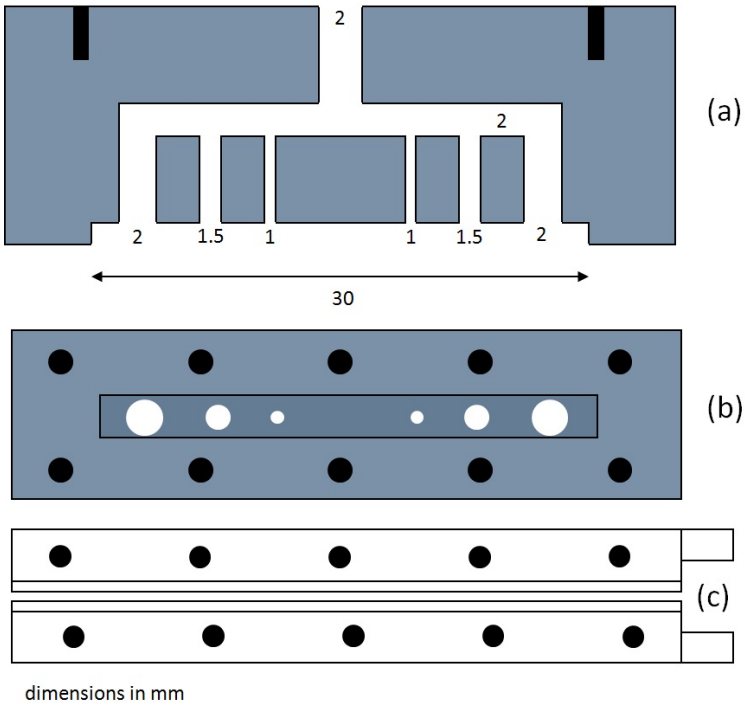

Figure 3.7: Design of the home-made multi-channel block and the jaws. (a) Cross section of the block, (b) Bottom view of the multi-channel block, and (c) adjustable jaws.

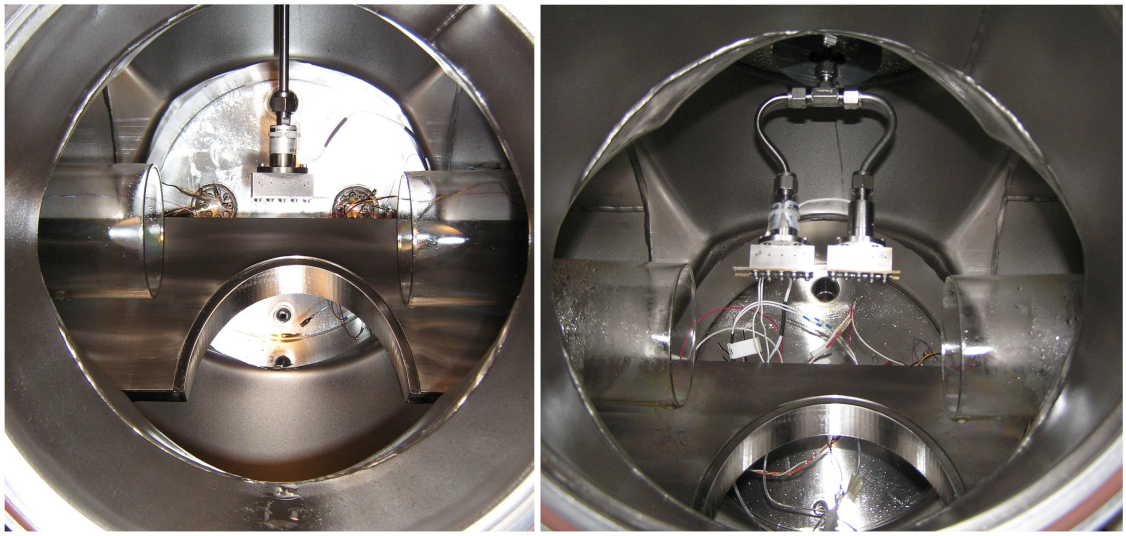

Figure 3.8: Single (left) and dual (right) pulsed valve configurations inside the vacuum chamber with multi-channel block.

3.3.2 Optics

The output from the laser is a multi-mode infrared beam that has to go through a monochromator (Laser Analytics SP5900) for mode selection. Since the laser output is a divergent beam, it is first collimated using a parabolic mirror. The collimated beam is then directed by means of two gold coated flat mirrors into the monochromator where a suitable mode is selected. The radiation from the monochromator is then divided into two portions with a 80:20 pellicle beam splitter. The stronger beam is directed into the vacuum chamber to probe the supersonic jet. The weaker beam is further divided into two parts by a 55:45 beam splitter. These beams are directed into an etalon and a cell containing a reference gas to simultaneously record their spectra. These spectra are used for frequency calibration of the absorption spectra of the supersonic jet.

The reference cell is a glass tube of length 300 mm and 45 mm in diameter with two CaF_2 windows at the ends. This cell contains a referecne gas with accurately known transition frequencies in the spectral region of interest. For the experiments presented in this thesis, OCS, N_2O, CO_2, or N_2O have been used as the reference gas. Transition frequencies for references gases are available from Ref. [55] or Ref. [56]. The etalon used for frequency interpolation (Laser Analytics SP59450) is a passive confocal etalon with a free spectral range of 0.009976 cm^{-1}.

Spectra presented in this thesis are recorded using different tuneable diode lasers with a wavelength in the range 4 - 5 μm. The spectrometer is enclosed with a sheet of transparent plastic and purged with flow of nitrogen gas when strong atmospheric CO_2 absorptions pose difficulty. This happens around CO_2 ν_3 vibration, i.e. around 4.26 μm (Chapter 6).

3.3.3 Multi-pass absorption cell

In order to enhance the signal to noise ratio in the spectra, a multi-pass absorption configuration is mounted inside the jet chamber. This helps to increase the detection sensitivity

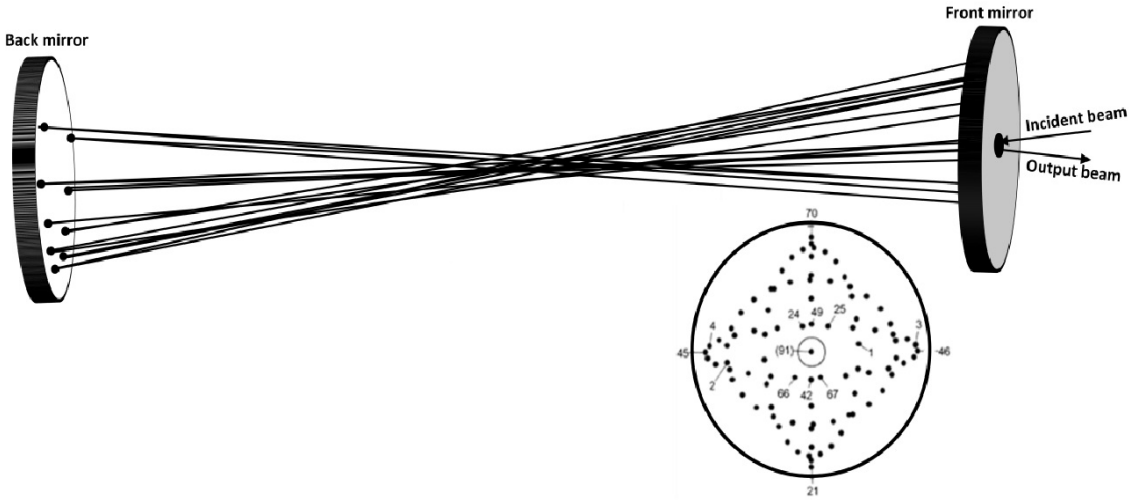

Figure 3.9: Schematic diagram of the multi-pass absorption cell together with a theoretical spot pattern on the front mirror. Numbered spots indicate their order of reflection.

specially for weak transitions of van der Waals clusters. The multi-pass cell utilized in this thesis is an AMAC-100 cell manufactured by Aerodyne Research Inc. [57] A schematic diagram for the multi-pass cell along with a theoretical spot pattern on the front mirror is shown in Figure 3.9. The spot pattern can be confined to a rectangular area to probe the middle of the jet stream. This is done by adjusting the angle of the incident beam (about 2.5° with respect to the cell optical axis) and rotating the base plate of the cell by 45°. The confined area measures about 3 cm(H)×2 cm(W). The actual spot pattern using a He-Ne laser is presented in Figure 3.10. The incident beam is focused at the center of the cell by two astigmatic mirrors with a reflectivity of 99.2%. The typical number of passes for this configuration ranges from 100 to about 180 passes. To prevent deposition of diffusion pump oil on the mirrors, two resistive heaters are mounted on the back of each mirror to keep them at a temperature of about 40 °C. Also, two glass tubes are mounted around the mirrors leaving a sufficient gap in the center of the chamber for the supersonic jet.

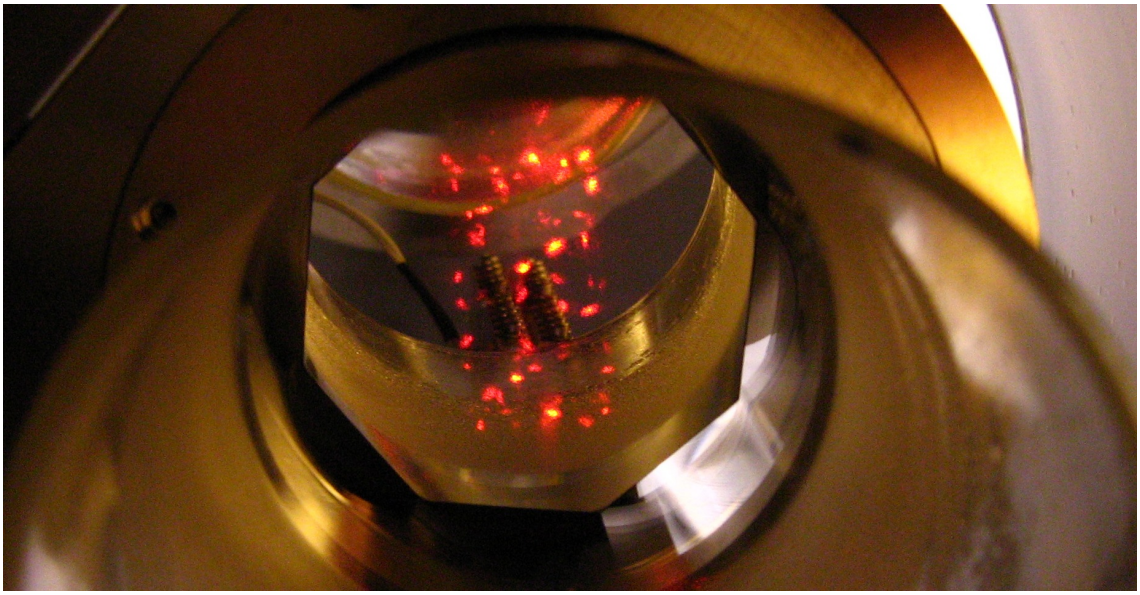

Figure 3.10: Modified spot pattern on the back mirror of the multi-pass absorption cell using a He-Ne laser source.

3.4 Data acquisition and control

In the following paragraphs, different components of the system that are responsible for data acquisition and control are described.

Data Acquisition: Three LN_2-cooled (InSb or HgCdTe) detectors serve to convert the infrared signals from the jet chamber, reference gas cell, and etalon to electric signals. These infrared detectors are high-speed, low noise detectors which makes them suitable for high-resolution spectroscopy of van der Waals clusters. Electric signals from the detectors are digitized at a rate of 4 MHz using a 12-bit data acquisition (DAQ) card (DAS4010/12), mounted on a PC motherboard, and stored on the computer. The input range for the DAQ card is adjustable and may be set to either ± 1 or ± 5 V by the user.

Control: The control assembly of the system consists of several parts: a commercial TDL controller (Laser Photonics L5830), an external function generator (WaveTek 395), pulsed valve controller(s) (IOTA One by Parker Hannifin), and a counter timer card (CTRO5 from Measurement Computing) mounted on a PC motherboard.

The TDL controller (L5830) is used to tune the frequency of the diode laser by adjusting

its current and/or temperature. The external function generator (WaveTek 395) sweeps the laser rapidly across a certain wavenumber interval (0.3 - 0.9 cm^{-1}) by applying a 1 kHz ramp waveform to the laser. Also the trigger signal from the function generator is used to synchronize data acquisition with the formation of the supersonic jet. This will be discussed further below.

Opening and closing times of the pulsed valve(s) is controlled by the IOTA One valve driver. This unit controls the repetition rate and duration of pulses. The pulse duration can be adjusted in the range of microseconds, milliseconds, seconds, or minutes using the front panel of Iota One valve driver units. In all the works discussed in this thesis the pulse duration has been adjusted to 2.5 milliseconds. The repetition rate is restricted by the capacity of the vacuum pumps. For single valve results (Chapters 4 and 5), it has been 2 Hz while in the dual nozzle configuration, the repetition rate has been 1 Hz in order to allow enough time for pressure inside the six-way cross to reach to about 10^{-6} Torr.

The CTRO5 counter timer controls the timing of the DAQ card with that of the pulsed valve(s). The timing sequence for data acquisition is depicted in Figure 3.11. The CTRO5 and the DAQ card are both configured using a LabVIEW-based computer program developed in the Laser Spectroscopy Lab. at the University of Calgary. The counter timer (CTRO5) triggers the DAQ card at the beginning of the second cycle of the trigger signal from the function generator (WaveTek). The DAQ card commences digitization and storage of the data at the rate of 4 MHz over the next four one-millisecond time intervals. Also, with a delay (indicated by d_1 (and d_2) in Figure 3.11), the counter timer triggers the IOTA One valve controller(s). The delay parameter(s), d_1 (and d_2), is (are) adjusted by the user (in μs). Because of the delay in mechanical response of the pulsed valve(s) to the trigger signal, the valve(s) are actually fully open after d_1+d_3 μs (and d_2+d_4 μs). As can be seen from Figure 3.11, pulsed valve(s) is (are) completely closed during the first scan and the recorded signal is merely the background. It should be noted that the fourth laser scan falls where the

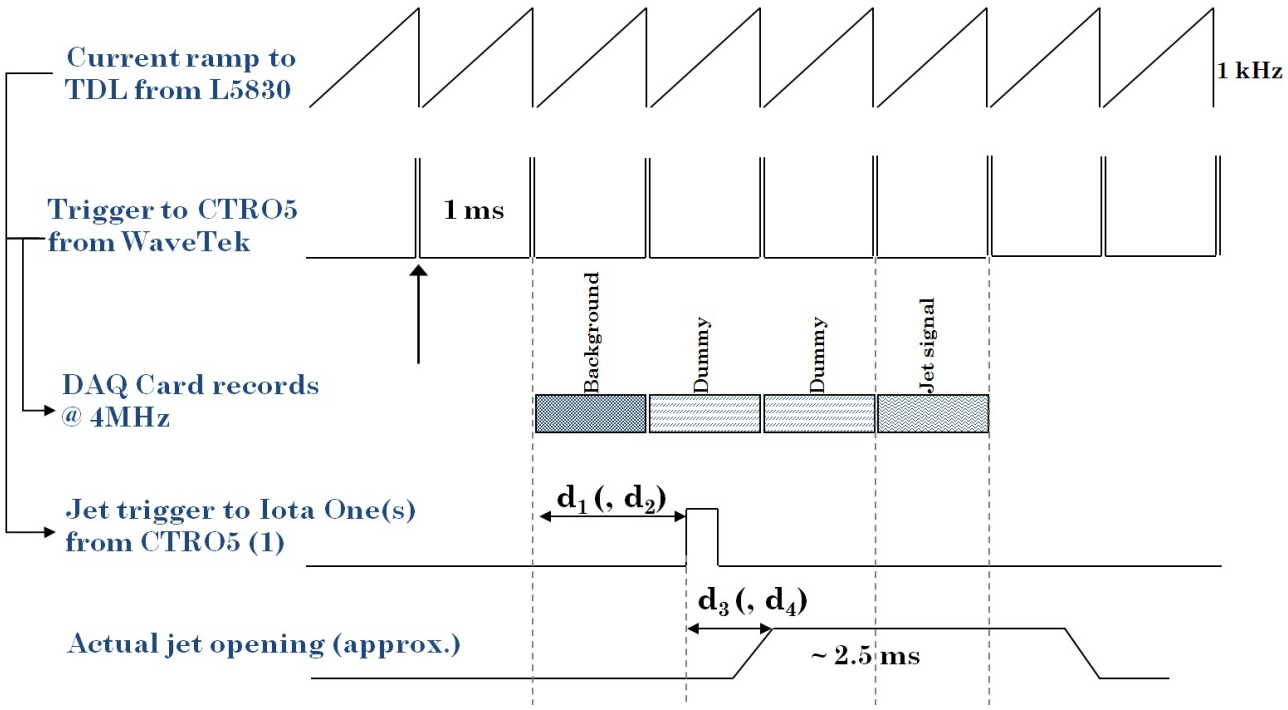

Figure 3.11: Synchronization of data acquisition with the formation of the supersonic jet.

jet valve(s) is (are) completely open and molecular clusters are formed. The second and third scans are dummy and during these scans the gas expansion is in its early stages and molecular clusters are not fully formed. These dummy scans give the user the possibility of adjusting the delay parameter(s), and will be discarded. Subtracting the first scan (background) from the fourth one yields the background removed jet spectrum. The jet spectrum is averaged for as many times as required depending on the strength of the transitions under study. Figure 3.12 is a typical screen shot of the LabVIEW-based program during data acquisition. Each panel is labeled with a brief description. The bottom left panel is the average jet signal with background. The bottom right panel shows the four successive laser scans as discussed above. The two bottom panels are used for testing and diagnostic purposes.

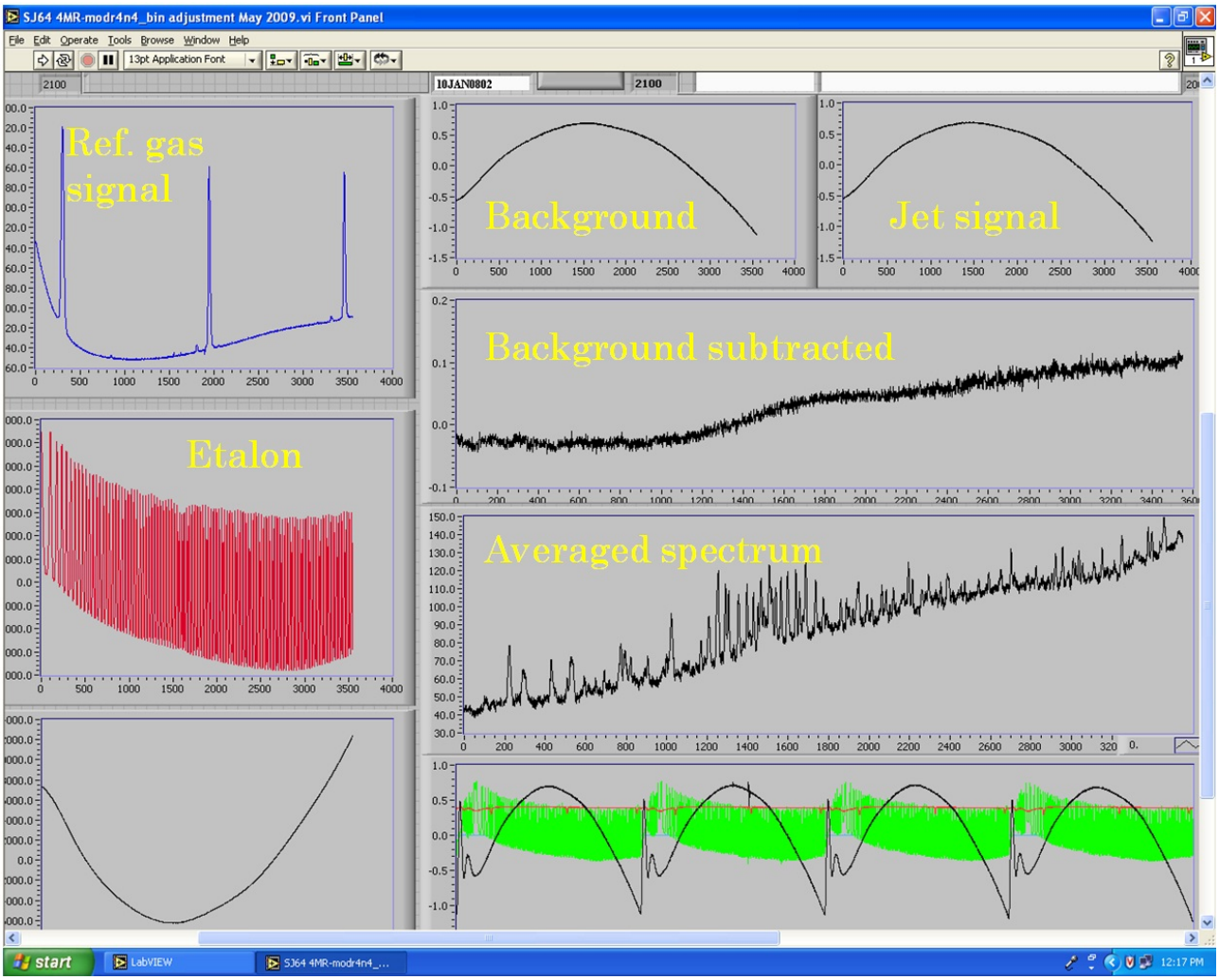

Figure 3.12: The computer screen while acquiring data for torsional band of OCS−CO_2−a. Note that the signal is so weak that the transitions appear only after ~ 300 averages.

3.5 Analysis

3.5.1 Data manipulation and frequency calibration

The LabVIEW-based program generates three files for the three absorption signals i.e. the jet signal, reference gas signal, and etalon signal. These files are single-column text files containing intensities for 4000 bin numbers rather than frequencies. These files are processed using Thermo Scientific GRAMS/AI™ spectroscopy software. As an example, Figure 3.13 shows the files for OCS−C_6H_6 and OCS−C_6H_6−He which are plotted in GRAMS. Three traces, from top to bottom, are simultaneously recorded signals of the jet, reference gas, and

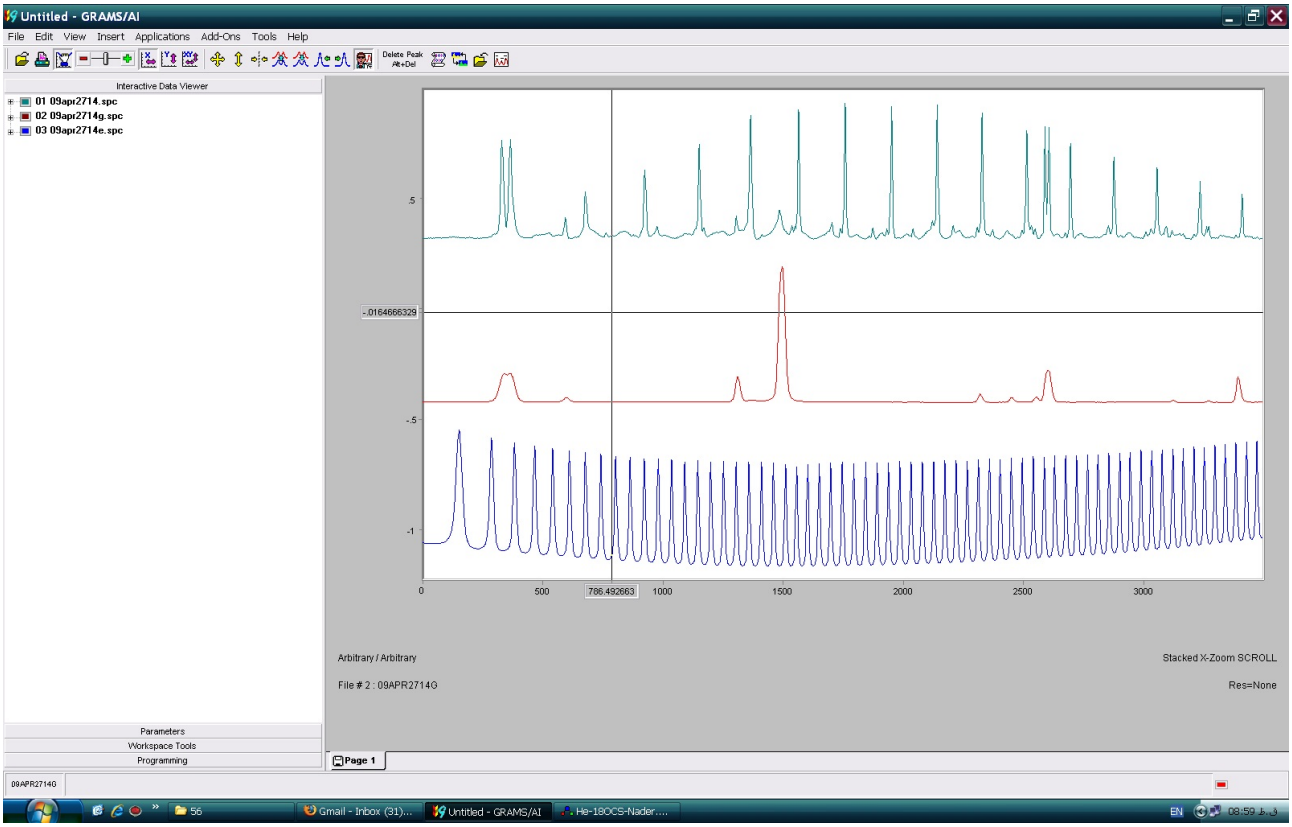

Figure 3.13: The three absorption signals from the jet, reference gas, and etalon plotted in GRAMS™ from top to bottom. Notice the slower scan rate at the beginning of the etalon signal due to laser chirping.

etalon. The etalon and reference gas signals are used by a calibration program written in Array Basic™ language which utilizes GRAMS as its platform, to calibrate the absorption signal.[1] The calibration program asks for the frequencies of at least two reference lines and the bin numbers corresponding to the peaks in the etalon signal. After the calibration program is concluded, the program displays the fitted value for the free spectral range of the etalon and its standard deviation. This value may be checked by the user to assess the quality of the resulting calibration and to check for any flaws. The results of the calibration process is the jet absorption signal in two different formats: A file with ".spc" extension which can be opened directly in GRAMS and another file with ".prn" extension which is a two-column, tab-delimited text file containing frequencies and the corresponding intensities

[1]The Array Basic™ program is kindly provided to us by Dr. A.R.W. McKellar from the National Research Council of Canada.

of the jet absorption signal. In rare cases where only one reference frequency falls in the scan range, the program prompts for the exact free spectral range (FSR) of the etalon and uses it as a constant number. However, this may decrease the accuracy of the calibration because of the "laser chirping" effect. This is most noticeable by looking at the spacing of the peaks in the etalon signal across the scan (see Figure 3.13).

Since the ro-vibrational band of a molecular cluster may not be fully covered in a single scan, multiple back-to-back scans are required to cover the entire spectrum, specially those of lighter clusters such as dimers and trimers. Two neighboring scans ought to have a small overlap of a few absorption lines for the purpose of intensity and frequency matching checks. Usually for a certain line in the overlapping region, frequency differences less than 0.0006 cm^{-1} is acceptable. After intensity and frequency tests are checked out, the ".prn" files can be patched together by any text editor software and saved as a text or data file containing the entire spectrum.

3.5.2 Simulation and fitting of data using PGOPHER

Simulation and fitting of all the results presented in this thesis is performed in PGOPHER software package [58]. PGOPHER is a general purpose program for simulating and fitting rotational, vibrational and electronic spectra with a graphical interactive interface which make it a very convenient program for simulation of spectra. The program can calculate simulated spectra of linear molecules, symmetric molecules, and asymmetric molecules.

A good account of basic operation of PGOPHER, such as how to interact with different parts of the software, overlaying an experimental spectrum, initiating a simulation, and definition of spectroscopic parameters is given in the documentation of the software. Therefore, only the concepts in simulating and fitting of data is presented briefly here.

In order to start the simulation of an experimental spectrum using PGOPHER, the user needs to make sure that some of the parameters and settings are adjusted correctly. The most common such parameters are the rotational temperature of the sample, line broadening

and line shapes, point group symmetry of the molecule, representation of the Hamiltonian, statistical weights, symmetry axes, symmetry of the ground and excited vibrational state, approximate band origin, maximum value of quantum numbers, and direction and strength of the transition moment. Then the final calibrated spectrum can be opened and analyzed in PGOPHER.

To perform line position assignment and frequency fitting, an initial simulation needs to be laid on/below the calibrated spectrum to make comparisons possible. The initial values for molecular parameters are often based on information known about the molecular system to be analyzed. This information can be a rough calculation of the molecular structure, an estimation of the band origin, or it can be an educated guess based on the composition of the gas mixture being used, appearance of the spectrum, and taking into account possible aggregation combinations for a given number of molecules in a cluster. The more pieces of information known prior to simulation of the spectrum, the faster a convergence may be obtained for the fit. The systematic way of line position assignment is to first assign transitions with low J values and only varying the rotational constants. Low J lines are usually located closer to the band center. For a given maximum value of J, one should try to fit the lines with the least number of parameters possible. It is important to vary parameters that result in a converging fit and at the same time allow for inclusion of lines with higher J and K values. If the convergence of the fit is successful, the simulated spectrum should look more similar to the observed spectrum and this should enable one to identify more transitions from the simulated spectrum to match with the experimental spectrum. As transitions with higher quantum numbers are included in the fit, higher order terms such as centrifugal distortion parameters, can be determined. In this iterative manner, the simulated spectrum will gradually resemble the observed spectrum more closely. The quality of single line assignments and the entire fit can be judged by the "obs-cal" value and the overall standard deviation of the fit, respectively.

Chapter 4

Infrared spectra of two isomers of OCS-C_2H_2 and OCS-C_2D_2 in the region of OCS ν_1 fundamental

Journal of Molecular Spectroscopy 257, 133-136 (2009)

J. Norooz Oliaee, Mahin Afshari, M. Dehghany, N. Moazzen-Ahmadi[1]

Department of Physics and Astronomy, University of Calgary, 2500 University Drive North West, Calgary, Alta., Canada T2N 1N4

and

A.R.W. McKellar

Steacie Institute for Molecular Sciences, National Research Council of Canada, Ottawa, Ont. Canada K1A 0R6

Received 19 June 2009; available online 19 July 2009

Abstract

Infrared spectra of OCS$-C_2H_2$ and OCS$-C_2D_2$ complexes in the region of the C-O stretching fundamental of OCS ($\sim$ 2060 cm^{-1}) are studied in a pulsed supersonic slit-jet expansion using a tunable diode laser. For each complex, two bands are observed and assigned to distinct near-parallel and the T-shaped isomers. Ground state parameters were previously determined from microwave studies, so analysis of the infrared spectra gives information on the vibrational shifts upon complex formation as well as rotational and centrifugal distortion parameters for the excited states. All four bands show a red shift with respect to the monomer band origin, with the T-shaped isomers having a much larger shift than the near-parallel isomer. Disappearance of the T-shaped isomer when argon is used as a carrier gas

[1]Corresponding author. Fax +1 403 289 3331. Email addresses: ahmadi@phas.ucalgary.ca (N. Moazzen-Ahmadi), robert.mckellar@nrc-cnrc.gc.ca (A.R.W. McKellar).

supports the notion that the near-parallel isomer is the lowest energy form of the complex.

4.1 Introduction

Weakly bound van der Waals complexes containing two or more monomer units are of fundamental interest for understanding intermolecular interactions responsible for collisional dynamics and properties of condensed phases. There are a large number of different complexes made from combinations of relatively simple molecules: for example OCS, N_2O, CO_2, and C_2H_2 which are relevant for the present work. Some complexes have been studied spectroscopically in both the microwave and infrared regions, such as polar $(N_2O)_2$ [32,33,59,60], polar $(OCS)_2$ [61,62], $(OCS)_3$ [63,64], $(C_2H_2)_2$ [65,66], OCS−CO_2 [67,68], CO_2−N_2O [69–71], CO_2−C_2H_2 [72, 73], and N_2O−C_2H_2 [74–78]. Others have been studied only by means of their infrared spectra, either because of their nonpolar structure like nonpolar $(N_2O)_2$ [30, 32, 60, 79–81], nonpolar $(OCS)_2$ [82, 83], and $(CO_2)_2$ [84, 85], or because of complications arising from extensive hyperfine structure, like $(N_2O)_3$ [31, 37]. Still other complexes have hitherto been studied only by microwave spectroscopy, for example the subject of the present paper, OCS−C_2H_2, which occurs as two distinct isomers as shown by Peebles and Kuczkowski [6, 7]. The first isomer has a slipped near-parallel geometry (C_s symmetry) whose structure is similar to those of the previously observed N_2O−C_2H_2 and OCS−CO_2 complexes. The second isomer has a T-shaped structure (C_{2v} symmetry) with OCS forming the stem of the T and the S-atom interacting with the acetylene C-C triple bond. Figure 4.1 illustrates these two isomers of OCS−C_2H_2. Semi-empirical and *ab initio* calculations [7] indicated that the near-parallel isomer is the lowest energy form of OCS−C_2H_2.

In the present paper, we report the first observation of infrared spectra of OCS-acetylene. Both isomers are studied in the region of the ν_1 fundamental of OCS (~ 2060 cm^{-1}) for the OCS−C_2H_2 and OCS−C_2D_2 isotopomers. Since the pure rotational spectra are already well studied, analysis of the infrared spectra provides information on vibrational shifts upon

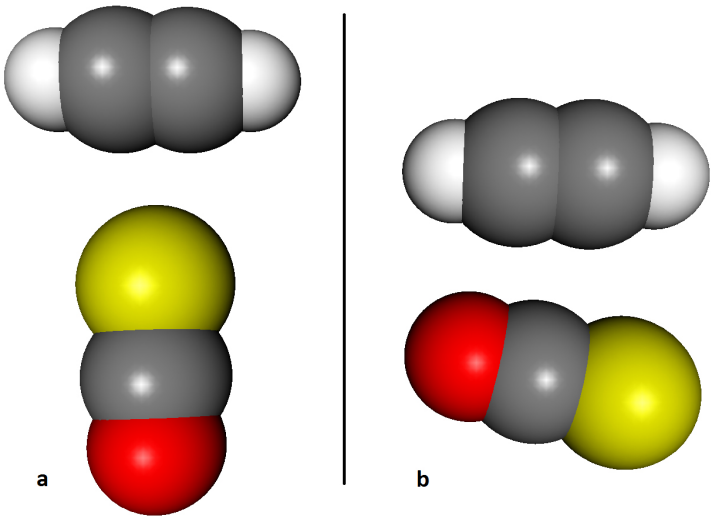

Figure 4.1: Illustration of the two isomers of the OCS−C_2H_2 complex: (a) T-shaped; (b) planar near-parallel. The near-parallel form is believed to be the lowest energy isomer.

complexation as well as rotational parameters for the excited states. All of the bands are found to be red-shifted with respect to the OCS monomer band origin, but the measured shift of the T-shape isomer (~ 5.7 cm^{-1}) is much larger than that of the near-parallel isomer (~ 0.3 cm^{-1}). Small (~ 0.001 cm^{-1}) perturbations are noted in some upper state rotational levels for the near-parallel isomer of OCS−C_2D_2 which are not present in the corresponding band of OCS−C_2H_2.

4.2 Results and Analysis

4.2.1 Experimental details

The spectra were recorded using a pulsed supersonic slit-jet apparatus at the University of Calgary, as described elsewhere [32, 33, 60]. The expansion gas was a dilute mixture of OCS and C_2H_2 or C_2D_2 ($\sim 0.5\%$) in helium, with a backing pressure of about 7 atmospheres. In order to minimize interference from He−OCS, whose spectrum overlaps that of the near-parallel isomer of OCS−C_2H_2, a ratio of 1:2 was chosen for OCS:C_2H_2. However,

the OCS−C_2D_2 spectra were recorded with an equal mixture of OCS and C_2D_2 in order to conserve the consumption of deuterated acetylene, which was obtained from C/D/N Isotopes with a stated purity of 99%.

4.2.2 The near-parallel isomer

We started our search for the infrared spectrum of OCS−C_2H_2 around the band origin of the ν_1 stretch of the OCS monomer ($\sim$ 2062 cm^{-1}). A relatively strong band was observed centered at 2061.92 cm^{-1} which is very close to the He−OCS [86] band origin (2062.31 cm^{-1}). Although we tried to minimize the formation of He−OCS as described above, there were still many strong He−OCS lines in the spectrum. The blank regions in the upper trace of Fig. 4.2, which shows the Q- and part of the R-branch for the observed OCS−C_2H_2 spectrum, are obscured due to strong absorption by the OCS monomer or He−OCS. The remaining lines are well reproduced in the simulated spectrum (second trace in Fig. 4.2) based on our analysis as described below. Both a- and b-type rotational transitions were observed for this band, with the ratio of the dipole transition moments being approximately $a/b = 1/\sqrt{1.5}$. A total of about 243 transitions were assigned with values of J and K_a up to 12 and 6, respectively, as listed in Table C.1 of the Supplementary Data.

The corresponding band for OCS−C_2D_2 was located in the same spectral region, with its band center red-shifted by only 0.04 cm^{-1} from that of OCS−C_2H_2. A portion of this band is shown in the third trace of Fig. 4.2. The close resemblance of the OCS−C_2H_2 and -C_2D_2 bands is evident. We assigned 233 transitions for OCS−C_2D_2, of which 14 were assigned weights of zero because of the existence of small perturbations (see below). The J and K_a limits for the assigned lines were 11 and 5, respectively. The assigned rotational transitions are listed in Table C.2 of the Supplementary Data.

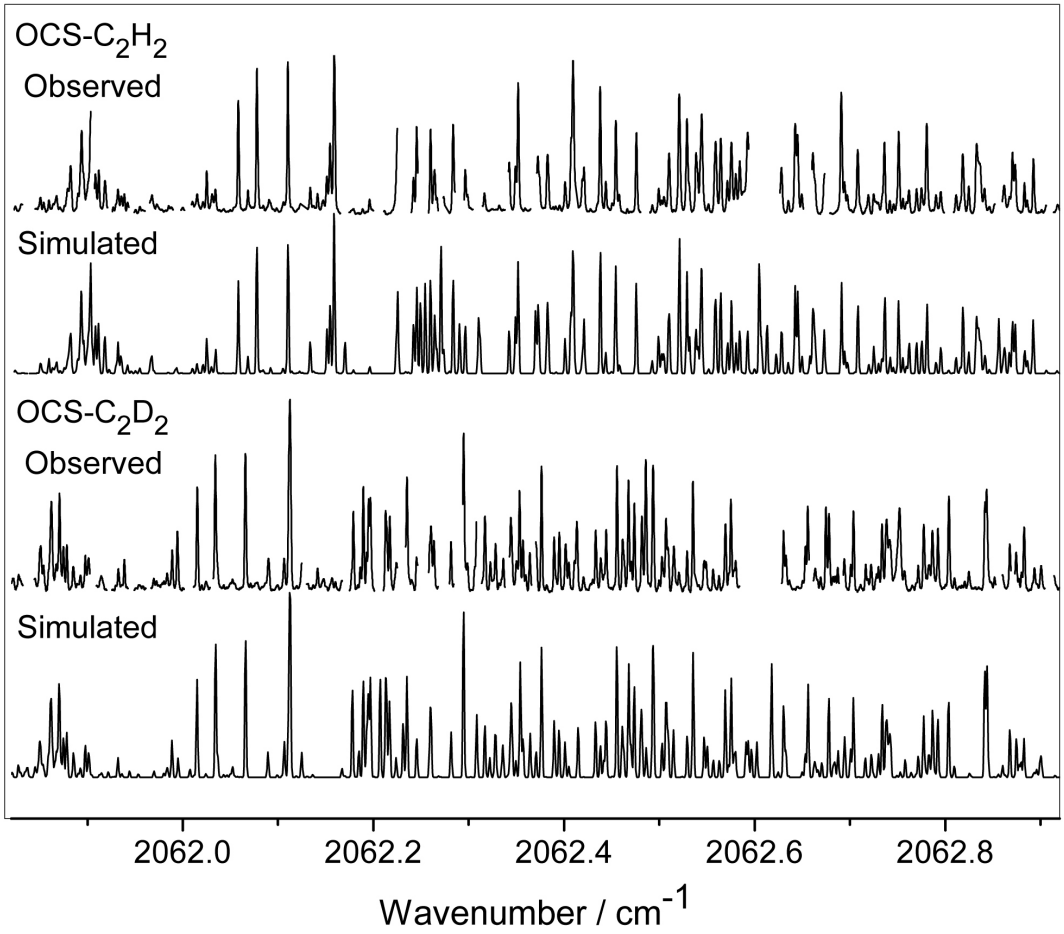

Figure 4.2: Observed and simulated spectra of the near-parallel isomer of the OCS−C_2H_2 and OCS−C_2D_2 complexes. These are hybrid *a*- and *b*-type bands. Gaps in the experimental spectra are obscured by absorption due to OCS monomers and OCS−He complexes.

4.2.3 The T-shaped isomer

Scanning to lower frequency by about 5.4 cm^{-1} from the origin of the near-parallel isomer, we observed a prominent new band, shown in the top trace of Fig. 4.3, which we assigned to T-shaped OCS−C_2H_2. This band contained only *a*-type transitions and had a relatively simple structure (discussed in more detail below). The blank regions in Fig. 4.3 are obscured by OCS monomer lines and also by unassigned features which are likely related to larger clusters of OCS or OCS and C_2H_2. In total 79 rotational transitions were assigned for this band with J and K_a up to 15 and 1, respectively, as listed in Table C.3 of the Supplementary Data.

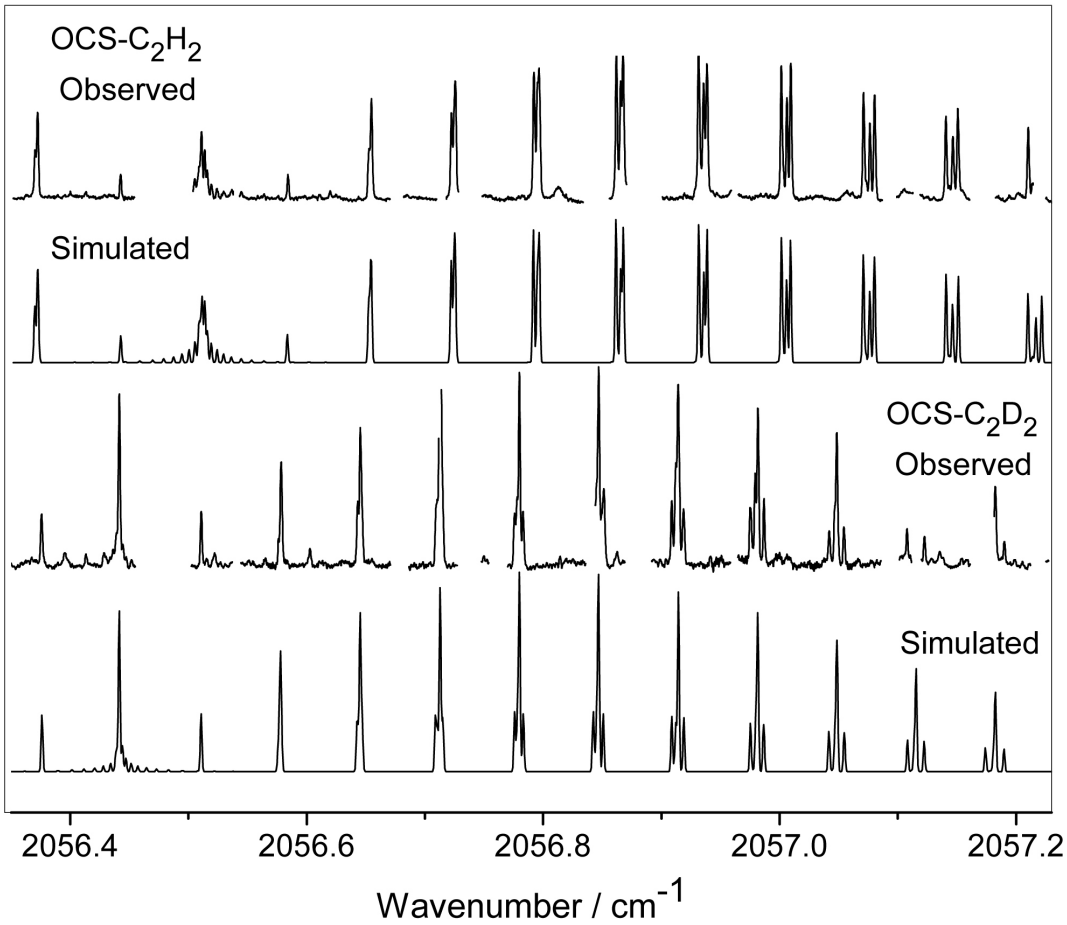

Figure 4.3: Observed and simulated spectra of the T-shaped isomer of the OCS−C_2H_2 and OCS−C_2D_2 complexes. This is the a-type band of a near prolate asymmetric rotor. Most of the difference in appearance of the OCS−C_2H_2 and OCS−C_2D_2 bands is due to different nuclear spin statistics (see text).

The corresponding band of the T-shaped isomer of OCS−C_2D_2 was red-shifted by 0.07 cm^{-1} from that of OCS−C_2H_2. The lower two traces of Fig. 4.3 show the observed and simulated spectra in the region of the Q- and R-branches. A total of 62 transitions with values of J up to 14 and K_a up to 2 were assigned, as listed in the Table C.4 of the Supplementary Data. The clear contrast between the spectra of OCS−C_2H_2 and OCS−C_2D_2 in Fig. 4.3 can be explained by the difference in spin statistical weights affecting K_a, since the a-axis coincides with the C_{2v} symmetry axis for the T-shaped isomer. In the case of OCS−C_2H_2, the two equivalent protons ($I = 1/2$) result in a weight of 1:3 for K_a = even:odd, whereas for OCS−C_2D_2 the deuterons ($I = 1$) give a weight of 2:1. Thus the $K_a = 1$ "satellite" lines

surrounding the central peaks are much stronger for OCS$-C_2H_2$ than for OCS$-C_2D_2$ for the R-branch transitions in Fig. 4.3.

4.2.4 Rotational Analysis

The line measurement, simulation and fitting were done using the PGOPHER computer program [58]. A conventional A-reduced asymmetric rotor Hamiltonian in the I^r representation was employed [87]. The molecular parameters obtained from fits for the near-parallel isomer are given in Table 4.1. For the normal isotopomer, the 24 microwave transitions measured by Peebles and Kuczkowski [6] were included in the analysis with a relative weight of 1000 to reflect their higher precision. A standard deviation of about 0.00014 cm^{-1} was obtained by varying 17 parameters, namely the band origin, lower and upper state rotational constants and all the quartic centrifugal distortion constants.

In the case of the near-parallel isomer of OCS$-C_2D_2$, some small ($\approx$ 0.001 cm^{-1}) perturbations affecting several upper state levels were noted. The perturbed levels were $J'_{K_aK_c} = 5_{05}, 5_{14}, 7_{34}, 7_{35}$ and 9_{27}, and 14 transitions involving these levels were assigned a weight of zero in the fit. We decided to fix the ground state parameters at their microwave values [6] so that any smaller perturbations possibly affecting other upper state levels would not contaminate the ground state parameters. As well, the upper state distortion parameter δ'_K was fixed to its ground state value since preliminary fits showed that it could not be determined with statistical significance. Results are shown in Table 4.1, and the standard deviation of the final fit for the OCS$-C_2D_2$ infrared data was 0.00018 cm^{-1}.

Results for the final fits for T-shaped isomer are given in Table 4.2. For each isotopomer, 12 transitions from the microwave study [7] were included with weights of 1000. In the final fits we varied the band origin, lower and upper state rotational constants and all the quartic centrifugal distortion constants except Δ_K and δ_K. In the case of OCS$-C_2H_2$, δ_J for the upper state could not be determined and was therefore fixed to its ground state value. The fits were very good, with rms deviations of about 0.00012 cm^{-1} for OCS$-C_2H_2$

Table 4.1: Molecular parameters for the near-parallel isomer of OCS-acetylene (in cm^{-1}).[a]

	OCS−C_2H_2 present work	OCS−C_2H_2 Ref. [6]	OCS−C_2D_2 present work	OCS−C_2D_2 Ref. [6]
ν_0	2061.9154(1)		2061.8816(1)	
A'	0.1934388(77)		0.1818433(73)	
B'	0.0685218(29)		0.0654548(35)	
C'	0.0504131(19)		0.0479600(28)	
$10^6 \times \Delta'_K$	0.94(29)		0.941[b]	
$10^6 \times \Delta'_{JK}$	-0.21(13)		0.52(17)	
$10^7 \times \Delta'_J$	3.26(19)		2.36(22)	
$10^6 \times \delta'_K$	1.27(26)		2.35(37)	
$10^7 \times \delta'_J$	1.20(12)		0.71(14)	
A''	0.194771675(82)	0.194771647(67)	0.18304535[c]	0.18304535(7)
B''	0.068562067(54)	0.068562058(43)	0.06550078[c]	0.06550078(4)
C''	0.050534258(51)	0.050534243(40)	0.04807713[c]	0.04807713(6)
$10^6 \times \Delta''_K$	1.481(18)	1.478(13)	0.941[c]	0.941(23)
$10^6 \times \Delta''_{JK}$	0.101(45)	0.097(33)	0.217[c]	0.217(3)
$10^7 \times \Delta''_J$	2.9003(86)	2.8987(67)	2.595[c]	2.595(16)
$10^6 \times \delta''_K$	0.938(22)	0.941(20)	0.705[c]	0.705(17)
$10^7 \times \delta''_J$	0.8430(33)	0.8429(27)	0.767[c]	0.767(13)

[a] Uncertainties in parentheses are 1σ from the least-square fits in units of the last quoted digit.
[b] This parameter was fixed at its ground state value.
[c] OCS−C_2D_2 ground state parameters were fixed at microwave [6] values (see text).

and 0.00015 cm^{-1} for OCS−C_2D_2. The inability to determine Δ_K and δ_K is largely due to the fact that only transitions involving $K_a = 0$ and 1 were assigned in our analysis. This is because the A rotational constants of these T-shaped isomers are rather large, meaning that only levels with $K_a \leq 2$ are significantly populated at the effective rotational temperature of the supersonic expansion (≈2.5 K). Even if they were populated, many higher K_a transitions would not be clearly resolved from $K_a = 0$ in our spectra. The weakness of the higher K_a transitions gives the simple band structure seen in Fig. 4.3 and means that the analysis is not sensitive to the parameters Δ_K and δ_K.

Table 4.2 summarizes the ground state parameters obtained from the infrared study of the T-shaped isomer and compares them with the corresponding values from the microwave study. Our results essentially agree with those of Ref. [7], except that our error limits should

Table 4.2: Molecular parameters for the T-shaped isomer of OCS-acetylene (in cm^{-1}).[a]

	OCS−C_2H_2 present work	OCS−C_2H_2 Ref. [7]	OCS−C_2D_2 present work	OCS−C_2D_2 Ref. [7]
ν_0	2056.5133(1)		2056.4432(1)	
A'	1.214(19)		0.8746(66)	
B'	0.0358406(11)		0.0344174(22)	
C'	0.0346730(12)		0.0329536(21)	
$10^5 \times \Delta'_{JK}$	0.855(67)		0.847(61)	
$10^7 \times \Delta'_J$	0.519(51)		0.711(68)	
$10^8 \times \delta'_J$	0.149[b]		1.29(63)	
A''	1.215(19)	1.214(8)	0.8751(66)	0.8753(23)
B''	0.035858030(34)	0.035858033(13)	0.034425768(36)	0.034425765(13)
C''	0.034686541(34)	0.034686539(13)	0.032963119(36)	0.032963117(13)
$10^5 \times \Delta''_{JK}$	1.0399(24)	1.0401(10)	1.0082(26)	1.0080(10)
$10^7 \times \Delta''_J$	0.5259(36)	0.5257(17)	0.4711(38)	0.4713(13)
$10^8 \times \delta''_J$	0.149(25)	0.150(10)[c]	0.270(27)	0.270(10)[c]

[a] Uncertainties in parentheses are 1σ from the least-square fits in units of the last quoted digit.
[b] This parameter was fixes at its ground state value.
[c] The reported values for δ''_J in Ref. [7] were 0.45(3) and 0.81(3) kHz for OCS−C_2H_2 and OCS−C_2D_2, respectively. We believe that due to typos in reporting, these values should be multiplied by a factor of 10, as given here (in cm^{-1}).

be more reliable since more input data were incorporated. We believe that discrepancies of factors of 10 for δ_J are typographical errors in reporting the microwave values [7].

4.3 Discussion and conclusions

The observed vibrational shifts of the OCS-acetylene band origins, relative to that of the free OCS monomer, are -0.286 or -0.320 cm^{-1} for the near-parallel isomer of OCS−C_2H_2 or OCS−C_2D_2, and -5.688 or -5.758 cm^{-1} for the T-shaped isomer. These red shifts indicate that the overall strength of the intermolecular interaction becomes slightly stronger when the OCS ν_1 mode is vibrationally excited, with the effect being significantly greater for the T-shaped isomer. In each case, we observe that the magnitude of the shift increases slightly in going from C_2H_2 to C_2D_2. For the related complex N_2O-acetylene only a near-parallel isomer has been observed so far, and the observed vibrational shifts in the analogous N_2O ν_1 fundamental band region are +5.346 and +5.420 cm^{-1} for N_2O−C_2H_2 and -C_2D_2,

respectively [78].

The semi-empirical and *ab initio* calculations of Peebles and Kuczkowski [6, 7] indicated that the lowest energy form of the OCS$-C_2H_2$ complex is the near-parallel isomer, with the T-shaped isomer having a significantly higher energy, and this energy ordering was consistent with the observed relative intensities in the microwave spectra. However, there appeared to be no dependence of the relative intensities on the supersonic expansion carrier gas [7], which can often be used to distinguish isomers (the greater collisional energy transfer possible with heavier carrier gases leads to more complete relaxation to the lowest energy form, whereas helium as a carrier tends to leave population in higher energy isomers).

In order to check the isomer energies further, we repeated our experiment with the addition of argon to the gas mixture. Although the observation was complicated by the appearance of new spectra due to argon-containing complexes, it was evident that the T-shape isomer of OCS$-C_2H_2$ disappeared while the near-parallel isomer was still present with argon in the mix. This result tends to confirm the idea that the near-parallel form is the lowest energy isomer of OCS$-C_2H_2$.

In conclusion, we have observed and analyzed vibration-rotation spectra of the weakly-bound OCS-acetylene complex in the region of the ν_1 fundamental band of OCS. As noted previously in the microwave region [6, 7] two distinct isomers were present for both OCS$-C_2H_2$ and OCS$-C_2D_2$: a planar near-parallel form, and a planar T-shaped form, with OCS forming the stem of the T. The two isomers have rather different vibrational shifts, so their bands are well separated. The symmetric near-prolate structure of the T-shaped isomer results in a rather simple and distinctive spectrum, in contrast to the more complicated-looking spectrum of the near-parallel isomer. Our observation that the T-shaped isomer disappears when argon is added to the supersonic expansion gas mixture strongly supports the notion that the near-parallel isomer is the lowest energy form of OCS$-C_2H_2$.

Acknowledgements

We thank L. Murdock for technical assistance. The financial support of the Natural Sciences and Engineering Research Council of Canada is gratefully acknowledged.

Supplementary Data

Supplementary data for this article (Tables C.1- C.4) are available in Appendix C of this thesis, and also on ScienceDirect (`www.sciencedirect.com`) and as part of the Ohio State University Molecular Spectroscopy Archives (`http://library.osu.edu/sites/msa/jmsa_hp.htm`). Supplementary data associated with this article can be found, in the online version, at doi:10.1016/j.jms.2009.07.003.

Chapter 5

Ubiquitous T-shaped isomers of OCS-hydrocarbon van der Waals complexes

Journal of Chemical Physics **131**, 161105 (2009)

J. Norooz Oliaee, M. Dehghany, Mahin Afshari, N. Moazzen-Ahmadi[1]

Department of Physics and Astronomy, University of Calgary, 2500 University Drive North West, Calgary, Alberta T2N 1N4, Canada

and

A.R.W. McKellar[2]

Steacie Institute for Molecular Sciences, National Research Council of Canada, Ottawa, Ontario K1A 0R6, Canada

Received 26 August 2009; Accepted 13 October 2009; Published online 27 October 2009

Abstract

Many weakly bound OCS-hydrocarbon complexes exhibit a relatively simple rotation-vibration band, characteristic of a T-shaped structure, which is redshifted (by 5 - 12 cm^{-1}) from the OCS monomer ν_1 frequency. Spectra of OCS with seven chain and ring hydrocarbons are described here. They allow a straightforward comparison of intermolecular force effects (vibrational shift and intermolecular separation) over a range of molecules, which could be extended to other hydrocarbons and other probes such as CO_2 and N_2O.

[1]Electronic mail: ahmadi@phas.ucalgary.ca
[2]Electronic mail: robert.mckellar@nrc-cnrc.gc.ca

5.1 Introduction

Studying infrared spectra of weakly-bound OCS−X complexes in the region of the C−O stretching fundamental of OCS (~ 2062 cm^{-1}), we observe that many hydrocarbon molecules, X, exhibit an easily-recognized vibration-rotation band due to a T-shaped isomer. With minimal analysis, two characteristic parameters can be extracted: a vibrational shift, measuring the effect of molecule X on the OCS vibration, and a rotational constant, giving the effective center of mass separation between OCS and X. These provide a straightforward "low-tech" comparison of intermolecular force effects. It should be possible to extend the comparison using further partner molecules and related probe molecules such as CO_2, N_2O, and CS_2, thus building up a range of structural information analogous to the large database now available for hydrogen- and halogen-bonded complexes [88]. The present communication is an overview of results obtained to date on these seemingly ubiquitous T-shaped complexes.

In 1999, Peebles and Kuczkowski reported microwave spectra of two distinct isomers of OCS-acetylene. One had a planar, near-parallel configuration [6] (with side-by-side OCS and HCCH) and the other had a planar T-shaped configuration [7] (with HCCH as the top of the T, OCS as the stem, and the S atom adjacent to the C≡C bond). Semi-empirical and *ab initio* calculations indicated that the near-parallel isomer was the lowest energy form. This was confirmed by the experimental observation that that the T-shape isomer of OCS−C_2H_2 disappears with argon in the gas mixture whereas the near parallel isomer does not [89]. Studying infrared spectra of OCS−C_2H_2 in the region of the OCS ν_1 fundamental, we observe the same parallel and T-shaped isomers. The experiments are performed using a pulsed supersonic jet expansion of a dilute mixture of OCS and C_2H_2 in helium carrier gas. Spectra are observed by direct absorption using a tunable diode laser [33, 35, 60, 78], and simulated using Colin Western's program, PGOPHER [58]. T-shaped OCS−C_2H_2 leads to a simple-looking band centered at 2056.5 cm^{-1}, shown in Fig. 5.1, while the parallel isomer leads to a stronger and more complicated band at 2061.9 cm^{-1} (not shown here). As we

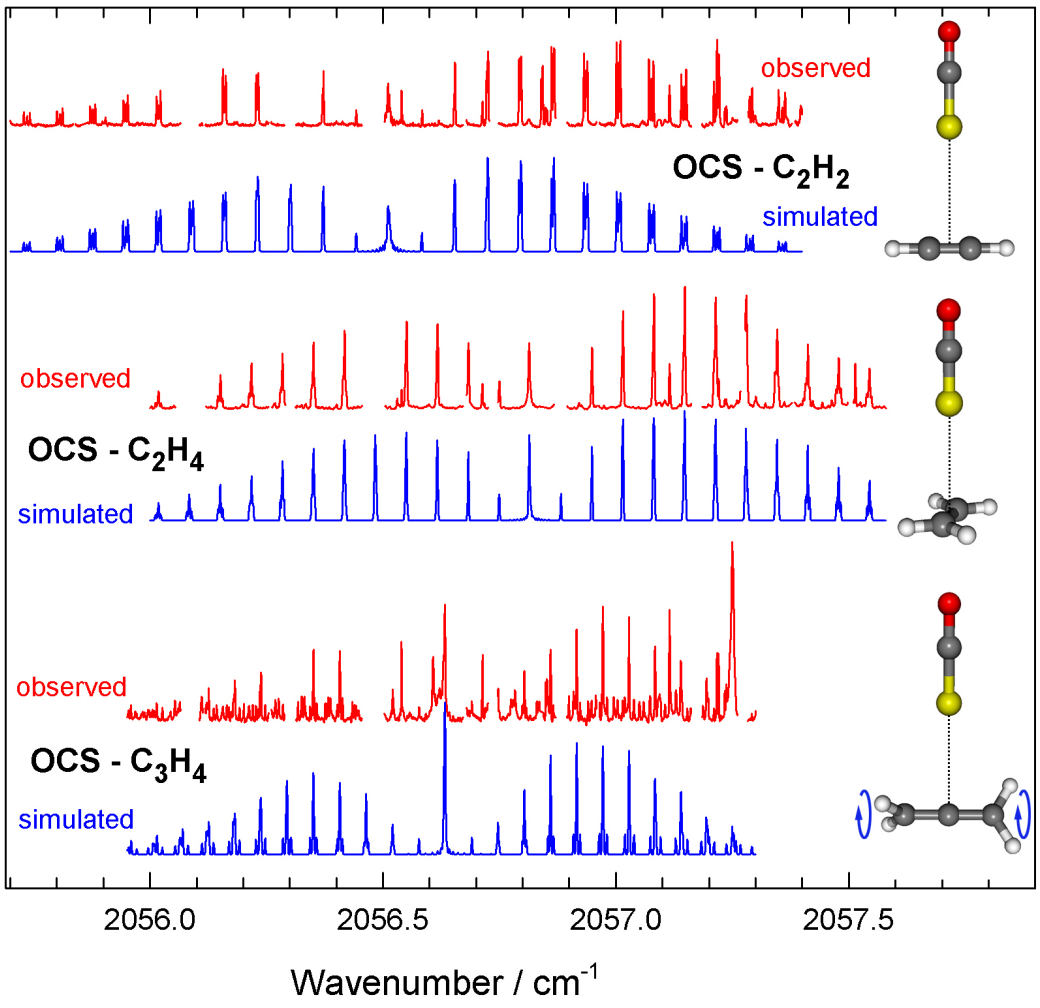

Figure 5.1: Observed and simulated spectra of the T-shaped complexes OCS-acetylene, OCS-ethylene, and OCS-allene. Gaps in the observed traces correspond to regions of strong OCS monomer absorption. In the simulations, the assumed rotational temperature is 2.5 K and the line width is 0.002 cm^{-1}.

continue to study other small hydrocarbons we discover that most also exhibit simple bands due to approximately "T-shaped" OCS−X structures in the same spectral region. (When X is a ring species, "wheel and axle" or "daisy-shaped" are perhaps more appropriate than "T-shaped").

5.2 Carbon Chain Molecules

The observed T-shaped complexes are summarized in Table 5.1. A brief description of each spectrum follows here, and more complete accounts of new results will be reported later. The analyses are relatively insensitive to the A rotational constant, which for a rigidly T-shaped complex is simply equal to the B or C rotational constant of monomer X. In the present simple analyses, the A parameters (apart from OCS$-C_2H_2$) are thus fixed at literature values for the isolated hydrocarbons. In the case of T-shaped OCS$-C_2H_2$, our results agree well with the microwave data [7], and these more precise rotational constants are given in Table 5.1. Observed linewidths are all about 0.002 cm^{-1} or bit less. Most (or all) of these are due to the residual Doppler broadening (nonzero velocity component parallel to the probe laser) and laser linewidth. So there is no evidence for lifetime broadening due to predissociation, even in cases (C_2H_2, C_2H_4) where we believe the T-shaped isomer is not the ground state.

Table 5.1: Parameters for the observed bands of T-shaped OCS$-$X complexes

Hydrocarbon X		ν_0	$\Delta\nu_0$	A_0[a]	B_0	C_0	R_0
C_2H_2	Acetylene[b]	2056.513	-5.688	1.2139	0.03586	0.03469	4.62
C_2H_4	Ethylene	2056.816	-5.385	0.8280	0.03365	0.03273	4.64
C_3H_4	Allene	2056.634	-5.567	0.2963	0.02966	0.02693	4.50
C_3H_4	Propyne	2054.822	-7.379	0.2851	0.03064	0.02733	4.45
C_4H_2	Diacetylene[c]	(2052.05)	(-10.15)	0.1469		(0.0294)	(4.43)
C_4H_6	Dimethylacetylene	2052.753	-9.449	0.1119	0.02692	0.02166	4.38
C_6H_6	Benzene	2051.064	-11.137	0.0957	0.02021		4.42
C_8H_8	Cyclo-octatetraene	2051.821	-10.380	0.0515	0.01489		4.76[d]

[a] The analyses are rather insensitive to the assumed A_0 values, which are simply literature B_0 values for monomer X (or C_0 in the case of ethylene, benzene, and cyclo-octatetraene).
[b] The A_0, B_0, C_0, and R_0 data for OCS$-C_2H_2$ are from Peebles and Kuczkowski [7].
[c] The OCS-diacetylene data are tentative (see text). The value given for C_0 refers to $(B_0 + C_0)/2$.
[d] Equivalent to a distance of 4.35 Å from the OCS center of mass to the adjacent CCCC plane.

Using a mixture of OCS and ethylene, we find a band at 2056.8 cm^{-1} (see Fig. 5.1) which is obviously due to T-shaped OCS$-C_2H_4$. In this case, a near-parallel stacked (non-planar) iso-

mer was previously observed in the microwave region [90] but the T-shaped form is new. The spectrum of the T-shaped isomer is a simple a-type band of a near-prolate asymmetric rotor. The K structure of each $P(J)$ or $R(J)$ line is mostly blended, but the asymmetry-doubled $K_a = 1$ transitions become resolved for $J > 5$. The analysis favors a non-planar structure in which the OCS axis is perpendicular to the C_2H_4 monomer plane, the same as observed for complexes of hydrogen halides and dihalogens with ethylene [88]. There is no evidence for internal rotation of ethylene within the complex. Analysis of the spectrum of $O^{13}CS{-}C_2H_4$ (not shown here) confirms a S-bonded structure, similar to $OCS{-}C_2H_2$ [7]. The resulting center of mass separation is 4.64 Å, only slightly greater than that of $OCS{-}C_2H_2$ (see Table 5.1). It yields 3.60 Å for the distance between the S atom and the ethylene C-C axis.

For OCS-allene, we also observe a simple a-type band, with resolved $K_a = 1$ "satellites" around each P- or R-branch line for $J > 2$, and some resolution of other K_a transitions for higher J lines. Parameters for this band are given in Table 5.1. The observed line intensities are consistent with a 7:3 intensity alternation between K_a=even:odd levels, showing that this is indeed a T-shaped complex with C_2 symmetry having the S atom "bonded" to the central C atom of the allene. In contrast, the HF-allene and ClF-allene complexes have L-shaped structures [91, 92], with the diatomic lying along an axis passing through the midpoint of one of the allene C-C bonds. There is a second OCS-allene band with similar rotational constants, a slightly different origin (2056.609 cm^{-1}), and different nuclear spin statistics for K_a. We interpret the two bands as evidence for relatively free internal rotation of the allene monomer unit (around its C-C-C axis) within the $OCS{-}H_2CCCH_2$ complex. The first band is the lowest A internal rotor state, and the second band is an excited E internal rotor state which is metastable due to nuclear spin conservation. Each band can be separately well fitted by an asymmetric rotor Hamiltonian ignoring internal rotation effects, but a more complete internal rotor analysis may be possible in the future.

The symmetry of the OCS-propyne (methyl acetylene, $HCCCH_3$) complex differs from

the others considered here in that we cannot expect a perfect T-shaped structure. We observe a somewhat complicated band with a prominent Q-branch at 2054.822 cm^{-1}. Located among these complicated structures is a simple near-prolate asymmetric rotor band, similar to those of the three complexes in Fig. 5.1, which can be well fitted in terms of the parameters listed in Table 5.1. In addition to this simple band there are unassigned transitions of approximately equal strength which we interpret in terms of methyl group internal rotation. We suspect that this is an intermediate-barrier case, in contrast to OCS-ethylene (high-barrier internal rotor with unresolved rotor splittings) and OCS-allene (low-barrier internal rotor with two distinct rotor states). For OCS-propyne, the simple band we fit then arises from the lowest A rotor state, but a complete internal rotor analysis will be necessary for the additional observed lines arising from excited rotor states. The important point is that we can extract rather precise quantitative information (vibrational shift, rotational constants, intermolecular separation) for OCS-allene and OCS-propyne (and OCS-dimethylacetylene, below) even before these internal rotation effects are fully understood.

In the case of OCS-diacetylene (HCCCCH), we observe a band (not shown here) due to a planar, near-parallel isomer, analogous to that observed [6] for OCS$-C_2H_2$, but we could not clearly observe a T-shaped isomer. However, there is a band at 2052.05 cm^{-1} whose structure is rather chaotic but with some regularly-spaced series of lines. This could be a highly-perturbed band of T-shaped OCS$-C_4H_2$, and if we interpret the regular spacing as being equal to $(B + C)$ then we obtain a reasonable intermolecular distance, as shown in Table 5.1.

For OCS-dimethylacetylene (H_3CCCCH_3), we observe a messy-looking band (not shown) with a sharp and prominent Q-branch at 2052.753 cm^{-1}. Analysis seems hopeless at first, but by starting with trial rotational constants assuming a structure similar to OCS-propyne, and simulating [58] the spectrum, we obtain a good match for many P- and R-branch lines. The refined rotational constants and band origin are shown in Table 5.1. There is a second band,

centered at 2052.772 cm^{-1}, with similar rotational constants and about half the intensity of the main band. We interpret these two bands in terms of distinct internal rotation states, as expected since dimethylacetylene itself exhibits rather free internal rotation (barrier height $\approx$6 cm^{-1}) [93]. Line strengths in the main band are consistent with a 3:5 intensity alternation between K_a=even:odd levels as expected for the lowest A internal rotor state. Full details of the spectrum remain to be worked out, but we still obtain precise vibrational shift and intermolecular separation parameters (Table 5.1). The possibility of using the simple A internal rotation state spectra to obtain quantitative information for those complexes affected by internal rotation (OCS-allene, OCS-propyne, OCS-dimethylacetylene) is advantageous. However, we should bear in mind that the A state rotational parameters are in general affected by internal rotation and may not perfectly reflect the mechanical moments of inertia. We believe that such errors are small compared to the level of accuracy quoted in this paper, but this remains to be verified by more detailed analysis.

For all the T-shaped OCS-carbon chain complexes, the *changes* in rotational constants with excitation of the OCS ν_1 vibration (not shown here) are small, negative, and relatively uniform. They range in magnitude from 0.03% to 0.11% of the parameter itself.

5.3 Carbon Ring Results

Simple parallel-band symmetric top spectra were observed for the complexes of OCS with the unsaturated ring molecules benzene (C_6H_6) and cyclo-octatetraene (C_8H_8), as shown in Fig. 5.2. These are ascribed to structures with the OCS monomer located along the ring symmetry axes. The very sharp Q-branch of OCS$-C_6H_6$ is well reproduced by the simulation. There is also a strong broad feature located very close to this Q-branch, and a weaker broad feature at about 2050.98 cm^{-1}, but experimental evidence indicates that these broad features arise from larger clusters. In addition to the $OC^{32}S-C_6H_6$ spectrum, we also observe that of $OC^{34}S-C_6H_6$ in natural abundance and confirm that the complex has

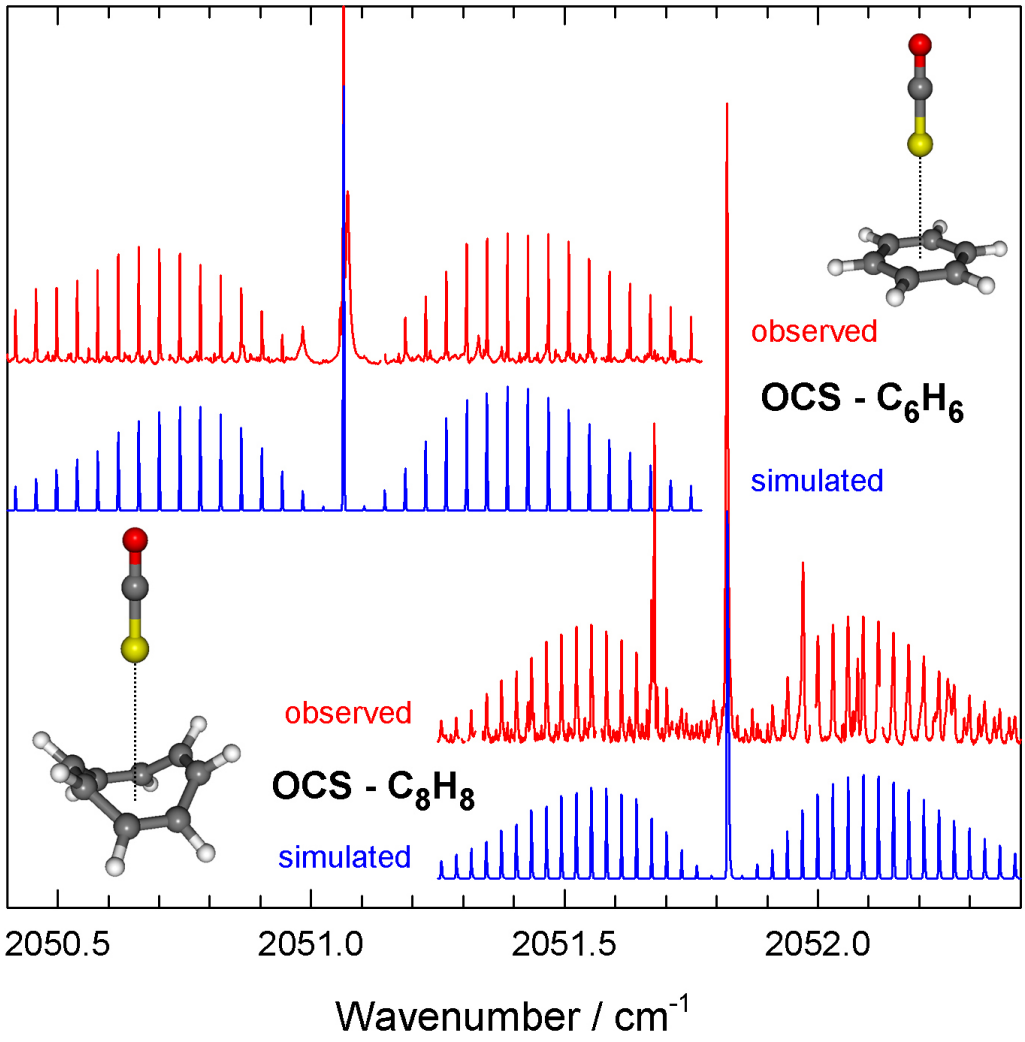

Figure 5.2: Observed and simulated spectra of the T-shaped (daisy-shaped) complexes OCS-benzene and OCS-cyclooctatetraene.

an S-bonded structure. The microwave spectrum of OCS-benzene was reported by Dahmen *et al.* [94], and our results agree well with theirs. In the case of OCS−C_8H_8, a similar-looking band is observed with parameters as given in Table 5.1. There is also a weaker second band whose intensity is about 17% of the main OCS−C_8H_8 band. Its origin is located about 0.26 cm^{-1} higher (at 2052.080 cm^{-1}) and it has essentially the same rotational constants. The Q-branch of the weaker band is visible in Fig. 5.2; two other extra features in this spectrum (at 2051.68 and 2051.97 cm^{-1}) are unassigned and probably unrelated. The second band is presumably a hot band, that is, evidence for nonrigid behavior in the form of a low frequency

(≈ 3 cm^{-1}) vibration. This could correspond to an internal rotation motion such as that as ascribed to ClF-benzene [95].

A precautionary note: Dahmen *et al.* [91] showed that the observation of a symmetric-rotor-like spectrum for linear molecule-ring complexes does not necessarily indicate a T-shaped (daisy-shaped) structure. That is, even if the OCS axes were perpendicular to the benzene ring axis, a symmetric top spectrum could result if the benzene had free or nearly free internal rotation around the ring axis. Nevertheless, the evidence supports the T-shaped structure for OCS-benzene [94], and in any case the observed B-values still give a good measure of the intermolecular center of mass separation. Vibrational changes in B and C (not shown) are very small ($< 0.02\%$) and negative for OCS$-C_6H_6$, but slightly positive ($< 0.1\%$) for OCS$-C_8H_8$.

5.4 Conclusions

There is clear evidence from the present and previous [7, 94] work that the complexes are S-bonded, that is, the S atom end of OCS is located closest to the hydrocarbon, in the case of OCS-acetylene, OCS-ethylene, and OCS-benzene. The same probably holds true for the other systems studied here, but this remains to be verified. Out of ten hydrocarbons tried so far, seven exhibit clear T-shaped bands, one is ambiguous (diacetylene), and two do not show T-shaped bands: ethane (C_2H_6) and cyclohexane (C_6H_{12}). The two negative cases are fully saturated, and the absence of T-shaped structures is not surprising in view of previous work on weakly-bound complexes [88, 96].

The existence of T-shaped OCS$-$X complexes can be rationalized in terms of rule 2 proposed by Legon [88] in connection with the geometry of B-YZ complexes, where B is a Lewis base (electron donor), Y is a halogen atom (electron acceptor), and Z can be a halogen or other atom. Rule 2 predicts that the electron acceptor of YZ lies along the symmetry axis of the Lewis base π orbital and that the electrophilic X interacts with the π-electron density.

The low-lying vacant molecular orbitals of OCS are Π^* and σ^*, so OCS has two electrophilic sites [97]. For Π^*, the electrophilic site is the carbon atom, whereas the σ^* orbital has charge accepting strength through S. The former (carbon) site has the larger electrophilicity. Thus if Legon's rule 2 is applied to OCS−X, it predicts both parallel isomers and higher energy T-shaped isomers where the electrophilic S interacts with the π bonding electrons in X. Of course the exact energy balance between the two isomers depends on the properties of molecule X and can be finally settled only by detailed experimental and theoretical studies.

Trends are evident in the vibrational shift data of Table 5.1. All the T-shaped complexes exhibit redshifts, indicating that the intermolecular bonding becomes slightly stronger when the OCS ν_1 stretching motion is excited. The magnitude of the shift clearly tends to increase with the number of C atoms in molecule X that are adjacent to the OCS. As might be expected, the shift for propyne is almost midway between those of acetylene and dimethylacetylene. We anticipate that this sort of database can be extended relatively easily, allowing such trends to be explored in greater scope.

Acknowledgements

We thank L. Murdock for technical assistance. The financial support of the Natural Sciences and Engineering Research Council of Canada is gratefully acknowledged.

Chapter 6

High resolution infrared spectroscopy of carbon dioxide clusters up to $(CO_2)_{13}$

The Journal of Chemical Physics **135**, 044315 (2011)

J. Norooz Oliaee,[1] M. Dehghany,[1] A.R.W. McKellar[2]

and

N. Moazzen-Ahmadi[1]

[1]*Department of Physics and Astronomy, University of Calgary, 2500 University Drive North West, Calgary, Alta., Canada T2N 1N4*

[2]*Steacie Institute for Molecular Sciences, National Research Council of Canada, Ottawa, Ont. Canada K1A 0R6*

Received 13 May 2011; accepted 30 June 2011; published online 28 July 2011

Abstract

Thirteen specific infrared bands in the 2350 cm^{-1} region are assigned to carbon dioxide clusters, $(CO_2)_N$, with N = 6, 7, 9, 10, 11, 12 and 13. The spectra are observed in direct absorption using a tuneable infrared laser to probe a pulsed supersonic jet expansion of a dilute mixture of CO_2 in He carrier gas. Assignments are aided by cluster structure calculations made using two reliable CO_2 intermolecular potential functions. For $(CO_2)_6$, two highly-symmetric isomers are observed, one with S_6 symmetry (probably the more stable form), and the other with S_4 symmetry. $(CO_2)_{13}$ is also symmetric (S_6), but the remaining clusters are asymmetric tops with no symmetry elements. The observed rotational constants tend to be slightly (≈2%) smaller than those from the predicted structures. The bands have increasing vibrational blueshifts with increasing cluster size, similar to those predicted by

the resonant dipole-dipole interaction model but significantly larger in magnitude.

6.1 Introduction

Molecular clusters bound by weak van der Waals forces are of wide interest. In the case of carbon dioxide, the study of clusters has practical importance for atmospheric and even industrial applications, and fundamental importance because of the basic nature of CO_2 itself. More generally, clusters represent the "missing" link between single molecules or molecular pairs and the bulk liquid or solid phases, and intermolecular forces play a key role in this transition region. Carbon dioxide dimers [13,79,84,85,98] and trimers [14,15,99] were extensively studied by high-resolution infrared spectroscopy in the period from 1984 to 1996. The dimer was shown to have a planar slipped-parallel structure, with centrosymmetric C_{2h} symmetry. Two trimer isomers were identified. One with a planar cyclic structure and C_{3h} symmetry, and the other with a twisted barrel shape and C_2 symmetry. Recent work on CO_2 dimers and trimers has focused on the study of various isotopes [16, 17], and the detection of combination bands [2, 17] which provide information on the important intermolecular vibrational modes. All high-resolution work on dimers and trimers has involved either the CO_2 ν_3 antisymmetric stretch fundamental vibration ($\sim$ 2350 cm^{-1}), or the $(\nu_1+\nu_3)/(2\nu_2+\nu_3)$ combination vibrations ($\sim$ 3700 cm^{-1}).

There have been many other spectroscopic studies of CO_2 clusters in which rotational structure was not resolved. Dimer features in the $\nu_1/2\nu_2$ Fermi-doublet region ($\sim$ 1300 cm^{-1}) received much attention [100–105], but have not been very informative, partly because these experiments are performed at relatively high temperatures (>180 K) and gas pressures. Larger clusters have been probed using a number of techniques [18–27], but $(CO_2)_3$ remained the largest cluster for which explicit infrared band assignments were supported by resolved rotational structure. Very recently, we reported assignments of specific vibration-rotation bands in the ν_3 region to medium-size carbon dioxide clusters, $(CO_2)_N$, with N = 6, 7, 9,

10, 11, 12, and 13. These are the largest such clusters to be characterized by rotationally resolved spectroscopy, and the results contribute to bridging the elusive gap between small (dimer, trimer) and large (e.g. microcrystalline [106]) clusters.

The present paper is an expansion and extension of the original brief report [28]. We observe new bands, further investigate the cluster structures, and provide additional details and supporting evidence. Highlights include assignment of a second isomer for the hexamer, $(CO_2)_6$, a combination band for the original hexamer, new red-shifted bands for $(CO_2)_{10}$ and $(CO_2)_{13}$, results for ^{18}O-substituted clusters, and a possible alternate structure for $(CO_2)_{10}$.

Intermolecular potential functions for the CO_2-CO_2 interaction have a long history because of its fundamental nature and practical importance. Recent *ab initio* results have utilized SAPT [107], CCSD(T) [108], and MP2 [109,110] techniques. Simplified model potential functions which can be quickly evaluated are very useful for molecular simulations, and these may be based on *ab initio* calculations, empirically derived from observed bulk properties, or both [110–113]. An older but noteworthy and widely accepted empirical function is the M-O-M or Murthy potential [29,114], which was based on solid CO_2 elastic constants but has also been shown to work rather well in predicting dimer and trimer structures, vibrational shifts, and transition moment orientations [15, 99].

6.2 Results

The apparatus used here has been described previously [34, 35, 115, 116]. Spectra were recorded using a rapid-scan tuneable diode laser spectrometer to probe a pulsed supersonic slit-jet expansion of dilute mixtures of carbon dioxide ($\sim 0.2\%$) in helium carrier gas. The jet backing pressure was 8 bars and effective cluster rotational temperatures were about 2.5 K. Signals from a fixed etalon and a reference gas cell were used for wavenumber calibration. The PGOPHER program [58] was used for analysis, simulation, and fitting of the spectra. Many of the cluster bands were first observed during searches for CO_2 dimer and trimer

combination bands [2, 17], which revealed numerous unexplained features after accounting for known and possible bands of $(CO_2)_2$, $(CO_2)_3$, and CO_2−He [117,118]. In addition to the normal species, some useful cluster results were also obtained using $^{12}C^{18}O_2$, but these were restricted due to limited sample and laser coverage. Earlier $^{13}C^{16}O_2$ spectra [17] had only limited coverage in the dimer and trimer regions and were not of use here.

6.2.1 Cluster Calculations

Our original assignments [28] were based on calculations of the lowest-energy structures for $(CO_2)_N$ clusters reported by Takeuchi [1], who used the M-O-M empirical intermolecular potential [29, 114]. This function has eight adjustable parameters and consists of atom-atom Lennard-Jones 12-6 terms for the C-C, C-O, and O-O interactions, plus five point charges distributed along the CO_2 axis. Takeuchi reported detailed structural parameters for $N = 4 - 40$ in his Supporting Information section of Ref. [1] which enabled us to readily calculate the cluster rotational constants, A, B, and C. Subsequently, we made further calculations using the SAPT-s potential, a simplified function based on the high-level *ab initio* results of Bukowski *et al.* [107] These numerical cluster simulations start with N molecules in random positions and orientations and adjust the $\{5(N-1)-1\}$-dimensional structure to find an energy minimum for $(CO_2)_N$ using the Powell method from Numerical Recipes [119]. This is repeated hundreds or thousands of times until we are reasonably confident that the true global minimum has been found. This works well for smaller clusters, but the method is crude, compared for example to that of Takeuchi [1], so it becomes impractical for larger clusters (say $N > 14$ in the present case) because of the high dimensionality.

A summary of the results for the minimum energy clusters with $N = 5 - 13$ using both potential functions is given in Table 6.1. For $N = 6$ and 10, the two lowest energy structures are given. In most cases the two potentials give very similar results for the structures and rotational constants, with the SAPT-s binding energies generally being about 4% larger. However, our calculation reveals an interesting difference for $N = 10$, where the identities

of the two lowest energy isomers interchange between the two potentials. As can be seen in Table 6.1, the lowest energy $(CO_2)_{10}$ isomer using M-O-M potential, which we label "10b," becomes the second lowest for the SAPT-s potential, and vice-versa for the other isomer labeled "10a". The energy differences are small - only 45 or 13 cm^{-1} in a total binding energy of 10000 cm^{-1} - so we can still say that the two potentials agree rather well. Although these two $(CO_2)_{10}$ isomers have distinct structures, their rotational constants are similar. As we will see below, isomer 10a seems to agree slightly better with experiment. The theoretical

Table 6.1: Theoretical binding energies (in cm^{-1}) and theoretical and observed rotational constants (in MHz) for $(CO_2)_N$ clusters.

	M-O-M[a]				SAPT-s[b]				Experiment[c]		
N	Energy	A	B	C	Energy	A	B	C	A	B	C
5	-3405	629.2	421.9	373.6	-3532	630.0	630.0	372.6			
6a	-4664		371.1	295.9	-4886			298.7		360.1	297.5
6b	-4646		359.6	309.7	-4849			312.0		352.9	308.7
7	-5891	325.8	272.9	216.8	-6095	322.6	322.6	215.1	314.8	270.7	210.9
8	-7095	297.8	180.4	159.2	-7321	294.2	294.2	158.9			
9	-8456	211.4	163.7	126.8	-8783	210.5	210.5	126.9	207	161	125
10a	-9733	158.8	145.8	110.6	-10145	158.6	158.6	111.1	155.4	144.0	111
10b	-9778	164.5	145.8	111.3	-10132	163.4	163.4	111.4			
11	-11183	138.6	116.1	99.2	-11644	137.9	137.9	99.8	136	114	106
12	-12646	111.4	107.7	95.2	-13191	111.0	111.0	95.8	109	106	93
13	-14499		94.5	92.8	-15147			93.1		92.6	90

[a] Structures from Takeuchi (Ref. [1]) based on the empirical potential of Murthy and co-workers. (Refs. [29, 114])
[b] Structures based on the SAPT-s fitted *ab initio* potential of Bukowski *et al.* (Ref. [107])
[c] Present results.

structures in this range are asymmetric tops ($A > B > C$) except for $N = 6$ and 13, which are oblate symmetric tops ($A = B > C$). But $N = 13$ is very close to the spherical limit, with B only slightly larger than C. Both the lowest (labeled 6a) and second-lowest (6b) energy isomers of $(CO_2)_6$ are symmetric tops and both have now been observed experimentally (see below). The cluster structures are discussed in more detail below. The special nature of the symmetric ones (especially $(CO_2)_{13}$) is emphasized by the plot of incremental binding energy (or chemical potential) shown in Fig. 6.1. This is the energy released when cluster N

is formed by adding a CO_2 monomer to cluster $(N-1)$. Note that $N = 6$ and 13 are local maxima in this plot (also $N = 9$), showing that their structures are especially favorable. Takeuchi shows that $N = 28$ and 40 are also "magic" clusters for CO_2 [1]. Vibrational shifts

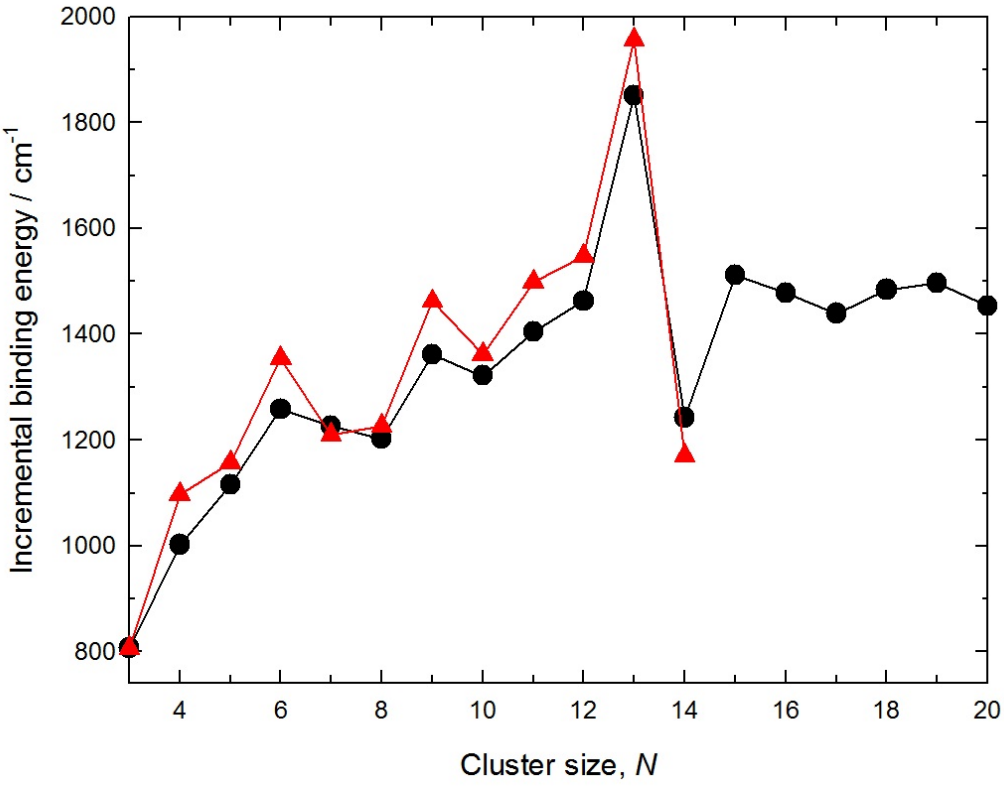

Figure 6.1: Incremental binding energy, or chemical potential, for CO_2 clusters, as calculated using the M-O-M (black circles) and SAPT-s (red triangles) intermolecular potentials. Data with $N > 14$ are not available for SAPT-s due to the limitations of our structure simulations.

of molecules in clusters and crystals are frequently modeled using a resonant dipole-dipole model [15,22,120,121], in which the pairwise interactions of transition dipoles lift the N-fold degeneracy of the cluster vibrational transition in a way that can be exactly calculated if the structure and transition moments are known. Although this approach should be suitable here because of the large ν_3 dipole transition moment of CO_2, it has actually been shown to be a rather poor model for the CO_2 trimer [122]. But at least it captures the qualitative behavior of CO_2 clusters [28] and represents a useful starting point for discussion. Results of such

calculations are shown in Tables 6.2 and 6.3. We used an experimental CO_2 transition dipole value [123] (the same as Weida *et al.* [99]) and the SAPT-s structures (M-O-M structures give similar results). For the asymmetric top clusters in Table 6.2 ($N = 7 - 12$), only the three strongest of the N allowed infrared bands are listed. Each band is characterized by its vibrational shift and by the components of its intensity in the directions of the $a-, b-$, and c-inertial axes. For the symmetric clusters, $N = 6$ and 13 (Table 6.3), all vibrations are listed with their symmetries, vibrational shifts, intensities.

Table 6.2: Summary of resonant dipole calculations for $(CO_2)_N$ clusters.[a]

			Intensity[b]		
N	Shift	Position	a	b	c
7	+0.53	2349.67	0.12	0.96	0.0
7	+4.12	2353.26	1.19	0.05	0.16
7	+5.77	2354.91	0.47	0.09	3.14
8	+1.78	2350.92	1.45	0.67	0.07
8	+5.25	2354.39	0.02	0.17	1.11
8	+6.75	2355.90	1.10	0.03	1.49
9	+1.98	2351.13	2.16	0.11	0.22
9	+3.02	2352.17	0.00	2.19	0.35
9	+4.24	2353.38	0.44	0.00	0.68
10a	-2.07	2347.08	1.61	0.01	0.03
10a	+3.41	2352.55	1.24	0.03	0.03
10a	+10.43	2359.57	0.32	0.44	1.16
10b	+1.19	2350.33	0.05	1.14	0.21
10b	+4.80	2353.94	1.37	0.27	0.88
10b	+6.57	2355.71	0.95	1.01	1.54
11	-3.55	2345.59	0.79	0.51	0.12
11	+3.95	2353.09	0.42	1.48	0.97
11	+10.39	2359.53	0.01	0.89	1.04
12	+3.79	2352.93	0.28	0.44	1.71
12	+4.67	2353.81	0.42	0.43	1.01
12	+12.14	2361.28	1.25	1.04	0.10

[a] Structures calculated from the SAPT-s potential (Ref. [107]). Shift and position in cm^{-1}. Only the three strongest bands are given for each cluster size.
[b] Intensities for transition dipole components along the a-, b-, and c-inertial axes, in units of CO_2 monomer transition moment. The total intensity for all bands of cluster $(CO_2)_N$ is equal to N.

These resonant dipole results are discussed below in the sections where the various sized

Table 6.3: Resonant dipole calculation for the two lowest energy isomers of $(CO_2)_6$ and the lowest isomer of $(CO_2)_{13}$.[a]

Isomer	Mode	Shift	Position	Intensity[b]
6a(S_6)	A_u	-3.50	2345.64	0.02
6a(S_6)	E_g	-1.11	2348.03	0.0
6a(S_6)	A_g	+2.00	2351.14	0.0
6a(S_6)	E_u	+1.86	2351.01	5.98
6b(S_4)	E	-3.55	2345.59	0.95
6b(S_4)	E	+1.21	2350.35	4.18
6b(S_4)	B	+2.07	2351.21	0.86
6b(S_4)	A	+2.62	2351.76	0.0
13(S_6)	A_u	-10.98	2338.16	0.30
13(S_6)	E_u	-6.15	2342.99	4.10
13(S_6)	E_g	-4.23	2344.91	0.0
13(S_6)	A_u	-1.16	2347.98	0.88
13(S_6)	A_g	-0.16	2348.98	0.0
13(S_6)	E_g	+1.27	2350.41	0.0
13(S_6)	A_g	+4.98	2354.12	0.0
13(S_6)	E_u	+5.47	2354.61	5.80
13(S_6)	A_u	+14.64	2363.78	1.93

[a] Shift and position in cm^{-1}. Structures calculated from the SAPT-s potential (Ref. [107]).
[b] Intensities are in units of CO_2 monomer transition moment, so that the total intensity for all bands of a given cluster is equal to 6 or 13.

clusters are considered in detail. Here we simply note that there is a general trend for the more intense bands to be blueshifted (positive shifts). Indeed, in Table 6.2 there is only one red-shifted band, and in Table 6.3 a clear majority of the total intensity is blueshifted. This trend for the CO_2 ν_3 mode to blueshift in clusters and condensed phases is experimentally known from previous low-resolution studies [22, 106]. It essentially means that the cluster binding energies tend to be slightly reduced for stronger bands (i.e., those for which the collective monomer ν_3 vibrations are aligned and in-phase.)

6.2.2 The carbon dioxide hexamer, $(CO_2)_6$

The predicted minimum energy structure of the CO_2 hexamer is a symmetric rotor with S_6 point group symmetry (six-fold rotation-reflection axis) as illustrated at the top of Fig. 6.2. It can be thought of as a "sandwich" of two cyclic CO_2 trimers with coincident C_3 symmetry

axes but with the "top" and "bottom" trimers rotated by 60° with respect to one another. Since all nuclear spins are zero in $^{12}C^{16}O_2$ (and $^{12}C^{18}O_2$), the threefold rotation axis implied by the S_6 symmetry means that only levels with $K = 3n$ are populated, where n is an integer. As explained in Ref. [28], a band centered around 2353.55 cm^{-1} (just above "band III" of noncyclic $(CO_2)_3$) (Ref. [15]) matches extremely well with that expected from the S_6 hexamer. It is characteristic of a symmetric top perpendicular ($\Delta K = \pm 1$) band for a molecule close to the spherical top limit, and the fitted rotational constants agree very well with the theoretical ones. This 2353.55 cm^{-1} band is shown in Fig. 2 of Ref. [28]. The analogous band for the isotopologue $(^{12}C^{18}O_2)_6$ occurs at 2318.51 cm^{-1}.

In addition to this perpendicular band, we have now also observed a weak parallel ($\Delta K = 0$) band at 2378.17 cm^{-1} for which the fitted B-value is virtually identical (as usual for a symmetric top parallel band the C-value was not well determined). The corresponding parallel band was not observed for $(^{12}C^{18}O_2)_6$ due to limited laser coverage. For our analysis, we assumed that the perpendicular and parallel bands arise from the same ground state, and performed a simultaneous fit with results as shown in Table 6.4. Coriolis coupling in the upper state of the perpendicular band was neglected, an approximation which is reasonable, based on the general observation that intramolecular vibrations are only loosely coupled in weakly bound complexes and on the rather similar case of the cyclic CO_2 trimer [99]. Most fitted lines in the analyses represent blends of numerous individual transitions, and there are many overlapping features from other CO_2 clusters, particularly for the perpendicular bands. For these reasons, the statistical errors in Table 6.4 probably underestimate the true parameter uncertainties.

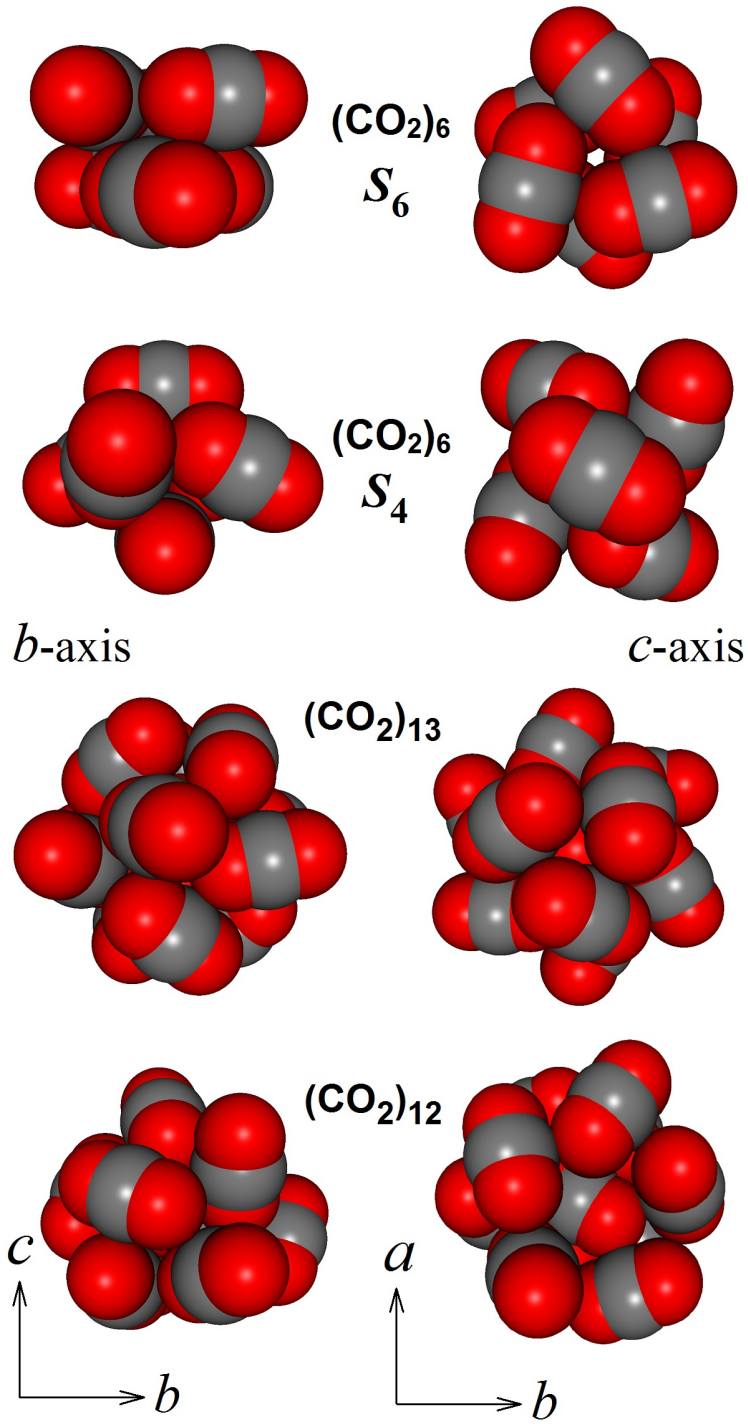

Figure 6.2: Illustration of $(CO_2)_6$, $(CO_2)_{13}$, and $(CO_2)_{12}$. These are "experimental" structures (see text) for $(CO_2)_6$ and theoretical (Ref. [1]) ones for $(CO_2)_{13}$ and $(CO_2)_{12}$, but the differences are indistinguishable at this scale. The two lowest-energy isomers of $(CO_2)_6$ have S_6 symmetry and S_4 symmetry as indicated, and the symmetry axis (which is also the c-inertial axis) is out of the plane of the figure in the right-hand views, and in the plane in the left-hand views. $(CO_2)_{13}$ has S_6 symmetry, and the axes are located similarly. $(CO_2)_{12}$ (bottom panel) is an asymmetric top, with inertial axes as indicated.

Table 6.4: Observed parameters for the S_6 and S_4 isomers of the CO_2 hexamer.[a]

	$(^{12}C^{16}O_2)_2$ S_6 isomer		$(^{12}C^{18}O_2)_2$ S_6 isomer	$(^{12}C^{16}O_2)_2$ S_4 isomer		$(^{12}C^{18}O_2)_2$ S_4 isomer
	Perpendicular fundamental	Parallel combination	Perpendicular fundamental	Perpendicular fundamental	Parallel fundamental	Parallel fundamental
ν_0/cm^{-1}	2353.5507(1)	2378.1720(1)	2318.5109(1)	2351.8583(1)	2354.4892(1)	2319.4818(1)
B'	360.114(42)	359.943(45)	328.483(63)	352.731(23)	352.566(19)	322.115(9)
C'	297.232(24)	297.304[b]	271.355(50)	308.534(46)	308.399(45)	[c]
B''	360.141(39)		328.571(61)	352.880(21)		322.367(10)
C''	297.505(15)		271.592(52)	308.726(43)		[c]

[a] Centrifugal distortion parameters and the Coriolis zeta parameter for the perpendicular band upper states were fixed at zero.
[b] The quantity $(C' - C'')$ was adjusted to reproduce the observed shape of the Q-branch for the parallel band.
[c] C'' was fixed at 282 MHz for $(^{12}C^{18}O_2)_6$ and $(C' - C'')$ was determined to be -0.025(7) MHz.

Table 6.5: Observed parameters for $(CO_2)_7$.[a]

	$(^{12}C^{16}O_2)_7$	$(^{12}C^{18}O_2)_7$
ν_0/cm^{-1}	2356.2545(1)	2321.1378(1)
A'/MHz	314.636(42)	287.895(88)
B'/MHz	270.531(46)	247.784(71)
C'/MHz	210.720(340)	193.525(397)
A''/MHz	314.809(45)	288.110(98)
B''/MHz	270.726(49)	247.324(96)
C''/MHz	210.860(242)	193.618(395)

[a] Centrifugal distortion parameters were fixed at zero. The parameters are slightly different from those reported previously (Ref. [28]) because the fit has been refined.

With the assumption of S_6 symmetry, the hexamer has four fundamental vibrational modes in the CO_2 ν_3 region (see Table 6.3). There is an infrared-forbidden mode with A_g symmetry, corresponding to in-phase ν_3 vibrations on all six monomers. There is a mode with A_u symmetry in which the "upper" three monomers vibrate in-phase, and the "lower" three also vibrate in phase, but with the two sets out-of-phase. Although this A_u mode gives rise to an allowed c-type band, it is very weak because the monomers have little projection on the c-axis (the individual trimer units within the hexamer are almost planar). There are two degenerate modes, a forbidden one with E_g symmetry, and an allowed one with E_u symmetry. It is the latter E_u mode which gives rise to a strong perpendicular band to which we assign the observed bands at 2353.55 and 2318.51 cm^{-1}. The parallel band at 2378.17 cm^{-1} could be due to the A_u fundamental, but because of its large blueshift we believe it is really a combination band involving the sum of an intramolecular fundamental plus a low-frequency intermolecular mode. The most likely intermolecular modes are those in which the trimer units within the hexamer execute out-of-plane "torsional" motions, because these are just the modes that have been observed for the cyclic trimer itself [2, 17]. In the trimer, these modes have frequencies of about 13 and 19 cm^{-1}. In the hexamer, this mode has a frequency of 25.62 cm^{-1} if the associated fundamental is the E_u one observed here (in which case the intermolecular mode would be E_g). But we cannot be sure of this because an upper state with the required A_u symmetry can also be generated by combining any one of the four intramolecular fundamentals with an intermolecular mode of the appropriate symmetry. What is clear is that the unambiguous observation [2, 17] of parallel combination bands for cyclic $(CO_2)_3$ makes the observation of an analogous band of $(CO_2)_6$ very plausible, since the hexamer is essentially composed of two trimers.

The observed vibrational shifts of the hexamer fundamental band origins with respect to the CO_2 monomer are +4.408 and +4.462 cm^{-1} for $(^{12}C^{16}O_2)_6$ and $(^{12}C^{18}O_2)_6$, respectively. These are in the same direction, but considerably larger than the shift of +1.86 cm^{-1}

predicted by the resonant dipole model (Table 6.3). The two experimental rotational constants determined for $(^{12}C^{16}O_2)_6$ are not sufficient to determine its structure completely, and the $(^{12}C^{18}O_2)_6$ data do not give much additional information. To estimate an experimental structure, we make the following assumptions: the monomer geometry remains unchanged in the hexamer; each trimer unit remains planar in the hexamer; and the in-plane orientation angle of the monomer in the trimer is $\beta = 40°$ [99, 122]. With these restrictions, the observed $(^{12}C^{16}O_2)_6$ constants give values of 2.897 Å for the distance between the two trimer planes, and 4.045 Å for the C-C distances within each trimer unit. For comparison, some values for these distances from theoretical potential surfaces are 2.813, 2.773, and 2.897 Å and 4.036, 4.060, and 4.064 Å [1, 107, 124]. The experimental C-C distance for the trimer is 4.030 Å [99]. However, note that the theoretical structures have slightly nonplanar trimer units in the hexamer, whereas we assume they are planar. Our "experimental" hexamer structure predicts isotope shifts of -31.02 and -26.14 MHz for B'' and C'' between $(^{12}C^{18}O_2)_6$ and $(^{12}C^{16}O_2)_6$, in good agreement with the observed values of -31.57 and -25.91 MHz.

6.2.3 Another isomer of the hexamer

The next lowest energy isomer of $(CO_2)_6$ is predicted to lie only 18 (M-O-M) or 36 cm^{-1} (SAPT-s) higher in energy. It is also a symmetric top, but this time with S_4 symmetry. As illustrated in Fig. 6.2, it consists of a ring of four equivalent monomers capped at the "top" and "bottom" by a pair of equivalent monomers. These two monomers are aligned orthogonally, so that by themselves they would have D_{2d} symmetry. The ring of four monomers is slightly puckered, meaning that the four equivalent C atoms are not (necessarily) planar. According to Liu and Jordan [125], the M-O-M potential predicts an interconversion barrier of about 1 kcal/mol (350 cm^{-1}) between isomers 6a and 6b.

We assign two bands to this form of the hexamer. There is a parallel band, already reported but unexplained [17], with a Q-branch at 2354.49 cm^{-1}, a clear R-branch, and a heavily obscured P-branch. Its analysis gave $B'' = 351$ MHz, about 8 MHz smaller than

the calculated value for isomer 6b in Table 6.1 Note that the observed B'' for isomer 6a is similarly about 10 MHz smaller than the calculated values. There is also a perpendicular band centered at 2351.86 cm^{-1} having a Q-branch similar to that of the original hexamer at 2353.55 cm^{-1}, but with narrower line spacing. This spacing (≈180 MHz) is close to that predicted (188 MHz) for the S_4 hexamer (this predicted value is equal to $2 \times 2 \times (B - C)$, where one factor of 2 comes from the fact that only levels with $K = 2n$ are populated due to spin statistics and the twofold rotation axis implied by the S_4 symmetry). These bands are illustrated in Fig. 6.3. The perpendicular one is heavily overlapped by transitions of $(CO_2)_2$ and $(CO_2)_3$, the latter including both the cyclic trimer and band III of the noncyclic trimer. As well, there is interference from other unassigned transitions, including the P-branch of the so-called Q_A band (which may be due to $(CO_2)_4$) [15,17,99]. In spite of this interference, we were able to assign a reasonable number of perpendicular band transitions and perform a simultaneous analysis of both bands, yielding the parameters listed on the right-hand side of Table 6.4. This gave values of B'' and C'' in good agreement with theory (see Table 6.1). For $^{12}C^{18}O_2$, we observed the analogous parallel band at 2319.48 cm^{-1} (see Table 6.4), but missed the perpendicular band due to limited laser coverage.

The S_4 hexamer has four fundamental modes in the CO_2 ν_3 region (see Table 6.3). There are two degenerate vibrations with E symmetry giving rise to perpendicular bands, a vibration with B symmetry giving rise to a parallel band, and a vibration with A symmetry which is infrared forbidden. According to the resonant dipole calculation in Table 6.3, we expect a redshifted (-3.5 cm^{-1}) perpendicular band, a much stronger blueshifted (+2.1 cm^{-1}) perpendicular band, and a more blueshifted (+2.6 cm-1) parallel band. The observed perpendicular and parallel bands, with shifts of +2.72 and +5.35 cm^{-1}, respectively, are indeed blueshifted, but, as usual [28], these shifts are considerably larger in magnitude than predicted by the simple model. Since another perpendicular band is predicted, we checked carefully and found a possible candidate Q-branch at about 2348.33 cm^{-1} (a vibrational shift

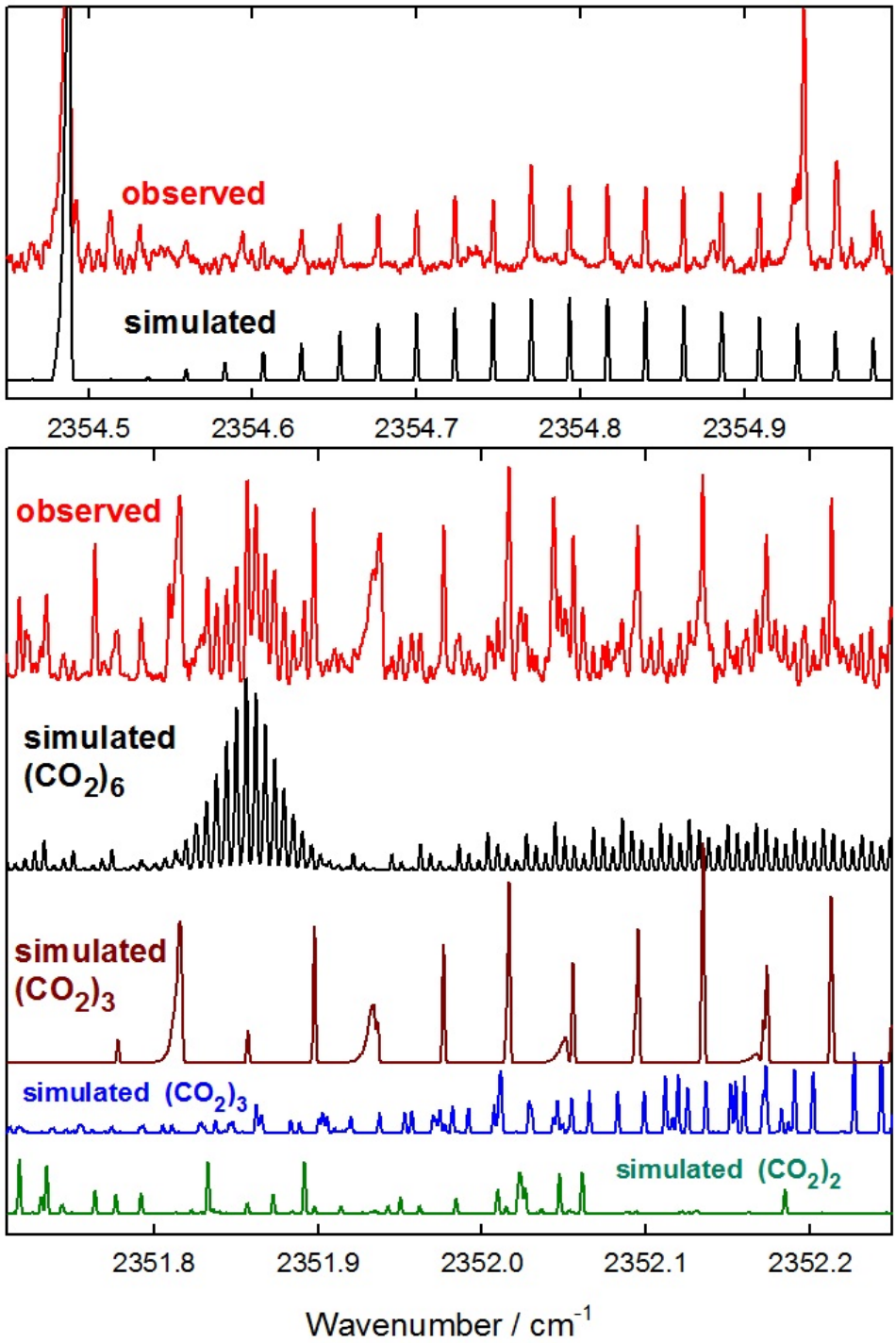

Figure 6.3: Observed and simulated spectra showing bands assigned to the S_4 isomer of $(CO_2)_6$. The perpendicular band in the lower panel is overlapped by bands of $(CO_2)_2$ and of the cyclic (brown) and noncyclic (blue) isomers of $(CO_2)_3$ as shown, while the Q- and R-branches of the parallel band in the upper panel are relatively clear.

of -0.81 cm^{-1}). However, this band was too weak to analyze in detail.

Assuming S_4 symmetry and unchanged monomers, three distances and three angles are required to specify the structure of isomer 6b, and these can be expressed as follows. First, the "ring radius" distance from the S_4 symmetry axis to one of the four equivalent C atoms. Second, the "hexamer length" distance between the two equivalent C atoms. Third, the "ring puckering" distance from the center of mass to the line connecting diagonally opposite pairs of the four equivalent C atoms (in the SAPT-s structure, this distance is 0.075 Å - if it is zero then the four equivalent C atoms are coplanar). Then there is the angle between the O-C-O axis of one of the two equivalent monomers and one of the lines connecting diagonally opposite pairs of the four equivalent C atoms (since each subunit is a symmetric top, this angle has no effect on the hexamer rotational constants - it is like internal rotation in ethane). More significant is the angle between the O-C-O axis of one of the four equivalent monomers and the line connecting its C atom with the diagonally opposite C atom. Finally, there is the dihedral angle between the O-C-O axis of one of the four equivalent monomers and the S_4 symmetry axis. With six unknowns and only two observables (or three, counting the $(^{12}C^{18}O_2)_6$ B-value) it is not possible to determine the structure experimentally. However, for illustration we keep all angles and the puckering distance fixed at the SAPT-s values and vary the two remaining distances to fit B'' and C'' of the normal isotopologue. By changing the "ring radius" from 2.818 (SAPT-s) to 2.836 Å we obtain the experimental C'' value. Then by changing the "hexamer length" from 5.043 (SAPT-s) to 5.115 Å we get the experimental B''-value. The isotope shift for B'' predicted by this "experimental" structure agrees perfectly with experiment.

6.2.4 The carbon dioxide heptamer (or septamer), $(CO_2)_7$

We assign bands at 2356.25 and 2321.14 cm^{-1} to $(^{12}C^{16}O_2)_7$ and $(^{12}C^{18}O_2)_7$, respectively [28]. They are (mostly) c-type bands with prominent Q-branches and extensive P- and R-branch structure, as illustrated in Fig. 6.4. The detailed match between observed and simulated

spectra is very good. The fitted rotational constants (Table 6.5) agree quite well with predicted ones (Table 6.1), and this agreement is somewhat better for $(^{12}C^{18}O_2)_7$ than for $(^{12}C^{16}O_2)_7$ (rms deviations of 4.4 vs. 5.4 MHz for the SAPT-s structure) as expected if part of the discrepancy is due to zero-point motion effects. There was a hint of some b-type contribution to the bands (at most 0.3 of the c-type), but not of any a-type transitions (¡0.2).

The predicted heptamer structure is unsymmetrical, with five monomers in a pentagonal ring approximately in the plane of the $a-$ and $b-$inertial axes and the remaining two located close to the c axis above and below the ring. In the absence of help from symmetry, there is no way to refine the theoretical structure using the experimental rotational constants. The results do at least provide a benchmark for future high-level calculations of the heptamer structure. Since there are no equivalent monomers, there should be seven infrared-allowed fundamentals in the ν_3 region of which we have observed one, with a vibrational shift relative to the CO_2 monomer of +7.11 or +7.09 cm^{-1} for $(^{12}C^{16}O_2)_7$ or $(^{12}C^{18}O_2)_7$, respectively. The resonant dipole model (Table 6.2) predicts that the strongest to be mostly c-type and shifted by +5.77 cm^{-1}, in reasonable qualitative agreement with experiment. The next lowest energy isomer of $(CO_2)_7$ predicted by the SAPT-s potential is about 56 cm^{-1} higher in energy and is also unsymmetrical, with rotational constants (A, B, C) = 302.9, 276.2, 193.6 MHz.

6.2.5 The carbon dioxide nonamer $(CO_2)_9$ and decamer $(CO_2)_{10}$.

The band at 2358.69 cm^{-1} which we assign to $(CO_2)_9$ has a strong sharp Q-branch with rather weak and indistinct P- and R-branches, as shown in the top trace of Fig. 6.5. There is regular P- and R-structure with a spacing corresponding to an effective rotational constant of about 180 MHz. From the theoretical rotational constants (Table 6.1), this spacing could be given either by an a-type band of $(CO_2)_8$ (predicted $(B + C)/2 \approx$170 MHz), or by a c-type band of $(CO_2)_9$ (predicted $(A + B)/2 \approx$ 188 MHz). A simulation based on $(CO_2)_8$ gives structure more pronounced than observed ($(CO_2)_8$ is relatively close to the prolate symmetric limit). A simulation with constants close to those predicted for $(CO_2)_9$ shown in the top panel of

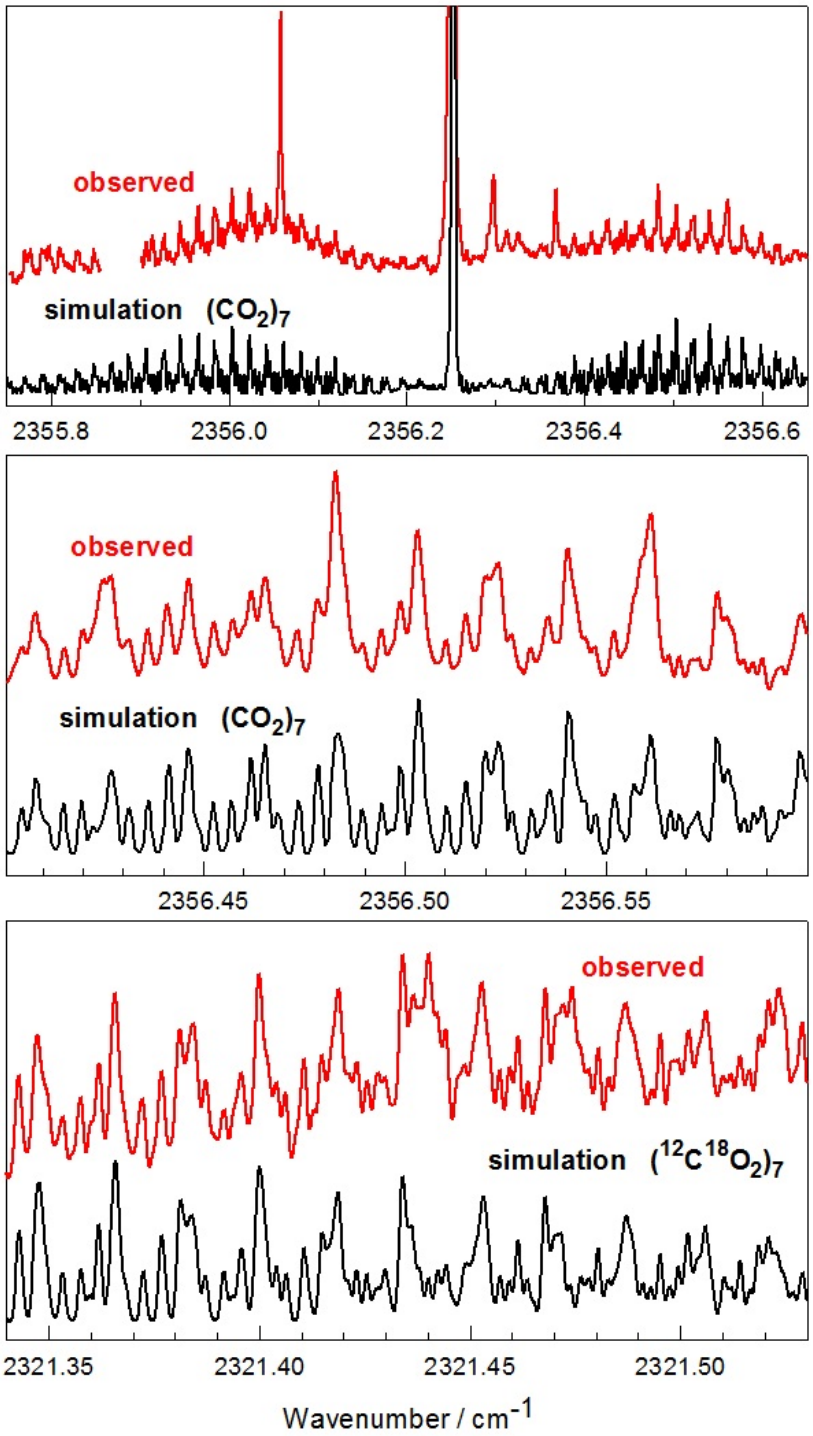

Figure 6.4: Observed and simulated spectra showing bands assigned to $(CO_2)_7$. The top panel is an overview of the entire $(^{12}C^{16}O_2)_7$ band. The middle and bottom panels show detailed views of the *R*-branch for $(^{12}C^{16}O_2)_7$ and $(^{12}C^{18}O_2)_7$, respectively.

Fig. 6.5, is much better. The corresponding $(^{12}C^{18}O_2)_9$ band may be located at 2323.669 cm^{-1}, but is less clear. It would represent a shift of +9.62 cm^{-1} from the monomer origin, as compared to +9.54 cm^{-1} for the normal isotope. The predicted structure of $(CO_2)_9$ is unsymmetric, with nine allowed bands in the ν_3 region of which the resonant dipole model predicts the third strongest to be predominantly *c*-type with a shift of +4.24 cm^{-1}. We are reasonably sure that $(CO_2)_9$ provides the correct assignment for this band, but the simulation is not perfect and this is one of our less secure identifications, together with $(CO_2)_{11}$ (below).

We observed a strong, sharp *Q*-branch at 2361.15 cm^{-1} which is accompanied by long and regular series of *P*- and *R*-branch lines (middle panel of Fig. 6.5). A good simulation of the band is obtained using constants (Table 6.6) close to those predicted for $(CO_2)_{10}$. The simulation shown is a *c*-type band with a weaker *a*-type contribution (intensity ratio $a : c$ = 1:4). This band is not sensitive to the absolute value of C, so the fitted value (111 MHz) is only approximate. Nevertheless, the good agreement with the predicted A and B values for $(CO_2)_{10}$ is strong support for the present assignment, compared to any other cluster size. A similar but much weaker band (not shown here) was observed at 2344.08 cm^{-1} whose shape was consistent with assignment as another *c*-type band of the same species. There is a corresponding band for $(^{12}C^{18}O_2)_{10}$ centered at 2326.109 cm^{-1}, but its P and R structure are barely evident so we cannot confirm the assignment. This would represent a shift of +12.06 cm^{-1} from the monomer origin, as compared to +12.01 and -5.09 cm^{-1} for the 2361.15 and 2344.08 cm^{-1} bands of the normal isotopologue. The two lowest energy predicted isomers of $(CO_2)_{10}$ are both oblate asymmetric tops with similar rotational constants. The main difference is in A which is smaller for isomer 10a (see Table 6.1). Both are in satisfactory agreement with experiment, but the predicted A value for isomer 10a is closer. The resonant dipole model predicts the strongest band for both isomers to be the most blueshifted one and to be predominantly *c*-type. Isomer 10a, with a predicted shift of +10.43 cm^{-1}, agrees better with experiment. Agreement is not so good for the observed redshifted band at 2344.08 cm^{-1},

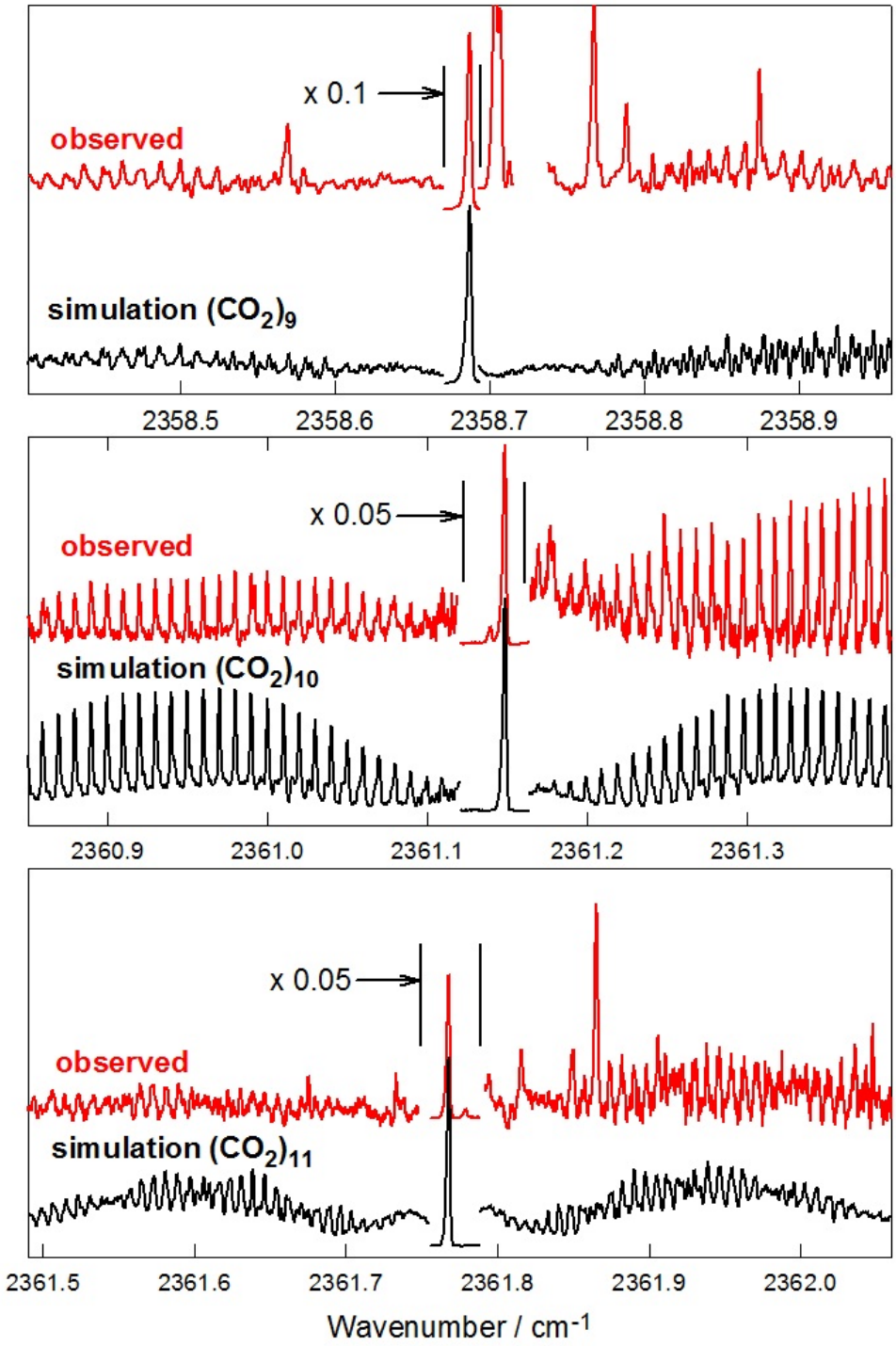

Figure 6.5: Observed and simulated CO_2 cluster spectra showing bands assigned to $(CO_2)_9$, $(CO_2)_{10}$, and $(CO_2)_{11}$. The signal in the regions around the strong central Q-branches are multiplied by a factor of 0.05 or 0.10 as indicated.

but the model does predict weaker c-type bands (not shown in Table 6.2) for isomer 10a with shifts of -6.57 and -7.75 cm^{-1}.

Table 6.6: Molecular parameters for $(CO_2)_9$, $(CO_2)_{10}$, $(CO_2)_{11}$, $(CO_2)_{12}$, and $(CO_2)_{13}$.

	$(CO_2)_9$[a]	$(CO_2)_{10}$[b]	$(CO_2)_{11}$[c]	$(CO_2)_{12}$[d]	$(CO_2)_{13}$[e]
ν_0/cm^{-1}	2358.6882	2361.1492 2344.0849	2361.769	2364.342	2367.7038 (I) 2368.0048 (II) 2345.0120 (III)
A''/MHz	207	155.40	136	109	-
B''/MHz	161	144.02	114	106	92.62
C''/MHz	125	111	97	93	90

[a] Centrifugal distortion parameters were fixed to zero. $A' - A'' = +0.40$,$B' - B'' =$ -0.12, $C' - C'' =$ -0.15 MHz.
[b] $A' - A'' =$ -0.08 or +0.02, $B' - B'' =$ -0.09 or +0.01, $C' - C'' =$ -0.04 or -0.07 MHz for band I or II, respectively.
[c] $A' - A'' =$ -0.06, $B' - B'' =$ -0.05, $C' - C'' =$ -0.04 MHz. The ratio of intensity components for the simulation was $(a : b : c) = (1.0 : 0 : 0.64)$. Individual rotational constants were only determined within about 5 MHz, but $(A + B)/2$ should be good to ± 2 MHz.
[d] $A' - A'' =$ -0.11, $B' - B'' =$ -0.12, $C' - C'' =$ -0.12 MHz. The ratio of intensities for the simulation was $(a : b : c) = (1.0 : 0.90 : 0.05)$.
[e] $B' - B'' =$ -0.08 or -0.07 or 0.00, and $C' - C'' =$ -0.06 or -0.04 or -0.04 MHz for band I or band II or band III, respectively. The intensity ratio for the simulation was 0.9:1.0 for band I:band II.

6.2.6 The carbon dioxide hendecamer $(CO_2)_{11}$ and dodecamer $(CO_2)_{12}$.

An even stronger Q-branch appears at 2361.77 cm^{-1}, just 0.6 cm^{-1} above that assigned to $(CO_2)_{10}$. It is accompanied by rather indistinct P- and R-branch structure whose spacing corresponds to an effective B-value of about 125 MHz, somewhat less than that of $(CO_2)_{10}$ which was about 150 MHz. This appears to be a parallel (a- and/or c-type) band of an asymmetric rotor which is heavier and more asymmetric than $(CO_2)_{10}$. Our best simulation, shown in the bottom panel of Fig. 6.5 together with the observed spectrum, reproduces the essential features of the band, but is less satisfactory as those of $(CO_2)_6$, $(CO_2)_7$, and $(CO_2)_{10}$. The main problem is the fuzzy character of the observed P and R structure, which means there is not much obvious information content. The rotational constants in

the simulation agree well with the predicted values for $(CO_2)_{11}$ (Tables 6.1 and 6.6). The simulation combines c- and a-type transitions with an intensity ratio of $c : a$ = 1:0.8, and its best determined aspect is the combination $(A + B)/2$ =125 MHz. There is a possible candidate for $(^{12}C^{18}O_2)_{11}$ centered at 2326.753 cm^{-1}, but its P and R structures are not clear. This would represent a shift of +12.70 cm^{-1} from the monomer origin, as compared to +12.63 cm^{-1} for the normal isotope. The predicted structure of $(CO_2)_{11}$ is unsymmetric, and the resonant dipole model predicts its second strongest band to be predominantly c-type with a shift of +10.39 cm^{-1}. This sounds good, but this predicted band also has significant b-type, and no a-type, character, in poor agreement with the observed band.

A strong and interesting feature which we assign as the Q-branch of $(CO_2)_{12}$ appears at 2364.34 cm^{-1}, as illustrated in Fig. 6.6 for two different experimental conditions. It is surrounded by periodic structure with a spacing corresponding to an effective B-value around 100 MHz. A simulation which is excellent for the Q-branch and reasonable for the rest of the band (see Fig. 3 of Ref. [28]) was achieved using a combination of a-, b- and c-type transitions of a nearly spherical asymmetric rotor with parameters as listed here in Table 6.6. These agree very well with those predicted for $(CO_2)_{12}$, whose structure is again unsymmetric (see Fig. 6.2). The resonant dipole model predicts (Table 6.2) the second strongest band of this cluster to be strongly blueshifted (+12.14 cm^{-1}), in reasonable accord with the observed value, +15.20 cm^{-1}. The predicted intensity ratio is $a : b : c$ = 1.00:0.83:0.08 as compared to that used in the simulation, $a : b : c$ = 1.00:0.95:0.22.

6.2.7 The carbon dioxide tridecamer (or triskaidecamer), $(CO_2)_{13}$

The remarkable symmetric structure of $(CO_2)_{13}$ shown in Fig. 6.2 has been predicted in many calculations [1,125–127]. This is calculated to the most stable isomer by over 400 cm^{-1} using the M-O-M potential, and there can be little doubt that it is the "true" $(CO_2)_{13}$ structure. There is a single CO_2 monomer at the center of mass aligned along the cluster c-axis, which is an S_6 rotation-reflection axis. This is surrounded by a cage of 12 monomers whose C atoms

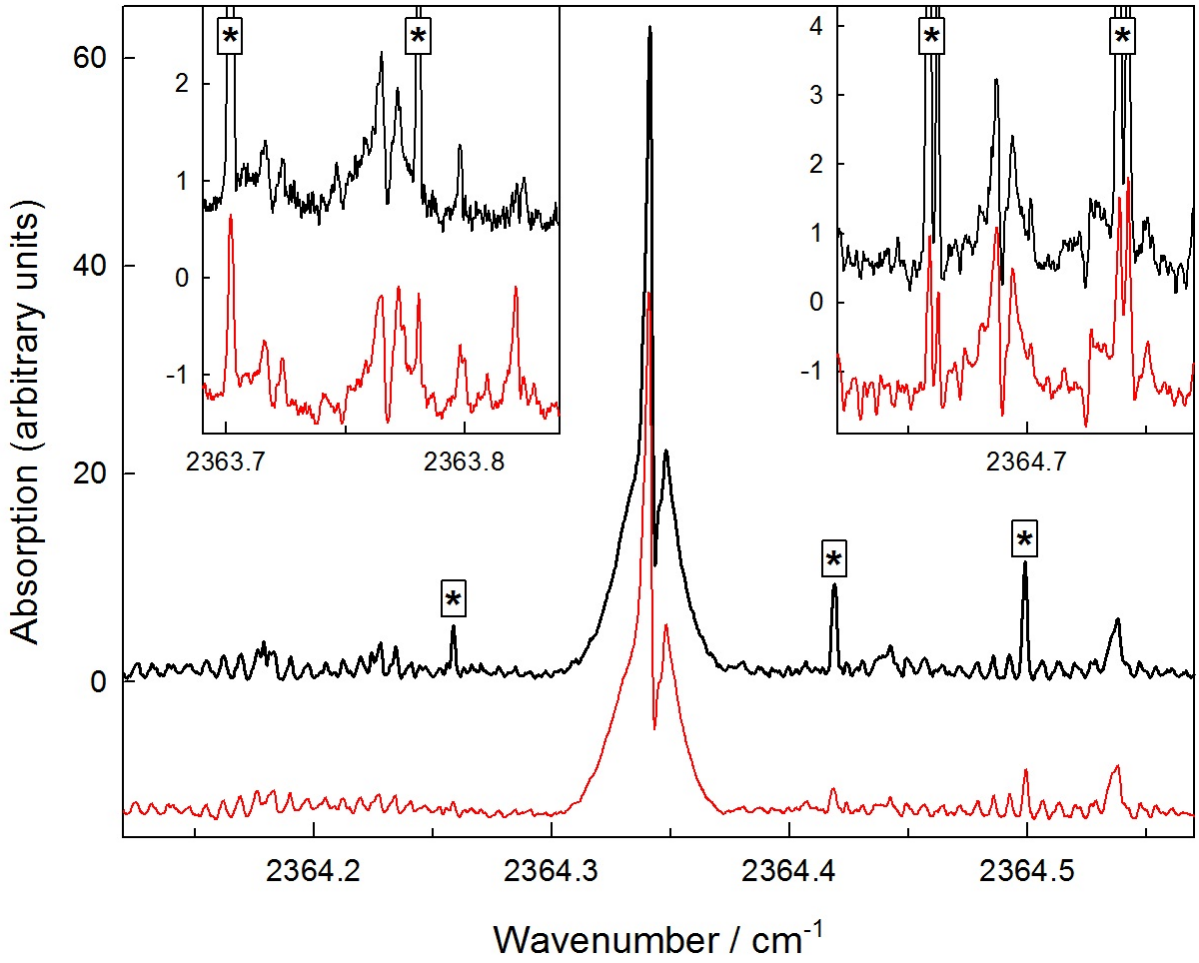

Figure 6.6: Observed spectra of the band assigned to $(CO_2)_{12}$. The lower (red) trace has a larger fraction of CO_2 in the expansion gas mix. Asterisks indicate known lines due to $(CO_2)_3$ (Ref. [2]) The insets show weak features (2363.77, 2364.69 cm^{-1}) that appear to mimic the strong $(CO_2)_{12}$ Q-branch at 2364.34 cm^{-1} (see text).

lie at the vertices of a slightly distorted icosahedron. There are two sets of six equivalent CO_2 monomers in the cage. The first ("equatorial") set forms a puckered ring located close to the "equatorial" plane (the plane perpendicular to the c-axis passing through the center of mass). Three of the C atoms are slightly "above" the plane, and the alternating three are "below" the plane. The second ("polar") set of six equivalent monomers consists of two separated rings of three located above and below the equatorial plane.

The fundamental $(CO_2)_{13}$ vibrations in the CO_2 ν_3 region can be visualized as follows. One A_u mode is associated with the central monomer, and gives rise to an infrared-allowed

parallel band. Two further A_u modes (one for each equivalent set of 6) have the "upper" three monomers in-phase with each other, the "lower" three also mutually in-phase, but with upper and lower sets are out-of-phase. Two infrared-forbidden A_g modes are associated with the in-phase vibrations of the two sets of six equivalent monomers. The remaining modes are degenerate ones, two with E_g symmetry and two with E_u symmetry. Each group of three monomers has a degenerate mode (like that of the cyclic CO_2 trimer) [99], which can either be in-phase or out-of-phase with the mirror-image group of 3, giving the total of 4 doubly degenerate modes. In reality, modes of a given symmetry are mixed and not pure as implied by these descriptions. For the resonant dipole model, the eigenvectors show that the most redshifted A_u mode (-10.98 cm^{-1}) tends to be associated with the central monomer vibration, while the middle one (-1.16 cm^{-1}) is associated with the "polar" monomers, and the blueshifted one (+14.64 cm^{-1}) with the central and "equatorial" ones. For E_u symmetry, the redshifted mode (-6.15 cm^{-1}) is more equatorial in character and the blueshifted one (+5.47 cm^{-1}) more polar, whereas the reverse is true for the E_g modes. The A_g modes are a fairly even mixtures of equatorial and polar.

Two neighboring bands near 2368 cm^{-1} with very strong Q-branches and clear P- and R-branches can be well simulated (see Fig. 3 of Ref. [28]) as symmetric top parallel bands arising from a common ground state with a rotational constant very close to that predicted for $(CO_2)_{13}$. Assignment of these bands to $(CO_2)_{13}$ is supported by the fact that true symmetric tops are rare among predicted CO_2 clusters in this size range. The slight difference between the observed (92.62 MHz) and predicted (e.g. 94.8 MHz, Table 6.1) B'' values is consistent with the other clusters observed here - the observed rotational constants are almost always 1% - 4% smaller than the predicted values (Table 6.1). This is at least partly explained by the effects of zero-point vibration (equilibrium bonds are shorter than zero-point bonds). We have now found another weaker but otherwise similar band at 2345.0 cm^{-1} whose fitted B'' value is the same to within less than 0.1 MHz, and conclude that it is also due to $(CO_2)_{13}$.

The parameters used to simulate the bands are summarized in Table 6.6.

Since the predicted $(CO_2)_{13}$ structure is very close to being an "accidental" spherical top ($B \approx C$), it is possible that one or more of the three observed bands could be perpendicular, rather than parallel, since this distinction vanishes at the spherical limit. Testing this possibility, we found that it could be valid as long as $(B - C)$ is less than about 1 MHz (rather than 1.7 MHz as predicted), and also found that the resulting B'' and C''-values (≈92.5 and 93.5 MHz) were then slightly closer to the theoretical ones. However, these simulations did not fit the experiment quite so well.

The resonant dipole model predicts a fairly strong blueshifted (+14.64 cm^{-1}) parallel band for $(CO_2)_{13}$, but we observe two such bands (+18.56 and +18.86 cm^{-1}) of almost equal strength. Of course we already know that the model is not especially reliable. But it still seems unlikely to have two fundamentals with such large shifts so close together. A possible explanation is that the two arise from an accidental Fermi-type resonance between a single "bright" blueshifted fundamental and a "dark" combination band which is the sum of one of the other fundamentals (perhaps a redshifted one) plus a low-frequency (≈20 cm^{-1}) intermolecular mode. This would help to explain the very similar appearance of these two bands. The red-shifted (-4.13 cm^{-1}) band at 2345.0 cm^{-1} could then be one of the remaining A_u (or possibly E_u) fundamentals.

Support for the combination band explanation is offered by fact that combination bands are observed [2, 17] for the somewhat similar $(CO_2)_3$ and $(CO_2)_6$ clusters, as noted above. Moreover, there appear to be weak "replicas" of the distinctive $(CO_2)_{12}$ Q-branch located nearby at 2363.77, 2364.69, and 2365.00 cm^{-1} (see the insets in Fig. 6.6). These could well be weak "background" combination bands which acquire some intensity from the main fundamental at 2364.34 cm^{-1}. We also observe unexplained features near the $(CO_2)_7$, $(CO_2)_9$, $(CO_2)_{10}$, and $(CO_2)_{11}$ bands which could be Q-branches of background combination bands of these clusters (see Figs. 6.4 and 6.5).

6.3 Discussion

6.3.1 Validity of the assignments

The experimental rotational constants determined here generally agree very well with calculations based on the M-O-M (Refs. [114] and [29] and SAPT-s(Ref. [107] potentials (see Table 6.1), though we have to keep in mind that this agreement formed the basis of the assignments in the first place. As already noted, most of the experimental A, B, and C values are a bit smaller than the theoretical ones, a difference which can be ascribed in part to the effects of anharmonicity and zero-point motion which tend to make actual ground state bonds longer than equilibrium ones (and hence make rotational constants smaller). But agreement between experiment and theory does not necessarily mean that all the calculated structures are exactly correct since, for a given cluster, there may a number of isomers which are similar in energy and which have similar rotational constants (such as isomers 10a and 10b).

Of the eight CO_2 clusters discussed in the previous section, the assignments for $(CO_2)_7$ and the two isomers of $(CO_2)_6$ are probably the most secure and those for $(CO_2)_9$ and $(CO_2)_{11}$ the least secure. It is natural that assignments become less certain as cluster size increases because the rotational structure becomes more difficult to fully resolve and also because the difference between predicted rotational parameters for successive clusters becomes smaller. What is certain is that we have made a series of specific and detailed assignments, which can be directly tested by future calculations and experiments. The regularity of vibrational shifts discussed in the following subsection provides further support, especially since it was not a criterion in the original assignments.

6.3.2 Vibrational shifts

A striking feature of the assigned CO_2 cluster bands is that they show a regularly increasing blueshift with cluster size, except for the $(CO_2)_{10}$ and $(CO_2)_{13}$ bands near 2345 cm^{-1}. This is

illustrated in Fig. 6.7, which includes the known CO_2 monomer, dimer [13], and trimer [15,99] fundamental band origins. It has been speculated that a prominent Q-branch feature at 2352.60 cm^{-1} (labeled "Q_A") (Refs. [99], [15], and [17]) might be due to $(CO_2)_4$ and this point is also included in Fig. 6.7 with a question mark. From this plot, it appears that a band of $(CO_2)_8$ is expected near 2357.5 cm^{-1}, but we have not been able to investigate this range for $^{12}C^{16}O_2$ due to a gap in laser coverage. In the case of $^{12}C^{18}O_2$, there are sharp Q-branches at 2321.945, 2321.955, and 2321.964 cm^{-1} with relative peak heights of 1.0:0.7:0.3. One or more of these could be due to $(CO_2)_8$, but the accompanying P- and R-branches were not strong or structured enough to be analyzed. The strongest one represents a shift of +7.90 cm^{-1} which would put the corresponding band for the $^{12}C^{16}O_2$ tetramer at 2357.04 cm^{-1}, within the gap region. It also seems that a band of $(CO_2)_5$ should appear around 2353 cm^{-1}, and there are possible candidate Q-branches at 2353.26, 2353.45, and 2353.75 cm^{-1} (these are visible in Fig. 2(a) of Ref. [28]).

We observe one to three bands per cluster, but of course the larger clusters have many more allowed fundamental bands in the CO_2 ν_3 region. Fig. 6.7 seems to indicate that the bands we actually observe, which are presumably the stronger or strongest ones, tend to blueshift increasingly from about 2350 to 2370 cm^{-1} with a slope of about +1.5 cm^{-1} per added CO_2 going from CO_2 to $(CO_2)_{13}$. The tendency of the CO_2 ν_3 vibration to blueshift for medium or large clusters is already known from low-resolution studies [22, 106]. As we have seen it is also predicted by the resonant dipole model, though with a smaller magnitude than observed here (see Fig. 1 of Ref. [28]). It is important to recognize that bands of larger clusters which happen to lie close to the monomer band origin (2349.14 cm^{-1}) are inherently difficult to detect and recognize because of the presence of stronger bands of small clusters (dimer, trimer, etc.). So there is a selection effect favoring bands with larger shifts which occur in clear regions of the spectrum. Another selection effect is that symmetric clusters (and unsymmetric ones with rotational constants closer to the prolate or oblate limit) are

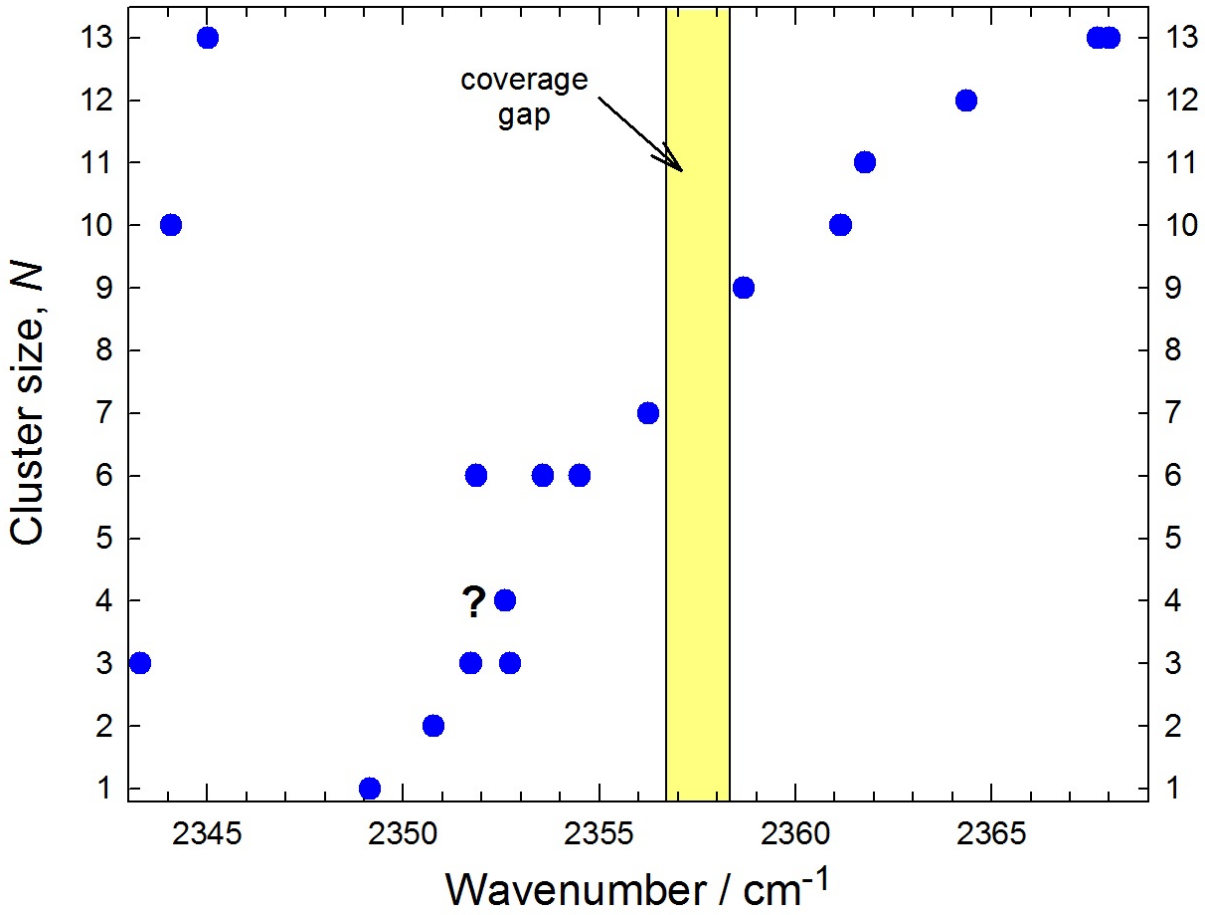

Figure 6.7: Observed band origins as a function of CO_2 cluster size.

more likely to be assigned because their spectra tend to be more easily recognized and stronger (less spread out).

6.3.3 Cluster structures

Acknowledging that the present results do not contain much structural information, we have not said much yet about the detailed cluster structures except for $(CO_2)_6$ and $(CO_2)_{13}$. However, since the results do support the general validity of the structures based on the M-O-M and SAPT-s potentials, it is interesting to examine their evolution in the size range from $N = 6$ to 13, focussing on the C atom positions rather than the individual monomer orientations.

The calculated structures are pictured in Fig. 6.8, proceeding from $(CO_2)_6$ in the upper

left corner to $(CO_2)_{13}$ in the lower right. Certain C-C bonds are added to help visualize the growth trends. The two symmetric isomers of $(CO_2)_6$ have already been described. $(CO_2)_7$ is approximately a pentagonal ring of CO_2 monomers with single monomers located "above" and "below" the (roughly) planar ring. This is more closely related to the S_4 isomer of $(CO_2)_6$ than to the lower energy S_6 isomer, since it can be formed by adding one more CO_2 to the ring of four equivalent monomers in the S_4 isomer. We can also think of $(CO_2)_7$ as being a shallow "cup" (formed by the pentagon and bottom monomers) holding a single "interior" CO_2 (the top monomer). From $N = 8$ to 12, a second pentagonal ring forms "above" the first one, steadily enclosing the interior monomer in a deeper cup. Finally, in $(CO_2)_{13}$ a top monomer is added to the cup and the interior monomer is completely enclosed. But a new symmetry emerges: rather than imagining $(CO_2)_{13}$ to be approximately composed of an interior monomer enclosed by two pentagonal rings plus top and bottom monomers (1-5-5-1 ring structure), we find that it is precisely composed of the interior monomer enclosed by a staggered ring of six equivalent monomers plus two equivalent rings of three monomers (3-6-3 ring structure), as described above in Section 6.2.7 and Fig. 6.2. This underlying 3-6-3 ring motif is sometimes evident in for clusters in the $N = 8$ - 12 range.

6.4 Conclusions

The predicted structures and resulting rotational constants for carbon dioxide clusters in the range $N = 5$ - 13 calculated assuming pairwise additivity show good agreement using two intermolecular potential functions obtained from very different sources, M-O-M (Refs. [114] and [29]) and SAPT-s [107]. With the help of these predictions, we assign 13 specific infrared bands in the CO_2 ν_3 fundamental region ($\approx$2350 cm^{-1}) to clusters with $N = 6$, 7, 9, 10, 11, 12, and 13. Three of these bands are also observed for $^{12}C^{18}O_2$ clusters. The clusters are produced in a pulsed supersonic expansion using a slit jet source and the spectra are recorded by direct absorption using a tuneable diode laser probe. Two isomers are observed for $(CO_2)_6$,

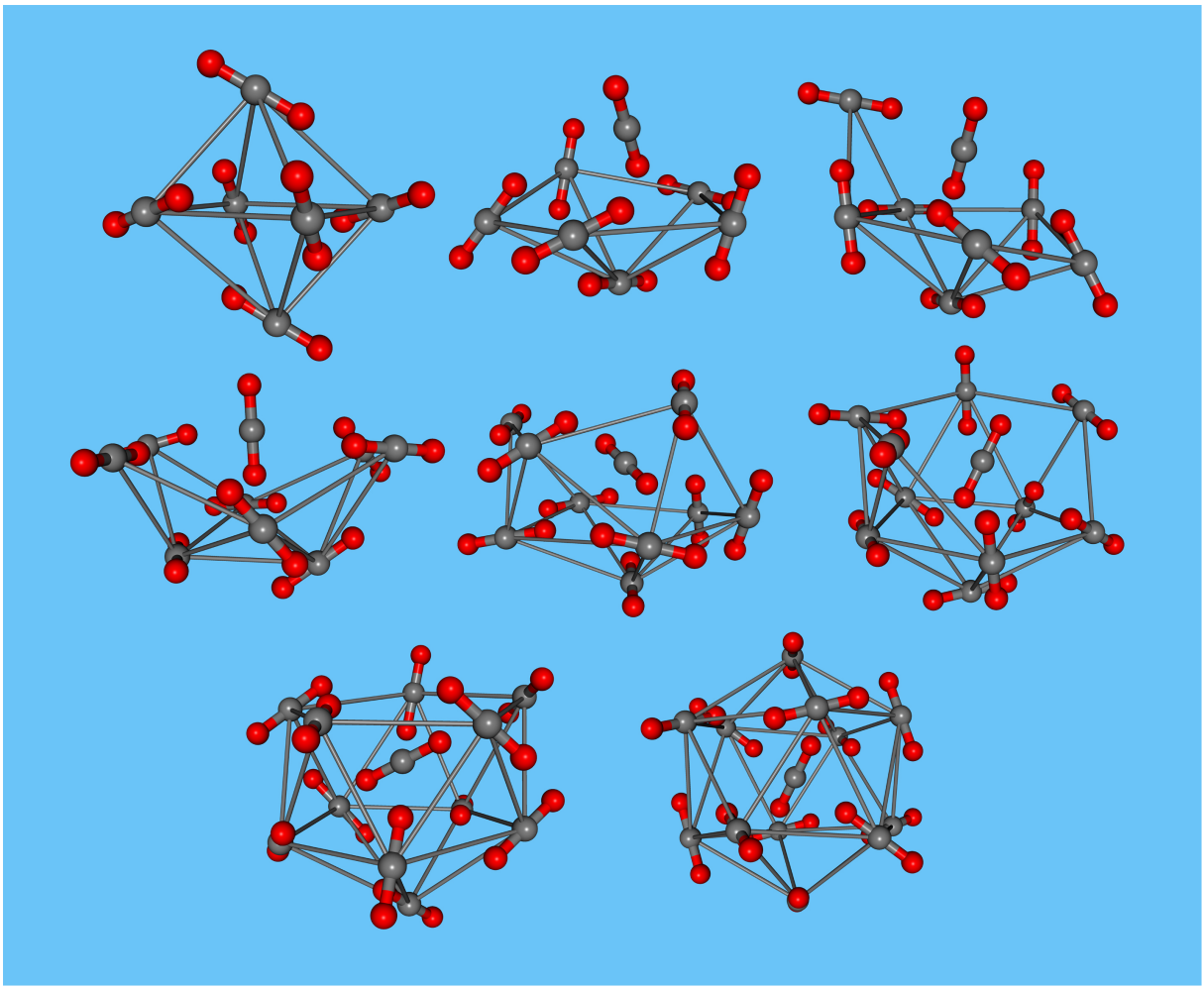

Figure 6.8: Calculated structures of $(CO_2)_N$ clusters from $N = 6$ (upper left) to 13 (lower right). Thin grey nearest-neighbor C-C bonds are added to illustrate cluster growth trends.

both of which are oblate symmetric tops. The lowest energy form has S_6 symmetry and the other has S_4 symmetry. $(CO_2)_{13}$ is also an S_6 oblate symmetric top, but the remaining clusters are asymmetric tops with no symmetry elements (C_1 point group). The effective rotational constants obtained by fitting or simulating the observed bands are generally 1% - 4% smaller than the equilibrium constants predicted by the intermolecular potentials, an effect which is at least partly due to zero point motion. The stronger observed bands show a progressive vibrational blueshift with increasing cluster size. Such shifts are similar to, but significantly larger in magnitude than, those predicted by the resonant dipole-dipole interaction model. These are the largest such molecular clusters to be assigned to specific infrared

bands with at least partial rotational resolution. The results provide precise benchmarks for future theoretical calculations. They should also enable the growth of different sized clusters to be monitored dynamically in various supersonic jet (and other) environments. As well, the sharp and strong nature of most of the observed Q-branches may facilitate new experiments in which energy could be selectively deposited into clusters of a particular size using a tuneable pump laser.

Acknowledgements We thank L. Murdock for technical assistance. Many of our results were greatly facilitated by use of PGOPHER, and we are pleased to acknowledge C.M. Western for helpful advice and program updates. We gratefully acknowledge the financial support of the Natural Sciences and Engineering Research Council of Canada.

Chapter 7

Nitrous oxide tetramer has two highly symmetric isomers

Journal of Chemical Physics **134**, 074310 (2011)

J. Norooz Oliaee, M. Dehghany, N. Moazzen-Ahmadi[1]

Department of Physics and Astronomy, University of Calgary, 2500 University Drive North West, Calgary, Alberta T2N 1N4, Canada

and

A.R.W. McKellar[2]

Steacie Institute for Molecular Sciences, National Research Council of Canada, Ottawa, Ontario K1A 0R6, Canada

Received 15 December 2010; Accepted 27 January 2011; Published online 17 February 2011

Abstract

Infrared spectra of the nitrous oxide tetramer, $(N_2O)_4$, are studied in the region of the N_2O ν_1 fundamental band ($\sim$ 2200 cm^{-1}). The spectra are observed using a tunable diode laser to probe a pulsed supersonic jet expansion. Parallel ($\Delta K = 0$) bands are observed for the previously observed isomer of $(N_2O)_4$, which is confirmed by isotopic substitution to have an oblate symmetric rotor structure with D_{2d} symmetry. A distinct new isomer of $(N_2O)_4$ is observed by means of a perpendicular ($\Delta K = \pm 1$) band. It has a prolate symmetric rotor structure with S_4 symmetry. These isomers represent two distinct, but almost equally favorable, ways of bringing together a pair of nonpolar N_2O dimers to form a tetramer. It is not clear at present which one represents the true ground state.

[1]Author to whom correspondence should be addressed. Electronic mail: ahmadi@phas.ucalgary.ca
[2]Electronic mail: robert.mckellar@nrc-cnrc.gc.ca

7.1 Introduction

In 1997, Miller and Pedersen [12] observed an infrared band in the N_2O monomer $\nu_1 + \nu_3$ region ($\sim$ 3500 cm^{-1}) which they assigned to the nitrous oxide tetramer. This band resembled that of a symmetric rotor molecule with parallel ($\Delta K = 0$) selection rules. As usual for such a band, the B rotational constant was well-determined (0.0248 cm^{-1}), but C could only be approximately estimated ($\sim$ 0.02 cm^{-1}). Combining this result with *ab initio* calculations, they concluded that the tetramer had a sort of barrel-shaped structure in which the four N_2O monomer units were approximately parallel but with alternating orientations, as illustrated here in Fig. 7.1(a). This geometry, in which all monomer units are equivalent, has D_{2d} point group symmetry and yields a single allowed parallel band accompanying each monomer stretching vibration, as observed. In the present paper, we report observation of the same N_2O tetramer in the ν_1 fundamental band region ($\sim$ 2200 cm^{-1}). This includes the normal $(^{14}N_2^{16}O)_4$ species, as well as three isotopically-substituted forms, $(^{15}N_2^{16}O)_4$, $^{14}N_2^{16}O$–$(^{15}N_2^{16}O)_3$, and $(^{14}N_2^{16}O)_3$–$^{15}N_2^{16}O$, whose observation helps to better define the tetramer structure. We also report observation of a distinct new N_2O tetramer isomer which turns out to be a prolate symmetric rotor, in contrast to the original [12] isomer which is oblate. The new tetramer, illustrated in Fig. 7.1(b), may be formed by twisting the original one into a sort of cyclic sandwich shape with S_4 symmetry. These isomers represent two different ways to bring together a pair of nonpolar N_2O dimers in order to form tetramers with very similar binding energies (see below).

Nitrous oxide dimers and trimers have been studied extensively. The most stable form of $(N_2O)_2$ was the first to be observed: it is nonpolar, with a planar slipped-antiparallel structure [30, 33, 35, 36, 60, 80, 81, 128]. Recently a higher-energy polar isomer was detected; it is also planar, but with a slipped-parallel structure [32, 59, 60]. The trimer, whose unsymmetric structure may be roughly described as a nonpolar dimer with a third N_2O sitting "on top", was originally observed by Miller and Pedersen [31] and has been more recently studied by

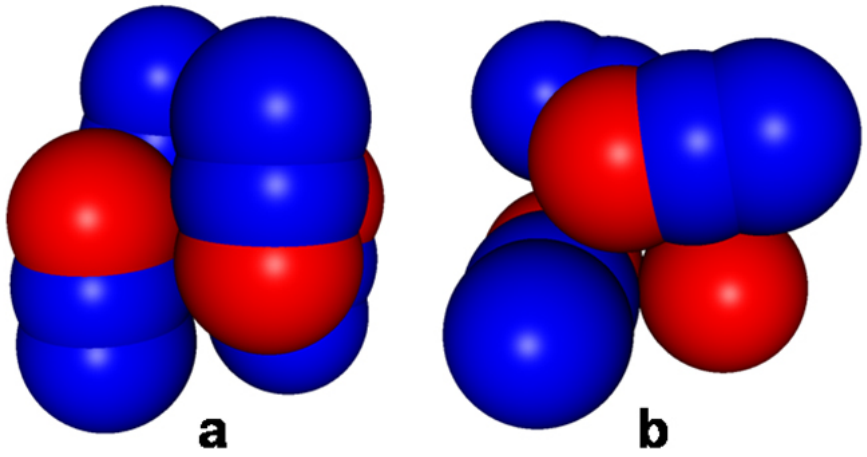

Figure 7.1: Illustration of the structures of the oblate (a) and prolate (b) isomers of the N_2O tetramer, corresponding to the point groups D_{2d} and S_4, respectively.

our group [37, 38].

7.2 Observations and Analysis

The spectra were recorded by direct infrared absorption in a pulsed supersonic expansion of a dilute N_2O+He gas mixture from a slit-jet source, as described previously [33, 37, 60]. Under these experimental conditions, the dimer, trimer, and tetramer all appear in the same spectra, but larger clusters can be favored by using a slightly higher concentration of N_2O in the expansion gas. The wavenumber scale for the rapid-scan tunable diode laser probe was established by simultaneously recording spectra from reference gas and etalon channels. The enriched $^{15}N_2O$ sample was obtained from Icon Isotopes and had an isotopic purity of 99%. Bands were assigned and analyzed with the aid of the PGOPHER computer program [58].

7.2.1 Observation of the oblate N_2O tetramer

We observed a band centered at 2237.43 cm^{-1} whose appearance was very similar to the N_2O tetramer band observed at 3473.21 cm^{-1} by Miller and Pedersen [12]. Molecular parameters arising from a fit to the band are listed in Table 7.1, and a simulation based on these parameters is shown in Fig. 7.2 along with the observed spectrum. This is a simple parallel

($\Delta K = 0$) band with relatively little change in rotational constants between the upper and lower states, so the underlying K-structure in the central Q-branch and the individual P- and R-branch lines is not resolved. Our ground state rotational constant, $B'' = 0.02512$ cm^{-1}, is slightly different from the earlier value [12] of 0.0248 cm^{-1}, but it is still clear that these bands arise from the same N_2O tetramer species. Since the present observed linewidth (<0.002 cm^{-1}) is considerably smaller than those in Ref. [12] (≈0.010 cm^{-1}), our value is likely to be more accurate. But the quoted statistical errors in Table 7.1 probably underestimate the true uncertainties since the spectrum was still only partly resolved. The analogous band for $(^{15}N_2^{16}O)_4$ was observed around 2167.9 cm^{-1} with results that are also shown in Fig. 7.2 and Table 7.1. The ground state rotational constants C'' in Table 7.1 are fixed at estimated values since by their nature these parallel bands are not sensitive to this parameter. One way to make this estimate is from the relative intensity of the Q-branch, as was done in Ref. [12]. However, in our case this could not be done very reliably because of the variation of laser power and other experimental parameters. Instead we estimated C'' based on the mixed-isotope results described in the following paragraphs.

Table 7.1: Molecular parameters for oblate symmetric rotor N_2O tetramers (values in cm^{-1}).

	$(^{14}N_2^{16}O)_4$	$(^{15}N_2^{16}O)_4$
ν_0	2237.4258(1)[a]	2167.8945(1)
B'	0.0250865(7)	0.0237629(9)
C'	0.023[b]	0.022[b]
D'_J	$1.23(4)\times10^{-7}$	$0.49(3)\times10^{-7}$
B''	0.0251256(8)	0.0237986(11)[a]
C''	0.023[b]	0.022[b]
D''_J	$1.17(3)\times10^{-7}$	$0.34(4)\times10^{-7}$

[a] Uncertainties in parentheses are 1σ expressed in units of the last quoted digit.
[b] $(C' - C'') = -0.00002$ cm^{-1} (manually fitted to high-J R-branch line shapes).

Using mixtures of normal $^{14}N_2^{16}O$ and enriched $^{15}N_2^{16}O$, we observed three new oblate tetramer bands. The clearest of these, located in the $^{15}N_2^{16}O$ region around 2164.15 cm^{-1}, is illustrated in Fig. 7.3. This band exhibits partially-resolved K-structure, and we could

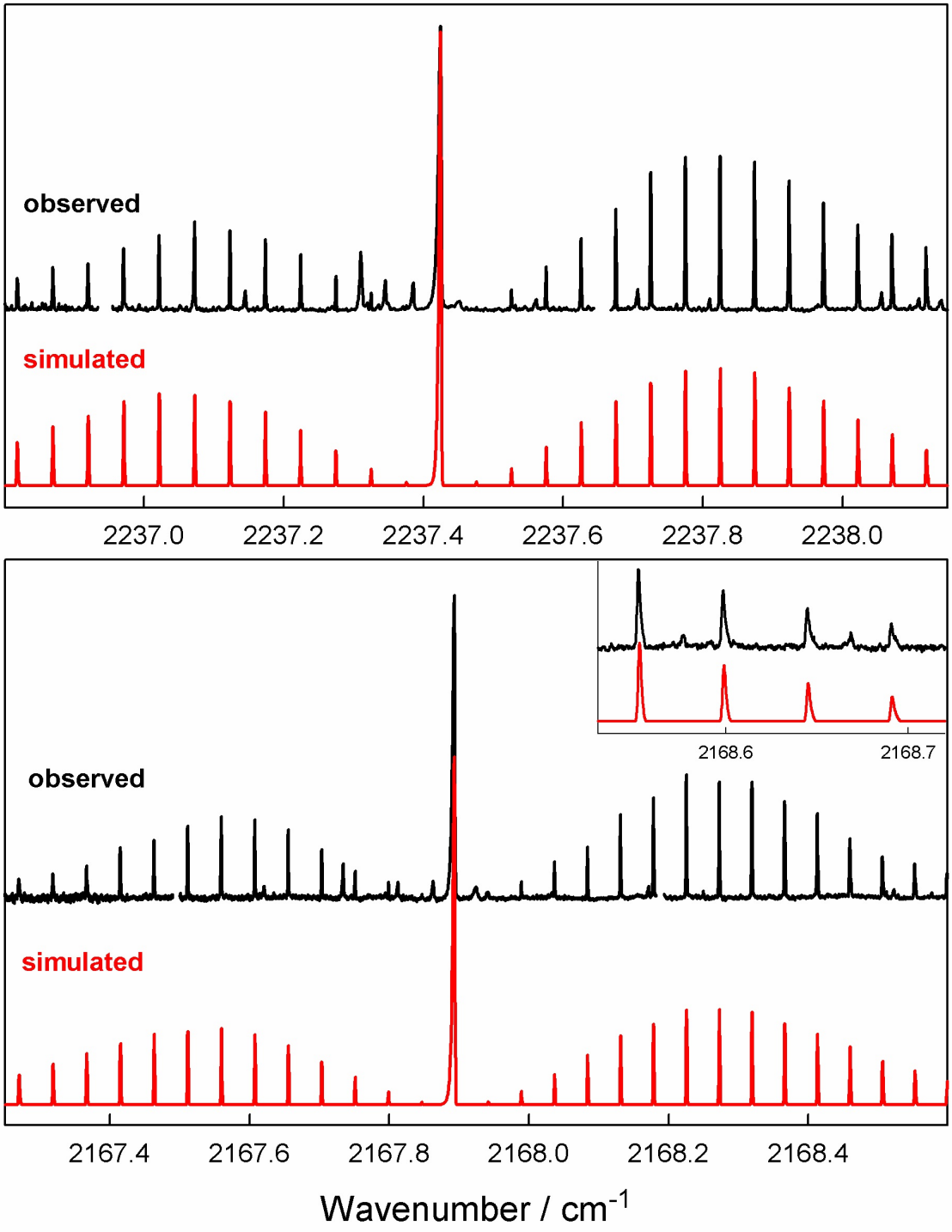

Figure 7.2: Parallel bands observed for the oblate isomer of the N_2O tetramer. Top panel: $(^{14}N_2^{16}O)_4$; bottom panel: $(^{15}N_2^{16}O)_4$. Simulations assume the parameters of Table 7.1 with a rotational temperature of 2.2 K and a Gaussian line width of 0.0016 cm^{-1}. The inset shows that the observed blue shading of higher-J R-branch lines is well reproduced by the simulated spectrum.

obtain an excellent fit assuming this was a c-type band of an asymmetric rotor with rotational parameters as given in Table 7.2. These parameters are consistent with those expected for a tetramer isotopologue containing one normal and three substituted monomers, namely $(^{14}N_2^{16}O)-(^{15}N_2^{16}O)_3$. The important result here is the reasonably precise determination of the C rotational constant, confirming that this form of $(N_2O)_4$ is indeed oblate, with $A \approx B > C$.

Table 7.2: Molecular parameters for asymmetric isotopically-substituted oblate N_2O tetramers (values in cm^{-1}).

	$(^{14}N_2^{16}O)-(^{15}N_2^{16}O)_3$	$(^{14}N_2^{16}O)_3-(^{15}N_2^{16}O)$	
ν_0	2164.1455(1)[a]	2234.5142(1)	2234.7312(1)
A'	0.024259(12)	0.0248098(50)	0.0250261(43)
B'	0.023921(13)	0.0244830(66)	0.0242452(49)
C'	0.02255(17)	0.0229203(81)	0.0227673(21)
A''	0.024240(14)	0.0249297(46)	
B''	0.023993(15)	0.0246735(56)	
C''	0.02256(17)	0.023 [b]	

[a] Uncertainties in parentheses are 1σ expressed in units of the last quoted digit.
[b] The ground C-value was fixed at this estimated value.

The other two mixed tetramer bands were located in the $^{14}N_2^{16}O$ region around 2234.6 cm^{-1}, as illustrated in Fig. 7.4. Their analysis was not so satisfactory, in part because of congestion due to their overlap but also because perturbations appeared to be present, particularly in the higher frequency band. We obtained a reasonable, but not perfect, simulation (see Fig. 7.4) assuming that these bands arise from a common lower state. The parameters are listed in Table 7.2, but we caution that their worth may be limited since the simulation was not completely convincing, particularly for higher-J transitions. Note that the higher frequency band centered at 2234.73 cm^{-1} involves large changes in rotational parameters (especially B) between the ground and excited state, which tends to support the idea that the upper state is perturbed. The ground state parameters obtained for these bands are appropriate for the tetramer isotopologue $(^{14}N_2^{16}O)_3-(^{15}N_2^{16}O)$. The simulations are distinctly worse if we use parameters appropriate for $(^{14}N_2^{16}O)_2-(^{15}N_2^{16}O)_2$ or $(^{14}N_2^{16}O)-(^{15}N_2^{16}O)_3$. The fact

that the vibrational shifts of these bands relative to the respective N_2O monomer (+10.76 and +10.97 cm^{-1}) are roughly similar to that of the securely assigned $(^{14}N_2^{16}O)-(^{15}N_2^{16}O)_3$ band in the preceding paragraph (+9.70 cm^{-1}) also supports the assignment of at least one of them to $(^{14}N_2^{16}O)_3-(^{15}N_2^{16}O)$. Vibrational assignment of these bands is discussed further in the following section.

7.2.2 Structure and vibrational effects for the oblate N_2O tetramer

The structure shown for the oblate tetramer in Fig. 7.1(a) has D_{2d} point group symmetry, with all four N_2O monomers equivalent. Diagonally opposite monomers are coplanar, and the four monomer axes may be parallel but more generally they can be symmetrically tilted and still maintain D_{2d} symmetry. This is essentially the structure obtained by Miller and Pedersen [12] in SCF and MP2 *ab initio* calculations, and it is consistent with their and our experimental results. We have checked tetramer structures using the empirical N_2O pair potential of Kuchta *et al.* [129] and the recent high-level *ab initio* pair potential of Dawes *et al.* [130] (assuming pairwise additivity), and found that they also yield an energy minimum with a similar D_{2d} structure.

Table 7.3 shows the result of a fit to the structure of the oblate tetramer based on the experimental rotational parameters from Tables 7.1 and 7.2. This fit assumes D_{2d} symmetry, as well as the monomer structure remaining unchanged in the tetramer, and the tetramer structure remaining unchanged with isotopic substitution. Because of these assumptions, the statistical errors given in Table 7.3 underestimate the true parameter uncertainties. Theoretical structures from the empirical [129] and *ab initio* [130] pair potentials are also given in Table 7.3. They are both quite close to the experimental one, with the former being a bit too large and the latter too small. The tilt angle is not well determined experimentally, but it is pleasing to note that its positive value (corresponding to an outward tilt of the O-atom ends of the N_2O monomers) agrees with the theoretical structures.

Note that it is possible to symmetrically "twist" the monomers in such a way that they

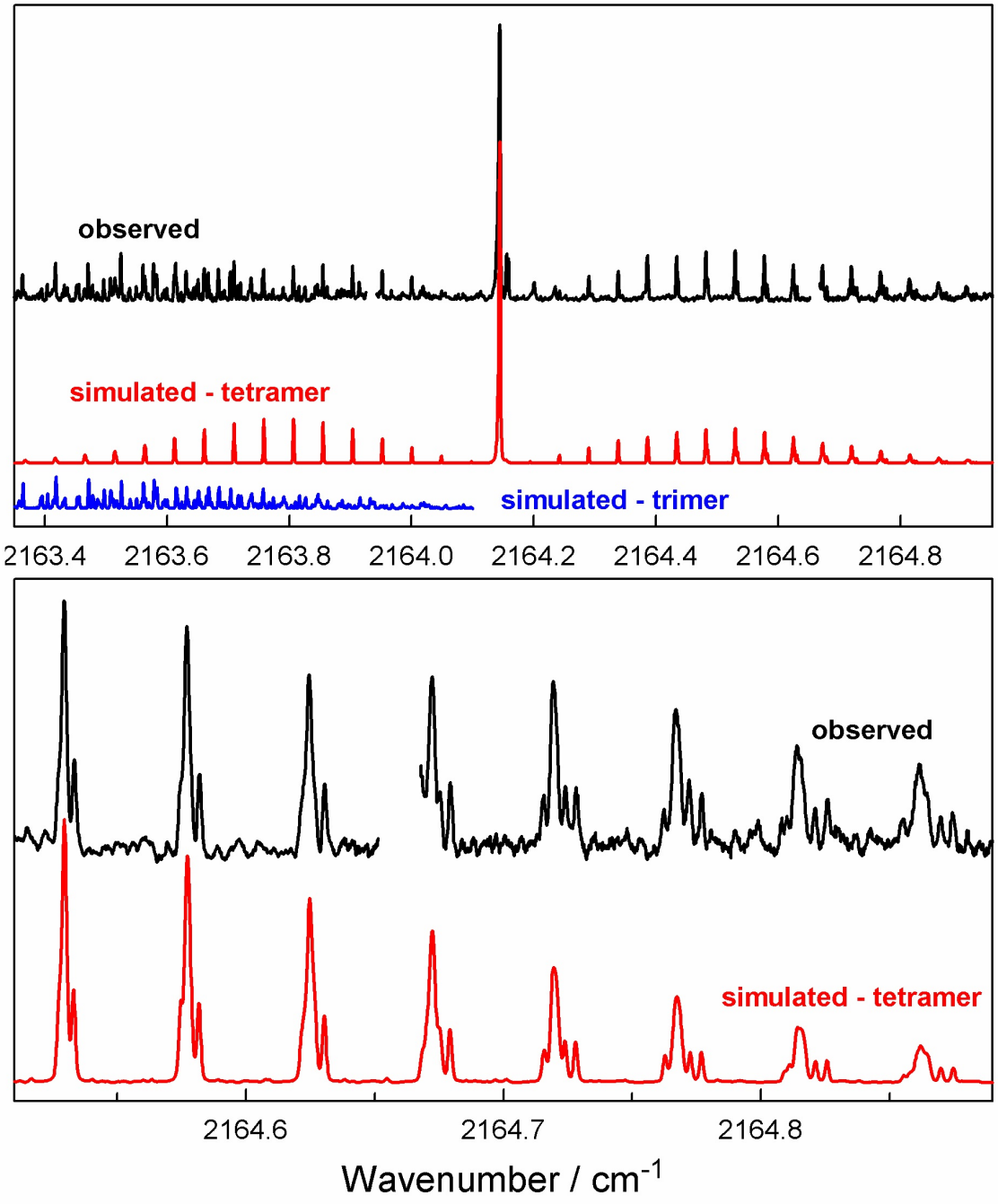

Figure 7.3: Band assigned to the isotopically-substituted oblate N_2O tetramer $(^{14}N_2^{16}O)$-$(^{15}N_2^{16}O)_3$.

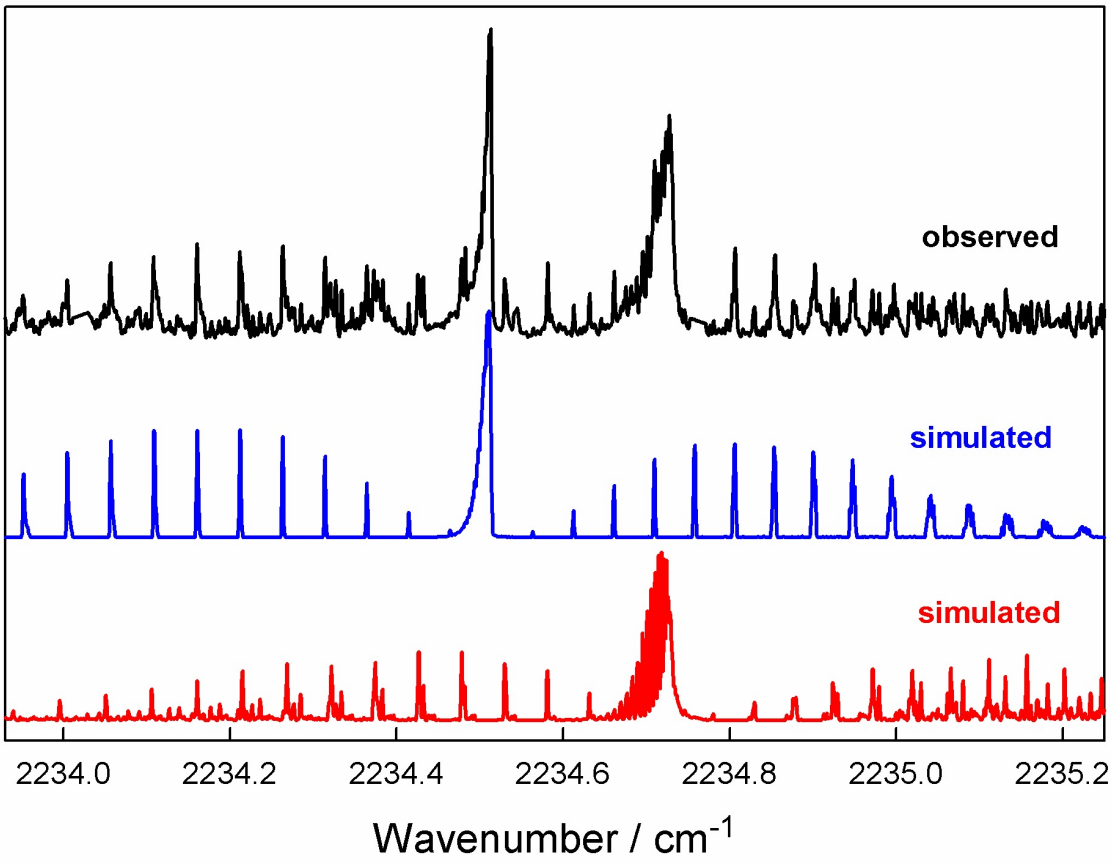

Figure 7.4: Two overlapping bands assigned to the isotopically-substituted oblate N_2O tetramer $(^{14}N_2^{16}O)_3$–$(^{15}N_2^{16}O)$.

remain equivalent, but diagonally opposite monomers are no longer coplanar. In this case, the tetramer loses D_{2d} symmetry but retains a four-fold rotation-reflection axis (S_4 point group). Small amounts of twist have relatively little effect on the rotational parameters; so a slightly twisted structure cannot be ruled out solely on the basis of experiment, but the empirical and *ab intio* results favor D_{2d}. Large amounts of twist lead to the distinct prolate isomer discussed in Section 7.2.3.

Vibrational shifts of cluster bands can be discussed in terms of a resonant/non-resonant model [17, 99, 131]. The initially degenerate (unperturbed) vibrational frequencies of the monomers in the cluster are shifted and split by interactions with the other monomers. The interactions can be resonant (off-diagonal) or non-resonant (diagonal). The well-known resonant dipole-dipole interaction plays an important role in the off-diagonal term, but other

Table 7.3: Structural parameters for the oblate N_2O tetramer.

Parameter[a]	Experiment (present work)	Empirical Potential (Ref. [129])	High-level *ab initio* potential (Ref. [130])
D	4.051(3)[b] Å	4.170 Å	4.012 Å
S	1.848(9) Å	1.810 Å	1.777 Å
θ	5(3)°	9.8°	4.4°
$R_1(N-N)$	4.039 Å	4.145 Å	4.001 Å
$R_2(N-N)$	3.481 Å	3.522 Å	3.420 Å

[a] D is the "diameter" of the tetramer (separation of centers of mass of diagonally opposite monomers). S is the "slip distance" (the separation between the centers of mass of one diagonally opposite monomer pair and the other diagonally opposite pair). θ is the "tilt angle" (the angle between a monomer axis and the tetramer symmetry axis), with the positive value indicating that the O atoms are tilted outwards. R_1 and R_2 are derived (not independent parameters): R_1 is inner N-N distance for diagonally opposite monomers; R_2 is inner N-N distance for adjacent monomers.
[b] The quoted 1σ experimental errors underestimate the true uncertainties (see text).

effects may also contribute [122]. The model is most useful for symmetric clusters where many or all of the constituent monomers are equivalent. For the nonpolar N_2O dimer, the two monomers are equivalent and there are two parameters in the model: a non-resonant shift, α, and a resonant term, β. The four band origins observed for $(^{14}N_2^{16}O)_2$, $(^{15}N_2^{16}O)_2$ and $^{14}N_2^{16}O{-}^{15}N_2^{16}O$ in the ν_1 region [33,36] can be very well fitted with values of $\alpha = +2.54$ cm^{-1} and $\beta = -3.06$ cm^{-1}. For comparison, the somewhat similar CO_2 dimer gives $\alpha = 0.37$, $\beta = -2.0$ cm^{-1} [17].

In the case of the oblate N_2O tetramer, the model requires 3 parameters. There is a single non-resonant shift α, since each monomer experiences the same surrounding environment. There are two resonant terms, β_1 for the interaction between adjacent monomers and β_2 for that between diagonally-opposite monomers. We assume that α and β are isotopically independent except for a scaling factor proportional to the N_2O monomer ν_1 frequency (the scaling has little effect on the result). Since the relative orientation of adjacent monomers in the tetramer is similar to the nonpolar N_2O dimer, we can approximate β_1 as -3.06 cm^{-1} and solve for α and β_2 using the data of Tables 7.1 and 7.2. The result is $\alpha = +3.93$, and

$\beta_2 = +3.71$ cm^{-1}. This solution is entirely satisfactory except that it predicts only one band for $(^{14}N_2^{16}O)_3 - ^{15}N_2^{16}O$ around 2234.6 cm^{-1}, rather than the two which have been assigned (Table 7.2). The two other vibrations of $(^{14}N_2^{16}O)_3 - ^{15}N_2^{16}O$ in this region are predicted to lie about 10 cm^{-1} lower, a stronger one around 2224.8 cm^{-1} and a very weak one around 2224.0 cm^{-1}. There seems to be no reasonable set of values for α, β_1, and β_2 which would give two bands close to 2234.6 cm^{-1}.

What is the solution of this discrepancy - why do we observe two bands? While it is possible that the model is inadequate or the assignments incorrect, we believe that the most likely explanation is that one of the observed bands is not a fundamental, but rather a combination band which gains intensity from an "accidental" Fermi-type interaction with the "true" fundamental vibration. In other words, in zeroth order the true fundamental happens to nearly coincide with a combination vibration which is the sum of another fundamental (i.e. one of those at 2224-2225 cm^{-1}) plus an intermolecular mode (with a frequency of about 10 cm^{-1}). The coincidence must be nearly exact (in zeroth order) since the two bands have virtually the same intensity, implying that the Fermi-type interaction has a strength of about 0.2 cm^{-1}.

7.2.3 Observation of the prolate N_2O tetramer

Another band with a very different appearance may be assigned to the N_2O tetramer. It is illustrated in Fig. 7.5 for both $(^{14}N_2^{16}O)_4$ and $(^{15}N_2^{16}O)_4$ (the latter is somewhat clearer). This band is somewhat masked by absorption due to $(N_2O)_3$, but fortunately we have previously analyzed this trimer band in detail [37]. The appearance of the tetramer absorption corresponds to that of a perpendicular ($\Delta K = \pm 1$) band of a symmetric rotor molecule close to the spherical limit, characterized by a distinctive feature (around 2232.2 or 2162.7 cm^{-1}) which is due to the close coincidence of the perpendicular Q-branches. It can be fitted very well as a prolate symmetric rotor with the parameters listed in Table 7.4. In this analysis we assume negligible Coriolis coupling in the degenerate upper state, as appears to be ap-

propriate for the similar case [99] of $(CO_2)_3$. The quality of the fit is illustrated in Fig. 7.6 by a close-up of the R-branch region for $(^{15}N_2^{16}O)_4$. The simulations in Figs. 7.5 and 7.6 include the effect of nuclear spin statistics, which is very small and most noticeable as an intensity alternation within the R-branch clusters in the simulated $(^{15}N_2^{16}O)_4$ spectrum of Fig. 7.6, where lines with even (odd) K'' values are slightly stronger (weaker) than otherwise expected. Our calculations of spin weights for N_2O tetramers are given as supplementary material.[3]

Table 7.4: Molecular parameters for prolate symmetric rotor N_2O tetramers (values in cm^{-1}).

	$(^{14}N_2^{16}O)_4$	$(^{15}N_2^{16}O)_4$
ν_0	2232.2094(1)[a]	2162.7643(1)
A'	0.0248869(25)	0.0235904(13)
B'	0.0231400(46)	0.0219534(30)
A''	0.0249346(25)	0.0236355(13)
B''	0.0231635(46)	0.0219745(33)

[a] Uncertainties in parantheses are 1σ expressed in units of the last quoted digit.

At first we were confused by the new band since its A-value (0.0249 cm^{-1}) was almost identical to the B-value of the original N_2O tetramer (0.0248 cm^{-1} in Ref. [12] or 0.0251 cm^{-1} in our analysis). As well, it was not certain that the original tetramer really was oblate until we had observed the mixed isotopic species. But careful analysis showed that the new perpendicular band really must arise from a distinct species: this was evident from its significantly different B-value (0.0232 cm^{-1}), and also from the fact that the perpendicular band of the original tetramer should be very weak since its individual monomers have little or no projection orthogonal to the tetramer symmetry axis [Fig. 7.1(a)]. We conclude that the new perpendicular band must be due to a separate isomer of $(N_2O)_4$ which is also a symmetric rotor, but now a prolate rotor ($A > B = C$) whose monomers have a significant projection perpendicular to the symmetry axis.

[3] See supplementary material in Appendix D or at `http://dx.doi.org/10.1063/1.3555629` for the determination of nuclear spin weights for the D_{2d} and S_4 structures of $(^{14}N_2^{16}O)_4$ and $(^{15}N_2^{16}O)_4$. Spin statistics also affect the oblate tetramer spectra in Fig. 7.2, but to an even lesser extent since K structure is not resolved.

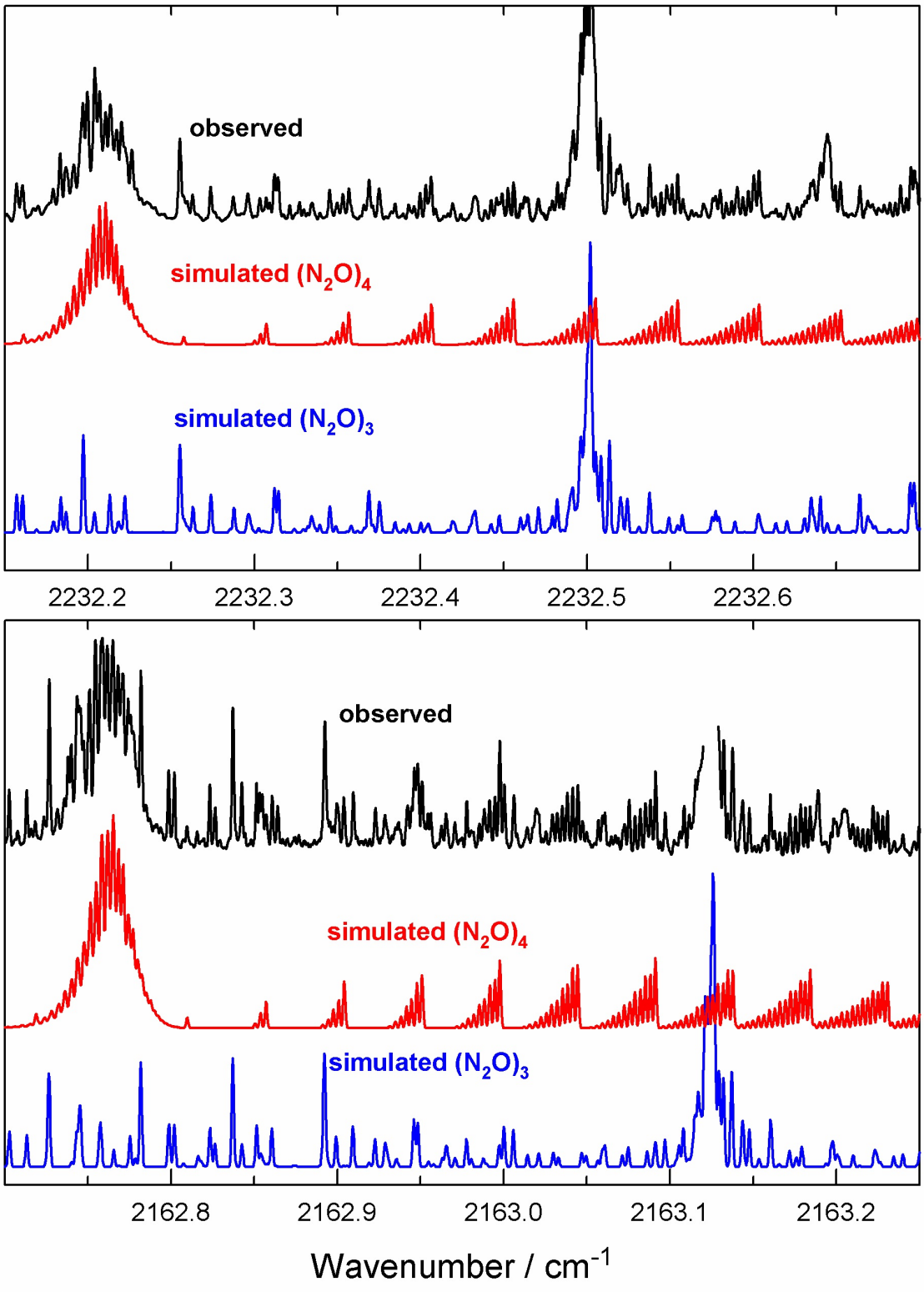

Figure 7.5: Perpendicular bands observed for the prolate isomer of the N_2O tetramer. Top panel: $(^{14}N_2^{16}O)_4$; bottom panel: $(^{15}N_2^{16}O)_4$. Simulations assume the parameters of Table 7.4 with a rotational temperature of 2.2 K and a Gaussian line width of 0.0016 cm^{-1}.

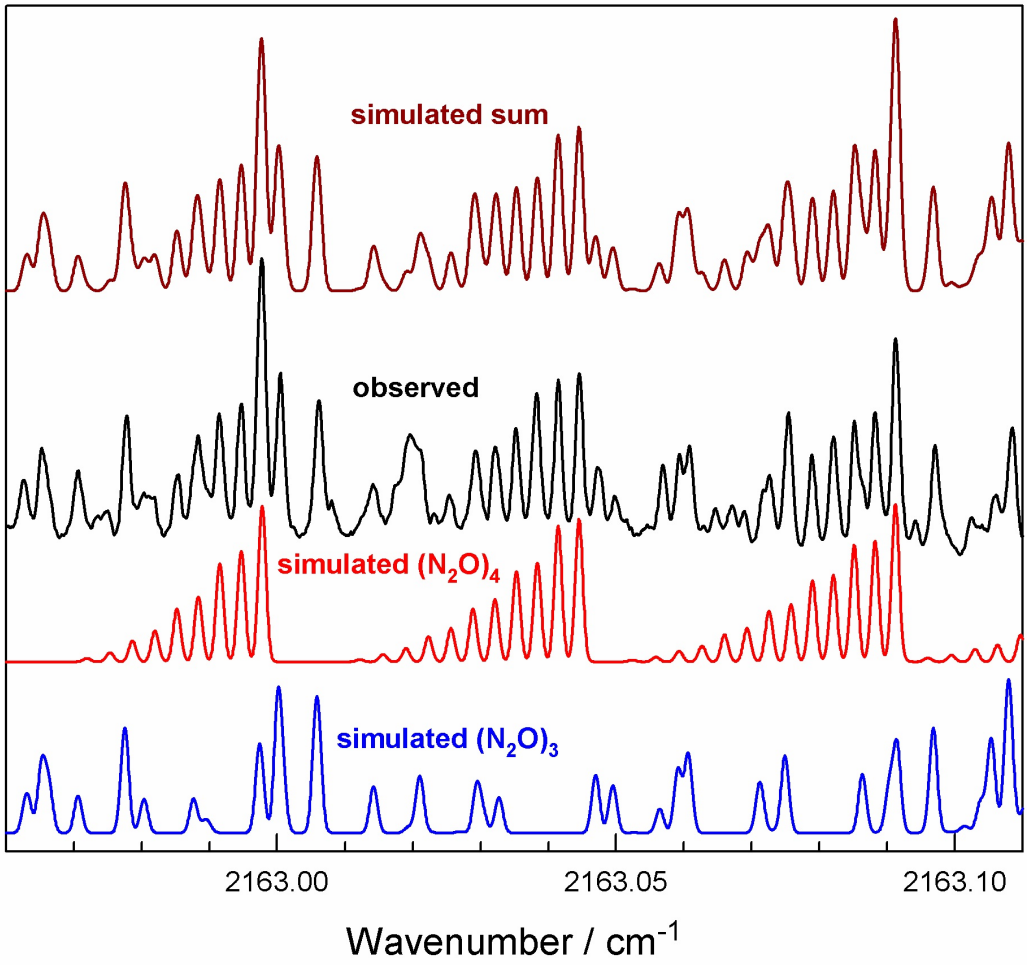

Figure 7.6: Expanded view of a section of the R-branch of the prolate tetramer $(^{15}N_2^{16}O)_4$.

7.2.4 Structure of the prolate N_2O tetramer

What is the structure of this new isomer? We believe that it is similar to that shown in Fig. 7.1(b), which can be thought of as a "sandwich" composed of two nonpolar N_2O dimers with one stacked on top of the other and rotated by 90°. This structure may be obtained by symmetrically twisting the original oblate tetramer so that D_{2d} symmetry is lost but the underlying S_4 symmetry is retained. In the oblate tetramer, adjacent pairs of monomers have a slipped-antiparallel configuration close to that of the nonpolar N_2O dimer, while diagonally opposite pairs are aligned in the same direction. Twisting this structure has the effect that these formerly diagonally opposite pairs now become antiparallel, with configurations close

to the nonpolar dimer, while the formerly adjacent pairs are no longer antiparallel and nearly coplanar but now become almost orthogonal.

Having concluded that there must be a new tetramer isomer with the structure of Fig. 7.1(b), it was gratifying to discover that this also corresponds to a minimum energy structure for both the empirical [129] and high-level *ab initio* [130] N_2O pair potentials. In the former case, the new prolate tetramer is slightly more stable than the original oblate tetramer (-2445 vs. -2352 cm^{-1}), whereas in the latter case the two energies are almost identical (-2625 vs. -2629 cm^{-1}).

With the restrictions of S_4 symmetry and unchanged monomer geometry, four parameters are required to specify the prolate tetramer structure, and these are given for the empirical and *ab initio* calculations in Table 7.5. An experimental structure which gives an essentially perfect fit to the observed spectrum is also given in Table 7.5, but no uncertainties are listed since the four structural parameters are determined by four rotational constants (Table 7.4). The true uncertainties are difficult to estimate. It is possible to obtain a good fit to the observations with other parameter sets because of correlations among the parameters. As well, there is some uncertainty in the derived A-values due to the neglect of Coriolis interaction. On the other hand, it is noteworthy that the observed and theoretical structures in Table 7.5 agree rather well. As in Table 7.3, the empirical tetramer is slightly too large and the *ab initio* one slightly too small.

The vibrational blue-shifts observed for $(^{14}N_2^{16}O)_4$ (+8.453 cm^{-1}) and $(^{15}N_2^{16}O)_4$ (+8.321 cm^{-1}) are similar, as expected. It is not possible to model these shifts as described above for the oblate tetramer because we have not been successful in observing any prolate tetramer bands due to mixed isotopic species.

Table 7.5: Structural parameters for the prolate N_2O tetramer.

Parameter[a]	Experiment (present work)	Empirical Potential (Ref. [129])	High-level *ab initio* potential (Ref. [130])
D	3.448 Å[b]	3.478 Å	3.362 Å
S	2.948 Å	3.010 Å	2.919 Å
θ_1	62.9°	65.4°	61.3°
θ_2	13.9°	9.3°	10.6°
$R_1(N-N)$	3.880 Å	3.932 Å	3.815 Å
$R_2(N-N)$	3.515 Å	3.540 Å	3.434 Å

[a] D is the center of mass separation of the monomers in each dimer pair. S is the separation of the center of mass of one dimer pair from that of the other. θ_1 is the angle between the monomer axes and the line connecting the monomer centers of mass for adjacent ("dimer pair") monomers (in Table 7.3 the equivalent of θ_1 was fixed at 90° to maintain D_{2d} symmetry). θ_2 is deviation from planarity for each monomer of the dimer pairs, with positive values indicating O atoms inward (the total out-of-plane angle is $2\theta_2$). This θ_2 is equivalent to (θ-90°) where θ is the tilt angle in Table 7.3. R_1 and R_2 are derived (not independent parameters). R_1 is the inner N-N distance for any two monomers in different "layers". R_2 is inner N-N distance for dimer pairs.
[b] No experimental uncertainties are given because four parameters were fit to four data points.

7.3 Discussion and Conclusions

Assuming D_{2d} structure, the oblate N_2O tetramer has three fundamental vibrations in the N_2O ν_1 region corresponding to upper states with A_1, B_2, and E symmetries. The A_1 band is infrared forbidden since in this case the transition dipoles of the four monomers exactly cancel. The B_2 vibration corresponds to our observed parallel band at 2237.426 cm^{-1} for $(^{14}N_2^{16}O)_4$, which is strongly allowed because the four monomers are aligned almost parallel to the tetramer symmetry axis. The degenerate E vibration corresponds to an allowed perpendicular transition, but it is expected to be very weak because the monomers have little or no projection perpendicular to the symmetry axis.

Assuming S_4 structure, the prolate tetramer has three analogous fundamentals with A, B, and E upper states. The A band is again forbidden, but the strengths of the parallel (B) and perpendicular (E) bands are interchanged since the prolate tetramer has its monomers aligned nearly orthogonal to the tetramer symmetry axis. We thus observe the strong per-

pendicular band at 2232.209 cm^{-1} but do not detect the much weaker parallel band.

As noted, the tetramer isomers represent two different ways of combining pairs of nonpolar N_2O dimers. More quantitatively, the nonpolar dimer structure [33] has $R = 3.42$ Å, $\theta = 61.4°$, where R is the separation of the monomer centers of mass and θ is the angle between a monomer axis and the line connecting the monomer centers of mass. For comparison, the "dimer pairs" have remarkably similar values of $R = 3.41$ Å, $\theta = 60.6°$ in the oblate tetramer and $R = 3.45$ Å, $\theta = 62.9°$ in the prolate tetramer. But there is a further difference, since the dimer is planar, whereas the dimer pairs have out-of-plane angles of 7.7° and 13.9° in the oblate and prolate tetramers, respectively (the total dihedral angles between monomers are twice these values).

In their analysis of the N_2O tetramer band at 3473.212 cm^{-1}, Miller and Pedersen [12] explored the possibility that it might be a hybrid band. In other words, there might be a small perpendicular contribution to this mostly parallel band. This would imply that the oblate tetramer is a (slightly) asymmetric rotor, or that it is a symmetric rotor with exactly coincident parallel (B) and perpendicular (E) vibrations (which is very unlikely). However, in our spectra, which have significantly narrower line widths than in Ref. [12], there is no evidence for any hybrid character or deviation from a symmetric rotor pattern.

In conclusion, we have recorded and analyzed high-resolution infrared spectra of nitrous oxide tetramers in the region of the N_2O ν_1 fundamental band. The tetramers were produced in a pulsed supersonic slit-jet expansion and probed by means of a tunable diode laser spectrometer. The previously known [12] oblate symmetric rotor tetramer, which has D_{2d} symmetry [Fig. 7.1(a)], was observed for the main isotopologue, $(^{14}N_2^{16}O)_4$, as well as three ^{15}N-substituted forms. The derived structure agrees rather well with, and is (mostly) intermediate between, those given by empirical [129] and *ab initio* [130] N_2O pair potential functions. A distinct prolate symmetric rotor form of the N_2O tetramer with S_4 symmetry [Fig. 7.1(b)] was observed for the first time, and its derived structure also agrees well

with theory. The best estimate of the relative stabilities of the two tetramer isomers (from Ref. [130]) puts them extremely close together, differing by only 5 cm^{-1} in 2630 cm^{-1}. These theoretical equilibrium binding energies can easily be affected by zero-point energy effects, so at present it is not at all clear which is the true tetramer minimum, oblate or prolate. Perhaps Miller and Pedersen's [12] failure to observe the prolate isomer suggests a slight preference for an oblate ground state. In any case, further theoretical studies of the structures and dynamics of $(N_2O)_4$ would be of great interest.

Acknowledgements

We thank L. Murdock for technical assistance, and gratefully acknowledge the financial support of the Natural Sciences and Engineering Research Council of Canada. Thanks also to Richard Dawes and Tucker Carrington, Jr., for providing the means to calculate N_2O pair potential energies from Ref. [130].

Chapter 8

Conclusions

In the present thesis the complexation of small weakly-bound van der Waals complexes and clusters were investigated by observation and analysis of their ro-vibrational spectra. This included: study of OCS−R complexes where R represents several chain and ring hydrocarbons; identification and assignment of specific infrared bands to carbon dioxide clusters, $(CO_2)_N$, with N=6, 7, 9, 10, 11, 12, and 13; observation and structure determination for two distinct highly symmetric isomers of $(N_2O)_4$.

The study of OCS-hydrocarbon complexes started with the infrared spectra of OCS−C_2H_2 and OCS−C_2D_2. For this complex, two different isomers with near-parallel and T-shaped geometries were observed and analysed in the region of C=O stretching fundamental of OCS around 2060 cm^{-1}. In the T-shaped isomer, the OCS molecule forms the stem with the sulphur atom interacting with the triple bond in acetylene. These isomers were initially observed in the microwave region. Therefore, ground state parameters were previously known from microwave studies [6] and [7] which facilitated the analysis to a great extent. Infrared analysis added information about vibrational shifts and excited vibrational state parameters. The observed vibrational shifts, relative to the free OCS monomer are -0.286 cm^{-1} for the near-parallel isomer, and -5.688 cm^{-1} for the T-shaped isomer. Because of the two isomers having quite different vibrational shift, their ro-vibrational bands were well separated. The symmetric near-prolate geometry of the T-shaped isomer dictates a distinctive pattern for the ro-vibrational spectrum. In order to check the isomers' energy ordering, argon was added to the gas mixture. Use of a heavier carrier gases leads to a greater collisional energy transfer which results in a more complete relaxation into the lowest energy form. Evidently the spectrum of the T-shaped isomer disappeared while the near-parallel isomer was still

present in the spectrum. This is in agreement with semi-empirical and *ab initio* calculations in Refs. [6] and [7] which indicate the lowest energy form to be the near-parallel isomer, with the T-shaped isomer having a significantly higher energy.

Observing that a T-shaped complex forms between OCS and C_2H_2, it was natural to wonder if the same holds true for OCS with other hydrocarbons. Continuing to study other small hydrocarbons, it was discovered that most of them also exhibit relatively simple rotation-vibration spectra characteristic of a T-shaped structure. Out of ten hydrocarbons tried, two did not show T-shaped geometries (ethane and cyclohexane). This was attributed to the fact that ehtane and cyclohexane are fully saturated hydrocarbons, based on previous works on weakly bound complexes [88, 96]. The bands were red-shifted between 5 cm^{-1} to 12 cm^{-1} relative to the OCS ν_1 frequency. The magnitude of the vibrational shift increased with the number of carbon atoms in the hydrocarbon under study. Extension of vibrational shifts data will allow the investigation of intermolecular effects on intramolecular potentials in wider scope.

The remarkable icon in climate change, CO_2, has received considerable attention in terms of spectroscopy of its clusters, but this has been limited to dimers and trimers thus far. Here, the calculated structures and resulting rotational constants for carbon dioxide clusters in the range N=1-13 were presented using two intermolecular potential functions, M-O-M [29, 114] and SAPT-s [107]. Thirteen specific infrared bands in the CO_2 ν_3 fundamental region were assigned to $(CO_2)_N$, with N=6, 7, 9, 10, 11, 12, and 13. Three of these bands are also observed for ^{18}O-substituted clusters. Two isomers are observed for $(CO_2)_6$, both of which are oblate symmetric tops. The lowest energy isomer has S_6 symmetry and the other has S_4 symmetry. $(CO_2)_{13}$ is also an S_6 oblate symmetric top, but the remaining clusters are asymmetric tops with no symmetry elements (C_1 point group symmetry). $(CO_2)_8$ was not observed most likely because of a gap in the laser coverage around 2357.5 cm^{-1} The effective rotational constants obtained from simulating the observed bands are generally 1%-4% smaller than

the equilibrium constants predicted by the intermolecular potentials, an effect which can partly be due to the zero point energy. The strongest observed bands show a progressive vibrational blue-shift with increasing cluster size. The resonant dipole-dipole interaction model correctly predicts the trend of the vibrational shifts, but significantly underestimates the shifts in magnitude. These are the largest such molecular clusters that are assigned to infrared bands with at least partial rotational resolution. These result provide a precise benchmark for future theoretical calculations.

The only study on N_2O tetramer was reported by Miller and Pedersen in 1997 [12]. The structure was only an approximate structure mainly because of high degree of symmetry which showed no K-structure at the resolution accessible ($\approx$0.010 cm^{-1}). In this thesis, high-resolution infrared spectra of two isomers of $(N_2O)_4$ are observed in the region of N_2O ν_1 fundamental band. The oblate symmetric isomer that was previously studied by Miller et al. was observed as well as three ^{15}N-substituted forms which achieve some K-structure helping to determine the structure (D_{2d} symmetry). The derived structure agrees fairly well with, and is intermediate between, those given by empirical [129] and *ab initio* [130] N_2O pair potential functions. Additionally, a distinct prolate symmetric rotor isomer of the N_2O tetramer with S_4 symmetry was observed for the first time for which the derived structure also agrees well with theoretical calculations. The oblate and prolate isomers of $(N_2O)_4$ represent two different ways of putting together two non-polar N_2O dimers. The rationalization of tetramer structures based on dimer structures emphasizes the significant role of pair-wise interactions. The relative stability of the two tetramer isomers is estimated to be a difference of only 5 cm^{-1} in 2630 cm^{-1} [130]. This small difference can easily be affected by zero-point energy effects, so at present it is not at all clear which isomer is the true minimum energy for N_2O tetramer.

Despite the fact that field of cluster spectroscopy is relatively old, most of high-resolution studies on molecular clusters and complexes have been on binary and, to a lesser extent, on

ternary systems. Prior to the works presented in this thesis, very few high-resolution studies on larger clusters (having 4 or more monomer units) of the CO_2 family[1] have been reported in the literature. This thesis represents a major advancement in the study of larger clusters at high-resolution and provides a benchmark for further theoretical calculations. Theoretical calculations that are successful in explaining the present experimental results can, in turn, set the path for further investigation of even larger clusters towards understanding of bulk properties at microscopic level.

8.1 Outlook and Future Directions

Although the high sensitivity of the detection system that is incorporated in the current supersonic apparatus has enabled the study of extremely weak intermolecular combination bands and high efficiency of the jet nozzles has proven to generate very weakly-bound higher energy isomers of van der Waals clusters, development of the current design could enhance the formation of clusters and quality of the spectra. Below a few suggestions are presented.

Cooling of the expansion gas mix before being pulsed into the vacuum chamber give lower effective rotational temperatures and increases the efficiency of cluster formation. For this purpose, a cooling jacket is constructed which can be mounted on top of the multi-channel block. The jacket will circulate cooled liquid methanol from a temperature-controlled refrigerated bath around the multi-channel block. This cooling technique was previously implemented in a supersonic jet system in order to study the solvation of carbonyl sulfide (OCS) in helium atoms [132].

The absorption path-length can be increased by installing one more pulsed valve inside the vacuum chamber. The addition of the second pulsed valve in the jet chamber has shown satisfactory results in improving the signal to noise. However, using a third pulsed valve inside the vacuum chamber requires a lower repetition rate and also a higher pumping

[1] CO_2 family molecules being CO_2, CS_2, OCS, and N_2O.

capacity for faster recovery of the high vacuum before the next pulse. Also, another counter timer will be needed to synchronize the third pulsed valve with the other two as well as with data acquisition time. Therefore, the addition of a third pulsed valve might be only beneficial for cases with really weak transitions such as intermolecular combination bands or difference bands.

Another way of increasing the absorption path-length is to increase the number of laser passes interacting with the jet stream. The current AMA-100 multi-pass absorption cell can be aligned in such a way that the laser beam passes the cell by about 360 times rather than 180 times which is the current number of laser passes. This will require a very accurate alignment of the incident laser beam because the solid angle available to the laser beam will be more limited.

Despite the fact that the resolution of the ro-vibrational spectra obtained from the current experimental setup ($\approx$ 0.0015 - 0.0025 cm^{-1} or 45 - 75 MHz) is enough to obtain rotational structure for even large clusters, but the current resolution is basically limited by the light source. Implementation of state-of-the art light sources such as an optical parametric oscillator (OPO) with linewidth of less than 1 MHz will help to achieve much higher resolutions which will be most useful in structure determination of molecular clusters. Plans are underway to interface an Argos™ Model 2400 SF-10 single frequency CW OPO obtained from Aculight® to the current supersonic jet system. The idler beam covers the range 3.9 - 4.6 μm and the coverage for the signal beam is 1.39 - 1.46 μm. This wavelength range of the OPO system should at least enable ultra high resolution study of large molecular clusters of CO_2 and N_2O. The wide tuneability and high power ($>$ 600 mW) of the OPO light source should facilitate the study of weak intermolecular vibrational modes to a great extent.

References

[1] H. Takeuchi, *J. Phys. Chem. A* **112**, 7492 (2008).

[2] M. Dehghany, M. Afshari, N. Moazzen-Ahmadi, and A.R.W. McKellar, *J. Chem. Phys.* **128**, 064308 (2008).

[3] W. H. Marlow, *J. Chem. Phys.* **73**, 6288 (1980).

[4] C. M. Roth, B. L. Neal, and A. M. Lenhoff, *Biophys. J.* **70**, 977 (1996).

[5] E. Hult and A. Kiejna, *Surface Science* **383**, 88 (1997).

[6] S. A. Peebles and R. L. Kuczkowski, *J. Phys. Chem. A* **103**, 3884 (1999).

[7] S. A. Peebles and R. L. Kuczkowski, *Chem. Phys. Lett.* **312**, 357 (1999).

[8] F. N. Keutsch and R. J. Saykally, *PNAS* **98**, 10533 (2001).

[9] K. Nauta and R. E. Miller, *Science* **287**, 293 (2000).

[10] J. D. Cruzan, L. B. Braly, Kun Liu, M. G. Brown, J. G. Loeser, and R. J. Saykally, *Science* **271**, 59 (1996).

[11] K. Liua, M. G. Brown, J. D. Cruzan, and R. J. Saykally, *Science* **271**, 62 (1996).

[12] R. E. Miller and L. Pedersen, *Chem. Phys. Lett.* **275**, 307 (1997).

[13] M. A. Walsh, T. H. England, T. R. Dyke, and B. J. Howard, *Chem. Phys. Lett.* **142**, 265 (1987).

[14] G. T. Fraser, A. S. Pine, W. J. Lafferty, and R. E. Miller, *J. Chem. Phys.* **87**, 1502 (1987).

[15] M. J. Weida and D. J. Nesbitt, *J. Chem. Phys.* **105**, 10210 (1996).

[16] T. Konno and Y. Ozaki, *Chem. Phys. Lett.* **394**, 198 (2004).

[17] M. Dehghany, A.R.W. McKellar, M. Afshari, and N. Moazzen-Ahmadi, *Mol. Phys.* **108**, 2195 (2010).

[18] G. A. Pubanz, M. Maroncelli, and J. W. Nibler, *Chem. Phys. Lett.* **120**, 3 (1985).

[19] F. Huisken, L. Ramonat, J. Santos, V. V. Smirnov, O. M. Stelmakh, and A. A. Vigasin, *J. Mol. Struct.* **410-411**, 47 (1997).

[20] A. Ramos, J. M. Fernndez, G. Tejeda, and S. Montero, *Phys. Rev. A* **72**, 053204 (2005).

[21] T. E. Gough, R. E. Miller, and G. Scoles, *J. Phys. Chem.* **85**, 4041 (1981).

[22] J. A. Barnes and T. E. Gough, *J. Chem. Phys.* **86**, 6012 (1987).

[23] J. A. Barnes, T. E. Gough, and M. Stoer, *J. Chem. Phys.* **95**, 4840 (1991).

[24] R. Disselkamp and G. E. Ewing, *J. Chem. Phys.* **99**, 2439 (1993).

[25] S. Bauerecker, M. Taraschewski, C. Weitkamp, and H. K. Cammenga, *Rev. Sci. Instrum.* **72**, 3946 (2001).

[26] G. Torchet, M.F. de Feraudy, A. Boutin, and A. H. Fuchs, *J. Chem. Phys.* **105**, 3671 (1996).

[27] A. Bonnamy, R. Georges, A. Benidar, J. Boissoles, A. Canosa, and B. R. Rowe, *J. Chem. Phys.* **118**, 3612 (2003).

[28] J. Norooz Oliaee, M. Dehghany, N. Moazzen-Ahmadi, and A.R.W. McKellar, *Phys. Chem. Chem. Phys.* **13**, 1297 (2011).

[29] C. S. Murthy, S. F. O'Shea, and I. R. McDonald, *Mol. Phys.* **50**, 531 (1983).

[30] Z. S. Huang and R. E. Miller, *J. Chem. Phys.* **89**, 5408 (1988).

[31] R. E. Miller and L. Pedersen, *J. Chem. Phys.* **108**, 436 (1998).

[32] M. Dehghani, Mahin Afshari, Z. Abusara, N. Moazzen-Ahmadi, and A.R.W. McKellar, *J. Chem. Phys.* **247**, 164310 (2007).

[33] M. Dehghany, Mahin Afshari, Z. Abusara, C. Van Eck, and N. Moazzen-Ahmadi, *J. Mol. Spectrosc.* **247**, 123 (2008).

[34] M. Dehghany, M. Afshari, R. I. Thompson, N. Moazzen-Ahmadi, and A.R.W. McKellar, *J. Mol. Spectrosc.* **252**, 1 (2008).

[35] M. Dehghany, M. Afshari, N. Moazzen-Ahmadi, and A.R.W. McKellar, *Phys. Chem. Chem. Phys.* **10**, 1658 (2008).

[36] M. Dehghany, Mahin Afshari, Z. Abusara, and N. Moazzen-Ahmadi, *Phys. Chem. Chem. Phys.* **11**, 7585 (2009).

[37] M. Dehghany, M. Afshari, N. Moazzen-Ahmadi, and A.R.W. McKellar, *J. Chem. Phys.* **130**, 044303 (2009).

[38] N. Moazzen-Ahmadi M. Dehghany, Mahin Afshari and A.R.W. McKellar, *Chem. Phys. Lett.* **476**, 143 (2009).

[39] J. Norooz Oliaee, M. Dehghany, N. Moazzen-Ahmadi, and A.R.W. McKellar, *J. Chem. Phys.* **134**, 074310 (2011).

[40] M. Rezaei, J. Norooz Oliaee, N. Moazzen-Ahmadi, and A.R.W. McKellar, *J. Chem. Phys.* **136**, 224308 (2012).

[41] M. Rezaei, K. H. Michaelian, and N. Moazzen-Ahmadi, *J. Chem. Phys.* **136**, 124308 (2012).

[42] Philip R. Bunker and Per Jensen, *Molecular Symmetry and Spectroscopy*, NRC Research Press, Ottawa, 2nd edition (1998).

[43] Richard N. Zare, *Angular Momentum: Understanding Spatial Aspects in Chemistry and Physics*, Wiley, New York (1988).

[44] T. D. Varberg and K. M. Evenson, *Astrophys. J.* **385**, 763 (1992).

[45] James K. G. Watson, *J. Chem. Phys.* **46**, 1935 (1967).

[46] O. F. Hagena, *Surf. Sci.* **106**, 101 (1981).

[47] J. Koperski, *Van der Waals Complexes in Supersonic Beams*, Wiley-VCH, Weinheim, Germany (2003).

[48] G. D. Hayman, J. Hodge, B. J. Howard, J. S. Muenter, and T. R. Dyke, *Chem. Phys. Lett.* **118**, 12 (1985).

[49] C. M. Lovejoy, M. D. Schuder, and D. J. Nesbitt, *Chem. Phys. Lett.* **127**, 374 (1986).

[50] A. De Piante, E. J. Campbell, and S. J. Buelow, *Rev. Sci. Instr.* **60**, 858 (1989).

[51] S. W. Sharpe, Y. P. Zeng, C. Witting, and R. A. Beaudet, *J. Chem. Phys.* **92**, 943 (1990).

[52] T. A. Hu, E. L. Chappell, and S. W. Sharpe, *J. Chem. Phys.* **98**, 6162 (1993).

[53] M. D. Brookes, C. Xia, J. Tang, J. A. Anstey, B. G. Fulsom, K. X. Au Yong, J. M. King, and A.R.W. McKellar, *Spectrochim. Acta A* **60**, 3235 (2004).

[54] C. M. Lovejoy and D. J. Nesbitt, *Rev. Sci. Instrum.* **58**, 807 (1987).

[55] G. Guelachvili and K. N. Rao, *Handbook of infrared standards with spectral coverage of 1.4 - 4 μm and 6.2 - 7.7 μm*, Academic Press Inc., Orlando, Florida, USA (1993).

[56] A. G. Maki and J. S. Wells, *Wavenumber Calibration Tables from Heterodyne Frequency Measurements*, National Institute of Standards and Technology, Gaithersburg, MD, USA (1998), (version 1.3) [Online] Available: `http://physics.nist.gov/wavenum`.

[57] J. B. McManus, P. L. Kebabian, and M. S. Zahniser, *App. Opt.* **34**, 3336 (1995).

[58] C. M. Western, "PGOPHER, a Program for Simulating Rotational Structure," University of Bristol, UK, available from: `http://pgopher.chm.bris.ac.uk`.

[59] N. R. Walker, A. J. Minei, S. E. Novick, and A. C. Legon, *J. Mol. Spectrosc.* **251**, 153 (2008).

[60] M. Dehghany, Mahin Afshari, R. I. Thompson, N. Moazzen-Ahmadi, and A.R.W. McKellar, *J. Mol. Spectrosc.* **252**, 1 (2008).

[61] A. J. Minei and S. E. Novick, *J. Chem. Phys.* **126**, 10101 (2007).

[62] Mahin Afshari, M. Dehghani, Z. Abusara, N. Moazzen-Ahmadi, and A.R.W. McKellar, *J. Chem. Phys.* **126**, 071102 (2007).

[63] J. P. Connelly, A. Bauder, A. Chisholm, and B. J. Howard, *Mol. Phys.* **88**, 915 (1996).

[64] Mahin Afshari, M. Dehghani, Z. Abusara, N. Moazzen-Ahmadi, and A.R.W. McKellar, *J. Chem. Phys.* **127**, 144310 (2007).

[65] D. G. Prichard, R. N. Nandi, and J. S. Muenter, *J. Chem. Phys.* **89**, 115 (1988).

[66] G. T. Fraser, R. D. Suenram, F. J. Lovas, A. S. Pine, J. T. Hogen, W. J. Lafferty, and J. S. Muenter, *J. Chem. Phys.* **89**, 6028 (1988).

[67] S. E. Novick, R. D. Suenram, and F. J. Lovas, *J. Chem. Phys.* **88**, 687 (1988).

[68] M. Dehghany, J. Norooz Oliaee, M. Afshari, N. Moazzen-Ahmadi, and A.R.W. McKellar, *J. Chem. Phys.* **130**, 224310 (2009).

[69] H. O. Leung, *J. Chem. Phys.* **108**, 3955 (1998).

[70] C. Dutton, A. Sazonov, and R. A. Beaudet, *J. Phys. Chem.* **100**, 17772 (1996).

[71] M. Afshari, M. Dehghany, N. Moazzen-Ahmadi, and A.R.W. McKellar, *J. Chem. Phys.* **129**, 074314 (2008).

[72] J. S. Muenter, *J. Chem. Phys.* **90**, 4048 (1989).

[73] Z. S. Huang and R. E. Miller, *Chem. Phys.* **132**, 185 (1989).

[74] H. O. Leung, *J. Chem. Phys.* **107**, 2232 (1997).

[75] R. A. Peebles, S. A. Peebles, R. L. Kuczkowski, and H. O. Leung, *J. Phys. Chem.* **103**, 10813 (1999).

[76] T. A. Hu, L. H. Sun, and J. S. Muenter, *J. Chem. Phys.* **95**, 1537 (1991).

[77] K. Didriche, C. Lauzin, P. Macko, M. Herman, and W. J. Lafferty, *Chem. Phys. Lett.* **469**, 35 (2009).

[78] M. Dehghany, M. Afshari, J. Norooz Oliaee, N. Moazzen-Ahmadi, and A.R.W. McKellar, *Chem. Phys. Lett.* **473**, 26 (2009).

[79] R. E. Miller and R. O. Watts, *Chem. Phys. Lett.* **105**, 409 (1984).

[80] H.-B. Qian, W. A. Herrebout, and B. J. Howard, *Mol. Phys.* **91**, 689 (1997).

[81] Y. Ohshima, Y. Matsumoto, M. Takami, and K. Kuchitsu, *Chem. Phys. Lett.* **152**, 294 (1988).

[82] R. W. Randall, J. M. Wilkie, B. J. Howard, and J. S. Muenter, *Mol. Phys.* **69**, 839 (1990).

[83] Mahin Afshari, Z. Abusara, M. Dehghani, N. Moazzen-Ahmadi, and A.R.W. McKellar, *Chem. Phys. Lett.* **437**, 23 (2007).

[84] K. W. Jucks, Z. S. Huang, D. Dayton, R. E. Miller, and W. J. Lafferty, *J. Chem. Phys.* **86**, 4341 (1987).

[85] K. W. Jucks, Z. S. Huang, R. E. Miller, G. T. Fraser, A. S. Pine, and W. J. Lafferty, *J. Chem. Phys.* **88**, 2185 (1988).

[86] Z. Abusara, L. Borvayeh, N. Moazzen-Ahmadi, and A.R.W. McKellar, *J. Chem. Phys.* **125**, 144306 (2006).

[87] J. K. G. Watson, *Vibrational spectra and structure*, volume 6, Elsevier, Amsterdam (1977), in: J. R. During (Ed.).

[88] A. C. Legon, *Struct. Bonding* **126**, 17 (2008).

[89] J. Norooz Oliaee, Mahin Afshari, M. Dehghany, N. Moazzen Ahmadi, and A.R.W. McKellar, *J. Mol. Spectrosc.* **257**, 133 (2009).

[90] S. A. Peebles and R. L. Kuczkowski, *Mol. Phys.* **99**, 225 (2001).

[91] A. C. Legon and L. C. Willoughby, *Chem. Phys. Lett.* **143**, 214 (1988).

[92] S. A. Cooke, J. H. Holloway, and A. C. Legon, *Chem. Phys. Lett.* **226**, 61 (1997).

[93] C. di Lauro, P. R. Bunker, J. W. C. Johns, and A.R.W. McKellar, *J. Mol. Spectrosc.* **184**, 177 (1997).

[94] U. Dahmen, H. Dreizler, and W. Stahl, *Ber. Bunsenges. Phys. Chem.* **99**, 434 (1995).

[95] S. A. Cooke, C. M. Evans, J. H. Holloway, and A. C. Legon, *J. Chem. Soc. Faraday Trans.* **94**, 2295 (1998).

[96] A. C. Legon, A. L. Wallwork, and H. E. Warner, *Chem. Phys. Lett.* **191**, 97 (1992).

[97] K. Hiraoka, K. Fujita, M. Ishida, K. Hiizumi, F. Nakagawa, T. Ichikawa, H. Okada, A. Wada, S. Yamabe, and N. Tsuchida, *Chem. Phys. Lett.* **387**, 76 (2004).

[98] A. S. Pine and G. T. Fraser, *J. Chem. Phys.* **89**, 100 (1988).

[99] M. J. Weida, J. M. Sperhac, and D. J. Nesbitt, *J. Chem. Phys.* **103**, 7685 (1995).

[100] L. Mannik, J. C. Stryland, and H. L. Welsh, *Can. J. Phys.* **49**, 3056 (1971).

[101] Y. I. Baranov and A. A. Vigasin, *J. Mol. Spectrosc.* **193**, 319 (1999).

[102] A. A. Vigasin, *J. Mol. Spectrosc.* **200**, 89 (2000).

[103] A. A. Vigasin, F. Huisken, A. I. Pavlyuchko, L. Ramonat, and E. G. Tarakanova, *J. Mol. Spectrosc.* **209**, 81 (2001).

[104] A. A. Vigasin, Y. I. Baranov, and G.V. Chlenova, *J. Mol. Spectrosc.* **213**, 51 (2002).

[105] Y. I. Baranov, W. J. Lafferty, G. T. Fraser, and A. A. Vigasin, *J. Mol. Spectrosc.* **218**, 260 (2003).

[106] A. Bonnamy, R. Georges, E. Hugo, and R. Signorell, *Phys. Chem. Chem. Phys.* **7**, 963 (2005).

[107] R. Bukowski, J. Sadlej, B. Jeziorski, P. Jankowski, K. Szalewicz, S. A. Kucharski, H. L. Williams, and B. M. Rice, *J. Chem. Phys.* **110**, 3785 (1999).

[108] S. Tsuzuki, W. Klopper, and H. P. L .

[109] S. Bock, E. Bich, and E. Vogel, *Chem. Phys.* **257**, 147 (2000).

[110] M. T. Oakley and R. J. Wheatley, *J. Chem. Phys.* **130**, 034110 (2009).

[111] G. Cardini, V. Schettino, and M. L. Klein, *J. Chem. Phys.* **90**, 4441 (1989).

[112] Z. Zhang and Z. Duan, *J. Chem. Phys.* **122**, 214507 (2005).

[113] T. Merker, C. Engin, J. Vrabec, and H. Hasse, *J. Chem. Phys.* **132**, 234512 (2010).

[114] C. S. Murthy, K. Singer, and I. R. McDonald, *Mol. Phys.* **44**, 135 (1981).

[115] M. Dehghany, M. Afshari, Z. Abusara, C. Van Eck, and N. Moazzen-Ahmadi, *J. Mol. Spectrosc.* **247**, 123 (2008).

[116] M. Dehghany, M. Afshari, J. Norooz Oliaee, N. Moazzen-Ahmadi, and A.R.W. McKellar, *Chem. Phys. Lett.* **473**, 26 (2009).

[117] M. J. Weida, J. M. Sperhac, D. J. Nesbitt, and J. M. Hutson, *J. Chem. Phys.* **101**, 8351 (1994).

[118] A.R.W. McKellar, *J. Chem. Phys.* **125**, 114110 (2006).

[119] W. H. Press S. A. Reukolsky W. T. Vetterling and B. P. Flannery, *Numerical Recipes in FORTRAN*, Cambridge University Press, 2nd edition (1992).

[120] J. Geraedts, M. Waayer, S. Stolte, and J. Reuss, *Faraday Discuss. Chem. Soc.* **73**, 375 (1982).

[121] R. Signorell, *J. Chem. Phys.* **118**, 2707 (2003).

[122] I. V. Boychenko and H. Huber, *J. Chem. Phys.* **124**, 014305 (2006).

[123] V. M. Devi, B. Fridovich, G. D. Jones, and D. G. S. Snyder, *J. Mol. Spectrosc.* **105**, 61 (1984).

[124] K. V. J. Jose and S. R. Gadre, *J. Chem. Phys.* **128**, 124310 (2008).

[125] H. Liu and K. D. Jordan, *J. Phys. Chem. A* **107**, 5703 (2003).

[126] J.-B. Maillet, A. Boutin, S. Buttefay, F. Calvo, and A. H. Fuchs, *J. Chem. Phys.* **109**, 329 (1998).

[127] R. D. Etters, K. Flurchick, R. P. Pan, and V. Chandrasekharan, *J. Chem. Phys.* **75**, 929 (1981).

[128] G.M. Berner, A. L. L. East, M. Afshari, M. Dehghany, N. Moazzen-Ahmadi, and A.R.W. McKellar, *J. Chem. Phys.* **130**, 164305 (2009).

[129] B. Kuchta, R.D. Etters, and R. LeSar, *J. Chem. Phys.* **97**, 5662 (1992).

[130] R. Dawes, X.-G. Wang, A. W. Jasper, and T. Carrington, Jr., *J. Chem. Phys.* **133**, 134304 (2010).

[131] A.R.W. McKellar, J. K. G. Watson, and B. J. Howard, *Mol. Phys.* **86**, 273 (1995).

[132] J. Tang and A.R.W. McKellar, *J. Chem. Phys.* **119**, 5467 (2003).

[133] M. Afshari, M. Dehghany, A. R. W McKellar, and N. Moazzen-Ahmadi1, *J. Chem. Phys.* **137**, 054304 (2012).

Appendix A

Derivation of Kratzer relation

In this appendix an approximate energy expression for a rotating semi-rigid diatomic molecule (Equation (2.111)) is obtained by a classical treatment. The Kratzer relation (Equation (2.112)) for the centrifugal distortion parameter, D, follows from this treatment.

In a rotating diatomic molecule with angular momentum L, the centrifugal force leads to an increase in the internuclear separation from r_e to r. If equilibrium is to hold, the centrifugal force must be equal to a restoring force. The restoring force, for small values of $(r - r_e)$, is proportional to the displacement $(r - r_e)$, because in the vicinity of the potential minimum the associated restoring potential can be described, to a good approximation, by a parabolic potential. The restoring force is approximated as

$$F_r = -\nabla_r(\frac{1}{2}k(r - r_e)^2) = -k(r - r_e), \tag{A.1}$$

So, the total energy of the diatomic molecule is the addition of the rotational kinetic energy and the potential energy created by the centrifugal distortion

$$E = \frac{\mathrm{L}^2}{2\mu r^2} + \frac{1}{2}k(r - r_e)^2. \tag{A.2}$$

The centrifugal force is,

$$F_c = \mu r\omega^2 = \mu r\omega^2 \times \frac{\mu}{\mu} \times \frac{r^3}{r^3} = \frac{\mu^2 r^4 \omega^2}{\mu r^3} = \frac{\mathrm{I}^2\omega^2}{\mu r^3} = \frac{\mathrm{L}^2}{\mu r^3}, \tag{A.3}$$

where I is the moment of inertia of the diatomic molecule, ω is the rotational angular frequency and μ is the reduced mass.

In equilibrium, using Equations (A.1) and (A.3),

$$|F_c| = |F_r| \tag{A.4}$$

$$\frac{\mathrm{L}^2}{\mu r^3} = k(r - r_e) \tag{A.5}$$

Therefore, one can write

$$r - r_e = \frac{\mathrm{L}^2}{k\mu r^3} \cong \frac{\mathrm{L}^2}{k\mu r_e^3} \tag{A.6}$$

Using Equation (A.6) the second term in Equation (A.2) can be rearranged as

$$\frac{1}{2}k(r - r_e)^2 = \frac{1}{2}k\left[\frac{\mathrm{L}^2}{k\mu r_e^3}\right]^2 = \frac{\mathrm{L}^4}{2k\mu^2 r_e^6}. \tag{A.7}$$

Again, using Equation (A.6), r can be expressed in terms of r_e as,

$$r = r_e\left(1 + \frac{\mathrm{L}^2}{k\mu r_e^4}\right) = r_e(1 + \xi) \quad \text{with} \quad \xi \ll 1, \tag{A.8}$$

using this and the following Taylor expansion

$$(1 + \xi)^{-2} = 1 - 2\xi + 3\xi^2 - 4\xi^3 + \cdots \tag{A.9}$$

one can write

$$\frac{1}{r^2} = \frac{1}{r_e^2(1 + \xi)^2} = \frac{1}{r_e^2}\left[1 - 2\frac{\mathrm{L}^2}{k\mu r_e^4} + 3\left(\frac{\mathrm{L}^2}{k\mu r_e^4}\right)^2 + \cdots\right]. \tag{A.10}$$

Thus, the total energy is

$$E = \frac{\mathrm{L}^2}{2\mu r_e^2}\left[1 - 2\frac{\mathrm{L}^2}{k\mu r_e^4} + 3\left(\frac{\mathrm{L}^2}{k\mu r_e^4}\right)^2 + \cdots\right] + \frac{\mathrm{L}^4}{2k\mu^2 r_e^6} \tag{A.11}$$

$$= \frac{\mathrm{L}^2}{2\mu r_e^2} - \frac{\mathrm{L}^4}{k\mu^2 r_e^6} + \frac{3}{2}\frac{\mathrm{L}^6}{k^2\mu^3 r_e^{10}} + \cdots + \frac{1}{2}\frac{\mathrm{L}^4}{k\mu^2 r_e^6} \tag{A.12}$$

$$= \frac{\mathrm{L}^2}{2\mu r_e^2} - \frac{1}{2}\frac{\mathrm{L}^4}{k\mu^2 r_e^6} + \frac{3}{2}\frac{\mathrm{L}^6}{k^2\mu^3 r_e^{10}} + \cdots . \tag{A.13}$$

Upon replacing the classical angular momentum, L, with its quantum mechanical operator $\hbar\hat{J}$, the energy expression is obtained as

$$E = \frac{\hbar^2}{2\mu r_e^2}\hat{J}^2 - \frac{1}{2}\frac{\hbar^4}{k\mu^2 r_e^6}\hat{J}^4 + \frac{3}{2}\frac{\hbar^6}{k^2\mu^3 r_e^{10}}\hat{J}^6 + \cdots \tag{A.14}$$

$$= B_e\hat{J}^2 - D_e\hat{J}^4 + H_e\hat{J}^6 + \cdots , \tag{A.15}$$

and the energy levels are

$$F(J) = B_e J(J+1) - D_e J^2(J+1)^2 + H_e J^3(J+1)^3 + \cdots . \tag{A.16}$$

Rotational and centrifugal distortion constants are

$$B_e = \frac{\hbar^2}{2\mu r_e^2} \quad \text{(in Joules) or } \frac{\hbar}{4\pi c \mu r_e^2} \quad \text{(in cm}^{-1}\text{)}, \tag{A.17}$$

$$D_e = \frac{\hbar^4}{2k\mu^2 r_e^6} \quad \text{(in Joules) or } \frac{\hbar^3}{4\pi k c \mu^2 r_e^6} \quad \text{(in cm}^{-1}\text{)}, \tag{A.18}$$

$$H_e = \frac{3\hbar^6}{2k^2\mu^3 r_e^{10}} \quad \text{(in Joules) or } \frac{3\hbar^5}{4\pi k^2 c \mu^3 r_e^{10}} \quad \text{(in cm}^{-1}\text{)}. \tag{A.19}$$

It can be shown that the Kratzer equation gives a relationship between B_e and D_e, as

$$D_e = \frac{\hbar^3}{4\pi k c \mu^2 r_e^6} = \frac{\hbar^3}{4\pi k c \mu^2 r_e^6} \times \frac{\mu}{\mu} \times \frac{c^2}{c^2} \times \frac{16\pi^2}{16\pi^2} \tag{A.20}$$

$$= \frac{\hbar^3}{64\pi^3 c^3 \mu^3 r_e^6} \times \frac{16\pi^2 \mu c^2}{k} = \left(\frac{\hbar}{4\pi c \mu r_e^2}\right)^3 \times \frac{16\pi^2 \mu c^2}{k} \tag{A.21}$$

$$= \frac{B_e^3 16\pi^2 c^2}{\frac{k}{\mu}} = \frac{B_e^3 16\pi^2 c^2}{\omega_e^2} = \frac{4B_e^3 (2\pi c)^2}{\omega_e^2} \tag{A.22}$$

$$= \frac{4B_e^3}{\left(\frac{\omega_e}{2\pi c}\right)^2} = \frac{4B_e^3}{\tilde{\omega_e}^2}. \tag{A.23}$$

Appendix B

Resonant dipole-dipole model

The resonant dipole-dipole model is a model which allows the prediction of vibrational spectra of molecular clusters and aggregates. This model describes the vibrational bands of molecular clusters in terms of couplings between transition dipoles. Figure B.1 illustrates a simplified model of a molecular cluster with (left) and without (right) dipole-dipole interactions. On the left-hand side, no coupling happens between the vibrating monomers (symbolized by arrows) and therefore their vibrational eigenstates are degenerate. However, on the right-hand side, dipole-dipole couplings (symbolized by dashed lines) lift the degeneracy of vibrational eigenstates and results in a structured vibrational band.

Pair-wise dipole-dipole interaction terms are added to the vibrational Hamiltonian of uncoupled monomers and treated as perturbation. The perturbation term is the classical interaction of two dipoles

$$\hat{H}_{d-d} = \sum_{i>j}^{N} \left\{ \frac{\boldsymbol{\mu}_i . \boldsymbol{\mu}_j}{r_{ij}^3} - \frac{3(\boldsymbol{\mu}_i . \mathbf{r}_{ij})(\boldsymbol{\mu}_j . \mathbf{r}_{ij})}{r_{ij}^5} \right\}. \tag{B.1}$$

Here, N is the number of monomers, r_{ij} is the center of mass separation of monomers i and j with dipole moments $\boldsymbol{\mu}_i$ and $\boldsymbol{\mu}_j$. The vibrational shifts are given by

$$\Delta\nu = \langle\psi|\hat{H}_{d-d}|\psi\rangle \tag{B.2}$$

where ψ is the vibrational wavefunction of the entire cluster that is formed from a linear combination of individual monomer vibrational excitations. As can be seen from Equation (B.1), the dipole-dipole interaction (and hence the vibrational shift) depends on the orientation of the monomer subunits. Therefore, observed vibrational shifts can be used in obtaining geometric information on molecular clusters, as has been done for the cyclic CO_2 trimer [99]. On the other hand, for a given cluster structure, vibrational shifts can be calculated.

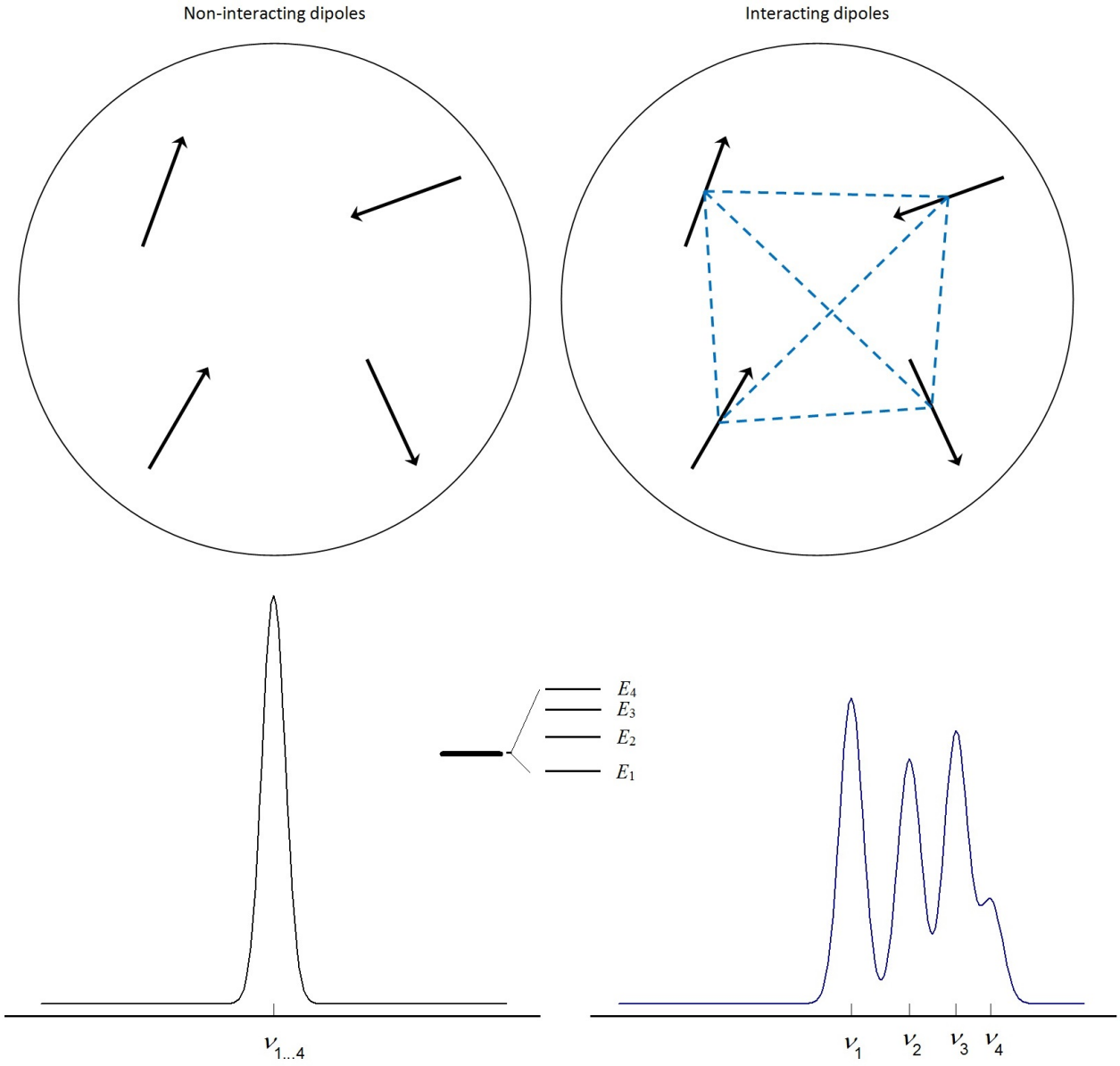

Figure B.1: Schematic representation of dipole-dipole interactions. For simplicity, the cluster is composed of only four molecules, each with a single non-degenerate vibrational mode. Left: Hypothetical non-interacting dipoles within a cluster. Vibrational excited states of the four monomers are degenerate and thus have the same infrared transition. Right: dipole-dipole interactions (represented by dashed lines) lift the degeneracy of vibrational states and leads to a structured vibrational band.

In the case of a dimer with the same constituent monomers, vibrational shifts can be obtained by

$$\begin{vmatrix} \nu_0 + \alpha & \beta \\ \beta & \nu_0 + \alpha \end{vmatrix} = 0. \tag{B.3}$$

Here ν_0 is the vibrational wavenumber for a non-degenerate mode of a lone monomer, and α and β are called "non-resonant" and "resonant" terms, respectively. The "non-resonant" effects may originate from a variety of phenomena.

Solving the second-order secular equation gives the dimer vibrational frequencies,

$$\nu_D^{\pm} = \nu_0 + \alpha \pm \beta. \tag{B.4}$$

where ν_D^+ and ν_D^- are the band centers of two fundamental bands of the dimer.

The resonant and non-resonant terms are isotopically independent and their roles in vibrational shifts may be clarified by isotopic substitution. Determination of resonant and non-resonant terms helps in estimating the vibrational wavenumber for bands that are inaccessible or infrared forbidden [133]. In the case of mixed dimers composed of isotopically different monomers, the secular equation is obtained from

$$\begin{vmatrix} \nu_0 + \alpha & \beta \\ \beta & \nu_0' + \alpha \end{vmatrix} = 0, \tag{B.5}$$

where ν_0 and ν_0' are the band origins of the two constituent monomer bands. Solving the secular equation in this case gives

$$\nu_{MD}^{\pm} = \frac{1}{2}(\nu_0 + \nu_0' + 2\alpha) \pm \frac{1}{2}(\nu_0 - \nu_0')\sqrt{1 + \frac{4\beta^2}{(\nu_0 - \nu_0')^2}}, \tag{B.6}$$

where ν_{MD}^+ and ν_{MD}^- are the band origins of the mixed dimer.

In the same manner, vibrational shifts for larger clusters can be calculated by solving the corresponding secular equation. In general, for a molecular cluster with N monomers, each with a single non-degenerate vibrational mode, there can be N distinct vibrational bands and the band centers are calculated by solving the secular equation of the corresponding $N \times N$

matrix. However, not all N bands may be observed in experiment because of weakness of transition moments, forbidden transitions, or unknown vibrational interactions giving rise to non-resonant effects.

The resonant dipole-dipole model has produced satisfactory results for various molecular clusters [15, 99, 133] but has not been sufficient in cases were the influence of dipole-dipole interaction is not dominant [121].

Appendix C

Supplementary Data for Chapter 4

Observed transitions of the two isomers of OCS−C_2H_2

Tables C.1- C.4 are also available on ScienceDirect (`www.sciencedirect.com`) and as part of the Ohio State University Molecular Spectroscopy Archives (`http://library.osu.edu/sites/msa/jmsa_hp.htm`). Supplementary data associated with this article can be found, in the online version, at doi:10.1016/j.jms.2009.07.003.

Table C.1: Observed transitions in the band of the near-parallel OCS−C_2H_2 (values in cm^{-1}).

J'	K'_a	K'_c	J''	K''_a	K''_c	Observed	Calculated	Obs.-Calc.	Weight
6	5	1	7	6	2	2059.5611	2059.56092	0.00017	1.0
8	4	5	9	5	4	2059.6015	2059.60156	-0.00006	0.2
8	4	4	9	5	5	2059.6049	2059.60470	0.00019	0.2
5	5	0	6	6	1	2059.6814	2059.68120	0.00019	1.0
6	4	2	7	5	3	2059.8417	2059.84187	-0.00017	0.2
8	3	5	9	4	6	2059.9166	2059.91644	0.00015	1.0
5	4	1	6	5	2	2059.9617	2059.96177	-0.00007	1.0
8	2	7	9	3	6	2059.9780	2059.97797	0.00002	0.2
7	3	5	8	4	4	2059.9921	2059.99216	-0.00006	1.0
4	4	0	5	5	1	2060.0820	2060.08192	0.00007	1.0
6	3	4	7	4	3	2060.1167	2060.11697	-0.00027	1.0
6	3	3	7	4	4	2060.1274	2060.12725	0.00014	0.2
7	2	6	8	3	5	2060.1693	2060.16909	0.00020	1.0
5	3	3	6	4	2	2060.2392	2060.23908	0.00011	1.0
5	3	2	6	4	3	2060.2428	2060.24252	0.00027	1.0
8	2	6	9	3	7	2060.3273	2060.32748	-0.00018	1.0
7	2	5	8	3	6	2060.3919	2060.39177	0.00012	1.0
6	2	4	7	3	5	2060.4669	2060.46679	0.00010	1.0
3	3	0	4	4	1	2060.4805	2060.48040	0.00009	0.2
5	2	4	6	3	3	2060.4868	2060.48664	0.00015	1.0

J'	K'_a	K'_c	J''	K''_a	K''_c	Observed	Calculated	Obs.-Calc.	Weight
11	1	10	12	2	11	2060.4935	2060.49332	0.00017	0.2
5	1	5	6	2	4	2060.5519	2060.55164	0.00025	1.0
5	2	3	6	3	4	2060.5542	2060.55385	0.00034	1.0
10	1	9	11	2	10	2060.5772	2060.57648	0.00071	1.0
4	2	3	5	3	2	2060.6236	2060.62349	0.00010	1.0
10	0	10	11	1	11	2060.7365	2060.73659	-0.00009	1.0
10	1	10	11	0	11	2060.7427	2060.74214	0.00055	1.0
3	2	2	4	3	1	2060.7522	2060.75195	0.00024	1.0
3	2	1	4	3	2	2060.7621	2060.76175	0.00034	1.0
4	1	4	5	2	3	2060.7650	2060.76472	0.00027	1.0
8	3	5	9	3	6	2060.7796	2060.77941	0.00018	1.0
7	1	6	8	2	7	2060.7899	2060.78973	0.00016	1.0
8	4	4	9	4	5	2060.7999	2060.79972	0.00017	1.0
8	4	5	9	4	6	2060.8041	2060.80386	0.00023	1.0
9	2	8	10	1	9	2060.8249	2060.82484	0.00005	1.0
8	1	7	9	1	8	2060.8270	2060.82690	0.00009	1.0
9	0	9	10	0	10	2060.8415	2060.84132	0.00017	1.0
9	1	9	10	1	10	2060.8438	2060.84385	-0.00005	1.0
9	1	9	10	0	10	2060.8477	2060.84752	0.00017	1.0
6	1	5	7	2	6	2060.8564	2060.85635	0.00004	1.0
8	2	7	9	2	8	2060.8632	2060.86314	0.00005	1.0
2	2	1	3	3	0	2060.8754	2060.87542	-0.00002	1.0
2	2	0	3	3	1	2060.8774	2060.87736	0.00003	1.0
7	2	5	8	2	6	2060.8898	2060.88963	0.00016	1.0
7	3	4	8	3	5	2060.9146	2060.91451	0.00008	1.0
5	1	4	6	2	5	2060.9262	2060.92627	-0.00007	1.0
7	1	6	8	1	7	2060.9335	2060.93349	0.00000	1.0
8	0	8	9	1	9	2060.9371	2060.93700	0.00009	0.2
8	0	8	9	0	9	2060.9434	2060.94348	-0.00008	1.0
3	1	3	4	2	2	2060.9512	2060.95138	-0.00018	1.0
8	1	8	9	0	9	2060.9542	2060.95423	-0.00003	1.0
5	3	2	5	4	1	2060.9630	2060.96280	0.00019	1.0
6	2	4	7	2	5	2061.0203	2061.02036	-0.00006	1.0
9	3	6	9	4	5	2061.0293	2061.02930	-0.00000	1.0
7	0	7	8	1	8	2061.0338	2061.03384	-0.00004	1.0
7	1	7	8	0	8	2061.0630	2061.06315	-0.00015	1.0

J'	K'_a	K'_c	J''	K''_a	K''_c	Observed	Calculated	Obs.-Calc.	Weight
3	1	2	4	2	3	2061.0857	2061.08566	0.00003	0.2
9	2	8	9	3	7	2061.1020	2061.10187	0.00012	0.2
2	1	2	3	2	1	2061.1147	2061.11471	-0.00001	1.0
7	2	6	8	1	7	2061.1182	2061.11809	0.00010	1.0
8	2	7	8	3	6	2061.1445	2061.14437	0.00012	0.2
6	0	6	7	0	7	2061.1460	2061.14605	-0.00005	1.0
5	2	3	6	2	4	2061.1535	2061.15318	0.00031	1.0
6	1	6	7	1	7	2061.1567	2061.15667	0.00002	1.0
5	1	4	6	1	5	2061.1608	2061.16113	-0.00033	0.1
6	1	6	7	0	7	2061.1755	2061.17542	0.00007	0.2
2	1	1	3	2	2	2061.1776	2061.17787	-0.00027	1.0
5	3	3	6	3	4	2061.1805	2061.18055	-0.00005	1.0
5	0	5	6	1	6	2061.2169	2061.21687	0.00002	0.2
4	2	3	4	3	2	2061.2270	2061.22698	0.00001	1.0
3	2	2	3	3	1	2061.2325	2061.23231	0.00018	1.0
7	1	7	7	2	6	2061.2374	2061.23721	0.00018	1.0
3	2	1	3	3	0	2061.2411	2061.24121	-0.00011	1.0
5	0	5	6	0	6	2061.2472	2061.24710	0.00009	1.0
4	2	2	4	3	1	2061.2525	2061.25244	0.00005	1.0
1	1	1	2	2	0	2061.2593	2061.25926	0.00003	1.0
5	1	5	6	1	6	2061.2622	2061.26210	0.00009	1.0
5	2	3	5	3	2	2061.2722	2061.27212	0.00007	1.0
6	2	5	7	1	6	2061.2759	2061.27567	0.00022	1.0
1	1	0	2	2	1	2061.2792	2061.27916	0.00003	1.0
4	2	2	5	2	3	2061.2865	2061.28634	0.00015	1.0
5	1	5	6	0	6	2061.2927	2061.29234	0.00035	0.2
6	2	4	6	3	3	2061.2999	2061.29980	0.00009	0.2
4	0	4	5	1	5	2061.3031	2061.30312	-0.00002	1.0
6	1	6	6	2	5	2061.3057	2061.30556	0.00013	1.0
4	2	3	5	2	4	2061.3175	2061.31736	0.00013	1.0
7	2	5	7	3	4	2061.3320	2061.33197	0.00002	1.0
4	0	4	5	0	5	2061.3494	2061.34946	-0.00006	1.0
5	1	5	5	2	4	2061.3644	2061.36445	-0.00005	0.2
4	1	4	5	1	5	2061.3686	2061.36846	0.00013	1.0
4	1	4	5	0	5	2061.4147	2061.41480	-0.00010	0.2
3	2	1	4	2	2	2061.4177	2061.41768	0.00001	1.0

J'	K'_a	K'_c	J''	K''_a	K''_c	Observed	Calculated	Obs.-Calc.	Weight
3	1	3	3	2	2	2061.4522	2061.45210	0.00009	1.0
3	0	3	4	0	4	2061.4549	2061.45487	0.00002	1.0
2	0	2	3	1	3	2061.4757	2061.47569	0.00000	0.2
2	1	2	2	2	1	2061.4809	2061.48082	0.00007	1.0
8	1	7	8	2	6	2061.5022	2061.50209	0.00010	1.0
6	0	6	6	1	5	2061.5112	2061.51106	0.00013	1.0
2	1	1	3	1	2	2061.5309	2061.53063	0.00026	1.0
2	1	1	2	2	0	2061.5335	2061.53333	0.00016	1.0
3	1	3	4	0	4	2061.5426	2061.54247	0.00012	1.0
7	1	6	7	2	5	2061.5459	2061.54609	-0.00019	0.2
3	1	2	3	2	1	2061.5517	2061.55172	-0.00002	1.0
2	0	2	3	0	3	2061.5647	2061.56464	0.00005	1.0
5	1	4	5	2	3	2061.5754	2061.57534	0.00005	1.0
2	1	2	3	1	3	2061.5844	2061.58434	0.00005	1.0
4	2	3	5	1	4	2061.5965	2061.59671	-0.00021	0.1
5	0	5	5	1	4	2061.5984	2061.59856	-0.00016	1.0
1	1	0	2	1	1	2061.6577	2061.65777	-0.00007	1.0
4	0	4	4	1	3	2061.6673	2061.66729	0.00000	1.0
0	0	0	1	1	1	2061.6699	2061.67005	-0.00015	1.0
2	1	2	3	0	3	2061.6732	2061.67329	-0.00009	1.0
1	0	1	2	0	2	2061.6786	2061.67880	-0.00020	1.0
1	1	1	2	1	2	2061.6937	2061.69374	-0.00004	1.0
3	0	3	3	1	2	2061.7172	2061.71727	-0.00007	1.0
2	0	2	2	1	1	2061.7506	2061.75078	-0.00018	1.0
3	2	2	4	1	3	2061.7538	2061.75376	0.00003	1.0
1	0	1	1	1	0	2061.7708	2061.77096	-0.00016	1.0
1	1	1	2	0	2	2061.8038	2061.80372	0.00007	1.0
2	1	2	2	1	1	2061.8596	2061.85943	0.00016	1.0
4	4	0	4	4	1	2061.8939	2061.89396	-0.00006	0.2
2	2	1	2	2	0	2061.9083	2061.90808	0.00021	1.0
2	2	0	2	2	1	2061.9119	2061.91170	0.00019	1.0
1	1	0	1	1	1	2061.9320	2061.93200	-0.00000	1.0
3	2	1	4	1	4	2061.9422	2061.94217	0.00002	1.0
7	1	7	6	2	4	2061.9505	2061.95036	0.00013	0.2
6	1	6	5	2	3	2061.9549	2061.95464	0.00025	0.2
2	1	1	2	1	2	2061.9677	2061.96780	-0.00010	1.0

J'	K'_a	K'_c	J''	K''_a	K''_c	Observed	Calculated	Obs.-Calc.	Weight
3	1	2	3	1	3	2062.0212	2062.02135	-0.00015	1.0
2	0	2	1	1	1	2062.0251	2062.02501	0.00008	1.0
1	0	1	0	0	0	2062.0342	2062.03429	-0.00009	1.0
1	1	0	1	0	1	2062.0582	2062.05821	-0.00001	1.0
4	1	3	3	2	2	2062.0684	2062.06840	-0.00000	1.0
2	1	1	2	0	2	2062.0778	2062.07778	0.00001	1.0
3	1	2	3	0	3	2062.1103	2062.11030	-0.00000	1.0
2	1	2	1	1	1	2062.1338	2062.13366	0.00013	1.0
2	0	2	1	0	1	2062.1512	2062.15122	-0.00002	1.0
3	0	3	2	1	2	2062.1545	2062.15444	0.00005	1.0
4	1	3	4	0	4	2062.1589	2062.15877	0.00012	0.2
5	1	4	5	0	5	2062.2255	2062.22542	0.00007	0.2
3	1	3	2	1	2	2062.2421	2062.24204	0.00005	1.0
5	2	3	5	1	4	2062.2454	2062.24534	0.00005	1.0
4	2	2	4	1	3	2062.2541	2062.25425	-0.00015	0.2
2	1	2	1	0	1	2062.2600	2062.25987	0.00012	1.0
3	0	3	2	0	2	2062.2641	2062.26442	-0.00032	1.0
3	2	2	2	2	1	2062.2666	2062.26665	-0.00005	0.1
3	2	1	2	2	0	2062.2737	2062.27387	-0.00017	0.1
4	0	4	3	1	3	2062.2837	2062.28370	-0.00000	1.0
3	1	2	2	1	1	2062.2964	2062.29645	-0.00005	1.0
2	2	1	2	1	2	2062.3425	2062.34255	-0.00005	1.0
4	1	4	3	1	3	2062.3491	2062.34904	0.00005	1.0
3	1	3	2	0	2	2062.3519	2062.35202	-0.00012	1.0
4	0	4	3	0	3	2062.3726	2062.37265	-0.00005	1.0
9	2	7	9	1	8	2062.3742	2062.37422	-0.00002	0.1
4	2	2	3	2	1	2062.4011	2062.40102	0.00007	1.0
4	2	3	4	1	4	2062.4073	2062.40740	-0.00010	0.2
5	0	5	4	1	4	2062.4094	2062.40925	0.00014	1.0
4	1	3	3	1	2	2062.4209	2062.42117	-0.00027	1.0
4	1	4	3	0	3	2062.4379	2062.43799	-0.00009	1.0
8	3	5	8	2	6	2062.4439	2062.44367	0.00022	1.0
5	1	5	4	1	4	2062.4544	2062.45449	-0.00009	0.2
10	2	8	10	1	9	2062.4579	2062.45786	0.00003	1.0
5	0	5	4	0	4	2062.4759	2062.47586	0.00003	0.2
5	2	4	4	2	3	2062.4994	2062.49921	0.00018	1.0

J'	K'_a	K'_c	J''	K''_a	K''_c	Observed	Calculated	Obs.-Calc.	Weight
5	3	3	4	3	2	2062.5023	2062.50230	-0.00000	1.0
5	3	2	4	3	1	2062.5049	2062.50470	0.00019	1.0
5	1	5	4	0	4	2062.5209	2062.52109	-0.00019	1.0
6	0	6	5	1	5	2062.5290	2062.52901	-0.00001	1.0
5	2	3	4	2	2	2062.5313	2062.53154	-0.00024	0.1
5	3	2	5	2	3	2062.5387	2062.53860	0.00009	0.2
2	2	1	1	1	0	2062.5444	2062.54469	-0.00029	0.2
2	2	0	1	1	1	2062.5644	2062.56454	-0.00014	1.0
3	3	0	3	2	1	2062.5714	2062.57155	-0.00015	1.0
3	3	1	3	2	2	2062.5803	2062.58029	0.00000	1.0
4	3	2	4	2	3	2062.5844	2062.58437	0.00002	1.0
5	3	3	5	2	4	2062.5928	2062.59269	0.00011	1.0
9	1	8	9	0	9	2062.6354	2062.63556	-0.00016	1.0
7	0	7	6	1	6	2062.6426	2062.64270	-0.00010	1.0
3	2	2	2	1	1	2062.6449	2062.64526	-0.00036	1.0
8	2	7	8	1	8	2062.6494	2062.64953	-0.00013	1.0
7	1	7	6	0	6	2062.6910	2062.69106	-0.00006	1.0
8	1	7	7	2	6	2062.6944	2062.69464	-0.00024	1.0
9	3	7	9	2	8	2062.6971	2062.69715	-0.00005	1.0
3	2	1	2	1	2	2062.7082	2062.70834	-0.00014	1.0
7	2	6	6	2	5	2062.7250	2062.72499	0.00000	1.0
4	2	3	3	1	2	2062.7362	2062.73641	-0.00021	1.0
7	3	5	6	3	4	2062.7418	2062.74206	-0.00026	1.0
10	3	8	10	2	9	2062.7458	2062.74575	0.00004	1.0
8	0	8	7	1	7	2062.7511	2062.75128	-0.00018	1.0
7	3	4	6	3	3	2062.7556	2062.75555	0.00004	1.0
9	4	5	9	3	6	2062.7593	2062.75935	-0.00005	0.2
8	1	8	7	1	7	2062.7619	2062.76204	-0.00014	1.0
8	0	8	7	0	7	2062.7699	2062.77003	-0.00013	1.0
7	1	6	6	1	5	2062.7751	2062.77527	-0.00017	1.0
8	1	8	7	0	7	2062.7805	2062.78079	-0.00029	1.0
8	4	4	8	3	5	2062.7903	2062.79023	0.00006	1.0
7	2	5	6	2	4	2062.7952	2062.79533	-0.00013	1.0
7	4	3	7	3	4	2062.8115	2062.81151	-0.00001	1.0
5	2	4	4	1	3	2062.8184	2062.81850	-0.00010	1.0
6	4	2	6	3	3	2062.8247	2062.82481	-0.00011	1.0

J'	K'_a	K'_c	J''	K''_a	K''_c	Observed	Calculated	Obs.-Calc.	Weight
9	0	9	8	0	8	2062.8674	2062.86724	0.00015	1.0
4	2	2	3	1	3	2062.8706	2062.87065	-0.00005	1.0
9	1	9	8	0	8	2062.8733	2062.87344	-0.00014	1.0
8	1	7	7	1	6	2062.8831	2062.88319	-0.00009	1.0
8	3	5	7	3	4	2062.8859	2062.88602	-0.00012	1.0
6	2	5	5	1	4	2062.8925	2062.89243	0.00006	1.0
8	2	6	7	2	5	2062.9244	2062.92434	0.00005	1.0
3	3	1	2	2	0	2062.9357	2062.93575	-0.00005	1.0
3	3	0	2	2	1	2062.9373	2062.93766	-0.00036	1.0
10	0	10	9	1	9	2062.9581	2062.95819	-0.00009	1.0
7	2	6	6	1	5	2062.9597	2062.95986	-0.00016	1.0
10	0	10	9	0	9	2062.9645	2062.96467	-0.00017	1.0
10	1	10	9	0	9	2062.9683	2062.96817	0.00012	1.0
9	1	8	8	1	7	2062.9850	2062.98536	-0.00036	1.0
9	3	6	8	3	5	2063.0195	2063.01980	-0.00030	1.0
8	2	7	7	1	6	2063.0234	2063.02333	0.00006	1.0
4	3	2	3	2	1	2063.0504	2063.05043	-0.00003	1.0
5	2	3	4	1	4	2063.0561	2063.05603	0.00006	1.0
4	3	1	3	2	2	2063.0600	2063.06009	-0.00009	1.0
11	1	11	10	0	10	2063.0641	2063.06421	-0.00011	1.0
9	2	8	8	1	7	2063.0860	2063.08613	-0.00013	0.2
10	2	9	9	1	8	2063.1514	2063.15169	-0.00029	0.2
5	3	3	4	2	2	2063.1581	2063.15824	-0.00014	1.0
5	3	2	4	2	3	2063.1872	2063.18723	-0.00003	1.0
11	2	10	10	1	9	2063.2224	2063.22256	-0.00016	1.0
12	1	11	11	2	10	2063.2246	2063.22467	-0.00007	1.0
6	3	4	5	2	3	2063.2560	2063.25590	0.00009	1.0
6	2	4	5	1	5	2063.2674	2063.26748	-0.00008	1.0
4	4	0	3	3	1	2063.3169	2063.31688	0.00001	0.2
6	3	3	5	2	4	2063.3222	2063.32251	-0.00031	1.0
7	3	5	6	2	4	2063.3411	2063.34139	-0.00029	1.0
8	3	6	7	2	5	2063.4142	2063.41445	-0.00025	1.0
7	3	4	6	2	5	2063.4703	2063.47042	-0.00012	1.0
9	3	7	8	2	6	2063.4762	2063.47623	-0.00003	1.0
7	2	5	6	1	6	2063.5056	2063.50579	-0.00019	1.0
10	3	8	9	2	7	2063.5289	2063.52876	0.00013	1.0

J'	K'_a	K'_c	J''	K''_a	K''_c	Observed	Calculated	Obs.-Calc.	Weight
6	4	3	5	3	2	2063.5518	2063.55188	-0.00008	1.0
6	4	2	5	3	3	2063.5551	2063.55523	-0.00013	1.0
8	3	5	7	2	6	2063.6363	2063.63622	0.00007	1.0
7	4	4	6	3	3	2063.6654	2063.66548	-0.00008	1.0
7	4	3	6	3	4	2063.6754	2063.67554	-0.00014	1.0
5	5	0	4	4	1	2063.6942	2063.69424	-0.00004	1.0
6	5	1	5	4	2	2063.8127	2063.81289	-0.00019	1.0

Table C.2: Observed transitions in the band of the near-parallel OCS−C_2D_2 (values in cm^{-1}).

J'	K'_a	K'_c	J''	K''_a	K''_c	Observed	Calculated	Obs.-Calc.	Weight
8	3	5	9	4	6	2059.9967	2059.99677	-0.00007	1.0
8	2	7	9	3	6	2060.0384	2060.03865	-0.00025	1.0
5	4	1	6	5	2	2060.0431	2060.04318	-0.00008	1.0
5	4	2	6	5	1	2060.0431	2060.04312	-0.00002	1.0
7	3	5	8	4	4	2060.0645	2060.06572	-0.00122	0.0
7	3	4	8	4	5	2060.0921	2060.09188	0.00021	1.0
7	1	7	8	2	6	2060.0947	2060.09509	-0.00039	0.2
4	4	0	5	5	1	2060.1578	2060.15790	-0.00010	1.0
6	3	4	7	4	3	2060.1847	2060.18524	-0.00054	1.0
6	3	3	7	4	4	2060.1955	2060.19587	-0.00037	1.0
7	2	6	8	3	5	2060.2238	2060.22424	-0.00044	1.0
5	3	3	6	4	2	2060.3018	2060.30197	-0.00017	1.0
5	3	2	6	4	3	2060.3051	2060.30553	-0.00043	1.0
6	1	6	7	2	5	2060.3514	2060.35188	-0.00048	1.0
6	2	4	7	3	5	2060.5158	2060.51622	-0.00042	1.0
5	1	5	6	2	4	2060.5835	2060.58359	-0.00009	1.0
4	2	3	5	3	2	2060.6627	2060.66251	0.00018	1.0
9	1	8	10	2	9	2060.6875	2060.68725	0.00024	1.0
4	2	2	5	3	3	2060.6913	2060.69184	-0.00054	1.0
10	2	9	11	1	10	2060.7130	2060.71316	-0.00016	1.0
8	1	7	9	2	8	2060.7550	2060.75474	0.00025	1.0
10	0	10	11	1	11	2060.7608	2060.76079	0.00000	1.0
10	1	10	11	0	11	2060.7651	2060.76539	-0.00029	1.0
9	2	8	10	2	9	2060.7758	2060.77580	-0.00000	0.2
8	2	6	9	2	7	2060.7812	2060.78132	-0.00012	1.0
3	2	2	4	3	1	2060.7856	2060.78550	0.00009	1.0
4	1	4	5	2	3	2060.7890	2060.78894	0.00005	1.0
7	1	6	8	2	7	2060.8186	2060.81849	0.00010	1.0
9	2	8	10	1	9	2060.8374	2060.83759	-0.00019	0.2
8	1	7	9	1	8	2060.8466	2060.84617	0.00043	0.2
9	0	9	10	1	10	2060.8571	2060.85704	0.00005	1.0
9	0	9	10	0	10	2060.8602	2060.86012	0.00007	1.0
9	1	9	10	1	10	2060.8623	2060.86229	0.00000	1.0

J'	K'_a	K'_c	J''	K''_a	K''_c	Observed	Calculated	Obs.-Calc.	Weight
6	1	5	7	2	6	2060.8819	2060.88179	0.00010	1.0
2	2	1	3	3	0	2060.9035	2060.90348	0.00001	1.0
2	2	0	3	3	1	2060.9054	2060.90542	-0.00002	1.0
5	1	4	6	2	5	2060.9490	2060.94803	0.00096	0.0
8	0	8	9	1	9	2060.9519	2060.95178	0.00011	1.0
8	1	8	9	1	9	2060.9613	2060.96103	0.00026	1.0
7	2	6	8	2	7	2060.9854	2060.98530	0.00009	1.0
5	3	2	5	4	1	2060.9928	2060.99269	0.00010	1.0
6	3	3	6	4	2	2060.9989	2060.99887	0.00002	1.0
4	1	3	5	2	4	2061.0197	2061.01989	-0.00019	1.0
6	2	4	7	2	5	2061.0270	2061.02681	0.00018	1.0
8	3	5	8	4	4	2061.0310	2061.03054	0.00045	1.0
7	0	7	8	1	8	2061.0445	2061.04423	0.00026	1.0
7	1	7	8	0	8	2061.0697	2061.06969	0.00000	1.0
9	1	9	9	2	8	2061.0843	2061.08409	0.00020	1.0
6	2	5	7	2	6	2061.0925	2061.09251	-0.00001	1.0
3	1	2	4	2	3	2061.0989	2061.09913	-0.00023	1.0
7	2	6	8	1	7	2061.1137	2061.11365	0.00004	0.2
6	0	6	7	1	7	2061.1335	2061.13354	-0.00004	1.0
6	0	6	7	0	7	2061.1498	2061.14993	-0.00013	1.0
5	2	3	6	2	4	2061.1535	2061.15353	-0.00003	1.0
8	2	7	8	3	6	2061.1567	2061.15686	-0.00016	1.0
6	1	6	7	1	7	2061.1594	2061.15957	-0.00017	1.0
5	1	4	6	1	5	2061.1634	2061.16249	0.00090	0.0
6	1	6	7	0	7	2061.1758	2061.17595	-0.00015	1.0
5	3	3	6	3	4	2061.1810	2061.18092	0.00007	1.0
2	1	1	3	2	2	2061.1865	2061.18673	-0.00023	1.0
7	2	6	7	3	5	2061.1892	2061.18911	0.00008	1.0
5	2	4	6	2	5	2061.2013	2061.20133	-0.00003	1.0
6	2	5	6	3	4	2061.2128	2061.21265	0.00014	0.2
5	2	4	5	3	3	2061.2287	2061.22863	0.00006	1.0
4	2	3	4	3	2	2061.2390	2061.23848	0.00051	0.2
3	2	1	3	3	0	2061.2525	2061.25268	-0.00018	1.0
5	1	5	6	1	6	2061.2599	2061.25979	0.00010	1.0
1	1	1	2	2	0	2061.2636	2061.26384	-0.00024	1.0
4	1	3	5	1	4	2061.2770	2061.27692	0.00007	1.0

J'	K'_a	K'_c	J''	K''_a	K''_c	Observed	Calculated	Obs.-Calc.	Weight
4	2	2	5	2	3	2061.2805	2061.28081	-0.00031	0.1
5	1	5	6	0	6	2061.2866	2061.28658	0.00001	1.0
4	3	1	5	3	2	2061.2947	2061.29471	-0.00001	1.0
4	3	2	5	3	3	2061.2971	2061.29707	0.00002	1.0
4	0	4	5	1	5	2061.3016	2061.30145	0.00014	1.0
6	1	6	6	2	5	2061.3054	2061.30545	-0.00005	1.0
10	1	9	10	2	8	2061.3350	2061.33501	-0.00001	1.0
7	2	5	7	3	4	2061.3410	2061.34094	0.00005	1.0
4	0	4	5	0	5	2061.3428	2061.34308	-0.00028	1.0
4	1	4	5	1	5	2061.3610	2061.36092	0.00007	0.2
5	1	5	5	2	4	2061.3625	2061.36238	0.00011	1.0
8	2	6	8	3	5	2061.3697	2061.36963	0.00006	1.0
3	1	2	4	1	3	2061.3943	2061.39454	-0.00024	0.1
4	1	4	5	0	5	2061.4026	2061.40255	0.00004	1.0
5	2	4	6	1	5	2061.4159	2061.41578	0.00011	1.0
3	2	2	4	2	3	2061.4234	2061.42325	0.00014	0.1
3	0	3	4	0	4	2061.4433	2061.44312	0.00017	1.0
3	1	3	3	2	2	2061.4473	2061.44719	0.00010	1.0
3	1	3	4	1	4	2061.4632	2061.46310	0.00009	1.0
2	0	2	3	1	3	2061.4657	2061.46562	0.00007	1.0
2	1	2	2	2	1	2061.4751	2061.47498	0.00011	1.0
6	0	6	6	1	5	2061.4941	2061.49388	0.00021	1.0
3	1	3	4	0	4	2061.5239	2061.52370	0.00019	1.0
2	1	1	2	2	0	2061.5253	2061.52564	-0.00034	0.2
2	2	0	3	2	1	2061.5289	2061.52886	0.00003	1.0
7	1	6	7	2	5	2061.5330	2061.53288	0.00011	1.0
3	1	2	3	2	1	2061.5432	2061.54312	0.00007	1.0
2	0	2	3	0	3	2061.5475	2061.54740	0.00009	1.0
1	0	1	2	1	2	2061.5541	2061.55413	-0.00003	1.0
4	1	3	4	2	2	2061.5579	2061.55792	-0.00002	0.1
5	1	4	5	2	3	2061.5657	2061.56430	0.00139	0.0
4	2	3	5	1	4	2061.5686	2061.56868	-0.00008	1.0
5	0	5	5	1	4	2061.5780	2061.57875	-0.00075	0.0
1	1	0	2	1	1	2061.6360	2061.63575	0.00024	1.0
4	0	4	4	1	3	2061.6460	2061.64563	0.00036	1.0
2	1	2	3	0	3	2061.6484	2061.64813	0.00026	0.2

J'	K'_a	K'_c	J''	K''_a	K''_c	Observed	Calculated	Obs.-Calc.	Weight
1	0	1	2	0	2	2061.6562	2061.65605	0.00014	1.0
1	1	1	2	1	2	2061.6705	2061.67052	-0.00002	1.0
3	0	3	3	1	2	2061.6943	2061.69429	0.00000	1.0
3	2	2	4	1	3	2061.7190	2061.71867	0.00032	0.2
2	0	2	2	1	1	2061.7270	2061.72688	0.00011	1.0
1	0	1	1	1	0	2061.7465	2061.74644	0.00005	1.0
2	1	2	2	1	1	2061.8278	2061.82760	0.00019	0.2
2	2	1	2	2	0	2061.8748	2061.87479	0.00000	1.0
2	2	0	2	2	1	2061.8784	2061.87841	-0.00001	1.0
3	2	1	3	2	2	2061.8851	2061.88508	0.00001	0.2
1	1	0	1	1	1	2061.8978	2061.89773	0.00006	1.0
2	1	1	2	1	2	2061.9324	2061.93231	0.00008	0.2
2	0	2	1	1	1	2061.9889	2061.98886	0.00003	1.0
1	1	0	1	0	1	2062.0152	2062.01528	-0.00008	1.0
2	1	1	2	0	2	2062.0342	2062.03423	-0.00003	1.0
3	1	2	3	0	3	2062.0657	2062.06582	-0.00012	1.0
2	1	2	1	1	1	2062.0899	2062.08959	0.00030	0.2
2	0	2	1	0	1	2062.1064	2062.10640	-0.00000	1.0
5	1	4	5	0	5	2062.1790	2062.17791	0.00108	0.0
5	1	4	4	2	3	2062.1862	2062.18505	0.00114	0.0
5	2	3	5	1	4	2062.1894	2062.18935	0.00004	1.0
3	1	3	2	1	2	2062.1929	2062.19277	0.00012	1.0
6	2	4	6	1	5	2062.1951	2062.19483	0.00026	1.0
4	2	2	4	1	3	2062.1969	2062.19697	-0.00007	1.0
3	2	1	3	1	2	2062.2128	2062.21276	0.00003	1.0
7	2	5	7	1	6	2062.2172	2062.21716	0.00003	0.1
3	2	1	2	2	0	2062.2241	2062.22399	0.00010	0.2
4	0	4	3	1	3	2062.2353	2062.23513	0.00017	1.0
3	1	2	2	1	1	2062.2453	2062.24529	0.00000	1.0
8	2	6	8	1	7	2062.2591	2062.25904	0.00005	0.2
6	1	5	6	0	6	2062.2604	2062.26025	0.00014	1.0
2	2	1	2	1	2	2062.2814	2062.28146	-0.00006	1.0
3	1	3	2	0	2	2062.2947	2062.29469	0.00000	1.0
4	0	4	3	0	3	2062.3170	2062.31691	0.00008	1.0
9	2	7	9	1	8	2062.3228	2062.32190	0.00089	0.0
4	2	3	3	2	2	2062.3282	2062.32826	-0.00006	0.2

J'	K'_a	K'_c	J''	K''_a	K''_c	Observed	Calculated	Obs.-Calc.	Weight
6	1	5	5	2	4	2062.3363	2062.33604	0.00025	1.0
4	2	3	4	1	4	2062.3443	2062.34417	0.00012	0.2
5	0	5	4	1	4	2062.3534	2062.35425	-0.00085	0.0
7	1	6	7	0	7	2062.3569	2062.35695	-0.00005	1.0
4	1	3	3	1	2	2062.3641	2062.36419	-0.00009	1.0
4	1	4	3	0	3	2062.3763	2062.37638	-0.00008	1.0
5	2	4	5	1	5	2062.3897	2062.38958	0.00011	1.0
5	1	5	4	1	4	2062.3951	2062.39490	0.00019	1.0
7	3	4	7	2	5	2062.4017	2062.40097	0.00072	0.0
10	2	8	10	1	9	2062.4050	2062.40507	-0.00007	1.0
5	0	5	4	0	4	2062.4135	2062.41485	-0.00135	0.0
6	3	3	6	2	4	2062.4332	2062.43315	0.00004	1.0
5	2	4	4	2	3	2062.4385	2062.43834	0.00015	1.0
6	2	5	6	1	6	2062.4442	2062.44417	0.00002	0.2
5	1	5	4	0	4	2062.4556	2062.45550	0.00009	1.0
5	3	2	5	2	3	2062.4615	2062.46135	0.00014	1.0
6	0	6	5	1	5	2062.4677	2062.46768	0.00001	1.0
5	2	3	4	2	2	2062.4704	2062.47035	0.00004	1.0
2	2	1	1	1	0	2062.4738	2062.47377	0.00002	1.0
3	3	1	3	2	2	2062.5028	2062.50277	0.00002	1.0
4	3	2	4	2	3	2062.5070	2062.50679	0.00020	0.2
6	0	6	5	0	5	2062.5090	2062.50930	-0.00030	0.2
5	3	3	5	2	4	2062.5153	2062.51503	0.00026	1.0
6	3	4	6	2	5	2062.5291	2062.52907	0.00002	1.0
6	1	6	5	0	5	2062.5352	2062.53533	-0.00013	1.0
7	3	5	7	2	6	2062.5491	2062.55033	-0.00123	0.0
6	3	4	5	3	3	2062.5564	2062.55637	0.00002	1.0
6	3	3	5	3	2	2062.5627	2062.56280	-0.00010	1.0
3	2	2	2	1	1	2062.5694	2062.56942	-0.00002	1.0
9	1	8	9	0	9	2062.5729	2062.57281	0.00008	0.1
7	0	7	6	1	6	2062.5751	2062.57529	-0.00019	1.0
8	2	7	8	1	8	2062.5782	2062.57834	-0.00014	0.2
8	3	6	8	2	7	2062.5801	2062.57995	0.00014	1.0
7	1	7	6	1	6	2062.5912	2062.59111	0.00008	1.0
6	1	5	5	1	4	2062.5933	2062.59307	0.00022	1.0
3	2	1	2	1	2	2062.6304	2062.63066	-0.00026	1.0

J'	K'_a	K'_c	J''	K''_a	K''_c	Observed	Calculated	Obs.-Calc.	Weight
8	1	7	7	2	6	2062.6328	2062.63272	0.00007	1.0
7	2	6	6	2	5	2062.6533	2062.65327	0.00002	1.0
4	2	3	3	1	2	2062.6558	2062.65595	-0.00015	1.0
7	3	5	6	3	4	2062.6693	2062.67047	-0.00117	0.0
8	0	8	7	1	7	2062.6780	2062.67811	-0.00011	1.0
8	1	8	7	1	7	2062.6872	2062.68736	-0.00016	1.0
8	0	8	7	0	7	2062.6941	2062.69449	-0.00039	0.2
7	1	6	6	1	5	2062.7009	2062.70090	-0.00000	1.0
8	1	8	7	0	7	2062.7037	2062.70374	-0.00004	1.0
7	4	3	7	3	4	2062.7165	2062.71619	0.00030	1.0
7	2	5	6	2	4	2062.7221	2062.72219	-0.00009	1.0
6	4	2	6	3	3	2062.7299	2062.72974	0.00015	1.0
5	2	4	4	1	3	2062.7337	2062.73376	-0.00006	1.0
8	2	7	7	2	6	2062.7573	2062.75774	-0.00044	1.0
9	1	8	8	2	7	2062.7716	2062.77155	0.00004	1.0
9	0	9	8	1	8	2062.7775	2062.77742	0.00007	1.0
4	2	2	3	1	3	2062.7865	2062.78646	0.00003	0.2
9	1	9	8	0	8	2062.7923	2062.79230	-0.00000	1.0
6	2	5	5	1	4	2062.8038	2062.80378	0.00001	0.2
8	3	5	7	3	4	2062.8096	2062.80937	0.00022	1.0
3	3	1	2	2	0	2062.8417	2062.84167	0.00002	1.0
3	3	0	2	2	1	2062.8434	2062.84359	-0.00019	1.0
7	2	6	6	1	5	2062.8677	2062.86772	-0.00002	1.0
10	0	10	9	1	9	2062.8744	2062.87434	0.00005	1.0
10	1	10	9	1	9	2062.8771	2062.87726	-0.00016	1.0
10	0	10	9	0	9	2062.8802	2062.87985	0.00034	1.0
8	2	7	7	1	6	2062.9281	2062.92817	-0.00007	1.0
4	3	2	3	2	1	2062.9508	2062.95078	0.00001	1.0
4	3	1	3	2	2	2062.9605	2062.96046	0.00003	1.0
5	2	3	4	1	4	2062.9649	2062.96485	0.00004	1.0
11	0	11	10	1	10	2062.9698	2062.96972	0.00007	0.1
6	5	2	6	4	3	2062.9807	2062.98059	0.00010	0.1
5	5	1	5	4	2	2062.9836	2062.98318	0.00041	0.2
9	2	8	8	1	7	2062.9885	2062.98846	0.00003	1.0
5	3	3	4	2	2	2063.0529	2063.05306	-0.00016	1.0
12	0	12	11	1	11	2063.0642	2063.06409	0.00010	0.2

J'	K'_a	K'_c	J''	K''_a	K''_c	Observed	Calculated	Obs.-Calc.	Weight
10	2	8	9	2	7	2063.0782	2063.07822	-0.00002	1.0
5	3	2	4	2	3	2063.0819	2063.08209	-0.00019	1.0
6	3	4	5	2	3	2063.1452	2063.14534	-0.00014	1.0
6	2	4	5	1	5	2063.1683	2063.16863	-0.00033	1.0
4	4	0	3	3	1	2063.2000	2063.20012	-0.00012	0.2
7	3	5	6	2	4	2063.2249	2063.22579	-0.00089	0.0
8	3	6	7	2	5	2063.2945	2063.29434	0.00015	1.0
9	3	7	8	2	6	2063.3523	2063.35226	0.00003	1.0
7	3	4	6	2	5	2063.3549	2063.35454	0.00035	1.0
6	4	3	5	3	2	2063.4240	2063.42381	0.00018	1.0
6	4	2	5	3	3	2063.4273	2063.42729	0.00000	1.0
7	4	4	6	3	3	2063.5318	2063.53170	0.00009	1.0
7	4	3	6	3	4	2063.5421	2063.54212	-0.00002	1.0
5	5	0	4	4	1	2063.5548	2063.55488	-0.00008	1.0
8	4	4	7	3	5	2063.6584	2063.65956	-0.00116	1.0
6	5	1	5	4	2	2063.6678	2063.66781	-0.00001	1.0
9	3	6	8	2	7	2063.6987	2063.69875	-0.00005	1.0
9	4	6	8	3	5	2063.7273	2063.72716	0.00013	1.0
6	6	1	5	5	0	2063.9073	2063.90704	0.00025	1.0
6	6	0	5	5	1	2063.9073	2063.90704	0.00025	1.0

Table C.3: Observed transitions in the band of the T-shaped OCS−C_2H_2 (values in cm^{-1}).

J'	K'_a	K'_c	J''	K''_a	K''_c	Observed	Calculated	Obs.-Calc.	Weight
14	1	13	15	1	14	2055.4440	2055.44365	0.00034	0.2
14	1	14	15	1	15	2055.4619	2055.46159	0.00030	0.2
13	1	12	14	1	13	2055.5154	2055.51500	0.00039	0.2
13	1	13	14	1	14	2055.5318	2055.53173	0.00006	1.0
12	1	11	13	1	12	2055.5864	2055.58635	0.00004	1.0
12	0	12	13	0	13	2055.5947	2055.59455	0.00014	0.2
12	1	12	13	1	13	2055.6021	2055.60186	0.00023	1.0
11	1	10	12	1	11	2055.6578	2055.65769	0.00010	1.0
11	0	11	12	0	12	2055.6652	2055.66530	-0.00010	0.2
11	1	11	12	1	12	2055.6720	2055.67198	0.00001	1.0
10	1	9	11	1	10	2055.7291	2055.72901	0.00008	1.0
10	0	10	11	0	11	2055.7360	2055.73604	-0.00004	1.0
10	1	10	11	1	11	2055.7422	2055.74210	0.00009	1.0
9	1	8	10	1	9	2055.8000	2055.80033	-0.00033	1.0
9	0	9	10	0	10	2055.8066	2055.80677	-0.00017	0.2
9	1	9	10	1	10	2055.8120	2055.81221	-0.00021	1.0
8	1	7	9	1	8	2055.8716	2055.87163	-0.00003	1.0
8	0	8	9	0	9	2055.8774	2055.87750	-0.00010	1.0
8	1	8	9	1	9	2055.8823	2055.88231	-0.00001	1.0
7	1	6	8	1	7	2055.9430	2055.94292	0.00007	1.0
7	0	7	8	0	8	2055.9480	2055.94821	-0.00021	1.0
7	1	7	8	1	8	2055.9523	2055.95240	-0.00010	1.0
6	1	5	7	1	6	2056.0142	2056.01419	0.00000	1.0
6	0	6	7	0	7	2056.0189	2056.01891	-0.00001	1.0
6	1	6	7	1	7	2056.0224	2056.02247	-0.00007	1.0
4	1	3	5	1	4	2056.1568	2056.15668	0.00011	1.0
4	0	4	5	0	5	2056.1602	2056.16026	-0.00006	1.0
4	1	4	5	1	5	2056.1626	2056.16257	0.00002	1.0
3	1	2	4	1	3	2056.2280	2056.22789	0.00010	1.0
3	0	3	4	0	4	2056.2308	2056.23091	-0.00011	1.0
3	1	3	4	1	4	2056.2324	2056.23260	-0.00020	1.0
1	1	0	2	1	1	2056.3703	2056.37024	0.00005	1.0
1	1	1	2	1	2	2056.3724	2056.37259	-0.00019	0.2
0	0	0	1	0	1	2056.4425	2056.44271	-0.00021	1.0
4	1	4	4	1	3	2056.5003	2056.50052	-0.00022	0.1

J'	K'_a	K'_c	J''	K''_a	K''_c	Observed	Calculated	Obs.-Calc.	Weight
3	1	3	3	1	2	2056.5052	2056.50531	-0.00011	0.1
1	1	1	1	1	0	2056.5110	2056.51129	-0.00029	1.0
1	1	0	1	1	1	2056.5137	2056.51363	0.00006	1.0
2	1	1	2	1	2	2056.5158	2056.51591	-0.00011	1.0
3	1	2	3	1	3	2056.5193	2056.51934	-0.00004	1.0
4	1	3	4	1	4	2056.5241	2056.52391	0.00018	0.2
1	0	1	0	0	0	2056.5842	2056.58376	0.00043	1.0
2	1	2	1	1	1	2056.6527	2056.65229	0.00040	0.2
2	1	1	1	1	0	2056.6547	2056.65462	0.00007	0.2
3	1	3	2	1	2	2056.7225	2056.72214	0.00035	1.0
3	1	2	2	1	1	2056.7256	2056.72563	-0.00003	0.1
4	1	4	3	1	3	2056.7922	2056.79197	0.00022	1.0
4	0	4	3	0	3	2056.7951	2056.79510	-0.00000	0.1
4	1	3	3	1	2	2056.7964	2056.79662	-0.00022	1.0
5	1	5	4	1	4	2056.8619	2056.86177	0.00012	1.0
5	0	5	4	0	4	2056.8656	2056.86547	0.00012	1.0
5	1	4	4	1	3	2056.8675	2056.86757	-0.00007	1.0
6	1	6	5	1	5	2056.9315	2056.93153	-0.00003	1.0
6	0	6	5	0	5	2056.9357	2056.93579	-0.00009	1.0
6	1	5	5	1	4	2056.9385	2056.93848	0.00001	1.0
7	1	7	6	1	6	2057.0014	2057.00126	0.00013	1.0
7	0	7	6	0	6	2057.0062	2057.00608	0.00011	1.0
7	1	6	6	1	5	2057.0094	2057.00935	0.00004	1.0
8	1	8	7	1	7	2057.0710	2057.07096	0.00003	1.0
8	0	8	7	0	7	2057.0764	2057.07631	0.00008	1.0
8	1	7	7	1	6	2057.0803	2057.08018	0.00011	1.0
9	1	9	8	1	8	2057.1406	2057.14062	-0.00002	1.0
9	0	9	8	0	8	2057.1465	2057.14651	-0.00001	1.0
9	1	8	8	1	7	2057.1508	2057.15098	-0.00018	1.0
10	1	10	9	1	9	2057.2103	2057.21024	0.00005	1.0
11	0	11	10	0	10	2057.2868	2057.28674	0.00005	1.0
11	1	10	10	1	9	2057.2925	2057.29244	0.00005	1.0
12	1	12	11	1	11	2057.3493	2057.34937	-0.00007	1.0
12	0	12	11	0	11	2057.3569	2057.35677	0.00012	1.0
12	1	11	11	1	10	2057.3632	2057.36310	0.00009	1.0
13	1	13	12	1	12	2057.4188	2057.41887	-0.00007	1.0

J'	K'_a	K'_c	J''	K''_a	K''_c	Observed	Calculated	Obs.-Calc.	Weight
13	0	13	12	0	12	2057.4267	2057.42676	-0.00006	1.0
13	1	12	12	1	11	2057.4336	2057.43372	-0.00012	1.0
14	1	14	13	1	13	2057.4882	2057.48833	-0.00013	1.0
14	0	14	13	0	13	2057.4965	2057.49668	-0.00018	0.1
15	1	15	14	1	14	2057.5576	2057.55775	-0.00015	0.2
15	0	15	14	0	14	2057.5666	2057.56655	0.00004	0.2
15	1	14	14	1	13	2057.5749	2057.57480	0.00009	0.2

Table C.4: Observed transitions in the band of the T-shaped OCS−C_2D_2 (values in cm^{-1}).

J'	K'_a	K'_c	J''	K''_a	K''_c	Observed	Calculated	Obs.-Calc.	Weight
13	0	13	14	0	14	2055.4989	2055.49875	0.00014	1.0
12	0	12	13	0	13	2055.5663	2055.56630	0.00007	1.0
11	0	11	12	0	12	2055.6336	2055.63382	-0.00016	1.0
10	0	10	11	0	11	2055.7012	2055.70133	-0.00011	1.0
10	1	10	11	1	11	2055.7089	2055.70909	-0.00018	1.0
9	1	8	10	1	9	2055.7610	2055.76113	-0.00004	1.0
9	0	9	10	0	10	2055.7687	2055.76883	-0.00008	1.0
9	1	9	10	1	10	2055.7757	2055.77585	-0.00005	1.0
8	1	7	9	1	8	2055.8292	2055.82939	-0.00011	1.0
8	1	8	9	1	9	2055.8424	2055.84260	-0.00013	1.0
7	1	6	8	1	7	2055.8978	2055.89761	0.00021	1.0
7	0	7	8	0	8	2055.9038	2055.90378	0.00005	1.0
7	1	7	8	1	8	2055.9093	2055.90933	0.00000	1.0
6	1	5	7	1	6	2055.9660	2055.96581	0.00024	1.0
6	0	6	7	0	7	2055.9712	2055.97124	0.00000	1.0
6	1	6	7	1	7	2055.9761	2055.97605	0.00007	1.0
5	0	5	6	0	6	2056.0389	2056.03870	0.00021	1.0
4	1	3	5	1	4	2056.1020	2056.10215	-0.00006	1.0
4	0	4	5	0	5	2056.1057	2056.10614	-0.00037	1.0
4	1	4	5	1	5	2056.1094	2056.10946	-0.00001	1.0
3	1	2	4	1	3	2056.1704	2056.17030	0.00011	1.0
3	1	3	4	1	4	2056.1759	2056.17614	-0.00017	1.0
2	0	2	3	0	3	2056.2409	2056.24100	-0.00006	1.0
1	0	1	2	0	2	2056.3086	2056.30842	0.00023	0.2
0	0	0	1	0	1	2056.3756	2056.37582	-0.00015	1.0
1	0	1	0	0	0	2056.5107	2056.51058	0.00018	1.0
2	1	2	1	1	1	2056.5759	2056.57600	-0.00001	1.0
2	0	2	1	0	1	2056.5783	2056.57793	0.00041	0.2
3	0	3	2	0	2	2056.6453	2056.64525	0.00008	1.0
5	1	5	4	1	4	2056.7758	2056.77568	0.00018	1.0
5	2	3	4	2	2	2056.7778	2056.77790	-0.00003	1.0
5	2	4	4	2	3	2056.7778	2056.77786	0.00000	1.0
5	0	5	4	0	4	2056.7798	2056.77980	0.00002	1.0
5	1	4	4	1	3	2056.7829	2056.78299	-0.00008	1.0
6	2	5	5	2	4	2056.8451	2056.84510	0.00000	0.2

J'	K'_a	K'_c	J''	K''_a	K''_c	Observed	Calculated	Obs.-Calc.	Weight
6	2	4	5	2	3	2056.8451	2056.84516	-0.00006	0.2
6	0	6	5	0	5	2056.8469	2056.84702	-0.00012	1.0
6	1	5	5	1	4	2056.8512	2056.85096	0.00024	0.2
7	1	7	6	1	6	2056.9087	2056.90868	0.00005	1.0
7	2	6	6	2	5	2056.9122	2056.91231	-0.00005	0.2
7	2	5	6	2	4	2056.9122	2056.91241	-0.00016	0.2
7	0	7	6	0	6	2056.9141	2056.91419	-0.00006	1.0
7	1	6	6	1	5	2056.9187	2056.91887	-0.00015	1.0
8	1	8	7	1	7	2056.9751	2056.97512	0.00005	1.0
8	2	6	7	2	5	2056.9793	2056.97965	-0.00029	0.1
8	2	7	7	2	6	2056.9793	2056.97949	-0.00013	0.1
8	0	8	7	0	7	2056.9816	2056.98130	0.00032	1.0
8	1	7	7	1	6	2056.9867	2056.98675	-0.00002	1.0
9	1	9	8	1	8	2057.0419	2057.04152	0.00037	1.0
9	0	9	8	0	8	2057.0483	2057.04835	0.00001	1.0
9	1	8	8	1	7	2057.0543	2057.05456	-0.00018	1.0
10	1	10	9	1	9	2057.1077	2057.10789	-0.00014	1.0
10	0	10	9	0	9	2057.1151	2057.11533	-0.00014	1.0
10	1	9	9	1	8	2057.1224	2057.12231	0.00018	1.0
11	0	11	10	0	10	2057.1824	2057.18223	0.00017	1.0
11	1	10	10	1	9	2057.1900	2057.18998	0.00008	1.0
12	0	12	11	0	11	2057.2488	2057.24904	-0.00015	1.0
12	1	11	11	1	10	2057.2577	2057.25756	0.00013	0.2
13	1	13	12	1	12	2057.3066	2057.30666	0.00003	1.0
13	0	13	12	0	12	2057.3157	2057.31576	-0.00003	1.0
13	1	12	12	1	11	2057.3250	2057.32505	-0.00005	1.0
14	1	14	13	1	13	2057.3728	2057.37279	0.00008	0.2

Appendix D

Supplementary Data for Chapter 7

Nuclear spin weights for the two isomers of N_2O tetramer

This appendix includes the details of determination of nuclear spin weights for the D_{2d} and S_4 structures of $(^{14}N_2^{16}O)_4$ and $(^{15}N_2^{16}O)_4$.

$(N_2O)_4$ with S_4 symmetry:

Table D.1: Character table for S_4 point group.

S_4	E	S_4	C_2	$(S_4)^3$	
A	1	1	1	1	R_z
B	1	-1	1	-1	z
E^+	1	i	-1	$-i$	(x, y)
E^-	1	$-i$	-1	$+i$	(R_x, R_y)

Reducible representation generated by the N=N stretching fundamentals:

S_4	E	S_4	C_2	$(S_4)^3$
$\chi_{N=N}$	4	0	0	0

$$\Gamma_{N=N} = A \oplus B \oplus E \tag{D.1}$$

B and E give rise to a parallel band and a perpendicular band, respectively.

For $(^{14}N_2O)_4$, the reducible representation generated by the spin functions is:

S_4	E	S_4	C_2	$(S_4)^3$
χ_{spin}	2×3^8	0	2×3^4	0

Using Equation (8-28) of reference [42],

$$\chi_{C_2} = 2\{(2I+1)(-1)^{2\times I(n-1)}\}^4$$

$$\chi_{C_2} = 2\{(3)(-1)^{2\times 1(2-1)}\}^4 = 2\times 3^4$$

$$a_A = \frac{1}{4}(2\times 3^8 + 2\times 3^4) = 3321$$
$$a_B = \frac{1}{4}(2\times 3^8 + 2\times 3^4) = 3321$$
$$a_{E^+} = \frac{1}{4}(2\times 3^8 - 2\times 3^4) = 3240$$
$$a_{E^-} = \frac{1}{4}(2\times 3^8 - 2\times 3^4) = 3240$$

$$\Gamma_{spin} = 3321A \oplus 3321B \oplus 6480E. \tag{D.2}$$

For $(^{15}N_2O)_4$, the reducible representation generated by the spin functions is:

S_4	E	S_4	C_2	$(S_4)^3$
χ_{spin}	2×2^8	0	2×2^4	0

$$\chi_{C_2} = 2\{(2I+1)(-1)^{2\times I(n-1)}\}^4$$
$$\chi_{C_2} = 2\{(2)(-1)^{2\times \frac{1}{2}(2-1)}\}^4 = 2\times 2^4$$

$$a_A = \frac{1}{4}(2\times 2^8 + 2\times 2^4) = 136$$
$$a_B = \frac{1}{4}(2\times 2^8 + 2\times 2^4) = 136$$
$$a_{E^+} = \frac{1}{4}(2\times 2^8 - 2\times 2^4) = 120$$
$$a_{E^-} = \frac{1}{4}(2\times 2^8 - 2\times 2^4) = 120$$

$$\Gamma_{spin} = 136A \oplus 136B \oplus 240E. \tag{D.3}$$

Fundamental vibrations:

S_4	E	S_4	C_2	$(S_4)^3$
χ	36	0	0	0

$$\Gamma_{Total} = 9A \oplus 9B \oplus 9E^+ \oplus 9E^-$$

$$\Gamma_{Rotation} = A \oplus E^+ \oplus E^-$$

$$\Gamma_{Translation} = B \oplus E^+ \oplus E^-$$

$$\Gamma_{Vibration} = 8A \oplus 8B \oplus 7E^+ \oplus 7E^-$$

$(N_2O)_4$ with D_{2d} symmetry:

Table D.2: Character table for D_{2d} point group.

D_{2d}	E	$2S_4$	$C_2(z)$	$2C_2'$	$2\sigma_d$	
A_1	1	1	1	1	1	
A_2	1	1	1	-1	-1	R_z
B_1	1	-1	1	1	-1	
B_2	1	-1	1	-1	1	z
E	2	0	-2	0	0	$(x, y), (R_x, R_y)$

For $(^{14}N_2O)_4$, the reducible representation generated by the spin functions is:

D_{2d}	E	S_4	C_2	C_2'	σ_d
χ_{spin}	2×3^8	0	162	162	0

$$n_{A_1} = 1701, \quad n_{A_2} = 1620, \quad n_{B_1} = 1701, \quad n_{B_2} = 1701, \quad n_E = 3240.$$

For $(^{15}N_2O)_4$, the reducible representation generated by the spin functions is:

D_{2d}	E	S_4	C_2	C_2'	σ_d
χ_{spin}	2×2^8	0	32	32	0

$$n_{A_1} = 76, \quad n_{A_2} = 60, \quad n_{B_1} = 76, \quad n_{B_2} = 60, \quad n_E = 120.$$

Candidate's contribution

Candidate's contributions in the published works presented in this thesis are briefly explained here.

Chapter 4

Infrared spectra of two isomers of OCS-C_2H_2 and OCS-C_2D_2 in the region of OCS ν_1 fundamental

The candidate has been involved in carrying out the experiments and collecting the data, performed post-experiment data manipulation and processing, and partially contributed in writing and preparing materials for the manuscript.

Chapter 5

Ubiquitous T-shaped isomers of OCS-hydrocarbon van der Waals complexes

The candidate has been involved in carrying out the experiments and collecting the data, performed post-experiment data manipulation and processing, and prepared the graphical materials for the manuscript.

Chapter 6

High resolution infrared spectroscopy of carbon dioxide clusters up to $(CO_2)_{13}$

The candidate has carried out the experiments and collected data for new infrared bands, re-measured previously recorded data with increased signal to noise ratio, and prepared graphical materials for the manuscript.

Chapter 7

Nitrous oxide tetramer has two highly symmetric isomers

The candidate has carried out the experiments and collected data for new infrared bands, re-measured previously recorded data with increased signal to noise ratio, and performed post-experiment data manipulation and processing.

List of Publications and Presentations

Refereed Journals

[1] M. Rezaei, **J. Norooz Oliaee**, N. Moazzen-Ahmadi, and A.R.W. McKellar, "Infrared spectrum of the CS_2 tetramer: Observation of a structure with D_{2d} symmetry," Accepted for publication in Chemical Physics Letters. DOI:10.1016/j.cplett.2013.03.074.

[2] **J. Norooz Oliaee**, M. Dehghany, N. Moazzen-Ahmadi, and A.R.W. McKellar, "Fundamental and torsional combination bands of the OCS$-CO_2$ complex in the CO_2 ν_3 region," Accepted for publication in Journal of Physical Chemistry A (in print).
DOI:10.1021/jp312339w.

[3] M. Rezaei, **J. Norooz Oliaee**, N. Moazzen-Ahmadi, and A.R.W. McKellar, "Spectroscopic observation of nitrous oxide pentamers," *Journal of Chemical Physics* **136**, 224308 (2012). DOI:10.1063/1.4729157.

[4] **J. Norooz Oliaee**, N. Moazzen-Ahmadi, and A.R.W. McKellar, "New spectroscopic results on acetylene dimers and trimers," *Molecular Physics* **110**, 2797 (2012).
DOI:10.1080/00268976.2012.697588.

[5] **J. Norooz Oliaee**, A.R.W. McKellar, and N. Moazzen-Ahmadi, "Observation of a planar isomer of the OCS$-(C_2H_2)_2$ trimer," *Chemical Physics Letters* **512**, 167 (2011). DOI:10.1016/j.cplett.2011.07.017.

[6] **J. Norooz Oliaee**, M. Dehghany, A.R.W. McKellar, and N. Moazzen-Ahmadi, "High resolution infrared spectroscopy of carbon dioxide clusters up to $(CO_2)_{13}$," *Journal of Chemical Physics* **135**, 044315 (2011). DOI:10.1063/1.3615543.

[7] M. Rezaei, **J. Norooz Oliaee**, N. Moazzen-Ahmadi, and A.R.W. McKellar, "Infrared spectrum of the CS_2 trimer: Observation of a structure with D_3 symmetry," *Physical Chemistry and Chemical Physics* **13**, 12635 (2011). DOI:10.1039/C1CP20900K.

[8] M. Rezaei, **J. Norooz Oliaee**, N. Moazzen-Ahmadi, and A.R.W. McKellar, "Spectro-

scopic observation and structure of CS_2 dimer," *Journal of Chemical Physics* **134**, 144306 (2011). DOI:10.1063/1.3578177.

[9] C. Lauzin, **J. Norooz Oliaee**, M. Rezaei, and N. Moazzen-Ahmadi, "The weakly-bound CO_2-acetylene complex: Fundamental and torsional combination band in the CO_2 ν_3 region," *Journal of Molecular Spectroscopy* **267**, 19 (2011). DOI:10.1016/j.jms.2011.01.008.

[10] **J. Norooz Oliaee**, M. Dehghany, N. Moazzen-Ahmadi, and A.R.W. McKellar, "Nitrous oxide tetramer has two highly symmetric isomers," *Journal of Chemical Physics* **134**, 074310 (2011). DOI:10.1063/1.3555629.

[11] **J. Norooz Oliaee**, M. Dehghany, N. Moazzen-Ahmadi, and A.R.W. McKellar, "Spectroscopic identification of carbon dioxide clusters: $(CO_2)_6$ to $(CO_2)_{13}$," *Physical Chemistry and Chemical Physics* **13**, 1297 (2011). DOI:10.1039/C0CP02311F.

Featured article in Chemistry World News, January 2011.

[12] **J. Norooz Oliaee**, F. Mivehvar, M. Dehghany, and N. Moazzen-Ahmadi, "Infrared spectroscopic investigation of two isomers of the weakly bound complex OCS$-(CO_2)_2$," *Journal of Physical Chemistry A* **114**, 12834 (2010). DOI:10.1021/jp107839k.

[13] **J. Norooz Oliaee**, F. Mivehvar, M. Dehghany, and N. Moazzen-Ahmadi, "Geometric isomerism in the OCS$-CS_2$ complex: Observation of a cross-shaped isomer," *Journal of Physical Chemistry A* **114**, 7311 (2010). DOI:10.1021/jp104305r.

[14] M. Dehghany, **J. Norooz Oliaee**, Mahin Afshari, N. Moazzen-Ahmadi, and A.R.W. McKellar, "Infrared spectra of OCS$-C_6H_6$, OCS$-C_6H_6-$He and OCS$-C_6H_6-$Ne van der Waals complexes," *Journal of Chemical Physics* **132**, 194303 (2010). DOI:10.1063/1.3430571.

[15] Mahin Afshari, M. Dehghany, **J. Norooz Oliaee**, and N. Moazzen-Ahamdi, "Infrared spectra of the OCS$-N_2O$ complex and observation of a new isomer," *Chemical Physics Letters* **489**, 30-34 (2010). DOI:10.1016/j.cplett.2010.02.041.

[16] **J. Norooz Oliaee**, M. Dehghany, Mahin Afshari, N. Moazzen-Ahmadi, and A.R.W. McKellar, "Ubiquitous T-shaped isomers of OCS-hydrocarbon van der Waals complexes,"

Journal of Chemical Physics **131**, 161105 (2009).

DOI:10.1063/1.3257934.

[17] **J. Norooz Oliaee**, Mahin Afshari, M. Dehghany, N. Moazzen-Ahmadi, and A.R.W. McKellar, "Infrared spectra of two isomers of OCS$-C_2H_2$ and OCS$-C_2D_2$ in the region of OCS ν_1 fundamental," *Journal of Molecular Spectroscopy* **257**, 133-136 (2009).

DOI:10.1016/j.jms.2009.07.003.

[18] M. Dehghany, **J. Norooz Oliaee**, Mahin Afshari, N. Moazzen-Ahmadi, and A.R.W. McKellar, "Infrared spectra of the OCS$-CO_2$ complex: observation of two distinct slipped near-parallel isomers," *Journal of Chemical Physics* **130**, 224310 (2009).

DOI:10.1063/1.3152743.

[19] M. Dehghany, Mahin Afshari, **J. Norooz Oliaee**, N. Moazzen-Ahmadi, and A.R.W. McKellar, "The weakly bound nitrous oxide-acetylene complex: fundamental and torsional combination bands of $N_2O-C_2H_2$ and $N_2O-C_2D_2$ in the N_2O ν_1 region," *Chemical Physics Letters* **473**, 26-29 (2009). DOI:10.1016/j.cplett.2009.03.037.

Conference Presentations

[1] **J. Norooz Oliaee**, M. Rezaei, N. Moazzen-Ahmadi, and A.R.W. McKallar, "New spectroscopic results on acetylene dimers and trimers," *Canadian Association of Physicists*, University of Calgary, Alberta, Canada (2012); Also presented in *95th Canadian Chemistry Conference*, Calgary, Alberta, Canada (2012).

[2] M. Rezaei, **J. Norooz Oliaee**, and N. Moazzen-Ahmadi, "Infrared diode laser spectroscopy of the weakly-bound N_2O-CS_2 complex," *95th Canadian Chemistry Conference*, Calgary, Alberta, Canada (2012).

[3] F. Mivehvar, **J. Norooz Oliaee**, and N. Moazzen-Ahmadi, "Infrared spectra of He$-CS_2$, Ne$-CS_2$ and Ar$-CS_2$," *66th International Symposium on Molecular Spectroscopy*, Ohio State University, Columbus, OH, USA (2011).

[4] C. Lauzin, **J. Norooz Oliaee**, M. Rezaei, and N. Moazzen-Ahmadi, "The weakly-bound CO_2-Acetylene complex: fundamental and torsional combination band in the CO_2 ν_3 region," *66th International Symposium on Molecular Spectroscopy*, Ohio State University, Columbus, OH, USA (2011).

[5] **J. Norooz Oliaee**, M. Dehghany, F. Mivehvar, Mahin Afshari, N. Moazzen-Ahmadi, and A.R.W. McKellar, "Fundamental and torsional combination bands of two isomers of the OCS$-CO_2$ complex," *65th International Symposium on Molecular Spectroscopy*, Ohio State University, Columbus, OH, USA (2010).

[6] M. Dehghany, **J. Norooz Oliaee**, Mahin Afshari, N. Moazzen-Ahmadi, and A.R.W. McKellar, "Infrared spectra of OCS$-C_6H_6$, OCS$-C_6H_6-$He and OCS$-C_6H_6-$Ne van der Waals complexes," *65th International Symposium on Molecular Spectroscopy*, Ohio State University, Columbus, OH, USA (2010).

[7] **J. Norooz Oliaee**, M. Dehghany, Mahin Afshari, N. Moazzen-Ahmadi, and A.R.W. McKellar, "Infrared spectroscopy of two isomers of the OCS$-CS_2$ complex," *64th International Symposium on Molecular Spectroscopy*, Ohio State University, Columbus, OH, USA (2009).

Poster Presentations

[1] M. Rezaei, **J. Norooz Oliaee**, and N. Moazzen-Ahmadi, "Infrared diode laser spectroscopy of the weakly-bound N_2O-CS_2 complex," *Canadian Association of Physicists*, University of Calgary, Alberta, Canada (2012).

[2] **J. Norooz Oliaee**, M. Dehghany, N. Moazzen-Ahmadi, and A.R.W. McKellar, "Spectroscopic identification of carbon dioxide clusters: $(CO_2)_6$ to $(CO_2)_{13}$," *Alberta Quantum-Nano Workshop*, Red Deer, Alberta, Canada (2011).

[3] **J. Norooz Oliaee**, F. Mivehvar, M. Dehghany, N. Moazzen-Ahmadi, and A.R.W. McKellar, "Structures of two isomers of nitrous oxide tetramer from their infrared spectra," *Canadian Association of Physicists Congress*, University of Toronto, Toronto, Ontario, Canada

(2010).

[4] **J. Norooz Oliaee**, M. Dehghany, F. Mivehvar, Mahin Afshari, N. Moazzen-Ahmadi, and A.R.W. McKellar, "Fundamentals and torsional combination bands of two isomers of the OCS−CO_2 complex," *Canadian Association of Physicists Congress*, University of Toronto, Toronto, Ontario, Canada (2010).